Scuola Internazionale Superiore di Studi Avanzati - Trieste

Area of Physics
Group of Astroparticle Physics

Neutrinos and voids in modern cosmology

Thesis Submitted for the Degree of
"Doctor Philosophiae"

Supervisors:
Matteo Viel
Ravi K. Sheth

Candidate:
Elena Massara

Academic year 2015/2016

SISSA - Via Bonomea 265 - 34136 TRIESTE - ITALY

Abstract

This thesis deals with the study of the large scale structure in the nonlinear regime. In particular, it focuses on two main topics: the impact of massive neutrinos on the cosmic web and the modeling of void profiles and void bias.

Neutrinos are known to be massive particles and thus to participate to the matter content of the Universe and to its evolution. In this era of precision cosmology, the analysis of observational datasets must account for neutrinos, both because cosmology can put strong constraints on the sum of their masses, and because ignoring them can bias the estimation of other cosmological parameters. Having this in mind, we provide a theoretical model to describe the nonlinear matter power spectrum in massive neutrino cosmologies. This model is obtained by generalizing the already existing halo model, to account for the presence of massive neutrinos. Then, we also discuss the clustering of galaxies in the same framework and provide a comparison with N-body simulations.

A promising environment where to study neutrinos is represented by cosmic voids. We perform a numerical analysis of statistical properties of voids, identified both in ΛCDM and massive neutrino cosmologies. The aim of this project is to understand how neutrinos change the void properties and which of them are more sensitive to their presence. This is the starting point for thinking about constraining neutrino masses using cosmic voids.

Voids are very interesting objects, that have been studied much less than halos and clusters. We present here a model for describing the void density profile. In particular, we present different models describing the abundance and spatial distribution of both halos and voids in the Lagrangian field, and explain how they can be applied to compute density profiles. Then, we evolve these Lagrangian profiles to the Eulerian space, where actual measurements are performed. We discuss the evolution described by the spherical model and the Zel'dovich approximations. Since the density profile around tracers is the cross-correlation between the tracers and the matter field, this quantity is sensitive to the bias of tracers with respect to the matter field. We discuss the void linear bias in Lagrangian and Eulerian space, and how it differs from the linear bias of halos.

List of publications

This thesis is the result of the research done during my Ph.D. in collaboration with M. Viel, R. K. Sheth, F. Villaescusa-Navarro and P. M. Sutter. It is based on the following papers:

- E. Massara, F. Villaescusa-Navarro and M.Viel, *The halo model in a massive neutrino cosmology*, *JCAP* **12** (Dec., 2014) 53, [arXiv:1410.6813].
- E. Massara, F. Villaescusa-Navarro, M. Viel, and P.M. Sutter, *Voids in massive neutrino cosmologies*, *JCAP* **11** (2015) 018, [arXiv:1506.03088].
- E. Massara and R. K. Sheth, *Density profiles around biased tracers of the cosmic web*, in preparation.

Foreword

N-body simulations show that the spatial distribution of matter in the Universe resembles a network, the so called cosmic web. The knots of this network represent highly dense regions, called halos, which are the main hosts of the galaxies we observe. Halos are connected by filaments, i.e. relatively thin and low density regions; between knots and filaments, voids are the less dense portions of the cosmic web. Nowadays, we have a good understanding of the evolution of the cosmological structures at the linear perturbation level, but we lack a description at the fully nonlinear level. This regime needs to be understood in order to interpret the observations of sky surveys.

In the Standard Cosmological Model, the majority of the matter content of the Universe is in the form of Cold Dark Matter (CDM), which forms the cosmic web together with baryons. However, a third species of massive particle is also known to fill the Universe: the neutrinos. The standard model of particle physics describe neutrinos as fermions of spin 1/2, neutral and massless. However, neutrino oscillation experiments have pointed out that they are massive (see [42, 72] for review), giving one of the clearest evidences pointing towards the existence of physics beyond the standard model. In this era of precision cosmology, the analysis of observational datasets must account for neutrinos, both because cosmology can put strong constraints on the sum of their masses, and because ignoring them can bias the estimation of other parameters.

This thesis is dedicated to the study of structures in the fully nonlinear regime, also in the presence of massive neutrinos.

In the first part we introduce all the main results achieved in the literature that are useful to understand the original work presented later. In particular, in Chapter 1 we review the statistical description of a random Gaussian field - which is how the matter density field in the early Universe is usually described - and the models describing the statistics of extrema of the density field. In Chapter 2 we focus on the minima of the matter field, i.e. the cosmic voids. A review of massive neutrinos and their impact at the linear level is presented in Chapter 3, together with an explanation of numerical tools to describe their nonlinear regime. Chapter 4 presents the N-body simulations and the void finder used in this thesis.

In Part II we present a theoretical model to quantify the effects of massive neutrinos on the matter power spectrum. Although N-body simulations allow to model these effects, they are computationally expensive and do not directly provide physical insight. A physically motivated model, the halo model, has been developed in the framework of the ΛCDM paradigm (where neutrinos are massless particles) in order to describe the clustering of matter at the nonlinear level. In Chapter 5 we review this model and in Chapter 6 we extend it to account for the presence of massive neutrinos, as

follows. Massive neutrinos have large, although non-relativistic, thermal velocities at low redshift. These large thermal velocities prevent their clustering within CDM halos. However, neutrinos from the low-velocity tail of the momentum distribution can cluster within the halo potential wells. Thus, we model the neutrino field as the sum of two components: a smoothed linear part and a clustered non-linear one. Two other important ingredients of the halo model are the halo mass function and bias, which have to be computed as a function of the linear CDM power spectrum only (not CDM+neutrinos) in order for the former to be universal and for the latter to be scale independent on large scale (as pointed out by [23]). The halo model can describe the clustering of galaxy as well. In Chapter 7 we present its extension to massive neutrino cosmologies, assuming an Halo Occupation Distribution (HOD) framework.

Part III shows how the presence of massive neutrinos modifies the statistical properties of cosmological voids. Voids, as elements of the cosmic web, can in principle be used as a complementary probe to halos for constraining neutrino masses. It is therefore important to understand how massive neutrinos impact their properties. Here, we perform a comprehensive numerical study of the statistical properties of voids, identified both in the matter and galaxy distributions, looking at relative differences arising in different cosmologies due to the presence of massive neutrinos. We analyze several independent N-body simulations with cold dark matter and neutrino particles in cosmologies with different values for the neutrino masses. Galaxies were modeled by populating the dark matter halos in simulations via an HOD. The properties considered are: void abundance, void density and velocity profiles, and void correlation function.

Part IV focuses on voids in ΛCDM cosmology (where neutrinos are massless) and presents a model to describe the void density profiles. In the past few years many studies addressed the phenomenology of void profiles from N-body simulations and real galaxy observations, but a theoretical understanding of these findings is still missing and highly needed. Here, we develop a theoretical description for the void density profiles as the cross-correlation between the voids and the matter field. The model is built on excursion set arguments in the initial Lagrangian space, as shown in Chapter 10. A description of their nonlinear evolution from the Lagrangian to the Eulerian space, together with their time evolution in the latter, are presented in Chapter 11. Having a model for the void profiles is useful for many purposes, e.g. the study and test of modified theories of gravity since voids are under-dense regions where some screening mechanisms are expected not to work.

Contents

Part I

Introduction

Chapter 1

Statistics of extrema

In the standard cosmological paradigm, the structures that we see today are thought to form from the evolution of primordial matter density perturbations, via gravitational instability. The early Universe was almost homogeneous with some small amplitude density fluctuations set by inflation: a short but violent period in which the universe expanded so fast that quantum fluctuations were stretched outside the horizon scale, becoming classical perturbations of the density field. We will assume them to be Gaussian, even if many inflationary models predict the presence of primordial non-gaussianities. As the universe evolves, perturbations grow under the influence of gravity, which introduces some late non-gaussianities. The growth is linear until the amplitude of perturbations is small, then the evolution becomes nonlinear and leads to the formation of the complex structures that we see today.

In this chapter we describe the statistical properties of the linear matter perturbations at early times and explain how the linear regime can be used to predict fully nonlinear quantities at later times, in a statistical sense. First, we review the important statistical quantities for describing the matter density field and present its evolution using linear theory and the spherical collapse model. Then we will discuss the theory for predicting the abundance of structures in the universe, i.e. the excursion set theory and the excursion set of peaks. In this last part we will focus on the maxima extrema of the density field, the overdensities, since these models have been developed for describing the statistics of halos, rather then voids. However, they can be generalized to underdensities as well. We discuss this case in Chapter 2 and Part IV.

Notice that here we consider the cold dark matter as the only matter component in the Universe. We discuss the presence of neutrinos in Chapter 3.

1.1 Linear density field and evolved objects

1.1.1 The initial Gaussian random field

The matter density fluctuations can be described in terms of the density contrast,

$$\delta(\vec{x}) \equiv \frac{\rho(\vec{x})}{\bar{\rho}} - 1\,, \tag{1.1}$$

where $\rho(\vec{x})$ is the matter density at the comoving position $\vec{x}$ and $\bar{\rho} = \langle \rho(\vec{x}) \rangle$ is the mean background density. The average $\langle ... \rangle$ is taken over all space. The real space density

contrast can be written as a sum over Fourier modes,

$$\delta(\vec{x}) = \int \frac{d^3k}{(2\pi)^3}\, \delta(\vec{k})\, e^{-i\vec{k}\cdot\vec{x}}\,, \tag{1.2}$$

with inverse Fourier transform,

$$\delta(\vec{k}) = \int d^3x\, \delta(\vec{x})\, e^{i\vec{k}\cdot\vec{x}}\,. \tag{1.3}$$

The primordial density contrast is a statistically homogeneous and isotropic Gaussian random field with mean value equal to zero, by definition. The two point correlation function, $\langle\delta(\vec{x}_1)\delta(\vec{x}_2)\rangle = \xi(\vec{x}_1,\vec{x}_2)$, is then invariant under translations and rotations, which means that it is only function of the separation distance $r = |\vec{x}_1 - \vec{x}_2|$ between the two points where it is evaluated. It has the form

$$\xi(r) = \int \frac{d^3k}{(2\pi)^3}\, P(k)\, e^{-i\vec{k}\cdot\vec{x}} = \int \frac{k^3}{2\pi^2}\, P(k)\, \frac{\sin(kr)}{kr} d\ln k\,, \tag{1.4}$$

where we used the definition for the power spectrum $P(k)$,

$$\langle\delta(\vec{k}_1)\delta(\vec{k}_2)\rangle \equiv (2\pi)^3\delta_{\rm D}(\vec{k}_1+\vec{k}_2)P(k_1)\,. \tag{1.5}$$

The power spectrum has the dimension of a volume and it is often convenient to use its dimensionless form,

$$\Delta^2(k) \equiv \frac{k^3P(k)}{2\pi^2}\,. \tag{1.6}$$

In the standard scenario overdense patches in the initial density field are expected to evolve into galaxies and clusters, while underdense regions should give rise to voids. The way to describe patches is to smooth the initial density field at their characteristic scale. Moreover, in N-body simulations and in surveys we observe the density field averaged at some resolution scale. Therefore, a relevant quantity is the initial density field $\delta(\vec{x},R)$ smoothed by some window function $W(R)$ at scale R,

$$\delta(\vec{x},R) \equiv \int d^3y\, \delta(\vec{y})\, W(|\vec{y}-\vec{x}|,R)\,, \tag{1.7}$$

where $W(R) = W'(R)/V_R$ has units of inverse volume, W' is a dimensionless window and V_R is its associated volume $V_R = \int d^3x W'(x)$. A convolution in real space become a product in momentum space, where the smooth density is simply,

$$\delta(\vec{k},R) = W(\vec{k},R)\delta(\vec{k})\,, \tag{1.8}$$

with $W(\vec{k},R)$ being the Fourier transform of the window function. The window function can have arbitrary shapes. The ones commonly used in cosmology and adopted in this thesis are three:

a) Top-hat in real space,

$$W(r,R) = \Theta(1-r/R)\left(4\pi/3R^3\right)^{-1}\,, \tag{1.9}$$

$$W(k,R) = \left[3/t^3\right](\sin t - t\cos t)\,, \quad t\equiv kR\,, \tag{1.10}$$

b) Gaussian:

$$W(r,R) = \exp\left[-(r/R)^2/2\right]\sqrt{2\pi R^2}\,, \quad (1.11)$$
$$W(k,R) = \exp(-k^2R^2/2)\,, \quad (1.12)$$

c) Sharp k-space:

$$W(r,R) = \left[3/t^3\right](\sin t - t\cos t)\left(4\pi/3R^3\right), \quad t \equiv r/R\,, \quad (1.13)$$
$$W(k,R) = \Theta(1-kR)\,. \quad (1.14)$$

In real space, the top-hat filter acts averaging the density field inside a sphere of radius R. In this case, the volume of the filter is well defined and the associated mass is $M = 4\pi R^3\bar{\rho}/3$. This is not the case for the sharp-k and the gaussian windows, which are however used because they are convenient from the analytic point of view. Moreover, it has been recently shown that halos identified in simulations should be described by a combinations of gaussian and top-hat windows in the initial conditions (ICs) [25].

The variance of the smoothed field is,

$$s_0^R \equiv \sigma^2(R) = \langle\delta(\vec{x},R)^2\rangle = \int d\ln k\,\Delta^2(k)W(kR)^2\,, \quad (1.15)$$

from which is clear that $\Delta^2(k)$ is the contribution to the variance from modes in a logarithmic interval in wavenumber. At late times, the variance is computed using the initial power spectrum, evolved to a later time via linear theory. The linear evolution will be described in the following section.

We can generalize the definition of variance as follows,

$$s_j^{RR'} \equiv \sigma_j^2(R,R') = \int d\ln k\,k^{2j}\Delta^2(k)W(kR)W(kR')\,, \quad (1.16)$$

where the density field has been smoothed at two different scales, R and R'. We will use these quantities in Part IV.

1.1.2 Linear theory

Let us describe how the initial Gaussian density fluctuations evolve via gravitational instability, using linear theory.

The evolution of the matter density is described by the Euler equation,

$$\frac{\partial(a\vec{v})}{\partial t} + (\vec{v}\cdot\vec{\nabla}_x)\vec{v} = -\frac{1}{\rho}\vec{\nabla}_x P - \vec{\nabla}_x\Phi, \quad (1.17)$$

the continuity equation,

$$\frac{\partial\rho}{\partial t} + 3H\rho + \frac{1}{a}\vec{\nabla}_x\cdot(\rho\vec{v}) = 0, \quad (1.18)$$

and the Poisson equation,

$$\nabla_x^2\Phi = 4\pi G a^2(\rho-\bar{\rho}), \quad (1.19)$$

where Φ is the gravitational potential, P is the pressure, a is the scale factor, H is the Hubble parameter and $\vec{v}(\vec{x},t) = a(t)\dot{\vec{x}}(t)$ is the peculiar velocity (overdots denote derivatives with respect to t).

The matter density can be written in terms of the density contrast as in Eq. (1.1). In the same way the quantities $\vec{v}$ and Φ can be expressed in terms of perturbations with respect to the background. For simplicity we replace the last quantities with their perturbation terms. Being in the linear regime means that $\delta \ll 1$, $|v| \ll 1$ and $|\Phi| \ll 1$. Then Eqs. (1.17), (1.18) and (1.19) can be linearized as,

$$\frac{\partial(\vec{v})}{\partial t} + H\vec{v} = -\frac{\vec{\nabla}_x P}{\rho a} - \frac{\vec{\nabla}_x \Phi}{a}\,, \tag{1.20}$$

$$\frac{\partial \delta}{\partial t} = -\frac{1}{a}\vec{\nabla}_x \cdot \vec{v}\,, \tag{1.21}$$

$$\nabla_x^2 \Phi = 4\pi G a^2 \bar{\rho}\delta\,, \tag{1.22}$$

respectively. These relations provide a good description of gravitational instability at very early times and from them we can obtain a second order differential equation for the density contrast $\delta(\vec{x})$,

$$\frac{\partial^2 \delta}{\partial t^2} + 2H\frac{\partial \delta}{\partial t} - 4\pi G\bar{\rho}\delta = \frac{\nabla_x^2 P}{\bar{\rho}a^2}. \tag{1.23}$$

Cold dark matter is a pressureless fluid with initial isentropic perturbations, i.e. it does not have initial entropy perturbations. In this case Eq. (1.23) reduces to

$$\frac{\partial^2 \delta}{\partial t^2} + 2H\frac{\partial \delta}{\partial t} - 4\pi G\bar{\rho}\delta = 0\,. \tag{1.24}$$

In a matter-dominated spatially flat Universe the mean density has the behavior $\bar{\rho} \sim t^{-2}$ [38]. If we demand that the solution take the form $\delta(\vec{x}, t) = D(t)\delta(\vec{x})$, then Eq.(1.24) admits two linear independent solutions $\delta(\vec{x}, t) = D_{\pm}(t)\delta(\vec{x})$, where

$$D_+(t) \propto a(t) \propto t^{2/3} \tag{1.25}$$

$$D_-(t) \propto a(t)^{-3/2} \propto t^{-1} \tag{1.26}$$

are the growing and decaying modes, respectively. The final solution will be a superposition of the two. However, at early times all fluctuations were very small and it is reasonable to assume that at more recent epochs only the growing mode has a significant amplitude. For a ΛCDM cosmology, the linear growth factor D_z evolves as

$$D_z \equiv D_+(z) = \frac{5}{2}\Omega_m H(z)\int_z^\infty dz \frac{1+z}{H(z)^3}\,, \tag{1.27}$$

where Ω_m is the matter density today and $H(z)$ is the Hubble parameter at redshift z.

In general, for isentropic initial perturbations with adiabatic evolution the pressure variation is $\vec{\nabla}_x P = (\partial P/\partial\rho)\vec{\nabla}_x\rho = c_s^2\vec{\nabla}_x\rho$, where $c_s \equiv \sqrt{\partial P/\partial\rho}$ is the adiabatic sound speed and $\vec{\nabla}_x\rho = \bar{\rho}\,\vec{\nabla}_x\delta$. Then Eq.(1.23) yields

$$\frac{\partial^2 \delta}{\partial t^2} + 2H\frac{\partial \delta}{\partial t} - \left[4\pi G\bar{\rho} + \left(\frac{c_s}{a}\right)^2 \nabla_x^2\right]\delta = 0. \tag{1.28}$$

In Fourier space it becomes

$$\ddot{\delta}_k + 2H\dot{\delta}_k + \omega_k^2\delta_k = 0\,, \qquad \omega_k^2 \equiv \frac{k^2 c_s^2}{a^2} - 4\pi G\bar{\rho}\,. \tag{1.29}$$

This equation describes a damped oscillator where the damping is due to the expansion of the Universe via the Hubble parameter. The condition $\omega_k^2 = 0$ defines the so-called Jeans-wavenumber, k_J,

$$k_J \equiv \frac{a\sqrt{4\pi G\bar{\rho}}}{c_s}. \tag{1.30}$$

Matter density perturbation with length $\lambda > \lambda_J = 2\pi a/k_J$ remain unaffected by pressure force and continue to grow in accordance with Eq.(1.24). On the other hand, small scale perturbations, $\lambda < \lambda_J = 2\pi a/k_J$, feel the effects of pressure gradients and oscillate as acoustic waves with a decreasing amplitude.

1.1.3 Spherical collapse model

Growing modes D_+ of the cold dark matter perturbations evolve, increasing their amplitude, into high density regions and lead to gravitational collapse of matter. During this process the density contrast becomes $\delta \gg 1$ and linear theory breaks down. The simplest description for the evolution of perturbations into collapse objects is given by the spherical collapse model, which is a nonlinear approximation that involves extrapolations of linear properties of the density field into the nonlinear regime. The description of this model is given in the following; the Lagrangian space will be the frame where small perturbations are evolved using linear theory, while the Eulerian space will be the one where perturbations have undergone fully nonlinear evolution.

We assume a zero-pressure and collision-less fluid. These assumptions describe cold dark matter, but do not apply to baryons. Indeed the later stages of collapse for baryons would be different from that of cold dark matter but, since they constitute only a small fraction of the total mass, this does not significantly affect the collapse of cold dark matter.

Since the temperature anistropies of the cosmic microwave background (CMB) are of the order of 10^{-5}, the matter fluctuations were very small at the time of photon decoupling and the nonlinear collapse of structures happened during matter or Λ domination. For simplicity, in this section we consider a flat matter dominated universe, also called Einstein–de Sitter universe, with $\Omega = \Omega_m = 1$. A generalization to ΛCDM cosmology is then possible.

Let us consider a spherical perturbation expanding in the homogeneous and isotropic background. In particular we consider a patch with initial radius R_i and uniform density $|\delta_i| \ll 1$, i.e. the density of a region smoothed with a top-hat filter at scale R_i. The mass inside this region is $M_i = 4\pi R_i^3 \bar{\rho}(1+\delta_i)/3$. The density parameter Ω' associated to the patch is different from the one of the background universe, Ω. A patch with $\Omega' > \Omega$ corresponds to an overdensity and it will evolve like a close universe ($\Omega' > 1$): it will expand to maximum size, turn around and then collapse. A spherical region with $\Omega' < \Omega$ corresponds to an underdensity and it will mimic an open universe ($\Omega' < 1$): it will always expand. Therefore, over and under dense regions in the initial field are thought to be proto-halos and proto-voids that will evolve into halos and voids, respectively.

The conservation of energy applied to the considered spherical region guarantees that

$$E = \frac{1}{2}\dot{R}^2 - \frac{GM}{R} = \text{const}\,, \tag{1.31}$$

where R and M are the radius and the mass of the region at generic time. Since the mass is conserved inside the patch, $M = M_i$ always. The equations of motion for the radius $R(t)$ can be found in a parametric way by integrating Eq.(1.18) and performing a change of variables,

$$\begin{aligned} R &= A(1-\cos\theta) \\ t &= B(\theta-\sin\theta) \end{aligned} \tag{1.32}$$

for $E < 0$ corresponding to $\delta_i > 0$, and

$$\begin{aligned} R &= A(\cosh\theta-1) \\ t &= B(\sinh\theta-\theta) \end{aligned} \tag{1.33}$$

for $E > 0$ corresponding to $\delta_i < 0$. The parameters A and B are,

$$A = \frac{GM}{2|E|}, \qquad B = \frac{GM}{(2|E|)^{3/2}}. \tag{1.34}$$

Overdensities

Let us focus on the overdensities. The solution in Eq.(1.32) implies that the sphere expands from $R = 0$ at $\theta = 0$, reaches a maximum radius $R_{\rm ta} = A$ at $\theta = \pi$, turn around and then it collapses back to $R = 0$ at $\theta = 2\pi$. The corresponding times are $t_{\rm ta} = \pi B$ for the maximum (or turnaround) radius, and $t_{\rm col} = 2\pi B = 2t_{\rm ta}$ for the collapse to $R = 0$. In principle the mass re-expands, actually other physical effects prevent this. Moreover, at collapse $R(t_{\rm col}) = 0$ and the density should be infinite. We will discuss all of this later.

Using Eq.(1.32), the mean density inside the sphere is given by

$$\rho(t) = \frac{3M}{4\pi R^3} = \frac{3M}{4\pi A^3}\frac{1}{(1-\cos\theta)^3}. \tag{1.35}$$

In a flat matter dominated Universe the background density reads [38]

$$\bar\rho(t) = \frac{1}{6\pi G t^2} = \frac{1}{6\pi G B^2}\frac{1}{(\theta-\sin\theta)^2}, \tag{1.36}$$

where the last expression is obtained using the solution (1.32). Then in Eulerian space the density contrast (generally nonlinear) inside the sphere is given by

$$\delta = \frac{\rho}{\bar\rho} - 1 = \frac{9(\theta-\sin\theta)^2}{2(1-\cos\theta)^3} - 1. \tag{1.37}$$

It is interesting to investigate the connection of the above equation with linear theory. Start considering the behavior of δ at small t, which corresponds to small θ. We can expand in Taylor series $\sin\theta$ and $\cos\theta$, for $\theta \ll 1$, which corresponds to $t \ll 1$. Thus, the density contrast at $t \ll t_{\rm ta}$ is given by

$$\delta \simeq \frac{3}{20}(6\pi)^{2/3}\left(\frac{t}{t_{\rm ta}}\right)^{2/3}, \tag{1.38}$$

which reproduce the growing mode of the linear perturbation theory $\delta \propto t^{2/3}$. For some early time $t_i \ll t_{\rm ta}$ we have $\delta = \delta_i$ given by

$$\delta_i = \frac{3}{20}(6\pi)^{2/3}\left(\frac{t_i}{t_{\rm ta}}\right)^{2/3}. \tag{1.39}$$

From now on, we distinguish between the Eulerian nonlinear overdensity $\delta_{\rm E}$ and the Lagrangian overdensity $\delta_{\rm L}$, extrapolated at the same time according to linear theory. By definition, for all t the latter evolves as,

$$\delta_{\rm L}(t) = \delta_i\left(\frac{t}{t_i}\right)^{2/3} = \frac{3}{20}(6\pi)^{2/3}\left(\frac{t}{t_{\rm ta}}\right)^{2/3}. \tag{1.40}$$

Let us compute the different values of $\delta_{\rm E}$ and $\delta_{\rm L}$ at specific times. At the turnaround, $t = t_{\rm ta}$, the Lagrangian overdensity is

$$\delta_{\rm L}(t_{\rm ta}) = \frac{3}{20}(6\pi)^{2/3} = 1.062, \tag{1.41}$$

while, using Eq.(1.37), the actual nonlinear overdensity is given by

$$1 + \delta_{\rm E}(t_{\rm ta}) = \frac{9\pi^2}{16} = 5.55. \tag{1.42}$$

At the collapse, $t = t_{\rm col} = 2t_{\rm ta}$, the Eulerian density is infinite and linear one reads,

$$\delta_{\rm sc} \equiv \delta_{\rm L}(t_{\rm col}) = \frac{3}{20}(12\pi)^{2/3} = 1.686\,. \tag{1.43}$$

The quantity $\delta_{\rm sc}$ is very important since it describes the value for the initial overdensity, linearly evolved at $t_{\rm coll}$, that will form a halo in the Eulerian space. Therefore, it is assumed to be the threshold scale in the Lagrangian space for the spherical collapse to happen. Its value is weakly sensitive to the cosmology [62], and Eq.(1.43) can be consider valid also in ΛCDM.

According to the spherical collapse model, a uniform sphere collapses down to a point with infinite density before re-expanding, but this is not physically realistic. In reality, the sphere will contain density inhomogeneities, which will generate random velocities in the dark matter during the collapse, leading to an equilibrium configuration in which the velocity dispersion of the dark matter balances its gravity. This dynamical process is called virialization. We therefore assume that the final dark matter sphere, the halo, is in dynamical equilibrium and so obeys the virial theorem:

$$2K_f + U_f = 0. \tag{1.44}$$

K_f is the final total kinetic energy in random motions which reads $K_f = M\sigma_v^2/2$, where σ_v is the velocity dispersion, $U_f = -(3/5)(GM^2/R_{\rm vir})$ is the total gravitational binding energy and $R_{\rm vir}$ is the radius of the virialized object. At maximum expansion, the sphere is at rest, so the kinetic energy vanishes. The total energy at the turnaround is then $E_{\rm ta} = U_{\rm ta} = -3GM^2/(5R_{\rm ta})$. The total energy of the sphere is conserved during the collapse since we assumed that the dark matter is collisionless. Thus, the radius of the virialized object is $R_{\rm vir} = R_{\rm ta}/2$ and the final density is 8 times the density

at turnaround. Virialization can be considered to happen at $t_{\rm vir} \simeq t_{\rm col}$. Then, since the background density varies as $\bar{\rho} \propto t^{-2}$ in a flat matter-dominated Universe and $t_{\rm col} = 2t_{\rm ta}$, the background density at turnaround is 4 times the background density at virialization. Finally, we obtain that the ratio $\Delta_{\rm vir}$ between the viarialized object's density and the background density at virialization is

$$\Delta_{\rm vir} \equiv \frac{\rho(t_{\rm vir})}{\bar{\rho}(t_{\rm vir})} = \left(\frac{\rho(t_{ta})}{\bar{\rho}(t_{ta})}\right)\left(\frac{\rho(t_{\rm vir})}{\rho(t_{ta})}\right)\left(\frac{\bar{\rho}(t_{ta})}{\bar{\rho}(t_{\rm vir})}\right) = \frac{9\pi^2}{16} \times 8 \times 4 = 18\pi^2. \tag{1.45}$$

This result is valid for an Einstein–de Sitter universe and extensions to other cosmologies has been computed (see e.g. [19]). For the ΛCDM model, the same quantity is

$$\Delta_{\rm vir} = \frac{18\pi^2 + 82x - 39x^2}{1+x}\,, \tag{1.46}$$

with $x \equiv \Omega(z) - 1$ and

$$\Omega(z) = \frac{\Omega_{\rm m}(1+z)^3}{\Omega_{\rm m}(1+z)^3 + \Omega_\Lambda}\,, \tag{1.47}$$

where $\Omega_{\rm m}$ is the CDM plus baryons density and Ω_Λ is the cosmological constant density, both evaluated at present time. Consequently, the virial radius $R_{\rm vir}$ of a halo is generally defined as the radius of a sphere with mean density equal to $\Delta_{\rm vir}$ times matter background density of the universe.

Underdensities

Underdense spherical regions evolve differently from overdensities. The density contrast inside these regions can be find in analogy to Eq.(1.37), but using Eq.(1.33), and it reads

$$\delta_{\rm E} = \frac{\rho}{\bar{\rho}} - 1 = \frac{9(\sinh\theta - \theta)^2}{2(\cosh\theta - 1)^3} - 1. \tag{1.48}$$

The expansion velocity of an underdense region is given by computing $dR_{\rm E}/dt$. The peculiar velocity with respect to the Hubble flow is $v_{\rm pec}(R_{\rm E}, t) = v(R_{\rm E}, t) - HR_{\rm E}(t)$ and it is given by [109]

$$v_{\rm pec}(R_{\rm E}, t) = HR_{\rm E}\left[\frac{3}{2}\frac{\sinh\theta(\sinh\theta - \theta)}{\cosh\theta - 1} - 1\right]. \tag{1.49}$$

Spherical concentric shells inside this patch satisfy the same relation with $R < R_{\rm E}$ and thus have different velocities. If the velocity decreases increasing the size of the shell and therefore moving from the center towards the edge of the patch, then shells that were close to the center will catch up with the shells further outside, until they eventually pass them. This event is called shell crossing. For a top-hat spherical region this happen at $\theta_{\rm shc} \simeq 3.53$, when the Eulerian density inside the patch is $\delta_{\rm E} = -0.8$ and the Lagrangian density extrapolated using linear theory is [109]

$$\delta_{\rm v} \equiv \delta_{\rm L}(\theta_{\rm shc}) = -2.7\,. \tag{1.50}$$

Analogously to the quantity $\delta_{\rm sc}$ for halos, $\delta_{\rm v}$ is defined to be the critical density in Lagrangian space for the formation of a void in the Eulerian space.

Lagrangian-Eulerian mapping

In this section we have implicitly assumed that the total mass and comoving volume of the Eulerian and the Lagrangian spaces are the same, therefore they also share the same background density. Moreover, the mass M of the considered spherical patch is conserved. Then, $M = \bar{\rho} V_{\rm L}(1+\delta_{\rm L}) \simeq \bar{\rho} V_{\rm L}$ in Lagrangian space, with $V_{\rm L} = (4\pi/3)R_{\rm L}^3$ and being $\delta_{\rm L} \ll 1$. In the Eulerian space the size $R_{\rm E}$ and the density contrast δ_E satisfy,

$$1 + \delta_{\rm E} = M/\bar{\rho} V_{\rm E} = (R_{\rm L}/R_{\rm E})^3 \,. \tag{1.51}$$

The spherical collapse model gives a relation between the Lagrangian size $R_{\rm L}$, the density $\delta_{\rm L}$ and the time z and size $R_{\rm E}$ in the Eulerian frame. In fact, we can rewrite Eq.(1.32) as

$$\frac{R_{\rm E}(z)}{R_{\rm L}} = \frac{1+z}{(5/3)\delta_{\rm L}} \frac{1-\cos\theta}{2} \,, \tag{1.52}$$

where $\delta_{\rm L}$ is extrapolated to present time and $1-\cos\theta$ has to be replaced with $\cosh\theta - 1$ if the patch is underdense. Using Eq.(1.51), this expression can be used to find the relation $\delta_{\rm L}(\delta_{\rm E})$ as an expansions in $\delta_{\rm E}$. If $R_{\rm E}$ and z are given, it describes a curve in the plane $(\delta_{\rm L}, R_{\rm L})$. To a good approximation, this spherical collapse relation is [77]

$$\frac{\delta_{\rm L}(R_{\rm L}|R_{\rm E},z)}{1+z} = \frac{3}{20}(12\pi)^{2/3} - \frac{1.35}{(1+\delta_{\rm E})^{2/3}} - \frac{1.12431}{(1+\delta_{\rm E})^{1/2}} + \frac{0.78785}{(1+\delta_{\rm E})^{0.58661}} \,, \tag{1.53}$$

where $1+\delta_{\rm E}$ depends on $R_{\rm L}$ via Eq.(1.51). A simpler approximation to this relation is [7, 102]

$$\frac{\delta_{\rm L}(R_{\rm L}|R_{\rm E},z)}{1+z} = \delta_{\rm sc} - \delta_{\rm sc}(1+\delta_{\rm E})^{-1/\delta_{\rm sc}} \,. \tag{1.54}$$

Given $R_{\rm E}$ and z, Eqs. (1.53) and (1.54) represent a curve in the plane $(R_{\rm L}, \delta_{\rm L})$ called barrier, $B(R_{\rm L}|R_{\rm E},z)$. Notice that when $R_{\rm E} \to 0$, then $1+\delta_{\rm E} \to \infty$, so Eqs.(1.53) and (1.54) become $\delta_{\rm L}(R_{\rm L}|R_{\rm E}=0,z) \to \delta_{\rm sc}(1+z)$, independent of $R_{\rm L}$. Therefore, when assuming that halos do have a zero Eulerian size we can consider their barrier to be constant and equal to $\delta_{\rm sc}$, which means that they form from regions in the Lagrangian space with $\delta_{\rm L} = \delta_{\rm sc}$ (as already stated above). When $R_{\rm E} > 0$, then $\delta_{\rm L}(R_{\rm L}|R_{\rm E},z)$ decreases monotonically as $R_{\rm L}$ decreases and the Lagrangian density (barrier) depends on the Lagrangian size. Motivations for going beyond the constant barrier are discussed in [106].

Finally, the expression that relates the density and the size in the Lagrangian and Eulerian space can be found using Eqs.(1.51) and (1.54) and it reads

$$1 + \delta_{\rm E}(z) = \left[1 - \frac{(D_z/D_0)\delta_{\rm L}}{\delta_{\rm sc}}\right]^{-\delta_{\rm sc}} = \left(\frac{R_{\rm L}}{R_{\rm E}(z)}\right)^3 \,, \tag{1.55}$$

where we generalized it to a ΛCDM cosmology with linear growth factor D_z given by Eq.(1.27).

This last relation holds for over and under densities, showing that $\delta_{\rm sc}$ is a relevant quantity for obtaining the Lagrangian-Eulerian mapping, in both cases. As stated before, in order to have a collapsed object it has to be $\delta_{\rm L} = \delta_{\rm sc}$. Then Eq.(1.55) shows that at $z = 0$ the Eulerian density diverge, $\delta_{\rm E} \to \infty$, and $R_{\rm E} = 0$: a halo has formed.

On the other hand, the Lagrangian threshold density for forming a void has found to be $\delta_{\rm v} = -2.7$. Therefore, when $\delta_{\rm L} = \delta_{\rm v}$, Eq.(1.55) shows that the Eulerian density of a void is $\delta_{\rm E} \sim -0.8$ and $R_{\rm E} \sim 1.7 R_{\rm L}$.

The Lagrangian-Eulerian mapping can be apply not only to study the evolution of the mean density of a spherical patch ending up in a halo or a void, it can also be used to study the evolution of its profile. Indeed, the enclosed profile at some scale $R_E(z)$ is nothing but the mean density inside this radius. Therefore, Eq.(1.55) can be use to map the Lagrangian profile of proto-halo(void) to the evolved halo(void) profile.

1.2 Excursion set theory

Dark matter halos are virialized objects. Assuming the spherical collapse model, they are expected to form from patches in the Lagrangian field with density $\delta_{\rm L} = \delta_{\rm sc}$. The mass of this patches is fully determined by their Lagrangian size. Suppose that, as the universe evolves, the number of these regions is conserved, as well as their mass, while their size changes. Then, the number density of Lagrangian patches of a give size $R_{\rm L}$ (mass M) with density $\delta_{\rm L} = \delta_{\rm sc}$ is equal to the number density of evolved halos with mass M. The abundance of evolved objects is fully determined by the statistics of the linear Lagrangian field. This easy remark gave rise to different models to compute the abundance of halos, together with their spacial distribution. In this section we will present these models, starting from the first attempt by Press and Schechter in 1974 [99], before discussing in the next section the framework of excursion set peaks [90], which incorporate the peak model [6] in the excursion set theory [11]. In this section we will drop the subscript L of the Lagrangian quantities since here most of the computations are in the Lagrangian space; we will specify it otherwise.

1.2.1 Press-Schechter approach

In 1974 Press and Schechter [99] proposed a method to compute the number density $n(M)dM$ of halos with mass between M and $M + dM$, once the cosmology is assumed. The spherical collapse suggest that their seed in the Lagrangian space are region with $\delta = \delta_{\rm sc}$. The way to describe regions in the universe is by smoothing the density field with a window function. In this way, there is a deterministic relation between the size R of the window function and the mass $M = \bar{\rho} V_R$ inside the region. For simplicity, we have in mind a gaussian window function, so $V_R = (2\pi)^{3/2} R^3$. Therefore, for a given cosmology, the mass M, the size R, and the variance of the smoothed density field $S \equiv s_0^R$ defined in Eq.(1.15) are equivalent variables. When $R \to \infty$, the field is smoothed over all the space and the variance is zero, $S = 0$. For most power spectra of interest the variance increases as the Lagrangian size decreases and $S \to \infty$ when $R \to 0$.

The initial density filed is Gaussian, then the probability distribution for the density contrast is

$$p(\delta, S) = \frac{1}{\sqrt{2\pi S}} e^{-\delta^2/(2S)} \,. \tag{1.56}$$

If the density smoothed at R exceed the threshold, there will be a scale $R' > R$ in which $\delta(R') = \delta_{\rm sc}$. Then, the probability for $\delta(R)$ to be above the threshold at R gives

the fractional volume of space occupied by virialized objects larger then R and it is

$$F(M) \equiv p(\delta > \delta_{\rm sc}, S) = \int_{\delta_{\rm sc}}^{\infty} d\delta \, p(\delta, S) = \frac{1}{2}\left[1 - {\rm erf}\left(\frac{\nu}{\sqrt{2}}\right)\right] , \tag{1.57}$$

where $\nu \equiv \delta_{\rm sc}/\sqrt{S}$ is the peak height. The fraction of volume in objects with mass between M and $M + dM$ is obtain differentiating $F(M)$, thus the number density $n(M)dM$ of objects with the same mass is

$$n_{\rm PS}(M)dM = \frac{\bar{\rho}}{M}\frac{dF(M)}{dM}dM \equiv \frac{\bar{\rho}}{M} f_{\rm PS}(\nu)d\nu \, , \tag{1.58}$$

where the last equality defines the function $f_{\rm PS}(\nu)$, which is given by

$$f_{\rm PS}(\nu)d\nu = \sqrt{\frac{1}{2\pi}} \exp\left(-\frac{\nu^2}{2}\right) d\nu \, . \tag{1.59}$$

The fraction $f_{\rm PS}$ written in terms of the peak height ν is a universal function since its form is independent of cosmology, redshift, and power spectrum. All this information are hidden in the variable ν.

This model represents a big step towards a description of halo abundance. However, as remarked already by Press and Schechter, these expressions cannot be fully correct. Since the variance $S(R)$ diverges when $R \to 0$, all the mass of the universe should be in collapsed objects. The quantity $F(R = 0)$ gives the fraction of mass in collapse objects and it is expected to be $F(R = 0) = 1$, while Eq.(1.57) shows that $F(R = 0) = 1/2$. Press and Schechter argued that the missing mass should come from underdensities that will collapse onto overdense regions, and corrected this simply adding by hand an overall factor of two in Eqs.(1.57) and (1.59). Actually, the reason for the lack of mass is that the above procedure does not consider the case in which the density smoothed at a scale R can be below the collapse threshold, but be above the threshold at some scale $R' > R$. This configuration corresponds to an object with mass $M' > M$, that is not taken into account in $F(M)$ since at scale M it is below threshold. This is the so called cloud-in-cloud problem.

1.2.2 The first crossing requirement

The problem of missing mass in the Press and Schechter method is related to not considering regions below threshold on a particular scale, but above threshold on a larger scale. In order to solve it, let us do a step back.

The obvious way to compute the number of regions undergoing collapse is counting the number of positions $\vec{x}$ of the Lagrangian space where the density smoothed at some scale exceeds the threshold value for the spherical collapse. However, we can notice the following. In each position $\vec{x}$ of the Lagrangian space there is a curve, $\delta(R)$, which describes the overdensity δ in a window of Lagrangian size R centered on that position. Then, a better procedure to compute the number density of collapsing regions is sitting at a position $\vec{x}$ and studying the different realizations of the density field there, as a function of the smoothing scale, or equivalently of the mass or of the variance. The curve $\delta(S)$ represents a trajectory in the plane (S, δ). Since $\delta(R) \to 0$ as $R \to \infty$, all these trajectories start from the origin $(S, \delta) = (0, 0)$ and they can reach positive or negative values for δ as S increases.

A trajectory describes a halo of mass M' if it crosses the barrier $B = \delta_{\rm sc}$ at the correspondent scale S'. In principle it can cross the barrier more than once, arising a possible issue in the determination of the halo mass. Actually, this case describes small substructures collapsing together to form a bigger object, therefore it is the larger crossing scale the one determining the size of the collapsed halo. Thus, both for solving the cloud-in-cloud problem of Press and Schechter and for determining the correct halo size, it seems necessary to compute the larger scale at which a trajectory crosses the barrier, which is called the first crossing problem.

The halo abundance

Bond et al. [11] reformulated the problem for computing the halo abundance by introducing the first crossing requirement. This formulation is called excursion set theory. They considered a sharp k-space filter to smooth the density field: in this case the trajectory $\delta(S)$ is a random walk where each step is uncorrelated and there exists an analytic solution for the first crossing problem.

Consider a smoothing scale S_1 for which $\delta_1 \equiv \delta(S_1) < \delta_{\rm sc}$. The density $\delta_2 = \delta_1 + \Delta\delta$ at $S_2 = S_1 + \Delta S$, after an increment Δ_S in the filtering scale, may depend on both the value of Δ_S and the value of the density at other scales. For a sharp-k window, increasing the scale corresponds to adding a set of independent Fourier modes to the smoothed density, which did not determine the density at other scales. Thus, the probability ψ for a change $\Delta\delta$ in the density associated to an increment ΔS of the scale is a Gaussian distribution with zero mean and variance equal to ΔS, independent on the starting point δ_1,

$$\psi(\Delta\delta, \Delta S) = \frac{1}{\sqrt{2\pi\Delta S}}\, e^{-(\Delta\delta)^2/(2\Delta S)}\,. \tag{1.60}$$

The probability for a transition from δ_1 to δ_2 is given by $p(\delta_2, S_2)d\delta_2 = \psi(\Delta\delta, \Delta S)d\Delta\delta$. The relation between the probability distribution of δ at scale S and the distribution at the following step $S + \Delta S$ is

$$p(\delta, S + \Delta S) = \int d(\Delta\delta)\, \psi(\Delta\delta, \Delta S) p(\delta - \Delta\delta, S)\,. \tag{1.61}$$

Assuming a small $\Delta\delta$, this expression can be Taylor expanded and integrated. Keeping the terms up to $(\Delta\delta)^2$ and using the fact that ψ has mean zero and variance ΔS yields the relation

$$\frac{\partial p}{\partial S} = \frac{1}{2}\frac{\partial^2 p}{\partial \delta^2}\,, \tag{1.62}$$

with boundary conditions: 1) $p(\delta, S)$ finite as $\delta \to -\infty$ and 2) $p(\delta_{\rm sc}, S) = 0$, which means that a trajectory is removed from the sample when it crosses the barrier. It is useful to consider an arbitrary starting point $\delta(S_0) = \delta_0$ for the random walk [62], so that the initial condition will be $p(\delta_0, S_0) = \delta_D(\delta_0)$, where δ_D is the Dirac delta.

Consider the new variable $\gamma = \delta_{\rm sc} - \delta$, so that the second boundary condition satisfy $p(\gamma = 0, S) = 0$. The Fourier transform of the probability distribution is

$$\tilde{p}(\omega, S) = \int d\gamma\, p(\gamma, S)\, e^{-i\omega\gamma}\,, \tag{1.63}$$

where ω is the conjugate variable. Then Eq.(1.62) becomes

$$\frac{\partial \tilde{p}}{\partial S} = -\frac{\omega^2}{2}\tilde{p}\,, \tag{1.64}$$

with solution of the type $\tilde{p}(\omega, S) = c(\omega)\exp(\omega^2 S/2)$. The boundary condition at $\gamma = 0$ guarantees that $c(\omega)$ is an odd function, then

$$p(\gamma, S) = \int_0^\infty d\omega\, c(\omega)\sin(\omega\gamma)\, e^{-\omega^2 S/2}\,. \tag{1.65}$$

Using the initial condition we obtain $c(\omega) = 2/\pi \sin(\omega\gamma_0)\, e^{-\omega^2 S_0/2}$, where $\gamma_0 = \delta_{\rm sc} - \delta_0$. By inserting the expression for $c(\omega)$ in Eq.(1.65) and doing the integral over ω, the final solution reads

$$p(\delta, S|\delta_0, S_0) = \frac{1}{\sqrt{2\pi\Delta S}}\left[\exp\left(-\frac{(\Delta\delta)^2}{2\Delta S}\right) - \exp\left(-\frac{[2(\delta_{\rm sc}-\delta_0)-\Delta\delta]^2}{2\Delta S}\right)\right]\,, \tag{1.66}$$

where $\Delta S = S - S_0$ and $\Delta\delta = \delta - \delta_0$. The first exponential describes the trajectories above threshold at scale S, while the second exponential accounts for the trajectories that have been removed because they crossed the threshold at scale $S' < S$, but they also crossed back below the threshold by S. In fact, having a sharp-k filter, there is equal probability for a trajectory that crossed the barrier to stay above or go back below it.

The probability distribution $p(\delta, S|\delta_0, S_0)$ is defined only for $\delta < \delta_{\rm sc}$, then the fraction of trajectory that have already crossed the barrier before S, given that they start from (δ_0, S_0), is

$$F(S|\delta_0, S_0) = 1 - \int_{\delta_{\rm sc}}^\infty p(\delta, S|\delta_0, S_0)\, d\delta = 1 - {\rm erf}\left(\frac{\delta_{\rm sc}-\delta_0}{\sqrt{2\Delta S}}\right)\,. \tag{1.67}$$

If $\delta_0 = 0$ and $S_0 = 0$ we recover the Press-Schechter result in Eq.(1.57) with the additional factor of two that they were forced to introduce by hand. In this procedure, the missing probability of Press and Schechter comes from the second exponential in Eq.(1.66), i.e. counting the trajectories that up-cross and down-cross the barrier before the considered scale S. The differential probability is obtain differentiating $F(S|\delta_0, S_0)$,

$$f_{\rm EST}(S|\delta_0, S_0) \equiv \frac{dF}{dS}dS = \frac{\delta_{\rm sc}-\delta_0}{\sqrt{2\pi}(\Delta S)^{3/2}}\exp\left[\frac{(\delta_{\rm sc}-\delta_0)^2}{2\Delta_S}\right]\,. \tag{1.68}$$

The function $f_{\rm EST}(S|\delta_0, S_0)$ is called conditional first-crossing distribution, since it assumes that the trajectory passes through the point (δ_0, S_0), and it is the fraction of trajectories describing halos of mass M that are embedded in regions with smoothed density δ_0 on scale S_0. When $\delta_0 = 0$ and $S_0 = 0$, the distribution becomes $f_{\rm EST}(S)$, which is the unconditional counterpart and it gives the fraction of trajectories that give rise to halos with mass between M and $M + dM$, in all space. The latter is equal to the Press-Schechter fraction in Eq.(1.59) (with the additional factor of two). The abundance of halos $n_{\rm EST}(M)$ in the same mass range is given by Eq.(1.58).

This prediction can capture the main features of the halo mass function measured in simulations, but it fails in describing the details: it predicts too many low-mass halos

and too few high-mass halos. Given the simplicity of the excursion set model, this is not surprising, but the level of agreement indicates that the excursion set model is a useful tool to understand the main features of halo abundance, formation and clustering, which are set by the statistics of the initial conditions. We will see below how the model can be improved to make better predictions. However, nowadays the most reliable and used theoretical mass functions are fitting formulas calibrated to N-body simulations. One of the most used ones is the Sheth-Tormen mass functions [107], which is inspired by the excursion set model.

The halo clustering

The clustering of dark matter halos differs from the overall clustering of matter, since it involves a special subset of points in the space. The excursion set theory provides a framework with which to understand the spatial distribution of halos, which was computed by Mo and White [77].

The conditional first-crossing distribution $f_{\rm EST}(S|\delta_0,S_0)|dS/dM|dM$ in Eq.(1.68) gives the fraction of mass in halos with mass M that are embedded in a larger region with density δ_0 and volume V_0 (corresponding to the smoothing scale S_0). Thus, the averaged number of M halos in a volume V_0 is

$$\begin{aligned}\mathcal{N}_{\rm EST}(M|\delta_0,S_0)dM &= \frac{M_0}{M} f_{\rm EST}(S|\delta_0,S_0)|dS/dM|dM \\ &= \frac{M_0}{\bar\rho}\, n_{\rm EST}(M|\delta_0,S_0)dM\,,\end{aligned} \tag{1.69}$$

where $n_{\rm EST}(M|\delta_0,S_0)$ is the conditional mass function defined as in Eq.(1.58) and the substitutions $F(M)\to F(M|\delta_0,S_0)$ and $f_{\rm EST}(S)\to f_{\rm EST}(S|\delta_0,S_0)$. The overdensity of these halos (inside regions with density δ_0 and volume V_0) compared to the mean number of halos of mass M in any position is given by

$$\delta_{\rm L}^h \equiv \frac{\mathcal{N}_{\rm EST}(M|\delta_0,S_0)}{n_{\rm EST}(M)V_0} - 1 = \frac{f_{\rm EST}(S|\delta_0,S_0)}{f_{\rm EST}(S)}(1+\delta_0) - 1\,, \tag{1.70}$$

where $n_{\rm EST}(M)$ is the mass function in Eq.(1.58). This last expression becomes simple when the mass M_0 in the larger region is much bigger than the halo mass M. In this limit $S_0\to 0$ and $n_{\rm EST}(M|\delta_0,S_0=0)$ can be expanded in a Taylor series around $\delta_0=0$. In this way $\delta_{\rm L}^h$ will be a sum of terms with different powers in δ_0

$$\delta_{\rm L}^h = \sum_{k>0} \frac{b_k^{\rm L}}{k!}\,\delta_0^k\,, \tag{1.71}$$

where the coefficients $b_k^{\rm L}$ are called Lagrangian halo biases. The first coefficient $b_1^{\rm L}\equiv b_{\rm L}$ is linearly proportional to the matter density and it is called linear halo bias. It reads

$$b_{\rm L}(\nu) = \frac{\nu^2-1}{\delta_{\rm sc}}\,, \tag{1.72}$$

and it depends on the peak height ν, or equivalently on the halo mass, only. Another way to compute $b_{\rm L}$ is by differentiating the unconditional mass function with respect to $\delta_{\rm sc}$ [89]

$$b_{\rm L}(\nu) = -\frac{\partial \ln \nu f_{\rm EST}(\nu)}{\partial \delta_{\rm sc}}. \tag{1.73}$$

1.2.3 The upcrossing requirement

The first-crossing distribution can be found analytically only when a sharp k-space filter is used, since it is the only case where trajectories in the (S, δ) plane have uncorrelated steps. However, the sharp-k filter is not physically motivated: the window function in Lagrangian space is expected to be a top-hat, a Gaussian or a combination of the two. For a generic filter the first-crossing distribution can be computed only using numerical methods, since it requires an infinite number of constraints (one for each smoothing scale) and each step is correlated with the others.

The halo abundance

Musso and Sheth [79] showed how to relax this requirement and handle the calculation of the halo abundance in the excursion set framework with a top-hat or Gaussian filter. They assumed that the trajectories do not double-cross the threshold and they scatter around a deterministic walk with completely correlated steps. In this case the steps are called strong correlated.

The requirements for forming a halo at scale S are $\delta(S) > \delta_{\rm sc}$ and $\delta(S - \Delta S) < \delta_{\rm sc}$, for $\Delta S \to 0$, the latter called upcrossing requirement. It is motivated by the fact that, for power spectra used in cosmology, we expect the trajectories to be kind of smoothed and not to cross the barrier many times. Therefore, asking to cross the barrier from below should be a good approximation to the first-cross passage.

In this case, it turns out to be straightforward to generalize the treatment to the case in which the barrier is not a constant, but depends on scale S, $B = B(S)$. The upcrossing requirement becomes $\delta(S - \Delta S) < B(S - \Delta S)$. Since ΔS is small, we can Taylor expand δ and B in a Taylor series. We use primes to denote derivatives with respect to S, then $\delta(S - \Delta S) = \delta(S) - \Delta S\, \delta'(S)$ and $B(S) - \Delta S\, B'(S)$. Thus, the upcrossing constraint translates into a constraint on the first derivative of δ and B. The two requirements become $B(S) < \delta(S) < B(S) + \Delta S\, (\delta'(S) - B'(S))$ and $\delta'(S) > B'(S)$. The fraction of walks satisfying these expressions is

$$f_{\rm up}(S)\Delta S = \int_0^\infty d\delta' \int_{B(S)}^{B(S)+\Delta S\,(\delta'-B')} p(\delta, \delta', S)\,, \tag{1.74}$$

where $p(\delta, \delta', S)$ is the joint probability of δ and its derivative $\delta' \equiv d\delta/dS$. Taking the limit $\Delta S \to dS$ implies

$$f_{\rm up}(S) = \int_0^\infty d\delta'\, p(B, \delta', S)\, (\delta' - B') = p(B, S) \int_0^\infty d\delta'\, p(\delta'|B, S)\, (\delta' - B')\,, \tag{1.75}$$

For a Gaussian density field the probability distribution $p(B, S)$ is a Gaussian and the conditional probability $p(\delta'|B, S)$ is also a Gaussian but with non-zero mean and shifted variance. If we define

$$\gamma^2 \equiv \frac{\langle \delta\delta' \rangle^2}{\langle \delta^2 \rangle \langle \delta'^2 \rangle}\,, \tag{1.76}$$

the mean of $p(\delta'|B, S)$ is $\langle \delta'|B, S\rangle = \gamma\, B \sqrt{\langle \delta'^2\rangle / \langle \delta^2\rangle}$ and its variance is $\langle \delta'^2\rangle(1 - \gamma^2)$. Note that $\langle \delta\delta' \rangle = 1/2$ and thus the mean is $\langle \delta'|B, S\rangle = B/2S$. For simplicity we define the normalized variables

$$x \equiv \frac{\delta' - B'}{\sqrt{\langle \delta'^2 \rangle}}, \qquad \beta(S) \equiv \frac{B(S)}{\sqrt{S}}, \qquad \beta_*(S) \equiv \beta(S) \frac{\partial \ln \beta(S)}{\partial \ln \sqrt{S}}\,. \tag{1.77}$$

Then the integral in Eq.(1.75) reads

$$S\, f_{\rm up}(S) = \frac{e^{-\beta(S)^2/2}}{2\gamma\sqrt{2\pi}} \int_0^\infty dx\, x\, \frac{e^{-(x-\gamma\beta_*(S))^2/2(1-\gamma^2)}}{\sqrt{2\pi(1-\gamma^2)}}\,. \tag{1.78}$$

We can use the relation $\nu f(\nu) = Sf(S)|d\ln S/d\ln\nu| = 2Sf(S)$ and solve the integral in the above equation that yields

$$\nu f_{\rm up}(\nu) = \frac{e^{-\beta(S)^2/2}}{\sqrt{2\pi}}\beta_*(S)\left[\frac{1+{\rm erf}(\Gamma\beta_*({\rm S})/\sqrt{2})}{2} + \frac{e^{-\Gamma^2\beta_*(S)^2/2}}{\sqrt{2\pi}\Gamma\beta_*(S)}\right], \tag{1.79}$$

with $\Gamma^2 = \gamma^2/(1-\gamma^2)$. For a constant barrier, $B(S) = \delta_{\rm sc}$ and $\beta(S) = \beta_*(S) = \delta_{\rm sc}/\sqrt{S} \equiv \nu$. In this case the above equation becomes

$$\nu f_{\rm up}(\nu) = \frac{\nu\, e^{-\nu^2/2}}{\sqrt{2\pi}}\left[\frac{1+{\rm erf}(\Gamma\nu/\sqrt{2})}{2} + \frac{e^{-\Gamma^2\nu^2/2}}{\sqrt{2\pi}\Gamma\nu}\right]. \tag{1.80}$$

Musso and Sheth showed that the upcrossing model provides a good description of the exact solution for the first-crossing distribution, in which the constraint on the walk height is satisfied on all scales. In particular they tested it with different power spectra and top-hat or Gaussian filters. Therefore, Eq.(1.80) effectively solves the same excursion set problem for correlated steps that Bond et al. [11] solved for uncorrelated steps.

The halo clustering

In analogy with the case of first-crossing distribution with uncorrelated steps, we can define the fraction $f_{\rm up}(S|\delta_0, S_0)$ with the additional constraint for the walks to pass through δ_0 on some large scale S_0, before crossing $\delta_{\rm sc}$ on scale $S > S_0$. This will allow to compute the halo bias for the upcrossing model.

In particular, we can use Eq.(1.73) to compute the large scale linear bias factor,

$$b_{10}^{\rm L} = \frac{\nu^2-1}{\delta_{\rm sc}} + \frac{1}{\delta_{\rm sc}}\frac{{\rm e}^{-\Gamma^2\nu^2/2}/\sqrt{2\pi}\Gamma\nu}{{\rm erfc}(-\Gamma\nu/\sqrt{2})/2 + {\rm e}^{-\Gamma^2\nu^2/2}/\sqrt{2\pi}\Gamma\nu}\,, \tag{1.81}$$

where the subscript 10 indicates that this is only part of the linear halo bias within the upcrossing model. The missing part b_{01}^L show some k dependence and we will discuss it in part IV.

1.3 Joining excursion set and peaks theory

Another commonly used model for identifying halos in the Lagrangian field is the peaks model by Bardeen et al. [6]. This model differs from excursion set mainly for two reasons. First, while the excursion set aims in a statistical description of the mass fraction in bound objects, and assumes that this can be done by consideration of all points in space, peaks theory aims to describe the point process involving the halo formation, since here bound objects are thought to form only in special points of the space, the ones where the density field present a peak, i.e. a local maximum. Second,

even if in both models the variable peak height, $\nu = \delta_{\rm sc}/\sqrt{S}$, is the fundamental one, they treat it in a different way. The excursion set considers the denominator S as a stochastic variable, and the analysis is performed changing the smoothing scale but keeping the value of $\delta_{\rm sc}$ fixed. Instead, the peak model treats the numerator $\delta_{\rm sc}$ as a variable and keeps the variance S fixed. Once the smoothing scale is chosen, the analysis involve the localization of local maxima in the smoothed density field.

Adding the requirement that halos form where there are local maxima of the Lagrangian density field to the upcrossing scheme could improve the prediction for the halo abundance and the halo clustering. Paranjape and Sheth [90] showed how to build an excursion set model of peaks, where all these constraints are implemented. We briefly recap here the main results of peaks theory, before discussing the excursion set of peaks.

1.3.1 Peaks Theory

The requirement for a position to be on a peak translates into constraints on the first and second derivatives of the density with respect to the spacial position $\vec{x}$, i.e. the three spatial derivatives of $\delta(\vec{x})$ must be zero, and the matrix of second derivatives $\partial^2\delta/\partial x_i \partial x_j$ must be negative definite (having three negative eigenvalues). Bardeen et al. [6] showed that in a Gaussian smoothed density field (smoothed at fixed scale R corresponding to the variance S) the number density of peaks of scaled height $\tilde{\nu} = \delta/\sqrt{S}$ is

$$n_{\rm pk}(\tilde{\nu}) = \int d\tilde{x}\, n_{\rm pk}(\tilde{x}, \tilde{\nu}) = \frac{e^{-\tilde{\nu}^2/2}}{\sqrt{2\pi}} \frac{G_0(\tilde{\gamma}, \tilde{\gamma}\tilde{\nu})}{(2\pi R_*^2)^{3/2}}\,, \tag{1.82}$$

where $\tilde{x} = -\nabla_x^2 \delta(S, \vec{x})/\sqrt{\langle [\nabla_x^2 \delta(S, \vec{x})]^2 \rangle}$ is the Laplacian of the field normalized by its rms value equal to σ_2^2 for a Gaussian filter, $\tilde{\gamma} = \sigma_1^2/\sigma_0\sigma_2$ and $R_* = \sqrt{3}\sigma_1/\sigma_2$, with the definition of σ_j as in Eq.(1.16), and

$$G_j(\gamma, y) = \int_0^\infty dx\, x^j F(x) \frac{e^{-(x-y)^2/2(1-\gamma^2)}}{\sqrt{2\pi(1-\gamma^2}} \tag{1.83}$$

with

$$\begin{aligned} F(x) \;=\; & \frac{x^3 - 3x}{2} \left\{ \mathrm{erf}\left(x\sqrt{\frac{5}{2}} \right) + \mathrm{erf}\left(x\sqrt{\frac{5}{8}} \right) \right\} + \\ & + \sqrt{\frac{2}{5\pi}} \left[\left(\frac{31x^2}{4} + \frac{8}{5} \right) \mathrm{e}^{-5x^2/8} + \left(\frac{x^2}{2} - \frac{8}{5} \right) \mathrm{e}^{-5x^2/2} \right]. \end{aligned} \tag{1.84}$$

The variable $\tilde{x}$ represents the curvature around the peak position, therefore $F(x)$ quantifies how different the set of curvatures is around a peak position compared to a randomly placed one. Note also that $\partial G_n(\gamma, y)/\partial y = (G_{n+1} - y\, G_n)/(1-\gamma^2)$.

In order to map from peak number densities to halo mass fractions, one must associate a mass to each peak. Eq.(1.82) is defined to a fixed smoothing scale R, so changes in $\tilde{\nu}$ are due to changes in δ. In excursion set theory one would really allow R to vary instead. The excursion set theory of peaks shows how to deal with this problem.

1.3.2 Excursion set theory of peaks

The halo abundance

For simplicity, we consider here a constant barrier $B(S) = \delta_{\rm sc}$. Within the upcrossing model, Musso and Sheth [79] and Paranjape and Sheth [90] noticed that among the peaks present on scale S, we want those which have a smaller height on the next larger smoothing scale (smaller variance). Therefore they would demand that the scaled peak height $\tilde{\nu}$ lie in the interval $\delta_{\rm sc}/\sqrt{S} < \tilde{\nu} < \Delta S\, x/2\gamma S$, where x and γ have been defined in Eq.(1.77) (with constant barrier $B = \delta_{\rm sc}$) and Eq.(1.76), respectively. The excursion set of peaks should then depend on three variable: $\tilde{\nu} \sim \delta$, $\tilde{x} \sim \nabla^2\delta$, and $x \sim \delta' = d\delta/dS$. However, for a Gaussian filter the Laplacian of the smoothed density filed is equal to its derivative with respect to S and therefore $x = \tilde{x}$; moreover $\gamma = \tilde{\gamma}$. Therefore, for a Gaussian filter, the relevant variables are only two because constraint on the value of the derivative with respect to smoothing scale becomes a constraint on the curvature of the field.

The same logic that leaded to Eq.(1.78) will lead here to the number density of peaks that satisfy the upcrossing requirement, i.e. the number density of halos of mass M in excursion set of peaks,

$$n_{\rm ESP}(\nu) = \frac{1}{\gamma\nu}\int_0^\infty dx\, x\, n_{\rm pk}(x,\nu)\,, \tag{1.85}$$

giving the fraction

$$f_{\rm ESP}(\nu) = \frac{e^{-\nu^2/2}}{\sqrt{2\pi}}\frac{V}{V_*}\frac{G_1(\gamma,\gamma\nu)}{\gamma\nu}\,, \tag{1.86}$$

where $G_1(\gamma,\gamma\nu)$ is defined in Eq.(1.83) and $V = M/\bar{\rho}$ is the Lagrangian volume associated with the tophat smoothing filter.

It is straightforward to compute the same quantities for a moving barrier, by substituting $\delta_{\rm sc}$ with a generic barrier $B(S)$. Then

$$n_{\rm ESP}(\nu) = \frac{1}{\gamma\nu}\int_0^\infty dx\, x\, n_{\rm pk}(x + 2\gamma\sqrt{S}B', \nu)\,, \tag{1.87}$$

with x given by Eq.(1.77).

We can notice that there is only a conceptual difference between $f_{\rm ESP}$ and $f_{\rm up}$, i.e. the latter averages over random positions in the field, whereas the former averages over special ones. In other words, $f_{\rm ESP}$ addresses both the cloud-in-cloud problem for peaks (the fundamental failing of the peaks approach), and the question of how the excursion set predictions are modified if one averaged over special positions in the initial field (the fundamental failing of the excursion set approach).

The halo clustering

The large scale linear bias factor associated to the mass function $f_{\rm ESP}$ with a constant barrier is

$$b_{10}^{\rm L} = \frac{\nu^2}{\delta_{\rm sc}}\left[1 - \Gamma^2\left(\frac{G_2/G_1}{\gamma\nu}\right)\right]\,. \tag{1.88}$$

We will discuss deeply the halo bias in excursion set of peaks in part IV, where we will show that also in excursion set of peaks the linear bias is k dependent; the term shown above its the k independent part.

Comparisons between the excursion set of peaks predictions and measurements from N-body simulations have been investigated by Paranjape et al. [88], who found good agreement between the model and the measurements of halo mass function and linear halo bias.

Chapter 2

Voids

Voids are underdense regions of the Universe and in a cosmological context they are treated as discrete and relevant objects rather than just absence of matter. The first identification and observation of voids goes back to 1978 thanks to two independent groups: Gregory and Thompson [48] and Joeveer, Einasto and Tago [58]. They stated that there are regions in the Local Universe of the size ~ 20 Mpc$/h$ with borders defined by filamentary structures that contain no galaxies. These observations came with the skepticism of the scientific community since there were not theoretical insight on how voids and filaments could form in a homogeneous Universe. The skepticism disappeared thanks to development in N-body simulations and big galaxy survey [30, 128], leading to the idea that the distribution of galaxies is not random. Galaxies are biased tracers of the underlying matter density field, which is thought to form a network, the so-called cosmic web, where knots are very dense regions, the halos, connected by filaments and walls. Between them, the voids represents the most underdense regions of the Universe.

2.1 Void properties

Voids are thought to form from negative density perturbations in the ICs. There, Gaussian fluctuations do not necessarily have spherical symmetry, however the spherical collapse model presented in Sec. 1.1.3 is useful to describe with a good approximation the evolution of voids. Indeed, any primordial asphericity in a negative perturbation is expected to be mitigated by its evolution [56].

In the framework of the spherical collapse model, an isolated underdense patch expand mimicking the behavior of an open universe. In this process, shells closer to the center expand faster than the ones near the edge and the moment in which the inner shells pass across outer shells is called shell-crossing. Because of this, the mass flows from the center towards the outer part of the underdense patch, bringing to the evacuation of matter and to the formation of overdensities at the edge of the region. Since the motion of matter from the interior of the void decreases with the distance from the center, an underdensity evolves into a reverse top-hat profile while building walls and filaments at the edge. Sheth and van de Weygaert [109] studied this evolution in the case of two different initial density profiles for the underdense patch: a reverse top-hat and a profile given by peaks theory (see Eq. 7.10 in [6]). Their results are presented in figure 2.1, which shows that both profiles expand, evacuate mass and

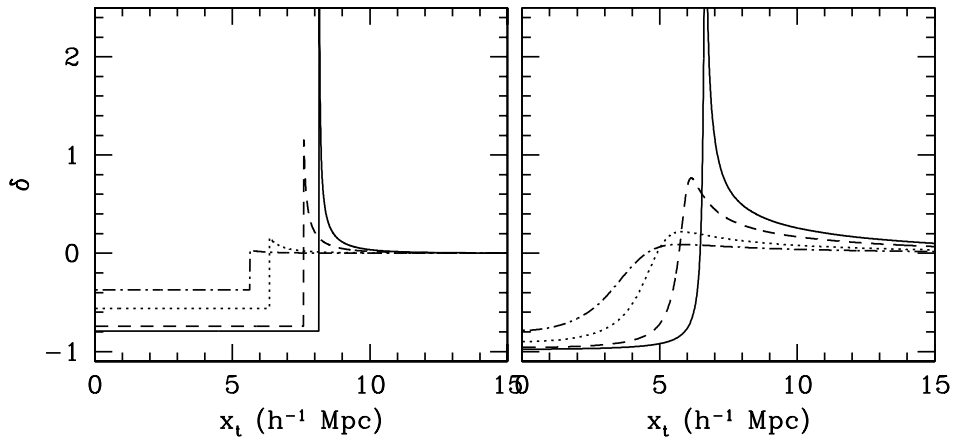

Figure 2.1: Figures taken from [109]. Spherical collapse model for the evolution of voids. Left: a pure top-hat void evolving up to the epoch of shell-crossing. Right: a void with an angular averaged profile (from [6], Eq. 7.10). Timesteps: a = 0.05, 0.1, 0.2 and 0.3. The tendency of this void to evolve into a top-hat configuration by the time of shell-crossing is clear. Shell-crossing, and the formation of an obvious ridge, happens only if the initial profile is sufficiently steep.

present a growing overdensity at the edge. However, as they noticed, the process of shell-crossing and the formation of a wall happen only if the profile is sufficiently steep. Otherwise, the voids expands and evacuate matter without building any overdensities. This is exactly what was observed in galaxy survey (although this case involves biased tracers of the matter density field, the qualitative features are expected to be the same). Figure 2.2 shows the measurements of void profiles performed by Paz et al. [93] using part of the SDSS survey data released 7 [2]. They found two types of voids: one with a wall at the edge, that they called S-type, and one without, called R-type.

Even if a description of isolated voids capture most of their properties, in the Universe there are no isolated voids nor smoothly unstructured ones. Voids are surrounded by other voids, filaments and halos and they do present internal structure. The standard cosmological structure formation scenario involve a hierarchical growth, where objects form from the interactions and merging of smaller structures that had formed earlier. For example, galaxies form clusters that merge giving rise to superclusters. The same happens for voids, which goes under the name of void hierarchy. It involves the bottom-up scenarios, in which voids emerge from the fusions of their internal substructures, and the interactions with the surroundings. This means that voids collide producing and enhancing the filaments and walls between them, as they evacuate matter. Then, they can eventually merge by gradually disappearance of the overdense structures between them. In this way small-scale voids embedded within a large-scale void gradually fade away.

Whereas the only relevant process in the hierarchic evolution of clusters is the merging, for voids there exists a second one: the disappearance of small voids when embedded in a larger overdensity. Indeed, a small underdense region surrounded by overdensities in the initial field could shrink because of the gravitational attraction between the dense regions and disappears. Thus, two effects affect the number of small voids within a generic density field and they are both relate to the embedding of a

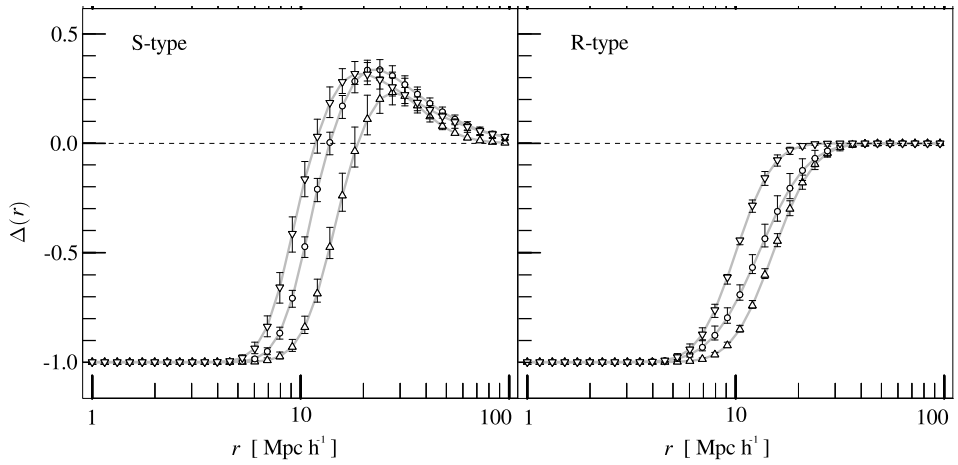

Figure 2.2: Figures taken from [93]. Radial galaxy density profiles for S-type (left) and R-type (right) voids in the S1 sample of SDSS data released 7. Different void radii ranges are indicated with downward triangles ($6-8\ h^{-1}$Mpc), circles ($8-9\ h^{-1}$Mpc) and upward triangles ($10-14\ h^{-1}$Mpc). Error bars indicate the region enclosing all curves within 68.3% uncertainty in parameter space.

density depression within the larger scale environment. A good description of void evolution, as well as void abundance and clustering, should take into account both of them.

The first is called void-in-void problem and it describes a small void surrounded by a larger underdense region which is a void itself. In order to not overestimate the number of small voids and thus the volume fraction in voids, we must count only the largest void and not the smaller ones inside it. This effect is analogous to the cloud-in-cloud problem for halos.

The second effect involves small voids surrounded by overdensities. The presence of the latter will dominate the evolution, shrinking the small voids until they disappear. This effect is called void-in-cloud problem. The analogous phenomenon for halos would be the cloud-in-void problem, which does not represent any problem at all since an underdense environment is irrelevant for halo formation. Indeed, virialized halo are not likely to be torn apart as the void expands around them.

Halos are thought to form from dense regions in the initial density field, while voids comes from underdense patches. Since the fluctuations in the ICs are Gaussian, there exist a symmetry between positive and negative perturbations which allows to describe protohalos and protovoids with the same tools. In the framework of excursion set, or peaks theory, halos form from dense patches in the ICs that satisfy some requirements, e.g. being above a threshold or being a local maximum of the density field. Voids should satisfy analogous requirements. The spherical collapse model set the threshold for the shell-crossing to occur at $\delta_{\rm v} = -2.7$. If we define a void as an underdense region that has undergone shell-crossing, then only regions with $\delta < \delta_{\rm v}$ will end up being a void. The upcrossing constraints becomes a down-crossing constraint, i.e. $d\delta/dS < 0$ and the peak requirement translates into a trough requirement with the protovoid being on a local minimum.

However, as noticed by Sheth and van de Weygaert, the void-in-cloud problem

breaks the symmetry between protohalos and protovoids in the initial Lagrangian field, since the cloud-in-void phenomenon is not relevant. As a consequence, the void formation cannot be describe in the framework of the excursion set model as a one barrier problem, like for halos; it requires a two barrier problem with the two barrier having the values $\delta_{\rm v}$ (related to the formation of a void) and $\delta_{\rm sc}$ (related to the collapse of a halo). If a random walk first crosses the collapsing barrier $\delta_{\rm sc}$ and then it crosses $\delta_{\rm v}$ at smaller scale, then it represents a small void contained in a dense region that has to collapse and thus it will disappear. This is a so-called void-in-cloud, which should not be counted as a void. Therefore, in the excursion set formalism, the problem of estimating the mass fraction in voids of size S reduces to the calculation of the fraction of trajectories that first cross $\delta_{\rm v}$ at scale S and did not cross $\delta_{\rm sc}$ at any $S' < S$. Sheth and van de Weygaert computed this first crossing distribution, which reads

$$\nu f(\nu) \simeq \sqrt{\frac{\nu}{2\pi}} \exp\left(-\frac{\nu}{2}\right) \exp\left(-\frac{|\delta_{\rm v}|}{\delta_{\rm sc}} \frac{\mathcal{D}^2}{4\nu} - 2\frac{\mathcal{D}^4}{\nu^2}\right) , \tag{2.1}$$

where we have defined $\nu = \delta_{\rm v}^2/S$. This expression is not exact; it is accurate for values of $\delta_{\rm sc}/|\delta_{\rm v}| \geq 1/4$. The fraction $f(\nu)$ present a cut-off on small masses, describing the fact that small voids in dense environments will disappear. The relation to the void abundance is then given by Eq.(1.58).

The two barrier formulation is important for computing the abundance of small voids, while it is not necessary for big ones, since they are not affected by the void-in-cloud problem. Anyway, this model is very easy and cannot describe with high accuracy the void abundance in simulations. It is nevertheless straightforward to incorporate the upcrossing requirement and the peak constraints in the one barrier void model, which should give better predictions. However, when comparing results from N-body simulations and theoretical predictions, issues do not arise only from the theoretical side, but are also related to the numerical one. It is still an open problem the definition of voids in simulations (and consequently in galaxy survey as well). We will discuss this in the next paragraph.

2.2 Void finder comparison

The definition of voids from the theoretical point of view is quite simple: voids are underdense regions that have undergone shell-crossing. This translates into a constraint on the value for the enclosed density of the related protovoid in the Lagrangian field, which must be equal to $\delta_{\rm v}$. Instead, the definition of voids in N-body simulations and galaxy survey is not so straightforward for many reason. First of all, in simulations one must deal with a sparse sapling of the matter density field and in galaxy survey only biased tracers of the underlying matter can be used. This issue comes from the fact that theory defines voids in the continuous matter field, while observations allow to identify voids in the galaxy or in the halo field, which are biased discrete tracers. Second, it is not obvious how to implement the definition of shell-crossing. Moreover, the voids in the matter or galaxy distributions seem to have very arbitrary shapes, most of the time very far from the spherical one. The question arising is then the following: does it make sense to identify voids imposing a spherical or ellipsoidal shape?

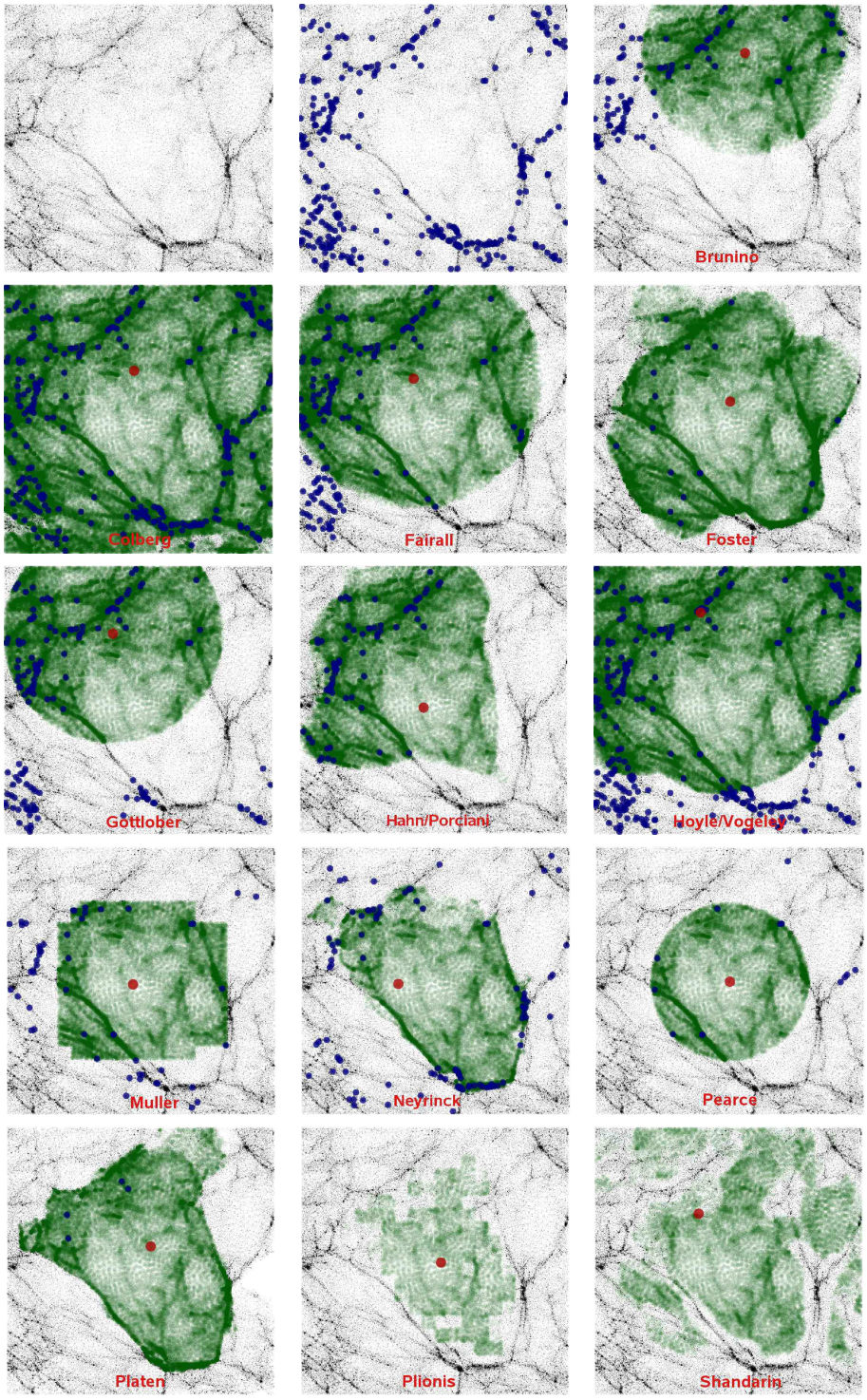

Figure 2.3: Figure from [27]. A slice of thickness 5 h^{-1}Mpc in the central 40 h^{-1}Mpc region of the Millennium simulation. The top left and top central panels show only the dark matter distribution and dark matter plus all galaxies (blue points) in the slice, respectively. The other panels show the locations of the largest void (with dark matter particles inside the void marked green), its center (red circle), and all void galaxies found by Brunino (top right), Colberg (second row, left column), Fairall (second row, center), Foster (second row, right column), Gottlober (third row, left column), Hahn/Porciani (third row, center), Hoyle/Vogeley (third row, right column), Muller (bottom, left column), Neyrinck (bottom, center), Pearce (bottom, right column). Platen/Weygaert (left column), Plionis/Basilakos (center), and Shandarin/Feldman (right column). Note that both Plionis/Basilakos and Shandarin/Feldman find no void galaxies.

There exist many different void finders that extend the theoretical definition of voids in different ways. Lavaux and Wandelt [64] classified them in three different categories depending on the criterion adopted for the identification of voids. The first class is based on a density criterion and defines voids as regions empty of galaxies or with local density well below a threshold [39, 45, 53, 92]. The second class identifies voids as geometrical structures in the dark matter distribution traced by galaxies, like e.g. spherical cells, polyedra, etc [28, 84, 97, 98, 101, 116]. The third class identifies voids dynamically by checking gravitationally unstable points in the distribution of dark matter [44, 49, 64]. Here galaxies are considered as test particles of the cosmic velocity field and not as tracers of the underlying mass distribution.

The Aspen–Amsterdam Void Finder Comparison Project [27] presented a systematic comparison study of thirteen different void finders constructed using dark matter particles, halos, and semi–analytical model galaxies [34]. The comparison was made running the different void finders on top of the same subvolume of the Millennium simulation [113]. For having a better description of the finder, we suggest the reader to look at the original paper [27]. Here we just list the names associated to them and the references where they were first discussed: Brunino [18], Colberg [28], Fairall, Foster [45], Gottlober [47], Hahn/Porciani [49], Hoyle/Vogeley [53], Muller [78], Neyrinck [84], Pearce, Platen/Weygaert [97], Plionis/Basilakos [98], and Shandarin/Feldman [101]. These void finders differ in type and in the parameters that they use, in addition to imposing or not a shape to the voids. The results are shown in Figure 2.3. Given the different assumptions of what a void actually is, it is not surprising to see large differences between some of the void finders. The details of the shapes and sizes found by each method are in same cases significantly different, the same happens for the number of voids, the size of the largest voids and their basic appearance. All of this is further enhanced by the existence of ad-hoc parameters in most of the existing void finders, which changes the exact definition of voids. However, there are also some encouraging agreements. For instance, the locations of the largest voids found by most of the groups agree quite well with each other.

In Chapter 4 we will describe the void finder used in the following part of the thesis. It is a watershed algorithm called VIDE [116], which is based on the void finder ZOBOV [84], that here is called Neyrinck from the creator. From figure 2.3 we can see that this void finder do not assume any arbitrary shape for the voids and it is one the few that identify the void as the region we would define looking at the snapshot by eyes.

Chapter 3

Massive neutrinos

3.1 Particle Physics

Neutrinos are one of the most enigmatic particles of the Standard Model (SM) of Particle Physics. Their existence was postulated in 1930 by Pauli to ensure energy conservation in beta decay processes. Few years later, in 1956, they were detected for the first time by Cowan and Reines [33].

In the framework of the SM, neutrinos are chargeless and massless particles that can interact only weakly. They are leptons and come with three flavors. However, there are extended model where neutrinos are massive and can interact via gravity. In 1957 Pontecorvo realized that if neutrinos were massive there could exist processes in which the neutrino flavor is not conserved: the so called neutrino oscillations. These effect take place on macroscopic distances for small neutrino masses and they can be detected if we are able to measure the flux of neutrinos from distant sources, identify their flavor and compare the results with the theoretical predictions for the initial neutrino fluxes. This procedure have been extensively performed in the past decades, using different neutrino beams and detection techniques and it have led to compelling evidences for the existing of neutrino oscillations from solar, atmospheric, reactor and accelerator neutrinos experiments (see e.g. the review [42]). This is a very important result, since the existence of neutrino oscillations implies that neutrinos do have mass and that the three known neutrino states with definite flavor ν_e, ν_μ, ν_τ are linear combinations of states ν_1, ν_2, ν_3 with definite mass m_1, m_2, m_3. The current neutrino phenomenology shows that two neutrino masses are relatively close, while the third one is lighter or heavier. Usually the two close masses are labeled as $m_1 < m_2$ and m_3 indicates the remain neutrino state.

Oscillation experiments can measure the differences of squared neutrino masses, but they are not sensitive to their absolute scale. In particular, the solar neutrino experiments are sensitive to $\Delta m^2_{21} = m^2_2 - m^2_1$, while the atmospheric one can measure $|\Delta m^2_{31}| = m^2_3 - m^2_1$. Their best fit values are [85]:

$$\Delta m^2_{21} \left[10^{-5}\text{eV}^2\right] = 7.54^{+0.26}_{-0.22} \qquad |\Delta m^2_{31} \left[10^{-3}\text{eV}^2\right] = 2.3 \pm 0.6 \tag{3.1}$$

The assumption for the sign of $\Delta m^2_{21} > 0$, but the impossibility to determine the one of Δm^2_{31} lead to two possible schemes for the mass hierarchy: the normal (NH) and the inverted (IH) hierarchies, which are shown in figure 3.1. These two schemes differ

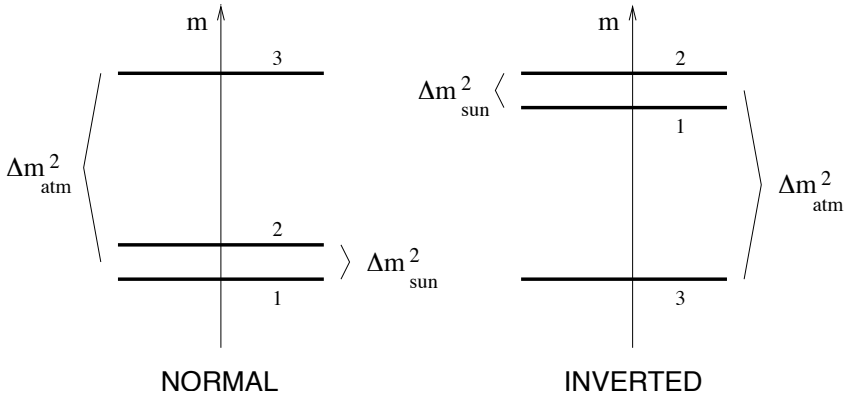

Figure 3.1: Figures taken from [67]. The two neutrino schemes allowed: normal hierarchy (NH) and inverted hierarchy (IH).

for the sign of Δm^2_{31}, which is positive (negative) for the NH (IH) scenarios.

Figure 3.2 shows the relation between the single neutrino masses and their sum, which can be found numerically. When the mass of the lighter neutrino, which is m_1 for NH and m_3 for IH, is small then the mass states follow a hierarchical scenario, while the three neutrino masses are degenerate if the mass of the lightest is big enough. In this thesis we will consider values for the sum of the neutrino masses that allow to assume the degenerate case. It is also interesting to notice that the two schemes allow for different lower bounds to the sum of the three neutrino masses,

$$\sum m_\nu \gtrsim 0.056(0.095)\,\mathrm{eV} \tag{3.2}$$

in the normal (inverted) hierarchy.

Oscillation experiments can put only lower bounds to the sum of the neutrino masses. Nowadays, the more stringent upper bounds comes from cosmology, which is directly sensitive to the absolute scale of the neutrino masses. The cosmological observables used to put upper bounds are the anisotropies in the cosmic microwave background (CMB), the spatial clustering of galaxies, and the clustering properties of neutral hydrogen absorbers in the Ly-α forest. Combining CMB and lensing with BAO probes, the Planck collaboration [96] set the upper bound to be

$$\sum m_\nu < 0.23\,\mathrm{eV} \quad \text{at } 95\,\%\,\mathrm{C.L}\,, \tag{3.3}$$

whereas analysis involving the Ly-α show a more stringent bound, $\sum m_\nu < 0.12\,\mathrm{eV}$ at 95 % C.L [86].

3.2 Background

The Standard Model of Cosmology predict the presence of relic neutrinos, generated in the early Universe by the frequent weak interactions. These neutrinos remain in thermal equilibrium with baryons and photons until weak interactions become inefficient, due to the progressive expansion of the Universe. The decoupling from the other plasma happens when the temperature of the Universe drops to $T \sim 1$ MeV. At

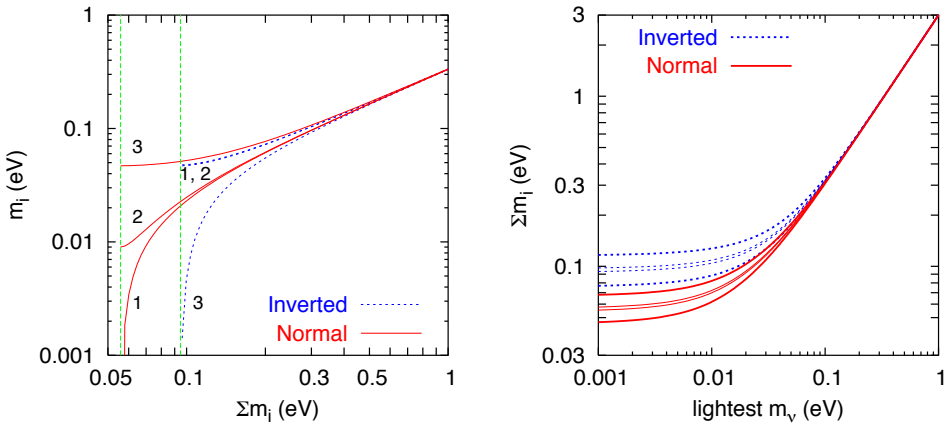

Figure 3.2: Figures taken from [67]. Expected values of neutrino masses according to the values in Eq. (3.1). Left panel: individual neutrino masses as a function of the total mass. Right panel: ranges of total neutrino mass as a function of the lightest state within the 3σ regions (thick lines) and for a future determination at the 5% level (thin lines).

this stage neutrinos are ultra-relativistic because their mass cannot be larger than few eV. Moreover, being fermions, their momentum distribution follows the Fermi-Dirac distribution,

$$f_\nu^0(q) = \frac{1}{1 + \exp(q/aT_\nu)}\,, \tag{3.4}$$

where $q = p/a$ is the comoving momentum and T_ν is the neutrino temperature, that falls as a^{-1} after the decoupling. This means that, after the decoupling, the number of neutrinos remains constant in a comoving volume. Just after that, the cosmic temperature drops below the electron mass and the annihilation of electrons and positron is favored. This process transfer entropy to photos and do not to neutrinos if we assume that they are already completely decoupled. Therefore, the neutrino temperature remain unchanged, while the photons get heat and become hotter then neutrinos. The ratio between their temperatures is $T_\gamma/T_\nu = (11/4)^{1/3}$ and the Fermi-Dirac distribution of neutrinos is smaller than the photon distribution by a factor of 7/8.

As long as neutrinos are relativistic, they contribute with photons to the total radiation energy density of the Universe. The energy density is the first moment of the distribution function. Therefore it can be written as

$$\rho_r = \left[1 + \frac{7}{8}\left(\frac{4}{11}\right)^{4/3} N_{\rm eff}\right]\rho_\gamma\,, \tag{3.5}$$

where ρ_γ is the energy density of photons, measured by CMB experiments, and $N_{\rm eff} = 3.046$ is the effective number of relativistic degrees of freedom for neutrino, that account for the fact that neutrinos are slightly coupled when electron-positron pairs annihilate transferring their entropy to photons [73, 115]. Experimentally, the value of $N_{\rm eff}$ is constrained by the Big Bang Nucleosynthesis (BBN) and the CMB anisotropies [67].

Neutrinos become non-relativistic when their mean thermal energy drops below

their mass m_ν, at a redshift $z_{\rm nr}$ given by

$$1 + z_{\rm nr}(m_\nu) \simeq 1890 \left(\frac{m_\nu}{1{\rm eV}}\right) . \tag{3.6}$$

At this stage, neutrinos contribute to the amount matter in the Universe with an energy density

$$\Omega_\nu = \frac{\rho_\nu}{\rho_{\rm crit}} = \frac{\sum_i m_i}{94.1 h^2 {\rm eV}} , \tag{3.7}$$

where $\rho_{\rm crit} = 3H^2/8\pi G$ is the critical density. The Planck collaboration [96] measured the matter energy density as $\Omega_{\rm m} \simeq 0.3$, which put an upper bound to the neutrino mass $m_\nu \lesssim 5$ eV (assuming 3 degenerate neutrino masses).

In the 1970-80s neutrinos have been considered as possible candidate for dark matter. Giving their high thermal velocities, this type of dark matter is called hot (HDM). In this scenario, big structures like superclusters are older, while smaller structures as clusters and galaxies form via a subsequent fragmentation of the first ones. However, observations show that this top-down scenario is wrong: big objects form via merging of small ones. For this reason neutrinos cannot constitute the whole amount of dark matter, but we know that they do exist and they do have mass, therefore they are at least a small fraction of the dark matter in the Universe.

There are many debate about the "coldness" of the remain part of dark matter. In this thesis, we assume the main part of the dark matter to be in the form of cold dark matter (CDM) particles, i.e. particles which were non-relativistic at the epoch when the universe became matter-dominated. We do not consider any possible warm dark matter particles. Therefore here $\Omega_{\rm m} = \Omega_{\rm b} = \Omega_{\rm c} + \Omega_\nu$, where the subscript b, c, ν stay for baryons, cold dark matter and neutrinos, respectively. Within this framework one can use the available cosmological data to find how large the neutrino contribution can be.

3.3 Linear theory

The impact of massive neutrinos on the Large Scale Structure are well know at the linear pertubation level. Here we present the main results, assuming that neutrinos are already in the non-relativistic phase.

In the previous section we have seen that the background phase-space distribution of neutrinos $f^0_\nu(q)$ is time-independent (see Eq. (3.4)). Linear order perturbations in the metric introduce some time and space corrections, at linear order. Therefore, at the first order the phase-space distribution is

$$f_\nu(q, x, \vec{n}, t) = f^0_\nu(q) \left[1 + \Psi(q, x, \vec{n}, t)\right] , \tag{3.8}$$

where $\Psi(q, x, \vec{n}, t)$ is the linear perturbation to the distribution function, $\vec{n} = \vec{q}/q$ and $f^0_\nu(q)$ has the form of Eq. (3.4). The evolution of the linearized phase-space distribution function is governed by the linearized collision-less Boltzmann equation. The neutrino perturbation can be computed by solving the Bolzmann equation since density contrast, pressure, velocity dispersion and anisotropic stress are moments of the distribution function.

Because of the absence of microscopic interaction, there is no reason for the anisotropic stress of neutrinos to be zero at linear order. Therefore neutrinos cannot be described as a perfect fluid. Since they are collision-less and have a large thermal velocity, they are not a fluid either. However, it has been shown in [110] that the fluid approximation holds for light neutrinos and long after the redshift $z_{\rm nr}$ of the non-relativistic transition. Usually the Bolzmann equation is expanded in an infinite hierarchy of terms. Applying the fluid approximation means that the hierarchy can be truncated and only the first two terms are the relevant ones.

As long as neutrinos are relativistic, they travel at the speed of light. When they become non-relativistic, their mean thermal velocity is

$$v_{th} \simeq \frac{3T_\nu}{m_\nu} \simeq 150(1+z)\left(\frac{1\text{eV}}{m_\nu}\right)\text{km}\,\text{s}^{-1}\,, \tag{3.9}$$

which make them free-streaming out from even high density perturbation of matter. In the fluid approximation framework, this can be described in analogy with sound waves propagating at finite sound speed on scales smaller than the sound horizon. Indeed, the neutrino thermal velocity introduce a typical scales, the free-streaming length

$$\lambda_{\rm FS}(z, m_\nu) = a(z)\frac{2\pi}{k_{\rm FS}} = 7.7(1+z)\frac{H_0}{H(z)}\left(\frac{1\text{eV}}{m_\nu}\right)h^{-1}\text{Mpc} \tag{3.10}$$

traveled by the neutrino perturbation between two different times. Here $k_{\rm FS}$ is the associated free-streaming wavenumber, H is the Hubble parameter and a the scale factor. For neutrinos becoming non-relativistic during matter domination, the free-streaming wavenumber reach a minimum at the transition given by

$$k_{\rm nr} = k_{\rm FS}(z_{\rm nr}) \simeq 0.018\Omega_m^{1/2}\left(\frac{m_\nu}{1\text{eV}}\right)h\text{Mpc}^{-1}\,. \tag{3.11}$$

The physical effect of free-streaming is the following: neutrino density perturbations are damped and washed out on scales smaller than $\lambda_{\rm FS}$, while large scale perturbations behave as CDM since on that scales the neutrino velocity can be considered as vanishing. In particular, modes with $k < k_{\rm FS}$ evolve as CDM perturbations. This leaves some clear feature on the total matter power spectrum.

The matter density perturbations δ_m in Fourier space can be written as weighted sum of the CDM, baryons and neutrinos density fluctuations

$$\delta_m = (1-f_\nu)\delta_c + f_\nu\delta_\nu\,, \tag{3.12}$$

where we have used $\delta_b = \delta_c$ and

$$f_\nu \equiv \Omega_\nu/\Omega_m\,, \tag{3.13}$$

being the fraction of matter in neutrinos. Then, the matter power spectrum $P_{mm}(k) = \langle\delta_m(k)\delta_m(k)\rangle$ is given by

$$P_{mm} = (1-f_\nu)^2 P_{cc} + f_\nu(1-f_\nu)P_{c\nu} + f_\nu^2 P_{\nu\nu}\,, \tag{3.14}$$

where P_{cc} and $P_{\nu\nu}$ are the cold dark matter (+baryons) and neutrino power spectra, respectively. $P_{c\nu}$ is the cold dark matter-neutrino cross-power spectrum. As we said,

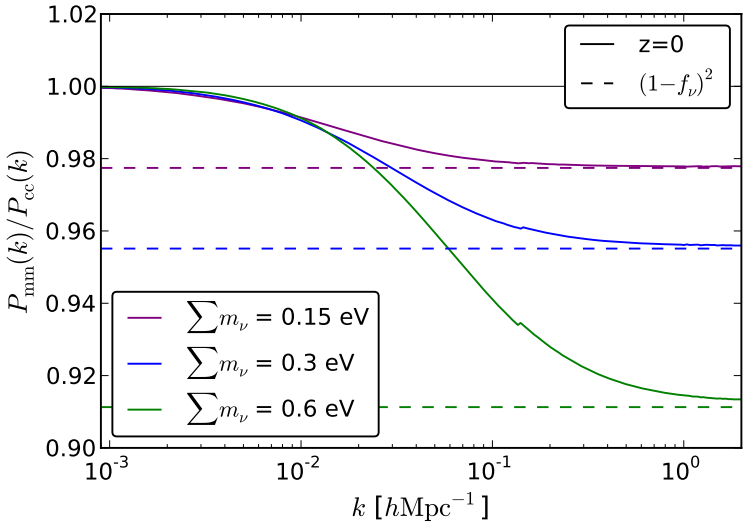

Figure 3.3: Ratio between the cold dark matter and the matter power spectra for different values of the sum of neutrino masses.

neutrino perturbations are washed out on scales $k > k_{\rm nr}$. This scale is typically larger than the scale at which nonlinear effects are relevant at low redshifts. Therefore, at the end of matter domination $\delta_\nu = \delta_c = \delta_b$ for $k < k_{\rm nr}$, while $\delta_\nu \ll \delta_c = \delta_b$ for $k \gg k_{\rm nr}$. The matter power spectrum is, then,

$$P_{mm}(k) = \begin{cases} P_{cc}(k) & \text{if } k < k_{\rm nr} \\ (1-f_\nu)^2 P_{cc}(k) & \text{if } k \gg k_{\rm nr} \end{cases} \tag{3.15}$$

from which we see that the $P_{mm}(k) \leq P_{cc}(k)$, at all scales. This behavior is shown in figure 3.3, where we plot the ratios between the matter and the cold dark matter power spectra for different values of the sum of the neutrino masses. This ratio have been computed running the code CAMB [68], that solves the Boltzmann equations for the evolution of matter perturbations at the linear level. On large scales the ratio is 1 and going towards smaller scales it increases reaching the asymptotic value $(1-f_\nu)^{-2}$ on very small scales. However, neutrinos modify also the evolution of CDM and baryons them-self, via back-reaction. This translates into an additional suppression of the total matter power spectrum on small scales.

The neutrino back-reaction acts in two different ways. First, the presence of a background neutrino field modifies the expansion rate of the Universe, which translate into a damping of CDM and baryon perturbations on small scales. Second, the density, pressure and velocity neutrino perturbations change the evolution of the metric perturbations and the neutrino shear induces a non-zero difference between the two gravitational potentials, which is however not relevant during matter domination. The main effect on the growth of matter perturbations comes from the first, i.e. the presence of the neutrino background.

In the absence of neutrinos and during matter domination, the density contrast of CDM and baryons grow like the scale factor $\delta_c \propto a$ as in Eq.(1.26). The same holds with massive neutrinos for scales much larger that the free-streaming length. Indeed,

neutrinos contribute both to the Poisson equation with $\delta_\nu = \delta_c$ and to the background evolution, so the density contrast of matter, and in particular the CDM one, grows like the growth factor. On small scales, $k \gg k_{\rm nr}$, the behavior is different. The presence of background neutrinos contribute to the expansion rate but the neutrino perturbations are damped and do not contribute to the clustering of matter. Then, the contribution of neutrino perturbations to the Poisson equation can be neglected. In this case, the CDM perturbations satisfy the equation

$$\ddot{\delta}_c + 2H(z)\dot{\delta}_c - \frac{3}{2}H^2(z)(1-f_\nu)\delta_c = 0\,, \tag{3.16}$$

which is different from Eq.(1.24) and has a growing solution [12]

$$\delta_c \propto a^{1-\frac{3}{5}f_\nu}\,, \tag{3.17}$$

assuming that $f_\nu \ll 1$. The above solution show that the evolution of CDM (and baryons) perturbations are reduced. Clearly, this is due to the fact that one of the component in the Universe contributes to the homogeneous expansion rate but not to the gravitational clustering. On intermediate scales, the CDM perturbations smoothly interpolate between the two asymptotic regimes resulting in scale dependent linear growth factor.

Let us see how this translate into the evolution of the matter power spectrum. We consider two different cosmology that share the same values of Ω_m and Ω_b, but differ for Ω_c according to the amount of neutrinos: $\Omega_c = \Omega_m - \Omega_b - \Omega_\nu$. Let the first one have massive neutrinos ($f_\nu > 0$) and be label as $\nu\Lambda$CDM, the second one be without neutrinos and thus called ΛCDM. On large scales, $k < k_{\rm nr}$, the CDM and neutrino perturbations are indistinguishable and they are equal to the CDM perturbations in a cosmology without neutrinos. Therefore, the ratio of the linear matter power spectra in the two cosmologies is equal to 1. It is interesting to notice that in these two cosmologies the matter-radiation equality does not take place at the same time. The value of the scale factor at equality is $a_{\rm eq} = \Omega_r/(\Omega_c + \Omega_b)$. Since neutrinos are still relativistic at equality, they have to be considered as radiation. Then the ratio between the scale factors in the two cosmology is

$$a_{\rm eq}^{\nu\Lambda{\rm CDM}}/a_{\rm eq}^{\Lambda{\rm CDM}} = (1-f_\nu)^{-1}\,, \tag{3.18}$$

which means that the equality is delayed by the presence of massive neutrinos. The delayed equality and the back-reaction mechanism in Eq. (3.17) damp the linear matter power spectrum in massive neutrino cosmologies on small scales. On scales $k \gg k_{\rm nr}$ and for small values for f_ν, the ratio between the matter power spectrum in the two cosmology can be approximated to [54]

$$\frac{P_{\nu\Lambda{\rm CDM}}(k)}{P_{\Lambda{\rm CDM}}(k)} \simeq 1 - 8f_\nu\,. \tag{3.19}$$

On intermediate scales, there is a smooth transition between the two asymptotic regimes. The ratio is shown in figure 3.4, where the two different asymptotic values can be seen.

The linear regime, on large scales, is probed by different cosmological observables such as CMB anisotropies and CMB gravitational lensing, commonly used to put constrains on the neutrino masses [96].

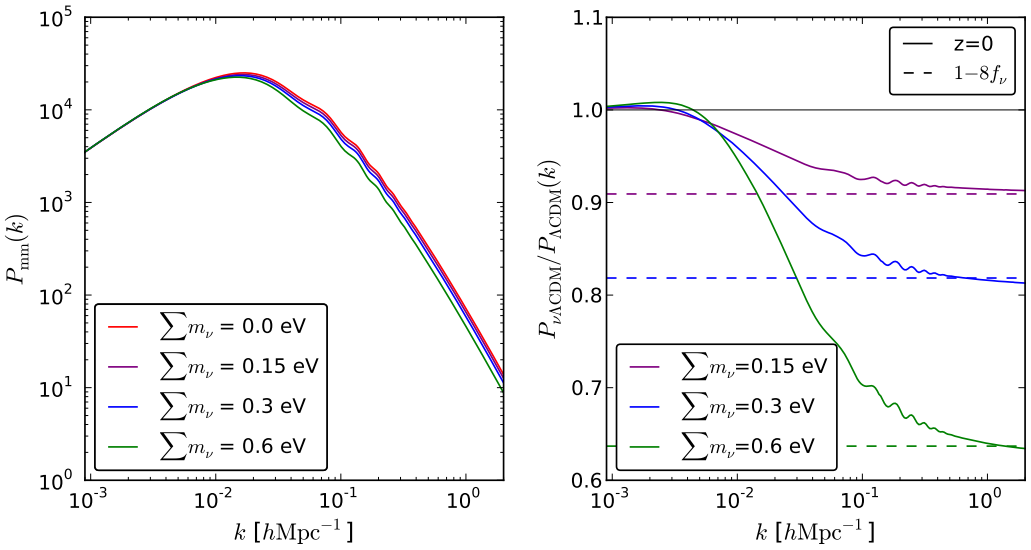

Figure 3.4: Impact of neutrino masses on the linear matter power spectrum. Left panel: matter power spectrum for different values of the sum of neutrino masses. Right panel: ratio of the linear matter power spectrum in a massive neutrino cosmology ($\nu\Lambda$CDM) with respect to the massless case (ΛCDM).

3.4 Nonlinear theory

Massive neutrinos also impact on the evolution of structures in the fully non-linear regime in many different ways. The cosmological observables involved are: the matter power spectrum at small scales [25–30], the halo-matter bias [31–34], the clustering within dark matter halos [35–41], the evolution of cosmic voids [42], the halo mass function [31, 32, 38, 43–45], the redshift-space distortions [43], the Ly-α forest statistical properties of the transmitted flux [28, 42, 46], the Sunyaev-Zeldovich effects in galaxy cluster surveys [47], the galaxy clustering [48].

Nowadays, we have a good understanding of the evolution of the cosmological structures at the linear perturbation level. We also understand the impact of massive neutrinos on them. Instead we lack a description of the fully non-linear regime, which will become important to interpret the data from the next generation of surveys. Here, we briefly review the two methods used to predict the evolution of structures in the nonlinear regime, which account for the presence of massive neutrino. They are a fitting-function method called HALOFIT, and the machinery of N-body simulations.

3.4.1 HALOFIT

Sometimes is sufficient and useful to rely on a fitting formula to describe what is complicated from the theoretical point of view. Here we discuss the fitting formula HALOFIT [112], which allows to compute the nonlinear matter power spectrum given the corresponding linear one.

The main idea of HALOFIT comes from [52], where the authors develop a method for mapping the linear theory on large scales into nonlinear predictions on small scales, assuming the stable clustering hypothesis. This hypothesis states that a nonlinear

collapsed object decouples from the global expansion of the Universe to form an isolated system in virial equilibrium. In particular, the authors propose the so called 'scaling ansatz': the nonlinear volume averaged two point correlation function of matter

$$\bar{\xi}(x) \equiv \frac{3}{x^3}\int_0^1 y^2 \xi(y) dy\,, \tag{3.20}$$

can be described as a simple function of the linear two point function, provided a transformation of scales due to nonlinear evolution. This transformation is performed in the spirit of the spherical collapse model. Supposed that the enclosed mass of a spherical overdensity in the initial density field is $m_0(< x_{\rm i})$ and it evolves into a mass $m(< x_{\rm f})$ of different size. If there is no shell-crossing, the mass is conserved and $\rho_i(< x_{\rm i}) x_{\rm i}^3 = \rho(< x_{\rm f}) x_{\rm f}^3$, where the densities are averaged over the volume. Let notice that the enclose correlation $1+\bar{\xi}$ measures by how much the density is enhanced compared to the mean. We can use this mapping to connect the linear (L) and the nonlinear (NL) overdensities and scales. If the linear correlation function is $\bar{\xi}_{\rm L} \ll 1$, then

$$x_{\rm L}^3 = x_{\rm NL}^3 \left[1 + \bar{\xi}_{\rm NL}(x,z)\right]\,, \tag{3.21}$$

where $x_{\rm NL}$ represents the nonlinear Eulerian scale and $x_{\rm L}$ is the linear Lagrangian one. Once the rescaling is done, the mapping between the two point functions is given,

$$\bar{\xi}_{\rm NL}(x_{\rm NL}, z) = f\left[\bar{\xi}_{\rm L}({\rm L}, z)\right]\,. \tag{3.22}$$

The function f is universal and it can be estimated analytically in two regimes: 1) in the linear regime, when $\bar{\xi}_{\rm L} \ll 1$ and $f = 1$; 2) in the case $\bar{\xi}_{\rm L} \gg 1$ where the stable clustering case apply, i.e. the linear enclosed correlation scales as the square of the scale factor, $\bar{\xi}_{\rm L} \propto a^2$, while the nonlinear one goes as $\bar{\xi}_{\rm NL} \propto a^3$. Then, in this second case the function is $f(y) \propto y^{3/2}$. On intermediate regimes, the solution for the function has to be found empirically, fitting the results from N-body simulations.

An additional important contribution was given by [94], where the mapping between linear and nonlinear regimes is extended to the power spectrum. The key idea is recognizing that $\bar{\xi}$ can be replaced by the adimensional power spectrum Δ^2 at some effective wavenumber. Then, the Fourier counterpart of Eqs. (3.21) and (3.22) is given by

$$\Delta^2_{\rm NL}(k_{\rm NL}) = f\left[\Delta^2_{\rm L}(k_{\rm L})\right]\,, \tag{3.23}$$

$$k_{\rm NL} = \left[\Delta^2_{\rm NL}(k_{\rm L})\right]^{1/3} k_{\rm L}\,. \tag{3.24}$$

Finally the authors in [112] formulated the HALOFIT prescription in ΛCDM cosmologies, rewriting the ideas presented below in the spirit of the halo model (see Chapter 5 for a review). This framework is based on the idea that all the matter is in virialized structures, the halos. Therefore, the matter power spectrum is written as the sum of two terms,

$$\Delta^2_{\rm NL}(k) = \Delta^2_{\rm Q}(k) + \Delta^2_{\rm H}(k)\,, \tag{3.25}$$

where $\Delta^2_{\rm Q}$ is the so called quasi-linear term that describes the power generated by the large-scale displacement of halos, and $\Delta^2_{\rm H}$ is the halo term representing the cluster of

matter inside each halo. These two contributions are then the 2- and 1-halo term in the standard framework of the halo model, respectively. They have the form,

$$\Delta^2_{\rm Q}(k) = \Delta^2_{\rm L}(k)\left[\frac{(1+\Delta^2_{\rm L}(k))^{\beta_n}}{1+\alpha_n\Delta^2_{\rm L}(k)}\right]\exp(-f(y))\,, \tag{3.26}$$

$$\Delta^2_{\rm H}(k) = \frac{\Delta^{2\,\prime}_{\rm H}(k)}{1+\mu_n y^{-1}+\nu_n y^{-2}}\,, \tag{3.27}$$

where $y \equiv k/k_\sigma$ with k_σ being the inverse of the scale where the variance of the density field is equal to 1, $f(y) = y/4 + y^2/8$ and

$$\Delta^{2\,\prime}_{\rm H}(k) = \frac{a_n y^{3f_1(\Omega_m)}}{1+b_n y^{f_2(\Omega_m)}+[c_n f_3(\Omega_m) y]^{3-\gamma_n}}\,. \tag{3.28}$$

The form of quasi-linear and the halo terms are quite complicated and they depend on many parameters, that are functions of the matter density Ω_m (f_1, f_2, f_3), or of the spectral index n (a_n, b_n, c_n, γ_n, α_n, β_n, μ_n, ν_n). All these functions are fit to N-body simulations and the details about them can be found in the Appendix C of [112].

There have been improvements to the first version of HALOFIT by [118]. This revised formula is expected to be an accurate prediction of the nonlinear matter power spectrum in a wide range of wavenumber ($k \leq 30\,h{\rm Mpc}^{-1}$) at redshifts $z \leq 10$, with 5% precision for $k < 1\,h{\rm Mpc}^{-1}$ at $z \leq 10$, and 10% for $k < 10\,h{\rm Mpc}^{-1}$ at $z \leq 3$.

A further extension has been done by [10] that, adding few parameters to the original HALOFIT, enables it to account for neutrinos effects on the nonlinear total matter power spectrum.

3.4.2 N-body simulation

N-body simulations are a very good tool to study the evolution of structures in the fully nonlinear regime. Nowadays there are two main ways to implement neutrinos in them: the so called grid-method [15] and particle-method [121].

The grid method describes the neutrino density on a grid, without introducing any neutrino particle, while the CDM component is implemented using a particle description, as in usual ΛCDM simulations. The neutrino density is evolved in time using linear theory and its gravitational force contributes only as a long-range force. This type of simulations have the advantage of being a fast implementation of the matter evolution in massive neutrino cosmologies which do not suffer from the presence of shot noise on small scales. However, they are not able to properly describe the nonlinearities of the neutrino component. Therefore, they can be used only in regimes where the nonlinear effects of neutrinos are negligible.

In the particle-method both CDM and neutrinos are simulated as collision-less particles with individual velocities. We make use of this type of simulations in this thesis, since they are able to capture the nonlinear regime of massive neutrinos once the short-range gravitational forces acting on neutrinos are taken into account. Ref. [123] showed that this feature is required to correctly account for the clustering of neutrinos within dark matter halos and to reproduce the neutrino halos down to small scales. We will present the setup and the main features of our simulations, along with the list of their specific parameters, in Chapter 4.

Chapter 4

Tools

In this chapter we will present some numerical tools broadly used in the next part of this thesis. In particular, we will describe the setup and properties of the N-body simulations run to compare our theoretical models to the fully nonlinear regimes achieved numerically (in Part II and Part IV), or to perform some statistical analysis directly from the output of the simulations (in Part III). Secondly, we will introduce the void finder used to identify voids in the simulations. This is the underlying tool used in Part III, to perform a numerical study of void properties and isolate the neutrino impact on them, and in Part IV, to test our theoretical predictions for the shape and evolution of void profiles and bias.

4.1 N-body simulations

Our N-body simulations are performed using the TreePM-SPH (Tree Particle Mesh-Smoothed Particle Hydrodynamics) code GADGET-3, which is an improvement of the publicly available GADGET-2 [113], as modified in [121] to account for massive neutrinos. Here, CDM and neutrinos are treated as two separate set of collision-less particles. In the PM the mass of each particle is interpolated on a fixed grid to compute the density. The Poisson equation is solved on the grid using a Fast Fourier transform and the gravitational forces are then interpolated back on the particles. Differently from the grid-method, the short-range tree is included to compute the gravitational forces acting on neutrinos on small scales; ref. [123] showed that this feature is required to correctly account for the clustering of neutrinos within dark matter halos and to reproduce the neutrino halos down to small scales. A part from the mass, the only difference between CDM and neutrinos concerns how they are initialized at the starting redshift of the simulation. Indeed, neutrinos receive an extra thermal velocity obtained by randomly sampling the neutrino Fermi-Dirac momentum distribution, whose mean is shown in Eq.(3.9).

The initial conditions (ICs) have been generated at $z = 99$ by displacing the particle positions according to the Zel'dovich approximation [131], for both CDM and neutrino particles. They share the same set of random numbers in each box, to reproduce the assumption of adiabatic primordial ICs. The transfer functions are obtained through CAMB [68]. There are not baryons in our simulations, however their effects (for instance the BAO wiggles) on the CDM field are included using a transfer function T_{cb}

that is a weighted average of the transfer functions of the CDM and the baryons:

$$T_{cb}(k) = \frac{\Omega_c T_c(k) + \Omega_b T_b(k)}{\Omega_c + \Omega_b} \,. \tag{4.1}$$

Other baryonic effects are expected to be mostly insensitive to the neutrino mass, and therefore not relevant when we will compare the effect of massive neutrinos on large scale structure measurements to the same quantities measured in a standard ΛCDM model. Moreover, any additional effect produced by the interplay of neutrinos with baryon physics should be of higher order. This is supported by [10], which shows that the neutrino induced suppression in the total matter power spectrum is very much the same in simulations with and without baryons.

The values of the cosmological parameters, for all simulations with the exception of few of them that we discuss below, are the ones found by the Planck collaboration [96]: $\Omega_{\rm m} = 0.3175$, $\Omega_{\rm b} = 0.049$, $\Omega_\Lambda = 0.6825$, $h = 0.6711$, $n_s = 0.9624$, $A_s = 2.13 \times 10^{-9}$. We have run simulations for four different cosmological models: a model with massless neutrinos and three models with massive neutrinos (three degenerate species) with masses $\sum m_\nu = 0.15$ eV, $\sum m_\nu = 0.3$ eV and $\sum m_\nu = 0.6$ eV. In our simulations the value of $\Omega_{\rm m}$ and $\Omega_{\rm b}$ is fixed, whereas the values of $\Omega_{\rm c}$ and Ω_ν depend on the neutrino masses (see Eq. (3.7)) such as $\Omega_{\rm c} = \Omega_{\rm m} - \Omega_{\rm b} - \Omega_\nu$. In order to investigate the $\sum m_\nu - \sigma_8$ degeneracy, we have also run simulations with massless neutrinos, but a value of σ_8 equal to the one of the $\sum m_\nu = 0.6$ eV model. The σ_8 value has been computed from the total matter or from the CDM power spectrum. In all simulations the softening length ϵ of both CDM and neutrino particles is set to 1/40 of the mean linear inter-particle distance.

In simulations with the sum of the neutrino masses lower than current tightest bounds $\sum m_\nu < 0.12$ eV [86] the effects of massive neutrinos may not be seen properly or they would be largely contaminated by cosmic variance. We chose values for the neutrino masses that do not respect this bound because we want to enhance the effects of massive neutrinos in the mildly-nonlinear and nonlinear regimes in order to isolate and study them, more than giving a precise estimation of their real magnitude. Note further that some groups are claiming that concordance cosmology between Planck CMB data and cluster abundance or weak lensing could be achieved by allowing a non-zero neutrino mass of 0.3 eV (±0.1 eV) (see however the discussion in the latest Planck cosmological parameter paper [96]).

The name of the simulations arises from their size (L for 1000 h^{-1}Mpc, M for 500 h^{-1}Mpc and S for 200 h^{-1}Mpc), from the number of CDM particles (f for 256^3 and m for 512^3) and from the value of neutrino masses (0 for 0.0 eV, 15 for 0.15 eV and so on). For instance, the simulation Lf30 has box-size equal to 1000 Mpc/h, 256^3 CDM particles and $\sum m_\nu = 0.3$ eV. Simulation with massless neutrinos but different σ_8 are labeled as s8 and s8CDM, depending if the σ_8 value has been computed from the total matter or from the CDM power spectrum, respectively. Depending on the need, we have run one or more realizations for each simulation type. A summary of our simulation suite is shown in table 4.1, where the group on top is used in Part II, while the one on bottom concerns Part III and IV.

For each simulation we have computed the CDM power spectrum, the neutrino power spectrum, the CDM-neutrino cross-power spectrum and the total matter power

Name	Box Size (Mpc/h)	$\sum m_\nu$ (eV)	$N_{\rm cdm}$	N_ν	ϵ (kpc/h)	σ_8 (z=0)	realizations
Lm0	1000	0.00	512^3	0	50	0.834	1
Lm15	1000	0.15	512^3	512^3	50	0.801	1
Lm30	1000	0.30	512^3	512^3	50	0.764	1
Lm60	1000	0.60	512^3	512^3	50	0.693	1
Sm0	200	0.00	512^3	0	10	0.834	1
Sm15	200	0.15	512^3	512^3	10	0.801	1
Sm30	200	0.30	512^3	512^3	10	0.764	1
Sm60	200	0.60	512^3	512^3	10	0.693	1
Lf0	1000	0.00	256^3	0	100	0.834	10
Lf0s8	1000	0.00	256^3	0	100	0.693	10
Lf0s8CDM	1000	0.00	256^3	0	100	0.717	10
Lf15	1000	0.15	256^3	256^3	100	0.801	10
Lf30	1000	0.30	256^3	256^3	100	0.764	10
Lf60	1000	0.60	256^3	256^3	100	0.693	10
Mm0	500	0.00	512^3	0	25	0.834	1
Mm15	500	0.15	512^3	512^3	25	0.801	1
Mm30	500	0.30	512^3	512^3	25	0.764	1
Mm60	500	0.60	512^3	512^3	25	0.693	1

Table 4.1: Specifications of our N-body simulation suite. The first letter of the simulation name indicates whether the box-size is (L) , medium (M) or small (S). The second letter refers to the number of CDM particles: many (m) or few (f). The values of the following cosmological parameters are the same for all the simulations (with the exception of the simulation L0s8 in which $A_s = 1.473 \times 10^{-9}$ and L0s8CDM where $A_s = 1.576 \times 10^{-9}$): $\Omega_{\rm m} = 0.3175$, $\Omega_{\rm b} = 0.049$, $\Omega_\Lambda = 0.6825$, $h = 0.6711$, $A_s = 2.13 \times 10^{-9}$, $n_s = 0.9624$.

spectrum. The amplitude of the neutrino and the total matter power spectrum has been corrected to account for the shot-noise associated to the neutrino density field.

4.2 Void finder

We identify voids using the publicly available Void Identification and Examination (VIDE) toolkit [116], which uses a modified version of ZOBOV [84] to perform a Voronoi tessellation of the particles and then a watershed transform to group the Voronoi cells into a hierarchical tree of subvoids and voids [97]. A pictorial explanation of the process is shown in Figure 4.1.

The first step is called called Voronoi Tessellation Field Estimator (VTFE) and it performs a density estimation at each dark matter particle. It divides the space into cells such that each cell contains only one particle i and it has volume $V(i)$ defined as the region of space closer to particle i than to any other particle. The density associated to particle i is $1/V(i)$. This step gives also a natural set of neighbors for each particle i (the set of particles whose cells adjoin the cell i), which will be used in the next step. Panel (a) of figure 4.1 shows a set of particles from the Millennium simulation [113],

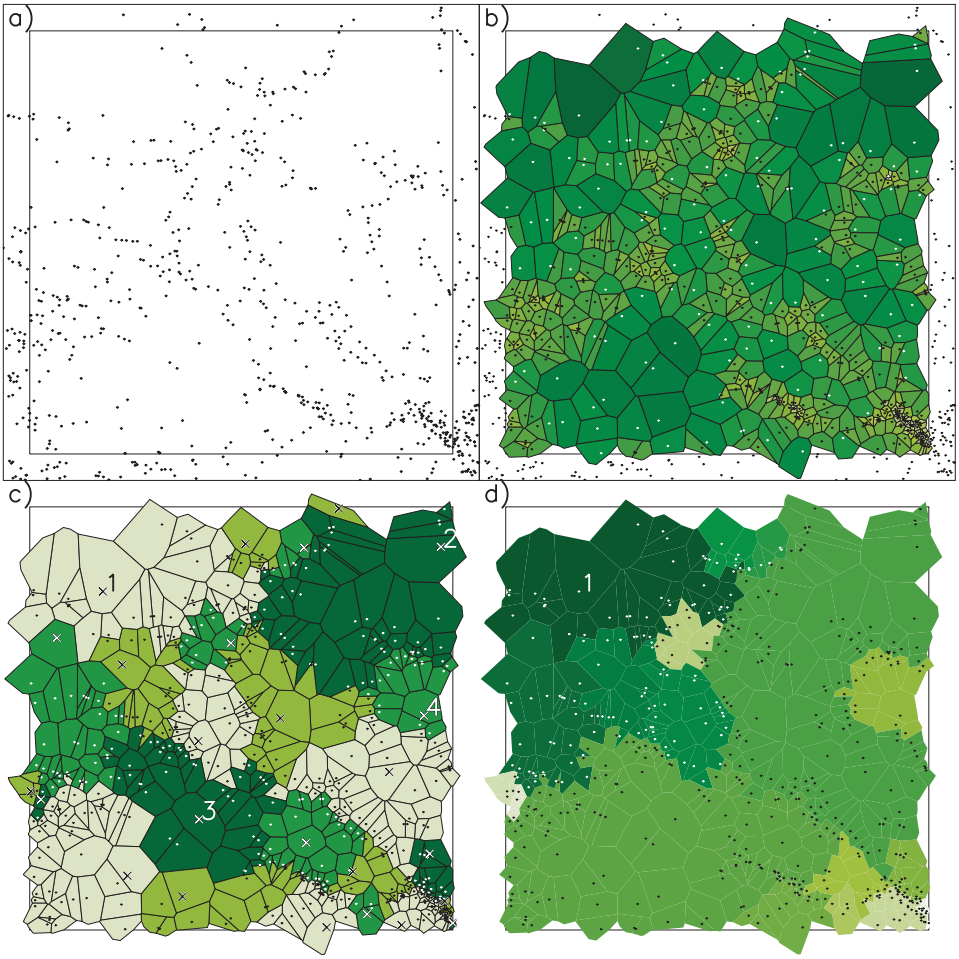

Figure 4.1: Figure from [84]. (a) Galaxies by Croton et al. [34] from a $40 \times 40 \times 5$ $(h^{-1}\mathrm{Mpc})^3$ slice. (b) The 2D Voronoi tessellation of galaxies in this slice, with each Voronoi cell shaded according to its area. The galaxies outside the inner ($40\ h^{-1}$ Mpc) boundary are shown because they contribute to the tessellation. (c) Zones of galaxies. The cores (density minima) of each zone are shown with crosses; the different colors merely demarcate different zones. (d) The growth of void 1, the deepest void in the sample. With analogy to a water tank, the water level (density) is increased and zones the water runs into are added to the void. Colors from dark to light indicate the stage at which the zone is added to the void. The darkest color is the original zone, the next darkest is the first zone or set of zones added, etc.

and panel (b) illustrates the corresponding Voronoi tessellation, where different colors describe different cells.

The second step involve the joining of Voronoi cells into zones around each local minimum, and it is called zoning. A local minimum is a particle with density lower than all its neighbor cells. The void finder sends all the particles to their minimum density neighbor until it arrives to the local minimum. Thus, a zone is the set of particles that flow towards the same minimum. Panel (c) of figure 4.1 shows the result of this process, where different colors correspond to different zones. Each of them could be considered a voids, but, because of discreteness noise, many zones are spurious. Thus, it is necessary to join some zones together to form the final voids.

The last step joins zones together using a watershed algorithm, as follows. For each zone z, the water level is set to the minimum density of z. Then, it is gradually raised so that the water can flow to neighbor zones, joining them to the zone z. The process stop when the water flows into a zone with a lower minimum. The final void related to z is defined to be the one just before this happens. If starting from the zone with the deepest minimum of the simulations, the algorithm will join all the zones and will identify all the space as a huge voids. Panel (d) of figure 4.1 shows the stages of growth that the deepest void in the set of particles undergoes. The process starts from the darker region, which is the deepest one. Successively lighter colors shade zones are added as the water level is increased. Since this is the deepest void, its final extent covers the whole simulation, except for the zone lighter zone in the lower right-hand corner of the figure, which has the highest density particle separating it from from the void. In order to avoid this percolation, we must take into account some criterion that stop the merging of zones. A possible one is related to measuring the probability that each void is real, based on how likely the void density contrast occurs in a Poisson realization. Then, a significance level at which to trust that a subvoid is real and independent void can be set. The probability that a void v is real is connected to the ratio $r(v)$ between the minimum particle density at the border with a deeper void and its minimum density. Neyrinck [84] estimated that this ratio is $r = 2.19$ at the 2σ level and $r = 7$ at 5σ. The void finder then excises subvoids above the significance level from parent voids, together with all zones which join the parent void in the same accretion event or in subsequent ones.

A final catalog of voids is then built using the criteria that the voids must be larger than the mean particle separation in the simulation. In the analysis performed in Part III we will only consider voids larger than 4.0 Mpc/h in the CDM field (low resolution simulations) and voids larger than 10 Mpc/h in the galaxy distribution (high resolution simulations). While voids naturally form a nested hierarchy, we only consider top-level (i.e., parent) voids.

When identifying voids in the matter density field, we run VIDE on top of the cold dark matter particles only, even if we are considering cosmologies with massive neutrinos. In principle we should select voids in the total matter field, including also neutrinos. However, VIDE cannot discriminate between two different particle populations having two different masses. Therefore we must select voids in one of the two density fields and the CDM is the one mainly responsible for the evolution of the cosmic structures. It would be interesting to understand the differences arising in defining voids in the CDM or in the total matter field and which of the two is the fundamental field to identify

voids. When selecting voids in the galaxy distribution we instead run VIDE on top of the whole mock galaxy catalog.

The output of VIDE is a catalog which contains much information about the identified voids. In this thesis we use only the following: position of the center, particle members, effective radius (R_{eff}) and ellipticity. The effective radius R_{eff} is defined as the radius of a sphere containing the same volume as the watershed region that delimits the void, and the center is the volume-weighted center of all the Voronoi cells in each void.

Part II

Halo Model with Massive Neutrinos

Based on:

E. Massara, F. Villaescusa-Navarro and M.Viel, *The halo model in a massive neutrino cosmology*, *JCAP* **12** (Dec., 2014) 53, [arXiv:1410.6813].

Abstract

We provide a quantitative analysis of the halo model in the context of massive neutrino cosmologies. We discuss all the ingredients necessary to model the non-linear matter and cold dark matter power spectra and compare with the results of N-body simulations that incorporate massive neutrinos. Our neutrino halo model is able to capture the non-linear behavior of matter clustering with a $\sim 20\%$ accuracy up to very non-linear scales of $k = 10$ h/Mpc (which would be affected by baryon physics). The largest discrepancies arise in the range $k = 0.5-1$ h/Mpc where the 1-halo and 2-halo terms are comparable and are present also in a massless neutrino cosmology. However, at scales $k < 0.2$ h/Mpc our neutrino halo model agrees with the results of N-body simulations at the level of 8% for total neutrino masses of < 0.3 eV. We also model the neutrino non-linear density field as a sum of a linear and clustered component and predict the neutrino power spectrum and the cold dark matter-neutrino cross-power spectrum up to $k = 1$ h/Mpc with $\sim 30\%$ accuracy. For masses below 0.15 eV the neutrino halo model captures the neutrino induced suppression, casted in terms of matter power ratios between massive and massless scenarios, with a 2% agreement with the results of N-body/neutrino simulations. Finally, we provide a simple application of the halo model: the computation of the clustering of galaxies, in massless and massive neutrinos cosmologies, using a simple Halo Occupation Distribution scheme and our halo model extension.

Introduction

The best way to study the impact of massive neutrinos on the mildly and fully non-linear regime is via N-body simulations. However these simulations are computationally expensive and thus, the parameter space can not be fully sampled. The aim of this Part of the thesis is to extend the halo model [31], which is a complementary approach to some Perturbation Theories (PT), in order to be able to compute the matter and cold dark matter power spectrum in massive neutrinos cosmologies. Notice that previous works have already tried to extend the halo model to incorporate the effects of massive neutrinos [1], although their results are in great tension with those from the N-body.

Having an analytic model allows to get physical insight on massive neutrino cosmologies at nonlinear scales. We use the model to understand the typical spoon-shape seen in N-body simulations when computing the ratio between power spectra in massless and massive neutrinos cosmologies. Moreover, we apply it to the study of galaxy clustering.

It is important to note that on small scales baryonic processes are very important [40, 41, 120] and can (at least partially) mimic the neutrino induced effects [81]. Here we do not account for these important processes since we want the isolate the effects of massive neutrinos w.r.t. the same simulation set-up without massive neutrinos. We thus caution the reader that on small scales the matter power spectrum has to be modeled more carefully by incorporating baryonic physical processes, e.g. galactic feedback, especially in view of future missions like Euclid.

This paper is organized as follows. In Chapter 5 we review the standard halo model, which is capable of predicting, with high accuracy, the matter power spectrum in cosmologies with massless neutrinos. Our extension of the halo model to incorporate cosmologies with massive neutrinos is presented in Chapter 6, where we compare the results of our extended halo model against N-body simulations. In section 6.3 we use the halo model to explain the small scale features present in the matter power spectrum of cosmologies with massive neutrinos. In Chapter 7 we present the galaxy clustering predicted by halo model, once a Halo Occupation Distribution (HOD) framework has been considered, and we compare it with measurements.

Chapter 5

Halo Model in pure ΛCDM cosmology

In this chapter we briefly review the halo model [31], as it was built for cosmologies without massive neutrinos.

Simulations showed that the initial smooth dark matter field evolves in a network of filaments and knots, which are highly nonlinear. The halo model provides a description of the statistical properties of this evolved dark matter field, assuming that all the matter is bound up in isolated knots, called halos. Let us call $\vec{x}_i$ the centers of these halos. Then, the matter density at position $\vec{x}$ is given by summing up the contribution from each halo

$$\rho(\vec{x}) = \sum_i \rho(\vec{x} - \vec{x}_i|M_i) \tag{5.1}$$

$$= \sum_i \int dM\, \delta(M - M_i) \int d^3x'\, \delta^3(\vec{x}' - \vec{x}_i)\; M\, u(\vec{x} - \vec{x}'|M)\,, \tag{5.2}$$

where $\rho(\vec{x} - \vec{x}_i|M_i)$ is the density around the $i-$th halo and we have assumed that it depends only on the mass M_i contained in the halo, whereas $u(\vec{x} - \vec{x}_i|M_i) \equiv \rho(\vec{x} - \vec{x}_i|M_i)/M_i$ is the normalized profile.

Let us consider the matter density contrast, which is defined as $\delta(\vec{x}) = \rho(\vec{x})/\bar{\rho} - 1$, where $\bar{\rho}$ is the comoving background matter density, and the power spectrum, which is the Fourier transform of the two-point correlation function $\langle \delta(\vec{x}_1)\delta(\vec{x}_2)\rangle$, with the average taken over the ensemble. The fully nonlinear matter power spectrum predicted by the halo model is given by the sum of two terms

$$P(k) = P_{1h}(k) + P_{2h}(k)\,. \tag{5.3}$$

The 1-halo term, $P_{1h}(k)$, counts for the correlations between particles that belong to the same halo and dominates on small scales, whereas the 2-halo term, $P_{2h}(k)$, describes the correlation between particles in different halos and becomes important on large scales. Since the comoving number density of halos of mass M, per mass unit, at redshift z is defined as

$$\left\langle \sum_i \delta(M - M_i)\; \delta^3(\vec{x}' - \vec{x}_i) \right\rangle \equiv n(M, z)\,, \tag{5.4}$$

and we assume a spherically symmetric profile $u(\vec{x}-\vec{x}_i|M_i) = u(r_i|M_i)$, the 1- and 2-halo terms are

$$P_{1h}(k,z) = \int_0^\infty dM\, n(M,z) \left(\frac{M}{\bar{\rho}}\right)^2 |u(k|M)|^2 \tag{5.5}$$

$$P_{2h}(k,z) = \int_0^\infty dM'\, n(M',z)\, \frac{M'}{\bar{\rho}}\, u(k|M') \times \int_0^\infty dM''\, n(M'',z)\, \frac{M''}{\bar{\rho}}\, u(k|M'')\, P_{hh}(k|M',M'',z), \tag{5.6}$$

where $P_{hh}(k|M',M'',z)$ is the power spectrum of halos of mass M' and M'' and $u(k|M)$ is the Fourier transform of the normalized profile

$$u(k|M) = \int_0^{R_{\rm vir}} dr\, 4\pi r^2\, \frac{\sin(kr)}{kr}\, u(r|M)\,. \tag{5.7}$$

The cut-off $R_{\rm vir}$ is the virial radius, which is the comoving radius of the spherical region containing the halo mass $M = 4\pi R_{\rm vir}^3\, \Delta_{\rm vir}\bar{\rho}/3$ with average comoving density $\Delta_{\rm vir}\bar{\rho}$, where the virial overdensity $\Delta_{\rm vir}$ is determined by the cosmology [19] via Eq.(1.46). For completeness we rewrite it here,

$$\Delta_{\rm vir} = \frac{18\pi^2 + 82x - 39x^2}{1+x} \tag{5.8}$$

$$x \equiv \Omega(z) - 1 \tag{5.9}$$

$$\Omega(z) = \frac{\Omega_{\rm c}(1+z)^3}{\Omega_{\rm c}(1+z)^3 + \Omega_\Lambda} \tag{5.10}$$

and $\Omega_{\rm c}$ being the cold dark matter plus baryons energy density today. The average density profile of cold dark matter halos has been extensively studied and it appears to be universal over a wide ranges of masses. Up to now, the fitting formula that better reproduces the density around halos in simulations is the Navarro-Frank-White (NFW) profile [83]

$$u(r|M) = \frac{F/4\pi}{r(r+r_s)^2}. \tag{5.11}$$

The parameter $r_s^3 = 3M/(4\pi c^3 \Delta_{\rm vir}\bar{\rho})$ defines a characteristic radius which is a function of the halo mass M; $F = 1/[\ln(1+c) - c/(1+c)]$, where $c = R_{\rm vir}/r_s$ is the concentration parameter. Simulations show that, for fixed halo mass and redshift, there is a distribution of concentrations which is well described by a log-normal distribution [59] with variance that does not depend on the halo mass and a mean value [20]

$$c(M,z) = 9\left(\frac{M}{M_\star(z)}\right)^{-0.13}, \tag{5.12}$$

where $M_\star(z)$ is the characteristic nonlinear mass scale defined such that the peak height (defined in Chapter 1 and explicitly rewritten below) is $\nu = 1$. Note also that the NFW profile goes like r^{-3} at large radii, therefore the mass within it diverges. In order to have a finite halo mass M, the profile has to be truncated at the virial radius $R_{\rm vir}$.

Halos form from regions in the initial density field which were sufficiently dense to collapse. We need first to estimate the number density $n(M)$ of objects of mass M. Here we briefly recap the relevant quantities already introduced in Chapter 1. The peak height ν is defined as

$$\nu = \frac{\delta_{sc}^2}{\sigma^2(M,z)}, \tag{5.13}$$

where $\delta_{\rm sc} \sim 1.686$ is the critical density for having the spherical collapse today and $\sigma^2(M,z)$ is the variance of the linear density field

$$\sigma^2(M,z) = \int_0^\infty \frac{dk}{2\pi^2} k^2 W^2(kR)\, P^L(k,z)\,, \tag{5.14}$$

when smoothed with a top-hat filter at scale R. Here, $W(x) = (3/x^3)[\sin(x) - x\cos(x)]$ is the Fourier Transform of the filter and $P^L(k,z)$ is the linear power spectrum at redshift z. The relation between the smoothing scale and the mass is dictated by the choice of the filter function; for a top-hat filter it is given by

$$M = \frac{4}{3}\pi\bar{\rho}R^3\,, \tag{5.15}$$

which shows that in this case M is actually the mass of the region in the Lagrangian space with radius R that collapses in a halo with same mass and radius $R_{\rm vir}$ in the evolved field.

Since there is a deterministic relation between M, R, $\sigma(M,z)$ and ν, the number density $n(M,z)$ can be expressed in terms of the peak height ν as

$$n(M,z)\, dM = \frac{\bar{\rho}}{M} f(\nu)\, d\nu\,, \tag{5.16}$$

where the mass function $f(\nu)$ is a universal function of ν, i.e. independent of redshift and the shape of the initial power spectrum. For what follows we will use the Sheth-Tormen (ST) mass function $f(\nu)$ [107], which provides a good fit to the number density of halos in simulations and it reads

$$\nu f(\nu) = A(p)\left[1 + (q\nu)^{-p}\right]\left(\frac{q\nu}{2\pi}\right)^{1/2}\exp(-q\nu/2), \tag{5.17}$$

where $p \simeq 0.3$, $A(p) = [1 + 2^{-p}\Gamma(1/2-p)/\sqrt{\pi}]^{-1} \simeq 0.322$ and $q \sim 0.707$.

On large scales, where the 2-halo term dominates, the halo-halo power spectrum $P_{hh}(k|M', M'', z)$ in (5.6) can be expressed in terms of the linear halo bias $b(M,z)$ with respect to the matter density field:

$$P_{hh}(k|M', M'', z) = b(M', z) b(M'', z) P^L(k,z)\,. \tag{5.18}$$

The linear bias has to be derived from the mass function, as in Eq.(1.73). Since we use the ST mass function, the linear bias $b(\nu)$ is

$$b(\nu) = 1 + \frac{q\nu - 1}{\delta_{\rm sc}} + \frac{2p/\delta_{\rm sc}}{1 + (q\nu)^p}\,. \tag{5.19}$$

Therefore, using (5.16) and (5.18) we can rewrite (5.5) and (5.6) as

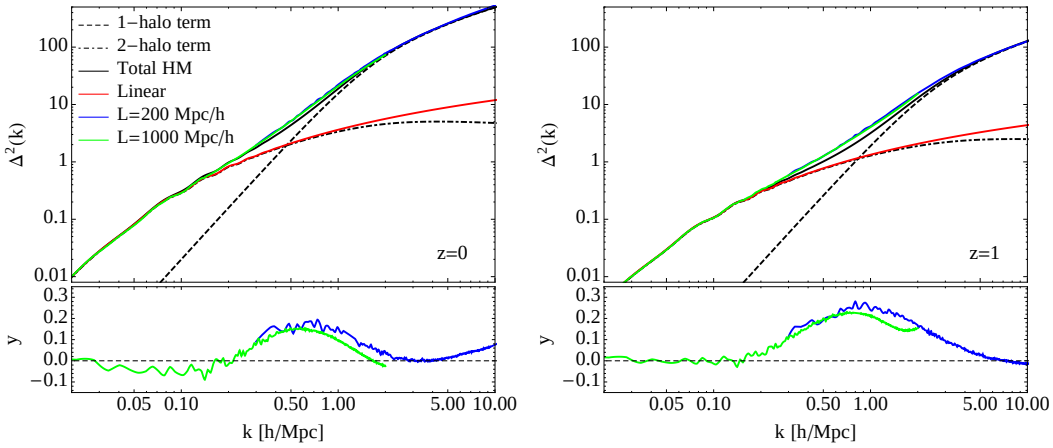

Figure 5.1: Matter power spectrum in a ΛCDM cosmology. The left and right panels display results at redshifts $z = 0$ and $z = 1$, respectively. Black lines show the matter power spectrum as computed from the halo model: the dashed line is the 1-halo term, the dot-dashed one is the 2-halo term and the solid one is the sum of the two terms. Red lines show the linear predictions whereas blue and green lines are the results from N-boby simulations with box size $L = 200$ Mpc/h and $L = 1000$ Mpc/h, respectively. The bottom panels show the relative difference between the power spectra from the halo model and from N-body simulations.

$$P_{1h}(k,z) = \int_0^\infty d\nu f(\nu)\frac{M}{\bar{\rho}}\left|u(k|\nu)\right|^2 , \tag{5.20}$$

$$P_{2h}(k,z) = \left[\int_0^\infty d\nu f(\nu)b(\nu)\,u(k|\nu)\right]^2 P^L(k,z)\,. \tag{5.21}$$

The ST mass function and the halo bias are normalized so that $\int_0^\infty d\nu f(\nu)b(\nu) = 1$, and from (5.11) is easy to show that $u(k \to 0, M) = \rho(k \to 0, M)/M = 1$. Therefore, here the 2-halo term tends to the linear power spectrum as k goes to zero, $P_{2h}(k \to 0) \to P^L(k)$, whereas they differ at high k where the halo profile contributes and it is k-dependent.

Now we have all the ingredients to compute the non-linear power spectrum of matter at any redshift. We consider a massless neutrinos, flat ΛCDM cosmology, with the same cosmological parameters as the N-body simulations L0 and S0 (see table 4.1). We use the CAMB code [68] to calculate the linear matter power spectrum $P^L(k)$. Next, we compute the power spectrum using the halo model (HM) and we compare it with the results of the N-body simulations (S) through

$$y(k) = \frac{\Delta^2_S(k) - \Delta^2_{HM}(k)}{\Delta^2_S(k)}\,, \tag{5.22}$$

where $\Delta(k) = k^3P(k)/(2\pi^2)$ is the dimensionless matter power spectrum. The results are presented in figure 5.1. The top panels show the halo model power spectrum for the pure ΛCDM cosmology, at redshift $z = 0$ (left) and $z = 1$ (right). The bottom panels show explicitly the comparison between the halo model and N-body simulations through the quantity y. At large scales, $k < 0.2\,h$/Mpc, the halo model reproduces well the prediction of simulations, whereas at intermediate scale, $k \sim 0.2 - 2\,h$/Mpc, there is a disagreement below the 20% level at $z = 0$, and around the $20 - 30\%$ level at

$z = 1$. This region is characterized by the transition between the 1-halo and 2-halo terms' dominance and here the halo model seems not to be very accurate. On smaller scales, up to $k \sim 10\,h/\mathrm{Mpc}$, the agreement is again better than 10%.

Chapter 6

Halo model with massive neutrinos

In this chapter we discuss how to extend the standard halo model to account for the effects of massive neutrinos. Here the quantities without subscript are related to the total matter field, whereas "c" denotes the cold field, which is the mass weighted average between the cold dark matter and the baryon fields and "ν" indicates the neutrino component only.

We consider three different massive neutrino cosmologies, characterized by the same amount of total matter but different neutrino masses (we have considered 3 degenerate families), which correspond to the three massive neutrino cosmologies presented in table 4.1.

In order to describe the neutrino density field it is important to account for the fact that massive neutrinos have large, although non-relativistic, thermal velocities at low redshift. These large thermal velocities, which set a free-streaming scale, prevent the clustering of neutrinos within dark matter halos. However, neutrinos from the low-velocity tail of the momentum distribution can cluster within the potential wells of CDM halos [17, 71, 100, 111, 123, 125]. Thus, it is useful to describe the neutrino density field as the sum of two terms

$$\delta_\nu = F_h \delta_\nu^h + (1 - F_h)\delta_\nu^L, \tag{6.1}$$

a linear one, δ_ν^L, and a non-linear one, δ_ν^h, which is a fraction F_h of the total neutrino density field. Whereas the former will simply obey linear theory, the latter account for the fully non-linear clustering of massive neutrinos within c-halos (CDM halos), forming neutrino halos (ν-halos). This approach takes into account also non-linearities unlike the approach of [5] (see their equation 64), in which only the linear neutrino clustering is considered. The two descriptions agree up to $k \sim 0.2\,h/\mathrm{Mpc}$ and there is a 50% extra clustering at $k \sim 0.5$ in our case due to the nonlinear behavior. We also assume that the mass of the ν-halos is only a function of the mass of the host c-halos, $M_\nu = M_\nu(M_c)$, and that the centers of the ν- and c-halos are the same. The density contrast of the total matter density field can then be written as

$$\delta = \frac{\bar{\rho}_\mathrm{c}}{\bar{\rho}}\delta_\mathrm{c} + \frac{\bar{\rho}_\nu}{\bar{\rho}}\left[F_h \delta_\nu^h + (1 - F_h)\delta_\nu^L\right], \tag{6.2}$$

where $\rho = \bar{\rho}_{\rm c} + \bar{\rho}_\nu$ is the mean background matter density. The matter power spectrum is given by

$$P(k) = \left(\frac{\bar{\rho}_{\rm c}}{\bar{\rho}}\right)^2 P_{\rm c}(k) + 2\,\frac{\bar{\rho}_{\rm c}\bar{\rho}_\nu}{\bar{\rho}^2}\,P_{{\rm c}\nu}(k) + \left(\frac{\bar{\rho}_\nu}{\bar{\rho}}\right)^2 P_\nu(k)\,, \tag{6.3}$$

where $P_{\rm c}(k)$, $P_\nu(k)$ and $P_{{\rm c}\nu}(k)$ are the cold, neutrino and cross power spectra, respectively.

Before presenting in detail the calculation of all these terms, we discuss the recipe to compute the mass function and the linear halo bias in a massive neutrino cosmology, which is not obvious a priori. From now on, we will not write explicitly the redshift's dependence since it can be understood from the description of the massless neutrinos ΛCDM case presented in Chapter 5.

6.1 Matter vs. cold dark matter prescription

Since the ν-halos are located around c-halos and, as we will clarify later, their mass can be assumed to be a function of the corresponding c-halos mass, there are two important consequences: their mass function is equal to the one of the cold field, $dM_\nu n(M_\nu) = dM_{\rm c} n(M_{\rm c})$, and the linear ν-halo bias is equal to the c-halo one $b(M_\nu) = b(M_{\rm c})$. In order to make the halo model machine working, we must express $n(M_{\rm c})$ and $b(M_{\rm c})$ in terms of the number of regions in the Lagrangian field that are dense enough to collapse, i.e. we have to recast it in terms of the peak height. There are two different ways in which we can do that.

It would be natural, following the procedure adopted for the ΛCDM case, to rewrite the number density of c-halos in terms of total matter quantities,

$$n(M_{\rm c})\,dM_{\rm c} = \frac{\bar{\rho}}{M} f(\nu) d\nu\,, \tag{6.4}$$

and the peak height as $\nu = \delta_{sc}^2/\sigma^2(M)$, with

$$M = M_\nu + M_c = \frac{4}{3}\pi\bar{\rho}R^3\,, \tag{6.5}$$

$$\sigma^2(M) = \int_0^\infty \frac{dk}{2\pi^2} k^2 W^2(kR)\,P^L(k), \tag{6.6}$$

and $P^L(k)$ being the linear total matter power spectrum. It would be natural to write the halo-halo power spectrum in terms of the halo bias $b(M_{\rm c})$ with respect to the total matter density field. This approach is the so called matter prescription [23, 32, 124].

Even if used in the literature (e.g. in [1]), this prescription has been shown to be not fully correct by Castorina et al. [23] (see also [55]), since the resulting mass function $f(\nu)$ is not universal and the resulting linear halo bias $b(M_{\rm c})$ is scale dependent even on large scales. The authors argued that this is due to the wrong choice of the density field used for computing the peak height and the halo bias, i.e. the total matter is not the fundamental density field involved in the clustering process. They showed that the more physical field is the cold one and this choice goes under the name of cold dark matter prescription. In this setup, the number density of c-halos is

$$n(M_{\rm c})dM_{\rm c} = \frac{\bar{\rho}_{\rm c}}{M_{\rm c}} f(\nu_{\rm c}) d\nu_{\rm c}, \tag{6.7}$$

where $\nu_{\rm c} = \delta_{sc}^2/\sigma_{\rm c}^2$ with

$$M_{\rm c} = \frac{4}{3}\pi\bar{\rho}_{\rm c}R^3\,, \tag{6.8}$$

$$\sigma_{\rm c}^2 \equiv \sigma^2(M_{\rm c}) = \int_0^\infty \frac{dk}{2\pi^2}k^2W^2(kR)\,P_{\rm c}^L(k)\,, \tag{6.9}$$

and $P_{\rm c}^L(k)$ is the linear cold power spectrum. Moreover, this prescription allows to express the halo-halo power spectrum in terms of the linear cold $P_{\rm c}^L(k)$

$$P_{hh}(k|M_{\rm c}', M_{\rm c}'') = b(M_{\rm c}')b(M_{\rm c}'')P_{\rm c}^L(k)\,. \tag{6.10}$$

Castorina et al. [23] showed that the resulting mass function is universal and the linear halo bias $b(M_{\rm c})$ is scale independent on large scales, as wanted. Therefore, we will use the cold dark matter prescription to build the halo model for a massive neutrino cosmology. The fact that this is the correct prescription tells us that neutrinos modify only the background in which the c-field clusters, without performing any back-reaction through its density perturbations.

Since the fraction F_h of neutrinos clustered in c-halos is very small, we expect that the total matter power spectrum will be well reproduced considering all the neutrinos, both linear and clustered, as driven by linear theory. Anyway, the neutrino and cross power spectra from N-body simulations are not well reproduced by the correspondent linear one, on small scales. Therefore, we will describe how to model not only the clustering of the cold field but also the clustering of neutrinos within the halo model formalism.

6.2 The power spectrum

6.2.1 Cold dark matter Power Spectrum

In analogy with what we have presented in Chapter 5 and using the Eqs.(6.7) and (6.10) of the cold dark matter prescription, we compute here the power spectrum of the cold field $P_{\rm c}(k) = P_{\rm c}^{1h}(k) + P_{\rm c}^{2h}(k)$, with

$$P_{\rm c}^{1h}(k) = \int_0^\infty d\nu_{\rm c}\, f(\nu_{\rm c})\frac{M_{\rm c}}{\bar{\rho}_{\rm c}}|u_{\rm c}(k|M_{\rm c})|^2\,, \tag{6.11}$$

$$P_{\rm c}^{2h}(k) = \left[\int_0^\infty d\nu_{\rm c}\, f(\nu_{\rm c})b_{\rm c}(\nu_{\rm c})\,u_{\rm c}(k|M_{\rm c})\right]^2 P_{\rm c}^L(k)\,, \tag{6.12}$$

where $u_{\rm c}(k|M_{\rm c})$ is the NFW profile of a c-halo of mass $M_{\rm c}$. Even if we are considering a massive neutrino cosmology, its concentration is well described by the standard formula (5.12) for the ΛCDM case, as our N-body simulations showed. The quantities $f(\nu_{\rm c})$ and $b_{\rm c}(\nu_{\rm c})$ are the ST mass function and bias, which can also be used in a massive neutrino cosmology [55, 124] and guarantee that the 2-halo term is well normalized: $P_{\rm c}^{2h}(k \to 0) \to P_{\rm c}^L$. Figure 6.1 shows the cold dark matter power spectrum, as predicted by the halo model, for three different cosmologies with massive neutrinos, $\sum m_\nu = 0.15$ eV on top, $\sum m_\nu = 0.3$ eV in the middle and $\sum m_\nu = 0.6$ eV on bottom, and for two different redshifts, $z = 0$ on the left and $z = 1$ on the right. The relative difference between our results and N-body simulations is shown in the bottom part of each plot,

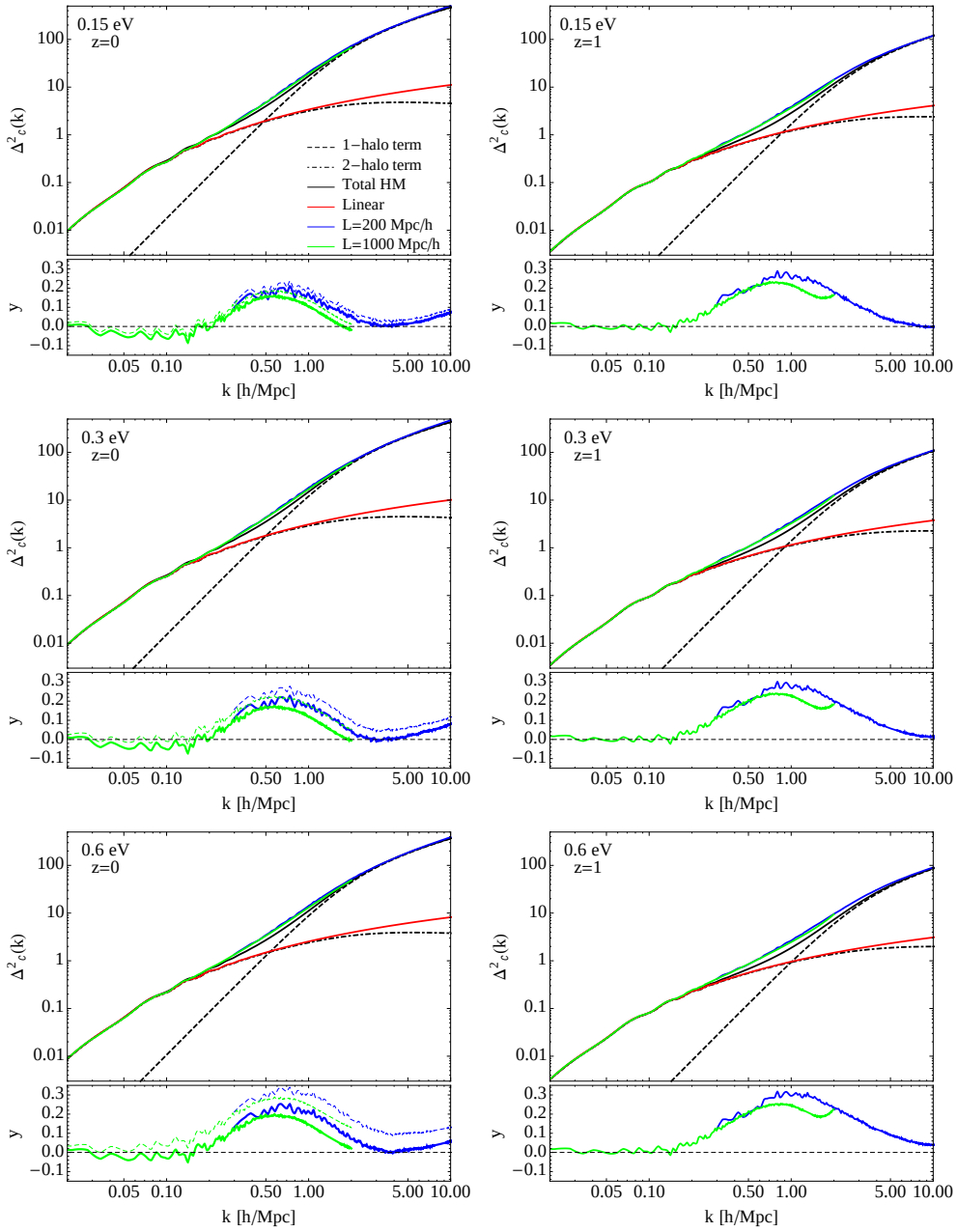

Figure 6.1: Cold dark matter power spectrum for $\sum m_\nu = 0.15$ eV (top), $\sum m_\nu = 0.3$ eV (middle) and $\sum m_\nu = 0.6$ eV (bottom) massive neutrino cosmologies. The left and right panels show the results at $z = 0$ and $z = 1$, respectively. Black curves display the predictions by the halo model: the dashed line is the 1-halo term, the dot-dashed one is the 2-halo term and the solid one is the sum of the two terms. Red curves show the linear predictions and blue and green curves are the results from N-boby simulations with box size $L = 200$ Mpc/h and $L = 1000$ Mpc/h, respectively. The bottom part of each plot shows the residuals between results from halo model and N-body simulations.

where the solid curves are obtained using the cold dark matter prescription and the thin dashed ones (shown only for $z = 0$) come from the matter prescription. The results are in agreement and reinforce the claim of Castorina et al., since the cold dark matter prescription agrees better with simulations. Using this right procedure we obtain a very good agreement on large scales, whereas a disagreement around $15 - 20\%$ level characterizes the intermediate scales $k \sim 0.2 - 2\,h/\mathrm{Mpc}$ at $z = 0$, and it increases until 30% at $z = 1$. On smaller scales, up to $k \sim 10\,h/\mathrm{Mpc}$, the disagreement is below 10% for all models.

6.2.2 Cross Power Spectrum

Here we compute the second term of Eq.(6.3), i.e. the cross power spectrum $P_{c\nu}(k)$. Following the description adopted in Eq.(6.1), the cross power is given by

$$P_{c\nu}(k) = F_h P^h_{c\nu}(k) + (1 - F_h) P^L_{c\nu}(k), \tag{6.13}$$

where $P^L_{c\nu}(k) = \sqrt{P_c(k) P^L_\nu(k)}$ describes the correlation between the cold field and the linear component of the neutrino density field, once we assume that the two fields are completely correlated. This assumption is well motivated on large scales and is a good approximation at intermediate ones, where this term is supposed to be relevant [5, 123, 124]. The cross power spectrum between the cold and the clustered neutrino fields can be written in the language of halo model as $P^h_{c\nu}(k) = P^{1h}_{c\nu}(k) + P^{2h}_{c\nu}(k)$, with

$$P^{1h}_{c\nu}(k) = \int_{M_{\rm cut}}^{\infty} dM_c\, n(M_c) \frac{M_c}{\bar\rho_c} \frac{M_\nu}{F_h \bar\rho_\nu}\, u_c(k|M_c)\, u_\nu(k|M_c) \tag{6.14}$$

$$P^{2h}_{c\nu}(k) = \int_0^{\infty} dM'_c\, n(M'_c)\, \frac{M'_c}{\bar\rho_c}\, u_c(k|M'_c) \times \int_{M_{\rm cut}}^{\infty} dM''_c\, n(M''_c)\, \frac{M_\nu}{F_h \bar\rho_\nu}\, u_\nu(k|M''_c)\, P_{hh}(k|M'_c, M''_c), \tag{6.15}$$

where $u_\nu(k|M_c)$ is the Fourier transform of the normalized density profiles, $\rho^h_\nu(r)/M_\nu$, of the ν-halo with mass $M_\nu = M_\nu(M_c)$. Villaescusa-Navarro et al. [123] measured the density contrast profile of neutrinos around c-halos in simulations, for $\sum m_\nu = 0.3, 0.6$ eV cosmologies. They found that it can be well reproduced by the fitting formula

$$\delta^{\rm sim}_\nu(r) \equiv \frac{\rho_\nu(r) - \bar\rho_\nu}{\bar\rho_\nu} = \frac{\rho_c(M_c)}{1 + [r/r_c(M_c)]^{\alpha(M_c)}}, \tag{6.16}$$

where ρ_c, r_c and α are functions of the corresponding c-halo mass M_c and they present different shapes depending on the chosen massive neutrino cosmology (see their figure 10). This profile was obtained considering all the neutrinos, both the linearly clustered ones (that we call linear), and the fully non-linearly clustered ones (that we call clustered). Because of our setup, we define the clustered neutrino profile as

$$\rho^h_\nu(r) \equiv \delta^{\rm sim}_\nu(r)\, \bar\rho_\nu = \rho_\nu(r) - \bar\rho_\nu, \tag{6.17}$$

which means that we consider as clustered the neutrinos measured around a halo, once the neutrino background, $\bar\rho_\nu$, has been subtracted. This is not the accurate procedure,

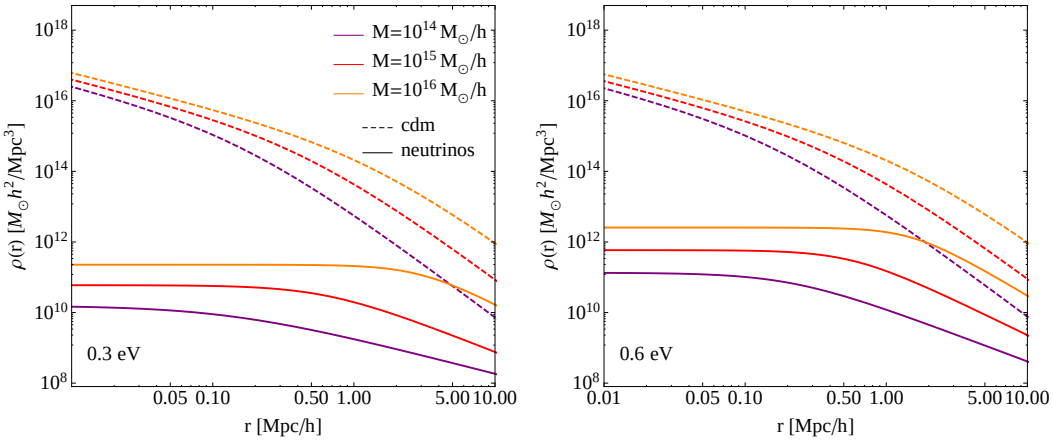

Figure 6.2: Density profile. The left and right panels show the $\sum m_\nu = 0.3$, 0.6 eV cases, respectively. Dashed lines depict the NFW profiles of cold dark matter halos with different masses; the solid lines are the correspondent neutrino profiles.

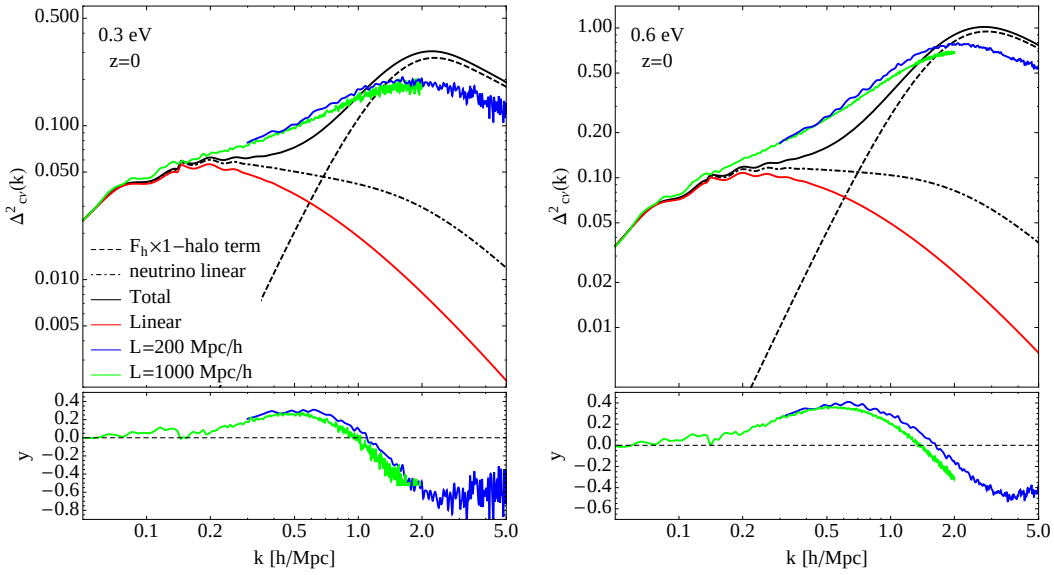

Figure 6.3: Cold dark matter-neutrino cross power spectrum in $\sum m_\nu = 0.3$ eV (left panel) and $\sum m_\nu = 0.6$ eV (right panel) massive neutrino cosmologies at redshifts $z = 0$. Black curves show the cross-power spectrum predicted by the halo model, red lines indicate the linear predictions and blue and green lines are the results from N-boby simulations with box size $L = 200$ Mpc/h and $L = 1000$ Mpc/h, respectively. The bottom part of each plots shows the relative difference between the cross-power spectra from the halo model and from simulations.

but a quite good estimation and the resulting profiles are shown in figure 6.2 together with the NFW profile of the cold dark matter halos. From these plots we can notice that the neutrino profiles have lower amplitude than corresponding cold dark matter ones. In analogy with Eq.(5.7), we define the Fourier transfer of the profile as

$$\rho_\nu^h(k|M_{\rm c}) = \int_0^{R_{\rm vir}} dr\, 4\pi r^2\, \frac{\sin(kr)}{kr}\, \rho_\nu^h(r)\,, \tag{6.18}$$

where we assume that the virial radius of the c- and ν-halos are equal. The corresponding mass is $M_\nu(M_{\rm c}) = \rho_\nu^h(k \to 0|M_{\rm c})$, which is a monotonic growing function in M_c. The cut-off mass $M_{\rm cut}$ in Eqs.(6.14) and (6.15) is a particular c-halo mass, for which the corresponding M_ν satisfies

$$M_\nu(M_{\rm cut}) = 0.1 \times \frac{4\pi\bar{\rho}_\nu}{3} R_{\rm vir}^3(M_{\rm cut}). \tag{6.19}$$

This means that we do not consider as clustered neutrinos the ones forming an halo with mass smaller than the 10% of the mass of background neutrinos enclosed in the same volume. Therefore, the fraction of clustered neutrinos is given by:

$$F_h = \frac{1}{\bar{\rho}_\nu} \int_{M_{\rm cut}}^{\infty} dM_{\rm c}\, n(M_{\rm c}) M_\nu(M_{\rm c})\,. \tag{6.20}$$

It would be natural to define $M_{\rm cut}$ as the c-halo mass for which the corresponding M_ν is vanishing. This does not happen for the neutrinos profile defined in Eq.(6.17) and the definition in Eq.(6.19) gives a convergent value for F_h, i.e. the mass in neutrinos contained in smaller halos is negligible. This fraction turns out to be very small: $F_h = 9.5 \times 10^{-4}$, 2.6×10^{-3} for $\sum m_\nu = 0.3, 0.6$ eV, respectively. However, even if small, this neutrino component is very important for having a good prediction for the cross and neutrinos power spectra at small scales, as we shall see below.

We use the Eqs.(6.7) and (6.10) of the cold dark matter prescription to rewrite $P_{{\rm c}\nu}^{1h}(k)$ and $P_{{\rm c}\nu}^{2h}(k)$ in terms of the peak height

$$P_{{\rm c}\nu}^{1h}(k) = \int_{M_{\rm cut}}^{\infty} d\nu_{\rm c}\, f(\nu_{\rm c}) \frac{M_\nu}{F_h \bar{\rho}_\nu}\, u_{\rm c}(k|M_{\rm c})\, u_\nu(k|M_{\rm c}) \tag{6.21}$$

$$P_{{\rm c}\nu}^{2h}(k) = \int_0^{\infty} d\nu'_{\rm c}\, f(\nu'_{\rm c})\, b(\nu'_{\rm c})\, u_c(k|M'_{\rm c}) \times \int_{M_{\rm cut}}^{\infty} d\nu''_{\rm c}\, f(\nu''_{\rm c} c)\, b(\nu''_{\rm c})\, \frac{M_\nu}{M''_{\rm c}} \frac{\bar{\rho}_{\rm c}}{F_h \bar{\rho}_\nu}\, u_\nu(k|M''_{\rm c})\, P_{\rm c}^L(k)\,, \tag{6.22}$$

where the mass function and bias are the usual Sheth-Tormen ones. Substituting the last expressions in Eq.(6.13) we compute the cross power spectrum for the two different massive neutrino cosmologies. The results at redshift $z = 0$ are shown in figure 6.3. Neither the linear cross power spectrum (red lines) nor the cross power spectrum between the clustered cold field and the unclustered component of neutrinos (dot-dashed black lines) can reproduce simulations at intermediate ($k \sim 0.2\, h$/Mpc) and up to small scales, for the two neutrino masses. Instead, our extension of the halo model (solid black line), which accounts for the clustered component of neutrinos, can describe the main behavior of N-body simulations at scales smaller than $k \sim 5\, h$/Mpc. We can notice that the main contribution to the power spectrum comes from the

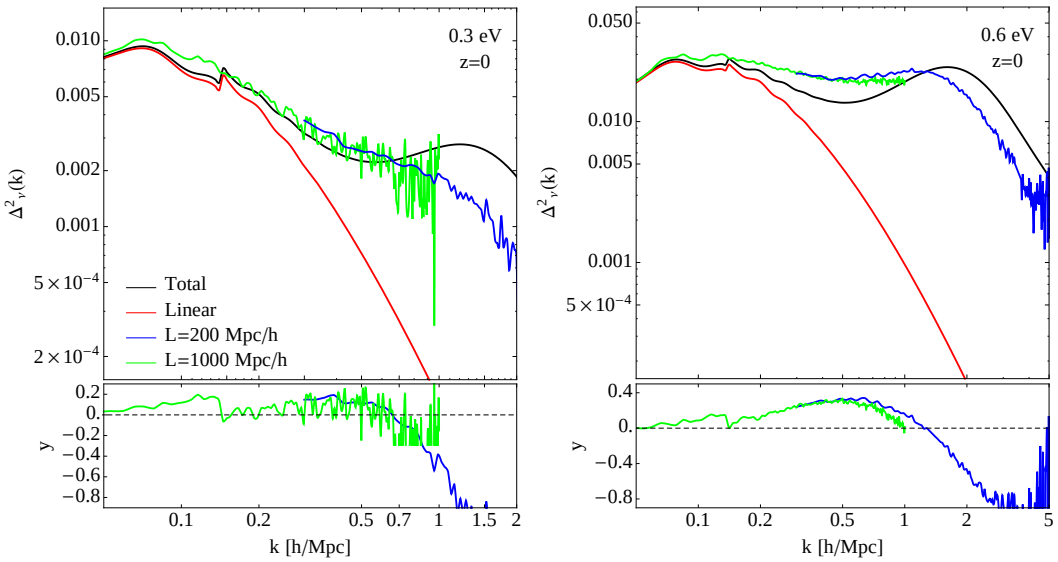

Figure 6.4: Neutrino power spectrum in $\sum m_\nu = 0.3$ eV (left panel) and $\sum m_\nu = 0.6$ eV (right panel) massive neutrino cosmologies at redshift $z = 0$. Black curves show the neutrino power spectrum predicted by the halo model, red curves indicate the linear predictions and blue and green curves are the results from N-boby simulations with box size $L = 200$ Mpc/h and $L = 1000$ Mpc/h, respectively. The bottom part of each plots shows the relative difference between the power spectra from the halo model and from simulations.

unclustered component of the neutrino field via $P^L_{c\nu}(k)$ (dot-dashed line) at large scales and from the 1-halo term $P^{1h}_{c\nu}(k)$ of the clustered neutrino component at small scales. The 2-halo term $P^{2h}_{c\nu}(k)$ is not shown because it is small and not relevant at any scales. To conclude, our model predicts the cross power spectrum from simulation with 30% accuracy until $k \sim 1\,h$/Mpc in the $\sum m_\nu = 0.3$ eV case (left panel). In the $\sum m_\nu = 0.6$ eV case (right panel), the accuracy is at the 40% level on scales $k < 5\,h$/Mpc.

6.2.3 Neutrino Power Spectrum

Using the definition of the neutrino density field in Eq.(6.1), we write the neutrino power spectrum as

$$P_\nu(k) = F_h^2 P^h_\nu(k) + 2F_h(1-F_h)P^{hL}_\nu(k) + (1-F_h)^2 P^L_\nu(k)\,, \tag{6.23}$$

where the auto-power spectrum of the linear component is just the linear power $P^L_\nu(k)$ and the cross term can be expressed as $P^{hL}_\nu(k) = \sqrt{P^h_\nu(k)P^L_\nu(k)}$, once we assumed that the clustered and smoothed fields are completely correlated. As for the other fields, the power spectrum of the non-linearly clustered component can be split in two terms, $P^h_\nu(k) = P^{1h}_\nu(k) + P^{2h}_\nu(k)$, with

$$P^{1h}_\nu(k) = \int_{M_{\rm cut}}^\infty dM_{\rm c}\, n(M_{\rm c}) \left(\frac{M_\nu}{F_h\bar\rho_\nu}\right)^2 |u_\nu(k|M_{\rm c})|^2 \tag{6.24}$$

$$P^{2h}_\nu(k) = \int_{M_{\rm cut}}^\infty dM'_{\rm c}\, n(M'_{\rm c})\, \frac{M_\nu}{F_h\bar\rho_\nu}\, u_\nu(k|M'_{\rm c}) \times \int_{M_{\rm cut}}^\infty dM''_{\rm c}\, n(M''_{\rm c})\, \frac{M_\nu}{F_h\bar\rho_\nu}\, u_\nu(k|M''_{\rm c})\, P_{hh}(k|M'_{\rm c}, M''_{\rm c})\,, \tag{6.25}$$

where all the quantities have already been defined in Sec. 6.2.2. Once again we apply the cold dark matter prescription yielding

$$P^{1h}_\nu(k) = \int_{M_{\rm cut}}^{\infty} d\nu_{\rm c}\, f(\nu_{\rm c}) \left(\frac{M_\nu}{F_h \bar{\rho}_\nu}\right)^2 \frac{\bar{\rho}_{\rm c}}{M_{\rm c}} \, |u_\nu(k|M_{\rm c})|^2 \tag{6.26}$$

$$P^{2h}_\nu(k) = \left[\int_{M_{\rm cut}}^{\infty} d\nu_{\rm c}\, f(\nu_{\rm c})\, b(\nu_{\rm c}) \frac{M_\nu}{M_{\rm c}} \frac{\bar{\rho}_{\rm c}}{F_h \bar{\rho}_\nu}\, u_\nu(k|M_{\rm c})\right]^2 P^L_{\rm c}(k)\,. \tag{6.27}$$

Next, we compute the neutrino power spectrum $P_\nu(k)$ at redshift $z = 0$ for two massive neutrino cosmologies with $\sum m_\nu = 0.3$ and 0.6 eV. The encouraging results are shown in figure 6.4: the disagreement with simulations is below 20% until $k \sim 0.7$ h/Mpc for the $\sum m_\nu = 0.3$ eV case (left panel), whereas it is under 30% until $k \sim 1.5$ h/Mpc for the $\sum m_\nu = 0.6$ eV case (right panel).

6.2.4 Matter Power Spectrum

In the previous subsections 6.2.1, 6.2.2, 6.2.3 we have presented all the terms needed to compute the total matter power spectrum in a massive neutrino cosmology. However, looking at Eq. (6.3) one can notice that the cross and the neutrino power spectra are multiplied by $\bar{\rho}_{\rm c}\bar{\rho}_\nu/\bar{\rho}^2$ and $(\bar{\rho}_\nu/\bar{\rho})^2$, respectively. These two terms are much smaller than 1 for light neutrinos, as the ones considered here. Therefore, we expect that the improvements given by computing these terms with halo model will be highly suppressed once we compute the total matter power spectrum, which should be well reproduced using just the linear cross and neutrino power spectra. And this is the case: we computed the total matter power spectrum using both the fully non-linear and the linear cross and neutrino power spectra, finding that their difference is well below the 1% level for all the cosmologies studied in this paper.

Then, we present here the resulting total matter power spectra in massive neutrinos cosmologies, computed using the linear neutrino and cross power spectra and the fully non-linear cold dark matter one, at redshifts $z = 0$ and $z = 1$. Figure 6.5 shows the $\sum m_\nu = 0.15, 0.3, 0.6$ eV cosmologies in the top, middle and bottom panels, respectively. Once again, the halo model (solid black curves) reproduces well the simulations on small and on large scales; on intermediate scales a disagreement $< 20\%$ is present at $z = 0$ and $< 30\%$ at $z = 1$. We also show the comparison between simulations and the halo model computed with the matter prescription, which is represented by the thin dashed curves. We can again confirm that this is not the ideal prescription since it reproduces worse the results from the N-body/neutrino simulations.

6.3 The ratio $\Delta^2_\nu(k)/\Delta^2_{\Lambda\rm CDM}(k)$

6.3.1 Halo model and N-body simulations

It is interesting to plot the ratio $\Delta^2_\nu(k)/\Delta^2_{\Lambda\rm CDM}(k)$, where the subscripts ν and ΛCDM indicate a massive and massless neutrinos cosmology, respectively. Figure 6.6 shows this quantity for the $\sum m_\nu = 0.15$ eV (top), $\sum m_\nu = 0.3$ eV (middle) and $\sum m_\nu = 0.6$ eV (bottom) cosmological models at redshifts $z = 0$ (left panels) and $z = 1$ (right panels); we emphasize that here the unit scale varies for different cosmologies. The

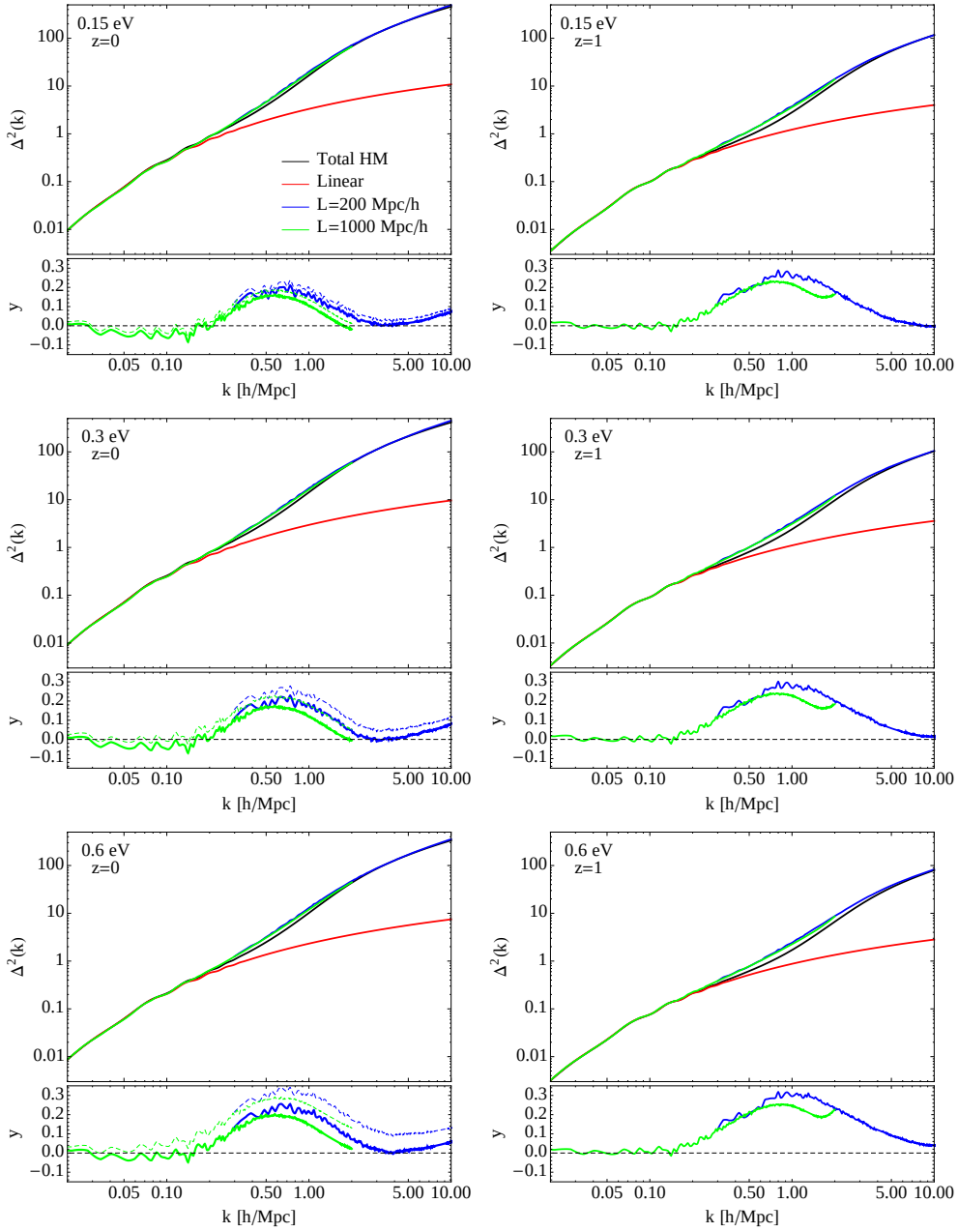

Figure 6.5: Matter power spectrum in $\sum m_\nu = 0.15$ eV (top), $\sum m_\nu = 0.3$ eV (middle) and $\sum m_\nu = 0.6$ eV (bottom) massive neutrino cosmologies. The left and right panels show the results at redshifts $z = 0$ and $z = 1$, respectively. Black curves display the matter power spectrum as predicted by the halo model, red curves show the linear predictions and blue and green curves are the results from N-boby simulations with box size $L = 200$ Mpc/h and $L = 1000$ Mpc/h, respectively. The bottom part of each plots shows the relative difference between the power spectrum from the halo model and from simulations.

ratio obtained from N-body simulations presents a well known spoon-shape around $k \sim 1\,h/\mathrm{Mpc}$ [4, 10, 16, 121, 127], which is not captured by linear theory. Interestingly, halo model reproduces this feature and can help us to understand its physical meaning.

First of all, we must remember that in the range $0.1 < k\,(h/\ \mathrm{Mpc}) < 1$ there is the transition between the 1- and the 2-halo terms where they are comparable, whereas on smaller scales, $k > 1\,h/\mathrm{Mpc}$, the 1-halo term dominates. Then, in order to study in more detail the spoon-shape trend, we can focus on the 1-halo term only. Moreover, on these scales the contribution of the neutrino and the cross power spectra to the total matter one is negligible. Therefore, in this analysis we consider just the cold dark matter power contributing to the 1-halo term of the total matter power spectrum in Eq.(6.3). The 1-halo term accounts for the correlations between particles that belong to the same halo, therefore, only halos with size larger than the scale associated with the given k can contribute. This means that on intermediate scales only relatively large halos give power to the 1-halo term, whereas for $k > 1\,h/\mathrm{Mpc}$ both small and large halos can in principle contribute. However, the number of small halos is much larger than the number of big ones; thus, on small scales the power comes primarily from small halos.

The left panel of figure 6.7 shows the 1-halo term (see Eq.6.11) once the integral is computed for different mass-intervals,

$$P_i^{1h}(k) = \int_{\nu_{\rm c}(M_{\rm c}^i)}^{\nu_{\rm c}(M_{\rm c}^i+\Delta M_{\rm c})} d\nu_{\rm c}\, f(\nu_{\rm c}) \frac{M_{\rm c}}{\bar{\rho}_{\rm c}} |u_{\rm c}(k|M_{\rm c})|^2\,, \tag{6.28}$$

for the $\sum m_\nu = 0.0, 0.3, 0.6$ eV cosmologies that we are considering in this paper, at redshift $z = 0$. As we expect, small halo-masses give power at large k. What is more interesting is that the ratios $[P_i^{1h}(k)]_\nu/[P_i^{1h}(k)]_{\Lambda\rm CDM}$ between 1-halo terms of massive and massless neutrino cosmologies computed in the same mass-bin i are almost independent of k. Then, they can be well approximated by the ratios between the limits of $P_i^{1h}(k)$ on large scales,

$$P_i^{1h}(k \to 0) = \int_{\nu_{\rm c}(M_{\rm c}^i)}^{\nu_{\rm c}(M_{\rm c}^i+\Delta M_{\rm c})} d\nu_{\rm c}\, f(\nu_{\rm c}) \frac{M_{\rm c}}{\bar{\rho}_{\rm c}}\,, \tag{6.29}$$

which are independent of the halo profile. This tells us that the main features of the spoon-shape are given by the mass function through the quantity $n(M_{\rm c})M_{\rm c}^2$. In the four cosmologies considered in this work, this quantity is known to be quite similar for small halo-masses (around $10^{12}\mathrm{M}_\odot$) and very different for big ones ($> 10^{14}\mathrm{M}_\odot$).

We can now understand what creates the spoon-shape in $\Delta^2_\nu(k)/\Delta^2_{\Lambda\rm CDM}(k)$: the drop at intermediate scales, $0.1 < k < 1\,h/\mathrm{Mpc}$, is due to the fact that the fraction of big halos is very different in the two cosmologies, whereas the rising comes from the fact that the fraction of small halos is very similar in the two cosmologies. In support of this, the right panel of figure 6.7 shows that the spoon-shape is present also when the ratio is taken between two identical ΛCDM cosmologies, but with different $\sigma_8 \equiv \sigma(R = 8\ \mathrm{Mpc}/h)$. Indeed, this suggests that the spoon-shape is due to different relations between the peak height and the halo mass, which is what is needed to build the mass function.

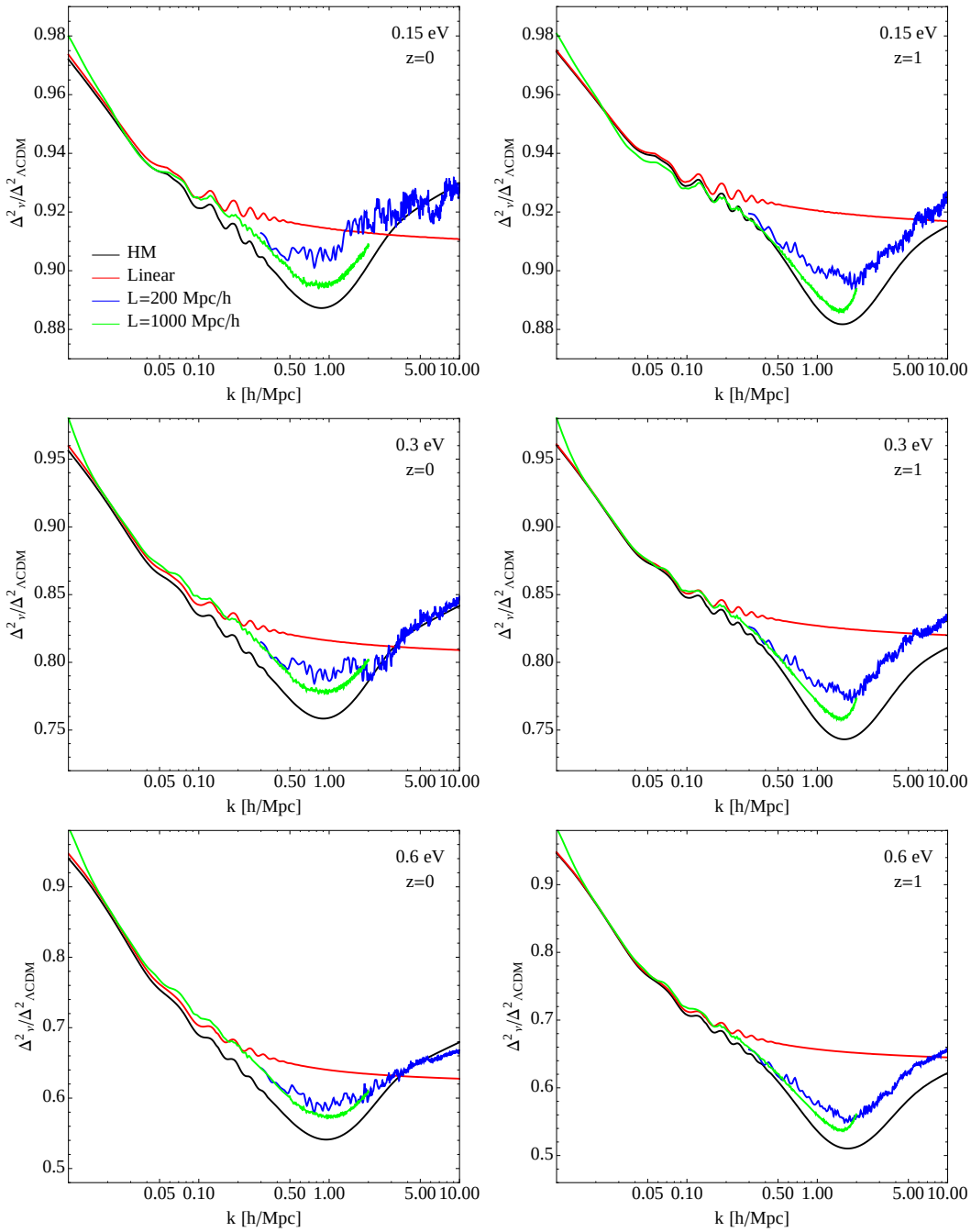

Figure 6.6: Ratio $\Delta^2_\nu(k)/\Delta^2_{\Lambda\mathrm{CDM}}(k)$ for $\sum m_\nu = 0.15$ eV (top), $\sum m_\nu = 0.3$ eV (middle) and $\sum m_\nu = 0.6$ eV (bottom). The left and right panels show results at redshifts $z = 0$ and $z = 1$, respectively. Black lines show the ratio computed from halo model, red lines show the linear predictions, blue and green lines are the results from N-boby simulations with box size $L = 200$ Mpc/h and $L = 1000$ Mpc/h, respectively.

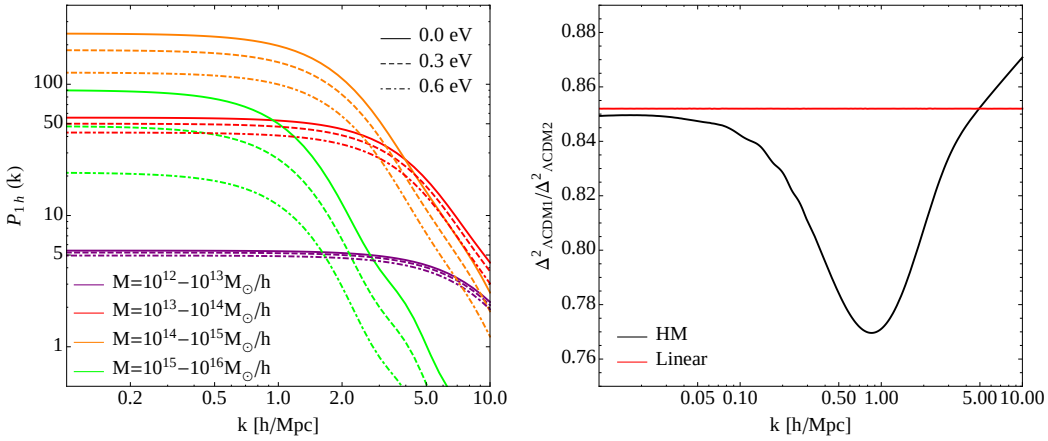

Figure 6.7: Left panel: 1-halo term computed by integrating in different bins of mass. The different colors indicate different mass-bin, the solid, dashed and dot-dashed lines show the results for the $\sum m_\nu = 0.0, 0.3, 0.6$ eV cosmologies, respectively. Right panel: Ratio $\Delta^2_{\Lambda\mathrm{CDM1}}(k)/\Delta^2_{\Lambda\mathrm{CDM2}}(k)$ for two ΛCDM massless neutrinos cosmologies that differ only for the value of σ_8. The red line shows the linear prediction, the black one shows the results predicted by halo model, as described in section 6.2.4.

Now that we understand the reason for this particular shape in the ratio of the matter power spectra, we want to stress the following point. Figure 6.5 points out that halo model can reproduce the non-linear power spectrum from N-body simulations with 20% accuracy at $z = 0$ and 30% accuracy at $z = 1$. However, it works much better in predicting the ratio $\Delta^2_\nu(k)/\Delta^2_{\Lambda\mathrm{CDM}}(k)$, as figure 6.6 demonstrates. In this case the disagreement between halo model and simulations is below 2%, 5%, 10% for $\sum m_\nu = 0.15, 0.3, 0.6$ eV massive neutrinos cosmologies, respectively, at both redshifts and for the whole set of scales considered here ($k < 10\,h/\mathrm{Mpc}$).

6.3.2 Halo model and HALOFIT

Here we compare the predictions from our extension of the halo model against HALOFIT [112], the fitting formula described in Chapter 4. The discrepancy between the new version of HALOFIT [118] and N-body simulations is claimed to be below 10% for $k < 10\,h/\mathrm{Mpc}$. This made HALOFIT a useful and popular tool to compute the non-linear power spectrum, without running any simulation. Therefore we think that it is important to show a comparison also between our model for massive neutrino cosmologies and the extension of HALOFIT presented by Bird et al. [10].

We compute the quantity $\Delta^2_\nu(k)/\Delta^2_{\Lambda\mathrm{CDM}}(k)$ with HALOFIT, for all the cosmologies considered in this paper. The comparison with halo model is shown in Figure 6.8, where we plot the ratio between $\Delta^2_\nu(k)/\Delta^2_{\Lambda\mathrm{CDM}}(k)$ computed with halo model (see section 6.3.1) and HALOFIT. The disagreement is below 2% for $\sum m_\nu = 0.15$ eV, 4% for $\sum m_\nu = 0.3$ eV and 10% for $\sum m_\nu = 0.6$ eV.

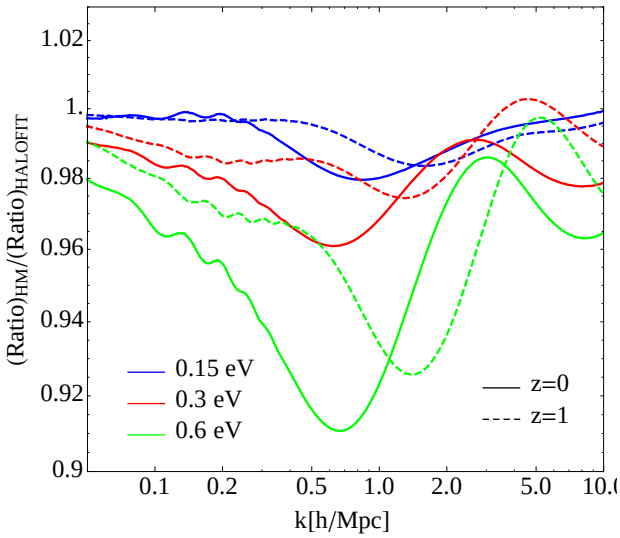

Figure 6.8: Ratio between $\Delta^2_\nu(k)/\Delta^2_{\Lambda\mathrm{CDM}}(k)$ computed with halo model and HALOFIT. Different colors indicate different massive neutrino cosmologies: $\sum m_\nu = 0.15$ eV in blue, $\sum m_\nu = 0.3$ eV in red, $\sum m_\nu = 0.6$ eV in green. Solid and dashed lines show results at $z = 0$ and at $z = 1$, respectively.

Chapter 7

Galaxy clustering

As an application of our halo model extension we study the clustering of galaxies in massless and massive neutrinos cosmologies. In Villaescusa et al. [124] authors populated with galaxies the dark matter halos of N-body simulations using a simple Halo Occupation Distribution (HOD) model. For a given cosmological model, the authors calibrated the values of the HOD parameters to reproduce the clustering properties of the galaxies in the main sample of the Sloan Digital Sky Survey (SDSS) II Data Release 7 [129]. Our purpose here is to use those HOD parameters and see whether our extension of the halo model is able to reproduce the clustering properties of the SDSS galaxies.

In this section we present the HOD model used in [124], we describe the formalism needed to compute the galaxy clustering using the halo model ingredients and we show the results for models with massless and massive neutrinos.

An HOD model requires two ingredients: 1) the probability distribution $p(N|M)$ of having N galaxies inside a c-halo of mass M (in this section we drop the subscript "c" for indicating the cold dark matter field, since all the quantities related to halos corresponds to CDM ones) and 2) the way galaxy positions and velocities are related with those of the underlying matter within halos. The HOD model adopted in [124], which has three free parameters, $M_{\rm min}$, α and M_1, works as follows. The first HOD ingredient is modeled assuming that halos with masses below $M_{\rm min}$ do not host any galaxy, whereas halos with masses above $M_{\rm min}$ host one central galaxy (c) and a number of satellites (s) following a Poissonian distribution with a mean equal to $(M/M_1)^\alpha$. Mathematically this can be written as

$$\langle N_c|M\rangle = \begin{cases} 1 & \text{if } M \geq M_{\rm min} \\ 0 & \text{if } M < M_{\rm min} \end{cases} \qquad \langle N_s|M\rangle = \begin{cases} (M/M_1)^\alpha & \text{if } M \geq M_{\rm min} \\ 0 & \text{if } M < M_{\rm min}\,. \end{cases} \tag{7.1}$$

The second ingredient of the HOD states that the central galaxy resides in the center of the halo whereas satellites follow the distribution of the underlying cold dark matter within the halo. The value of the HOD parameters, for the cosmological models with $\sum m_\nu = 0.0$, 0.3 and 0.6 eV, obtained by [124] for galaxies with magnitudes $M_r - 5\log_{10} h = -21.0$, are shown in table 7.1.

Given the above HOD model, and the values of the HOD parameters in table 7.1, we can compute the clustering of galaxies with magnitudes $M_r - 5\log_{10} h = -21.0$ using the halo model. We begin depicting the required formalism. The 1-halo term of

$\sum m_\nu$ (eV)	M_1 $(M_\odot/h)$	α	$M_{\rm min}$ $(M_\odot/h)$
0.0	1.15×10^{14}	1.27	5.33×10^{12}
0.3	1.02×10^{14}	1.32	4.91×10^{12}
0.6	8.90×10^{13}	1.36	4.47×10^{12}

Table 7.1: Values of the HOD parameters, for two different cosmologies and for galaxies with magnitudes $M_r - 5\log_{10} h = -21.0$ (from [124]).

the halo model describes the correlation between particles belonging to the same halo. Therefore, it must be proportional to the average number of galaxy pairs $\langle N(N-1)|M\rangle$ in a halo of mass M, where $N = N_c + N_s$ indicates the total number of galaxies. This quantity can be written in terms of central and satellite galaxies as

$$\langle N(N-1)|M\rangle F(r) = 2\langle N_c N_s|M\rangle F_{cs}(r) + \langle N_s(N_s-1)|M\rangle F_{ss}(r)\,, \qquad (7.2)$$

where $F(r)$ is the cumulative radial distribution of galaxy pairs and $F_{cs}(r)$ and $F_{ss}(r)$ are restricted to central-satellite and satellite-satellite pairs, respectively. Since the above HOD model assumes that the central galaxy is located in the halo center and that the distribution of satellites follow the underlying CDM, $F_{cs}(r)$ is given by the normalized NFW profile and $F_{ss}(r)$ is a convolution of two normalized NFW profiles. The term $\langle N_s(N_s-1)|M\rangle$ can be simplified taking into account that satellites follow a Poisson distribution, i.e. $\langle N_s(N_s-1)|M\rangle = \langle N_s|M\rangle^2$, while $\langle N_c N_s|M\rangle = \langle N_c|M\rangle\langle N_s|M\rangle$ because the occupation number of central and satellites are independent. Given the partition in centrals and satellites, the galaxy power spectrum can be written as

$$\begin{aligned} P_{gg}(k) &= P_{cc}(k) + 2P_{cs}(k) + P_{ss}(k) \qquad (7.3)\\ &= [2P_{cs}(k) + P_{ss}(k)]_{1h} + [P_{cc}(k) + 2P_{cs}(k) + P_{ss}(k)]_{2h} \\ &= P_{gg}^{1h}(k) + P_{gg}^{2h}(k)\,, \end{aligned}$$

where the last two equations have been written as sums of the correspondent 1- and 2-halo terms. Notice that a halo can have at most one central galaxy and therefore $P_{cc}(k) = P_{cc}^{2h}(k)$. In analogy to Eqs.(5.5) and (5.6) and using the decomposition in Eq.(7.2), where the central-satellite term is multiplied by the NFW profile and the satellite-satellite is multiplied by the same term squared, the 1- and 2-halo terms of the galaxy power spectrum become

$$\begin{aligned} P_{gg}^{1h}(k) &= \int_0^\infty dM\, n(M) \left[2\frac{\langle N_c N_s|M\rangle}{\bar{n}_g^2}u(k|M) + \frac{\langle N_s(N_s-1)|M\rangle}{\bar{n}_g^2}u^2(k|M)\right] \qquad (7.4)\\ &= \int_0^\infty dM\, n(M) \left[2\frac{\langle N_c|M\rangle\langle N_s|M\rangle}{\bar{n}_g^2}u(k|M) + \frac{\langle N_s|M\rangle^2}{\bar{n}_g^2}u^2(k|M)\right] \\ P_{gg}^{2h}(k) &= \left\{\int_0^\infty dM n(M) b(M) \left[\frac{\langle N_c|M\rangle}{\bar{n}_g} + \frac{\langle N_s|M\rangle}{\bar{n}_g}u(k|M)\right]\right\}^2 P^L(k)\,, \qquad (7.5) \end{aligned}$$

where the convolution of NFW profiles in configuration-space has become multiplications in Fourier-space. Using the cold dark matter prescription (Eqs.(6.7)-(6.10)), we write

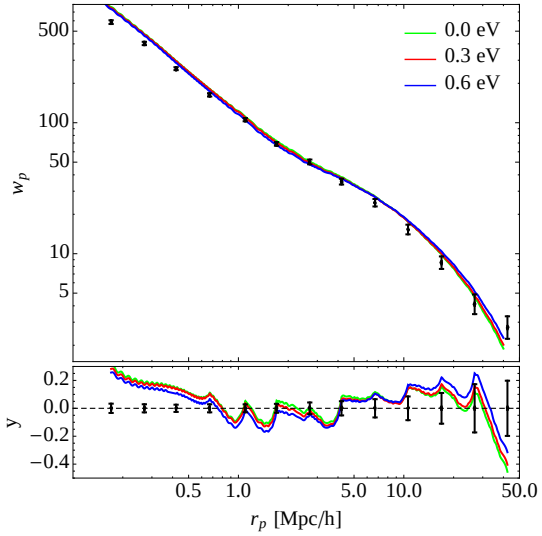

Figure 7.1: Projected correlation function. Black dots are the w_p measurements for galaxies with $M_r - 5\log_{10} h = -21.0$ from Zehavi et al. [130] and the error bars are the diagonal terms of the covariance matrix. Green, red and blue lines show the predictions from halo model for $\sum m_\nu = 0.0$, 0.3, 0.6 eV cosmologies. The bottom panel shows the relative difference between them and the measurements.

these terms as a function of the peak height ν:

$$P_{gg}^{1h}(k) = \int_0^\infty d\nu\, f(\nu)\frac{\bar{\rho}}{M}\left[2\frac{\langle N_c|M\rangle\langle N_s|M\rangle}{\bar{n}_g^2}u(k|M) + \frac{\langle N_s|M\rangle^2}{\bar{n}_g^2}u^2(k|M)\right] \quad (7.6)$$

$$P_{gg}^{2h}(k) = \left\{\int_0^\infty d\nu\, f(\nu)\, b(\nu)\frac{\bar{\rho}}{M}\left[\frac{\langle N_c|M\rangle}{\bar{n}_g} + \frac{\langle N_s|M\rangle}{\bar{n}_g}u(k|M)\right]\right\}^2 P^L(k)\,. \quad (7.7)$$

We compute the galaxy power spectrum for the massless ΛCDM and the $\sum m_\nu = 0.3$, 0.6 eV massive neutrino cosmologies, using Eqs.(7.6) and (7.7). We calculate the mean occupation numbers $\langle N_c|M\rangle$ and $\langle N_s|M\rangle$ as described in Eq.(7.1), using the HOD parameters M_1, α, M_{min} from Villaescusa-Navarro et al. [124] (see table 7.1).

Having calculated the galaxies power spectrum using the above formalism, we then compute the galaxies correlation function

$$\xi_{gg}(r) = \int_0^\infty dk\, k^2\, \frac{\sin(kr)}{kr}\, P_{gg}(k)\,. \quad (7.8)$$

However, this quantity cannot be measured directly from galaxy surveys because of the unknown peculiar motion of the galaxies along the line-of-sight. What can be computed from observations is the redshift-space correlation function $\xi(r_p, r_\pi)$, which is a function of the redshift-space separations parallel (r_π) and perpendicular (r_p) to the line-of-sight. In order to compare the model with observations we must consider the projected correlation function, $w_p(r_p)$, which is defined as

$$w_p(r_p) \equiv 2\int_0^{r_{max}} dr_\pi\, \xi(r_p, r_\pi)\,, \quad (7.9)$$

and it is related to the galaxy correlation function in configuration-space through [35]

$$w_p(r_p) = \int_{r_p}^{\infty} dr \, \frac{2r}{\sqrt{r^2 - r_p^2}} \, \xi_{gg}(r) \, . \tag{7.10}$$

Figure 7.1 shows the projected correlation function predicted by our model, together with the one measured by Zehavi et al. [130]. As we see from the relative difference between model and observations in the bottom panel, both cosmologies reproduce very well the measurements for $r_p > 1$ Mpc$/h$. This result confirms that the calibration of the HOD parameters can be carried out, for massive neutrino cosmologies, using the above formalism together with our extension of the halo model. Since direct calibration of the HOD parameters with N-body simulations is difficult, CPU time consuming and its subject to resolution and cosmic variance, the above formalism is fast and precise, allowing us to explore a wider parameter space.

We conclude this section noticing that the effect of massive neutrinos on many cosmological observables, such as galaxy clustering, can be mimicked by varying the value σ_8 from a massless neutrino cosmology. This is the well known $\Omega_\nu - \sigma_8$ degeneracy (see for instance [43, 74]). Our formalism is capable of reproducing such degeneracy at the same time it provides us with a physical insight.

Part III

Voids in massive neutrino cosmologies

Based on:

E. Massara, F. Villaescusa-Navarro, M. Viel, and P.M. Sutter, *Voids in massive neutrino cosmologies*, *JCAP* **11** (2015) 018, [arXiv:1506.03088].

Abstract

Cosmic voids are a promising environment to characterize neutrino-induced effects on the large-scale distribution of matter in the universe. We perform a comprehensive numerical study of the statistical properties of voids, identified both in the matter and galaxy distributions, in massive and massless neutrino cosmologies. The matter density field is obtained by running several independent N-body simulations with cold dark matter and neutrino particles, while the galaxy catalogs are modeled by populating the dark matter halos in simulations via a halo occupation distribution (HOD) model to reproduce the clustering properties observed by the Sloan Digital Sky Survey (SDSS) II Data Release 7. We focus on the impact of massive neutrinos on the following void statistical properties: number density, ellipticities, two-point statistics, density and velocity profiles. Considering the matter density field, we find that voids in massive neutrino cosmologies are less evolved than those in the corresponding massless neutrinos case: there is a larger number of small voids and a smaller number of large ones, their profiles are less evacuated, and they present a lower wall at the edge. Moreover, the degeneracy between σ_8 and Ω_ν is broken when looking at void properties. In terms of the galaxy density field, we find that differences among cosmologies are difficult to detect because of the small number of galaxy voids in the simulations. Differences are instead present when looking at the matter density and velocity profiles around these voids.

Introduction

Besides the anisotropies in the cosmic microwave background, the vast majority of the constraints on the values of cosmological parameters arise from the observations of only one element of the cosmic web: the dark matter halos (or the galaxies residing within them). Much attention has been put in understanding the spatial distribution and statistics of galaxies and dark matter halos. This is because it is believed that those objects are biased tracers of the underlying matter distribution. Thus, by measuring their spatial correlations on large scales it is possible to constrain the values of the cosmological parameters. Additional information on the value of the cosmological parameters can be obtained by measuring the abundance of dark matter halos as a function of their mass, i.e. via the halo mass function (see for example [14]).

Recently, it has been pointed out that cosmic voids can also be used to constrain the values of cosmological parameters [21, 22, 57, 65, 66, 95, 114, 117, 122, 126, 132]. As a different element of the cosmic web, the information embedded into the properties of voids will complement the one obtained from the dark matter halos. That additional information can then be used to break degeneracies and to further constrain the parameters of the cosmological model. Among the different observables that can be used to retrieve cosmological information with voids there are: the distribution of void ellipticities [66], the Alcock-Paczynski test [21, 65, 117], the integrated Sachs-Wolfe effect [57] and the weak lensing effect [60].

Cold dark matter and baryons are not the only massive particles present in the universe that could play a role in the formation of structure, and in particular in the evolution of voids: there are also neutrinos. The existence of a neutrino cosmic background is one of the predictions of the Big Bang theory and it is timely to investigate the impact of massive neutrinos on the large scale structure.

There are reasons to expect that massive neutrinos affect more strongly the properties of cosmic voids than the properties of dark matter halos. Given their large thermal velocities, neutrino clustering within dark matter halos and galaxies will be limited to the neutrinos populating the low-momentum tail of the Fermi-Dirac distribution [124]. In other words, the relative contribution of relic neutrinos to the total mass of dark matter halos is much smaller than the cosmic ratio $\Omega_\nu/\Omega_{\rm cdm}$. A consequence of this fact is that most of the properties of the dark matter halos, such as their mass function or their spatial bias, can be described in terms of the CDM density field, rather than the total matter density field [9, 23, 32, 55, 69, 70, 124]. On the other hand, the large thermal velocities of the neutrinos will prevent their evacuation from cosmic voids. This should manifest as an extra mass within voids that will affect their overall evolution. It is thus expected that voids in a massive neutrino universe would be smaller and denser.

This fact was firstly noted by [126], who studied the properties of voids in massive neutrino cosmologies using the Lyα forest.

In this part of the thesis we investigate for the first time the impact of massive neutrinos on cosmic voids, as identified in the spatial distribution of galaxies and in the underlying matter density field. We study the properties of voids in the spatial distribution of matter by running large box N-body simulations in cosmologies with massless and massive neutrinos, described in Chapter 4 and listed the bottom part of Table 4.1. The spatial distribution of galaxies is modeled using a halo occupation distribution (HOD) model and requiring that the resulting mock galaxy catalogues reproduce, for a given galaxy population, the observed number density and two-point correlation function of a particular survey. We use the publicly-available code VIDE [116] to identify the voids in both the matter and galaxy distribution. The void catalogs obtained with this void finder - a watershed void finder presented in Chapter 4 - depend on the resolution of the N-body simulation considered. However, in this work we are interested in the relative differences between cosmologies with and without massive neutrinos, rather than absolute results. Therefore, we compare catalogs and void properties obtained from simulations at the same resolution.

This part is organized as follows. A comparison between the different properties of voids detected in the matter density field in the different cosmological models is shown in Chapter 8, while in Chapter 9 we present the properties of voids identified in the galaxy distribution.

Chapter 8

Voids in the matter distribution

In this chapter we present the analysis for voids identified in the matter density field, which is modeled via our low resolution N-body simulations. As explained in the above section, voids are selected in the matter density field by running VIDE on top of all CDM particles, for every realization of each cosmological model. Our goal is to investigate the impact of massive neutrinos on the formation and evolution of cosmic voids. Thus, here we study some of the main properties of voids and examine how these depend on the cosmological model. The void properties analyzed are: number densities, ellipticities, two-point correlation functions, density profiles, and velocity profiles.

8.1 Number density

We compute the number density of voids at $z = 0$ and $z = 1$ as a function of their effective radius $R_{\rm eff}$, and show the results in Fig. 8.1. Different colors indicate different cosmologies while error bars represent the scatter around the mean value obtained from the 10 independent realizations divided by $\sqrt{10}$. The bottom panel of each plot displays the ratio between the number density of voids in massive to massless neutrinos cosmologies. We find that in cosmologies with massive neutrinos the abundance of small voids is larger than in massless neutrinos cosmologies, whereas the number density of big voids is highly suppressed in massive neutrino cosmologies. These trends take place both at $z = 0$ and $z = 1$, while relative differences are smaller at $z = 1$.

These results are in perfect agreement with our expectations: neutrinos have large thermal velocities, which gives rise to two main effects. On one hand it avoids their clustering within dark matter halos, and on the other hand it makes them less sensitive to void dynamics. Therefore, as a first approximation, the neutrinos density contrast can be approximated as $\delta_\nu = 0$ and the matter density as $\delta_{\rm m} = \delta_{\rm cdm}\rho_{\rm cdm}/\rho_{\rm m} + \delta_\nu\rho_\nu/\rho_{\rm m} \simeq \delta_{\rm cdm}\rho_{\rm cdm}/\rho_{\rm m}$, where the subscripts 'cdm' and 'm' stand for CDM and matter, respectively. This brings an extra mass inside the voids that will slow down their overall evolution. It is thus expected that voids in a massive neutrino universe would be smaller and denser, and therefore appear less-evolved. Moreover, the higher the neutrino mass the higher the ratio $\rho_\nu/\rho_{\rm m}$ and the additional mass inside the voids. Therefore the relative differences with respect to ΛCDM increases with the neutrino mass. We also expect differences to become smaller at higher redshift. At higher redshifts voids will be denser overall, and the additional mass given by neutrinos

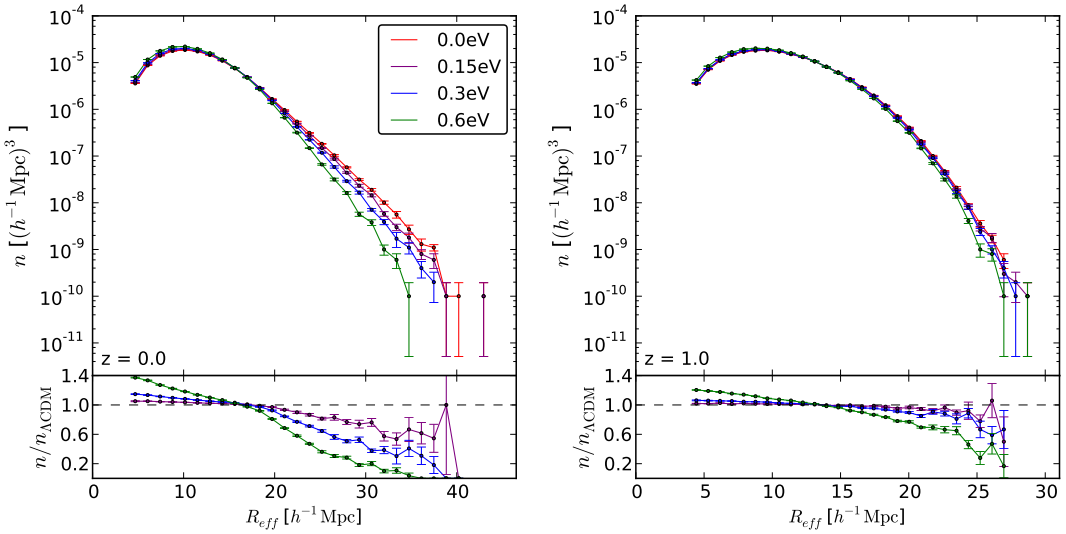

Figure 8.1: Number density of voids as function of their effective radius. The top panels show the results for different cosmologies: red line is the ΛCDM cosmology, purple, blue and green lines correspond to $\sum m_\nu = 0.15$ eV, $\sum m_\nu = 0.3$ eV and $\sum m_\nu = 0.6$ eV cosmologies, respectively. The bottom panels show the ratio between the void number density in massive and massless neutrino cosmologies. Left and right plots display results at redshift $z = 0$ and $z = 1$, respectively.

will play a less important role and the void number density will be more similar among different cosmologies.

We conclude that the number density of voids, identified in the matter density field, is very sensitive to the neutrino masses.

8.2 Ellipicity

We now investigate the distribution of voids ellipticities in cosmologies with massive and massless neutrinos. For each cosmological model we compute the fraction of voids with a given ellipticity and show the results in Fig. 8.2 at redshifts $z = 0$ (left) and $z = 1$ (right). The error bars represent the scatter around the mean value obtained from the 10 independent realizations normalized by $\sqrt{10}$. The bottom panels show the ratio between the models with massive neutrinos to the model with massless neutrinos. We find differences of the order of a few percent between ΛCDM and 0.15 eV cosmologies for void with ellipticities $\epsilon < 0.4$, where statistical error bars are relatively small. The differences increase as the sum of neutrino masses increases and it reaches 20% for the 0.6 eV cosmology for both redshifts $z = 0$ and $z = 1$. We find that relative differences among models slightly decrease at $z = 1$.

With our interpretation that voids in massive neutrino cosmologies appear younger than those in massless neutrino cosmologies, it is straightforward to understand the results. Voids in cosmologies with massive neutrinos will be in a earlier evolutionary stage and therefore we would expect to find more voids with low ellipticities than in a ΛCDM cosmology. For the same reason, there is a deficit of voids with large ellipticites in massive neutrino cosmologies.

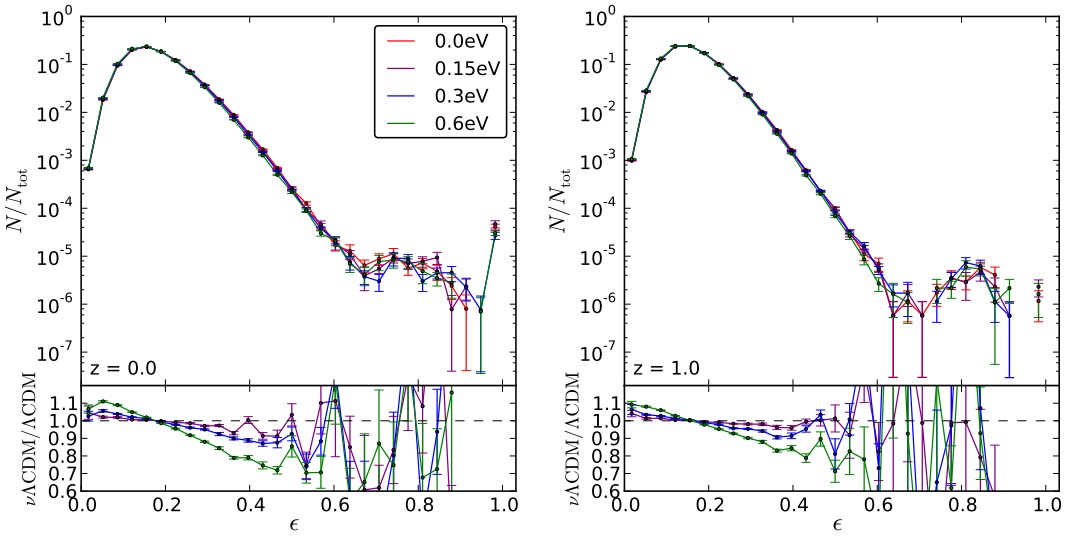

Figure 8.2: Number of voids with a given ellipticity, normalized by the total number of voids. The top panels show results from different cosmologies: red line is the ΛCDM cosmology, purple, blue and green lines correspond to $\sum m_\nu = 0.15$ eV, $\sum m_\nu = 0.3$ eV and $\sum m_\nu = 0.6$ eV cosmologies. The bottom panels show the ratio between the same quantity in a massive and a massless neutrino cosmologies. Left and right plots display results at redshift $z = 0$ and $z = 1$, respectively.

8.3 Correlation function

The structure of the void correlation function has been well studied (for example, in [51]), which identified the void-exclusion scale and the effects of galaxy bias. Here we investigate the clustering properties of voids in the different cosmological models. For each cosmology, we split our void catalogues in different groups depending on their size $R_{\rm eff}$ and compute the correlation function of the void centers belonging to the same group. The correlation function is measured using the Landy-Szalay estimator [63]. The random catalogue contains a number of points 20 times larger than the void catalogue.

Figure 8.3 shows the results at redshift $z = 0$ (on the left) and $z = 1$ (on the right), with error bars given by the scatter around the mean value obtained from the 10 independent realizations divided by $\sqrt{10}$. For clarity we show the correlation functions for only two cosmologies: the solid lines refer to ΛCDM and the dashed ones refer to $\sum m_\nu = 0.6$ eV cosmology. Different colors indicate different ranges in $R_{\rm eff}$. The results show that, for both cosmologies, the two-point correlation function goes to zero on large scales. It increases as R decreases and it reaches a maximum, whose height and position depend on the size of the voids considered. Finally, going towards smaller distances, the correlation function decreases until it reaches the lowest boundary -1.

The behavior of the correlation function on small scales is due to exclusion effects: top-level voids are extended objects that cannot overlap. In fact, if we imagine them as spheres of radius $R_{\rm eff}$, the probability of finding two void centers at a distance smaller than the sum of their effective radii (exclusion scale) is zero, which corresponds to a value of the correlation function equal to -1. We would naively expect to have a sharp transition from the positive correlation to the exclusion regime. However, this is not

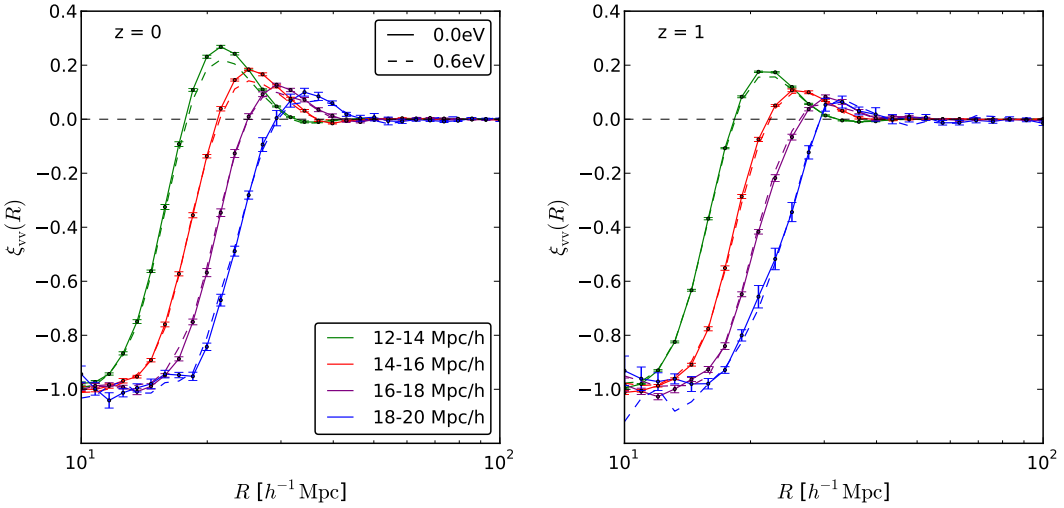

Figure 8.3: Two-point correlation function of voids with an effective radius in a given range. Solid lines show the results for the ΛCDM cosmology whereas the dashed lines indicate the results for the $\sum m_\nu = 0.6$ eV cosmology; different colors are related to different bins in the void radii as reported in the legend. Left and right plots display results at redshift $z = 0$ and $z = 1$, respectively.

the case for several reasons. First of all, the presence of different void sizes in each of the considered groups. Secondly, the void finder used in this paper does not return spherical voids, but under-dense regions with a complicated shape, and therefore it can happen that the distance between two void centers is smaller than the sum of their two effective radii. It can be seen that the exclusion scale increases with the effective radius of the voids considered.

The presence of a positive peak in the two-point correlation function arises from two different processes: the rise of the non-linear clustering of voids going to smaller scales and the exclusion effect. We can also understand why the clustering of voids in massive neutrino cosmologies is lower with respect to the massless neutrino case if we take into account that voids in the former are younger than those in the latter. Indeed, if we compare the clustering of voids at $z = 0$ and at $z = 1$, we find that the clustering decreases with redshift. Thus, since voids in the massive neutrino cosmologies are effectively younger, they are expected to exhibit a lower amplitude in the 2pt-correlation function, as our results show. At higher redshifts the properties of voids in cosmologies with massive and massless neutrinos get closer, and therefore it is natural that differences in their clustering properties decrease.

8.4 Density profile

Here we investigate the impact of massive neutrinos on the shape of the void density profiles. We compute the cold dark matter, massive neutrino, and total matter density profile in voids of different sizes.

The profiles have been computed in the following way. For each simulation box, we select the voids whose effective radius lie within a certain interval. For each void, we

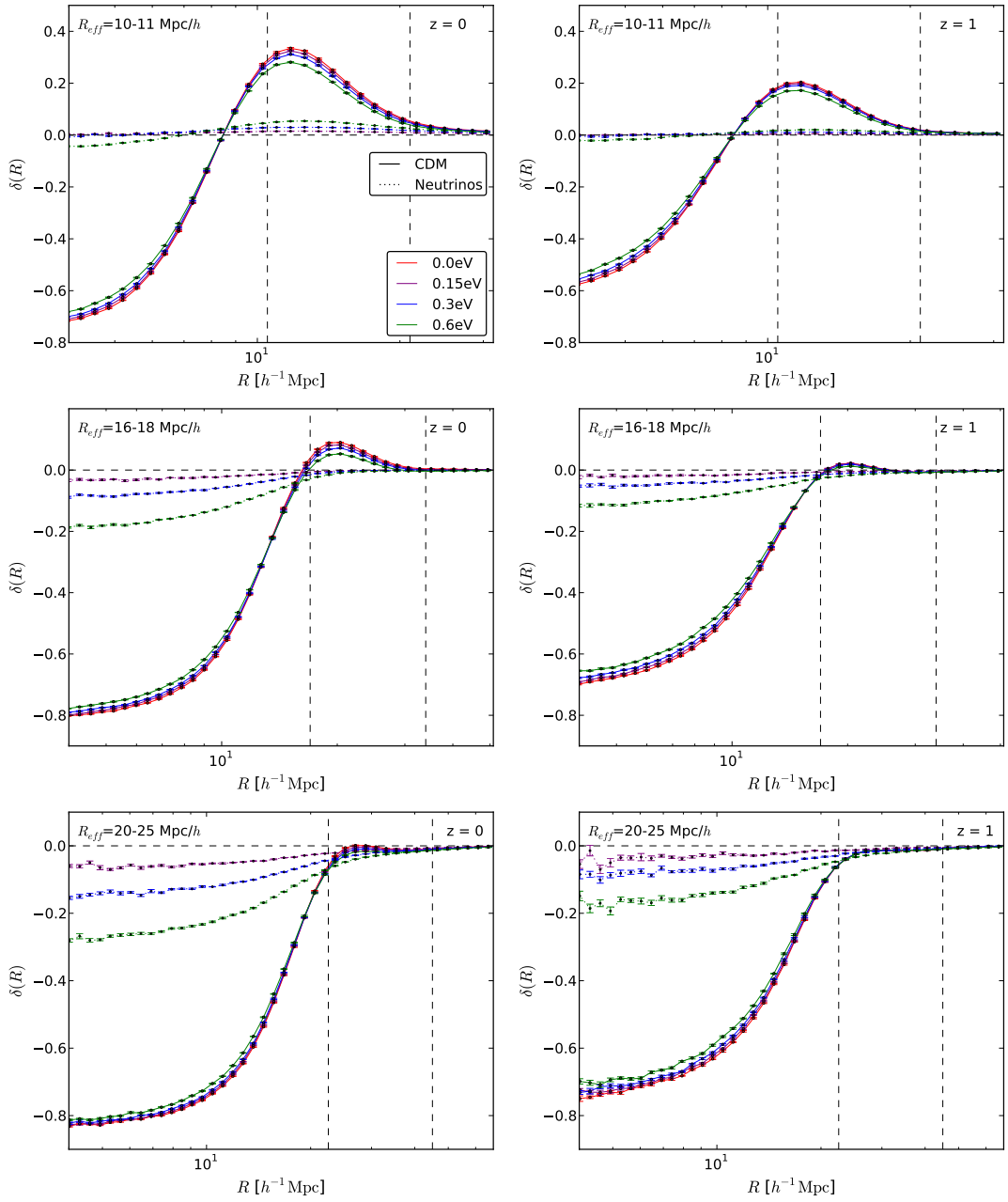

Figure 8.4: Average cold dark matter (solid lines) and neutrino (dotted lines) density profiles around voids with different sizes: $R_{\rm eff}$=10-11 Mpc/h (top), $R_{\rm eff}$=16-18 Mpc/h (center), $R_{\rm eff}$=20-25 Mpc/h (bottom). Left and right panels show results at redshifts $z = 0$ and $z = 1$, respectively. Red, purple, blue and green lines show the 0.0, 0.15, 0.3 and 0.6 eV cosmologies, respectively. The dashed black lines indicate the mean value of the void radii in the selected range and two times the same quantity.

compute the density field inside shells around the center, then we stack all the shells of the different voids to obtain the average density profile at a given distance from the void center. We repeat the procedure for all the ten realizations with the same cosmology, then we average over the realizations. The error that we present is the scatter between the different realizations normalized by $\sqrt{10}$. We repeat this procedure for different intervals in the void radius and for all the cosmologies considered in this paper.

Figure 8.4 shows the average cold dark matter (solid lines) and neutrino (dotted lines) density profiles around void centers with radius $R_{\rm eff}$=10-11 Mpc/h (top), $R_{\rm eff}$=16-18 Mpc/h (center), and $R_{\rm eff}$=20-25 Mpc/h (bottom). Left and right plots show results at redshift $z = 0$ and $z = 1$, respectively, and different colors indicate different cosmologies. Let us focus first on the cold dark matter density profile. We can immediately notice that small voids present a compensated wall at the edge, whereas the large ones have a negative density profile, as already shown in [50]. Moreover, fixing the cosmology, voids present a typical behavior: large voids are emptier; i.e., they present deeper underdensities in the core than small ones. However, we have checked that this behavior can change depending on the resolution of the considered simulations.

For voids with a given radius, we find that the height of the wall becomes higher when decreasing the neutrino mass. On the other hand, the inner part of the density profile is emptier in the massless neutrino case and it becomes denser as the neutrino mass increases. Voids evolve in time building a higher wall and becoming progressively emptier and emptier. Again we can understand the difference between the cosmologies: the impact of the neutrino mass can be described as slowing down the evolution of the void profiles and giving a less evolved universe in these regions.

The neutrino profile is found to follow the corresponding cold dark matter one. Around very small voids, the neutrino profile presents an overdensity at the void wall, whereas it presents troughs around very large voids. Any departure from the mean background density (both overdensities and troughs) is greater for larger neutrino masses. This corresponds to the neutrinos with lower thermal velocities, which are more susceptible to the presence of the cold dark matter gravitational field.

In Fig. 8.5 we show the total matter density profile, which is the most relevant quantity since most of the observables depend on the total matter distribution, e.g. weak lensing and the ISW effect. We present the results for the same void sizes as above and at $z = 0$ (left) and $z = 1$ (right). The bottom panel of each plots shows the ratio between the density profiles of the three massive neutrino cosmologies with respect to ΛCDM. The main features observed in the cold dark matter profiles are overall preserved, but enhanced here. In the void core, the differences between ΛCDM and the 0.15 eV cosmology are at the level of 1-3 %, depending on the void radius, and they reach 10% for the 0.6 eV case. Near the wall and for the very small voids, the difference is at the 5 % level for 0.15 eV and at the 20% level for 0.6 eV cosmologies. All the differences are more pronounced at $z = 1$.

8.4.1 Void-by-void comparison

Above we have compared the density profiles of voids with the same fixed size. It is also interesting, mainly for model building purposes, to study the differences among

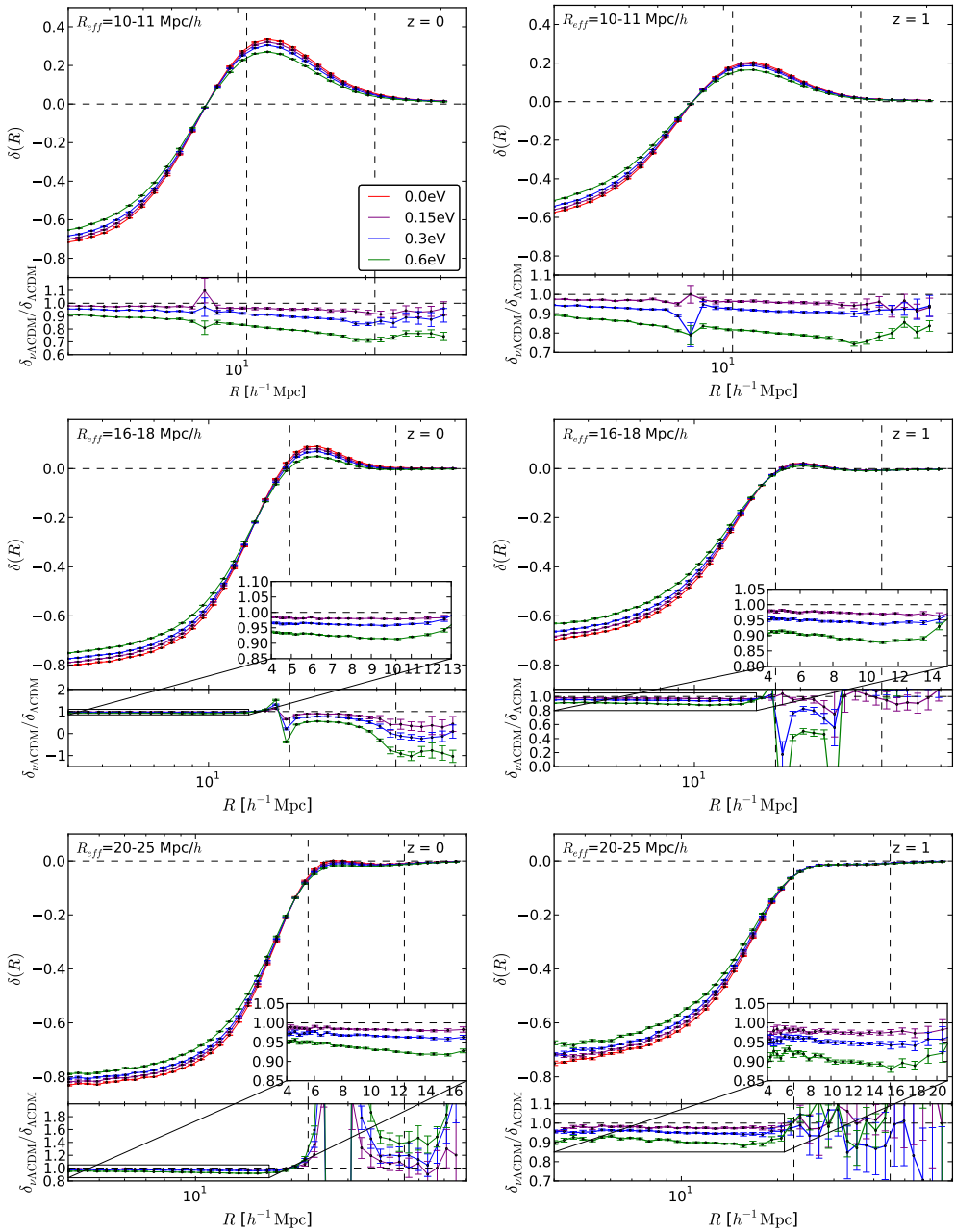

Figure 8.5: Average total matter density profiles around voids with different sizes: $R_{\rm eff}$=10-11 Mpc/h (top), $R_{\rm eff}$=16-18 Mpc/h (center), and $R_{\rm eff}$=20-25 Mpc/h (bottom). Left and right panels show results at redshifts $z = 0$ and $z = 1$, respectively. Red, purple, blue and green lines show the 0.0, 0.15, 0.3 and 0.6 eV cosmologies, respectively. At the bottom of each panel we display the ratio between the results from the massive neutrino cosmologies and the ΛCDM one. The vertical dashed black lines indicate the mean value of the void radii in the selected range and two times the same quantity.

different cosmologies by performing a void-by-void comparison. The procedure we use to perform a void-by-void comparison is as follows. We first select all voids of a given size in the ΛCDM cosmology. Then, for each of the selected void, we find the

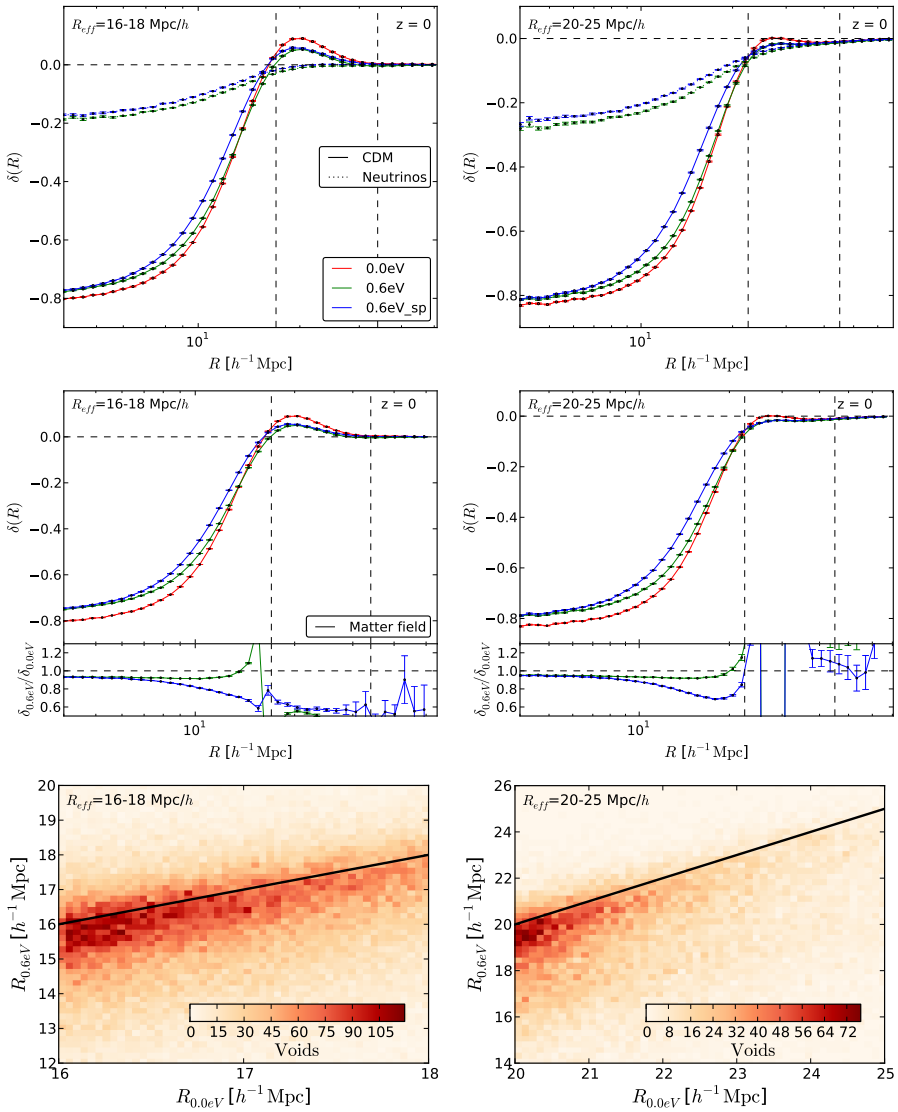

Figure 8.6: Comparison void-by-void between the ΛCDM and the $\sum m_\nu = 0.6$ eV cosmologies. We have selected all voids in the ΛCDM cosmology with radii $R_{\rm eff}$=16-18 Mpc/h (left column) and $R_{\rm eff}$=20-25 Mpc/h (right column) and we plot their density profiles in red. The upper panels show the CDM and neutrino density profiles whereas middle panels display the results for the total matter density profiles. For the 0.6 eV cosmology we have chosen the voids using two different procedures: we select all voids in above radii range (green lines) and we choose the voids by matching their positions to these of the ΛCDM cosmology (blue lines). The vertical dashed black lines indicate the mean value of the void radii in the selected range and two times the same quantity. The lower panels show the void-by-void comparison between the radii of the ΛCDM and the 0.6 eV voids. Each pixel in those panels displays the number of void pairs as a function of the void radius $R_{0.0\rm eV}$ in the ΛCDM (x-axis) and the radius of the corresponding void $R_{0.6\rm eV}$ in the 0.6 eV cosmology (y-axis). The solid black lines represent the curve $R_{0.6\rm eV} = R_{0.0\rm eV}$.

corresponding one in a massive neutrino cosmology by searching the void whose center lie closest to the center of the ΛCDM void. Finally, we use these voids to compute the mean density profile in the massive neutrino cosmology. We have explicitly checked that this simple procedure works well when dealing with large voids, whereas for small voids the comparison is not always satisfactory. Therefore, we limit our analysis to big voids. In figure 8.6 we compare the density profiles for CDM, neutrinos and total matter for voids in ΛCDM and $\sum m_\nu = 0.6$ eV cosmologies. For the latter cosmology we use both procedures, i.e. voids with radii within a given range (green lines) and voids selected by matching them with those of the ΛCDM cosmology (blue line).

The comparison between the density profiles of voids in the ΛCDM cosmology and the corresponding voids in the massive neutrino cosmology confirms that the presence of massive neutrinos makes the voids matter evacuation slower and therefore they are less empty in the center and they present a lower wall at the edge. The comparison between void profiles in the same cosmology ($\sum m_\nu = 0.6$ eV) but found using the two different ways (blue and green lines) is enlightening. Indeed, voids selected using the ΛCDM catalogue appear to be smaller than the one selected looking at the void size, since their slope is closer to the center. This is even more clear when plotting the void radii in the void-by-void selection for ΛCDM and $\sum m_\nu = 0.6$ eV cosmology (lower row in figure 8.6). The black line indicates the equality between the radii in the two cosmologies and most of the points are below that line, which means that majority of voids in massive neutrino cosmology are smaller that the ones in the massless case. This is even stronger evidence of what we expected: the presence of massive neutrinos slow down the evolution (expansion) of voids.

8.5 Velocity profile

We now present the radial velocity profiles of the cold dark matter, neutrino, and total matter fields. The first two have been computed directly from simulations in the following way. We select voids with radii in a given range and then we compute the radial velocity profiles of particles inside a shell of radius r around each void center, using

$$v(r) = \frac{1}{N}\sum_{i=1}^{N} \vec{v}(r_i)\cdot\frac{\vec{r}_i}{|\vec{r}_i|}\,, \tag{8.1}$$

where N is the number of particles in the shell and $\vec{r}_i$ are the coordinates of the particles with respect to the void center. Next, we stack all the shells from the different voids for computing the average velocity at a given distance from the void center. Finally, we average over the ten realizations with the same cosmology. The error associated with the profiles is the scatter between the ten realizations divided by $\sqrt{10}$. The velocity of the total matter field is instead computed as the density weighted average between the velocity profiles of the cold dark matter and neutrino particles, via

$$v_{\rm m}(r) = \frac{v_{\rm cdm}(r)\rho_{\rm cdm}(r) + v_\nu(r)\rho_\nu(r)}{\rho_{\rm cdm}(r)+\rho_\nu(r)}\,, \tag{8.2}$$

where the subscripts m, cdm and ν stand for matter, cold dark matter and neutrinos, respectively. The associated errors are computed via error propagation. Other velocity

estimators have been used in literature, e.g. the Voronoi weighting estimator [50]. However, we have checked that the relative differences between cosmologies (massive vs massless) are also reproduced by this estimator.

The results for the cold dark matter (solid lines) and the neutrino (dotted lines) fields are shown in figure 8.7. As for the density profile, we consider three ranges for the void radius and we plot on the left/right the results at redshifts $z = 0/z = 1$.

The cold dark matter particles have a positive radial velocity inside the effective radius (first vertical dashed lines from the left), meaning that the inner part of the voids is expanding and becoming more and more empty. The behavior outside the effective radius changes depending on the void size. Around very small voids (top panel), the cold dark matter velocity becomes negative, meaning that the particles are moving towards the void. Therefore, there is an ongoing construction of the wall around the edge of the void. The void will eventually shrink and later collapse because it is surrounded by an overdense region (this is the so-called void-in-cloud effect). Around bigger voids, the radial velocity is always positive; it presents a peak near half of the void radius and it decreases on large distances from the center. Therefore, the outer region of the void expands slower than the inner part, producing nevertheless a concentration of mass around the edge of the void. Looking at different cosmologies, the average radial velocity is higher in ΛCDM and it decreases as the sum of the neutrino masses increases. Going from redshift $z = 0$ to $z = 1$, the velocities increase for all void radius and cosmologies and differences between models become more pronounced.

As expected, we find that the neutrino radial velocity field follows the cold dark matter one. The velocity is positive inside the void radius and remains positive also outside, apart from the case of very small voids, where it becomes negative. However, the neutrino velocity appears to be smaller than cold dark matter one, which is only due to cancellation effects. Neutrinos have large thermal velocities that make them free-stream in every direction, therefore the average velocity is expected to be close to zero. To better understand this effect, Fig. 8.9 shows the average measured positive and negative neutrino radial velocity profile, which correspond to the profiles for the outgoing and incoming neutrinos, and their theoretical prediction. The predicted mean thermal velocities of incoming and outgoing neutrinos are equal due to spherical symmetry and it is computed as $v_{in} = v_{out} \simeq 160/2\,(3\mathrm{eV}/\Sigma m_\nu)$ km/s [67]. The two measured velocities are similar for small voids and small neutrino masses, but they differ otherwise. It is the gravitational interaction with the void and the surrounding matter which gives rise to this and to a positive (or negative) average neutrino velocity. At higher redshift ($z = 1$), the neutrinos are faster and they feel less the dynamics of the underlying cold dark matter structure. Indeed, the average neutrino radial velocity profile is lower at $z = 1$ than at $z = 0$.

The results for the total matter radial velocity field are presented in Fig. 8.8. The main features described for the cold dark matter radial velocity also apply here; however, the differences between different cosmologies are more pronounced. In the bottom panel of each plot we show the ratio between the results for the massive neutrino cosmologies to the ΛCDM case. At redshift $z = 0$ and in the inner part of the voids there are differences at the order of 5-10-15% for 0.15-0.3-0.6 eV cosmologies, respectively. Larger differences can be seen in the outer parts of the voids, in the ranges $R_{\rm eff}$=10-11 Mpc/h (top) and $R_{\rm eff}$=16-18 Mpc/h (center). At redshift $z = 1$ the differences are slightly

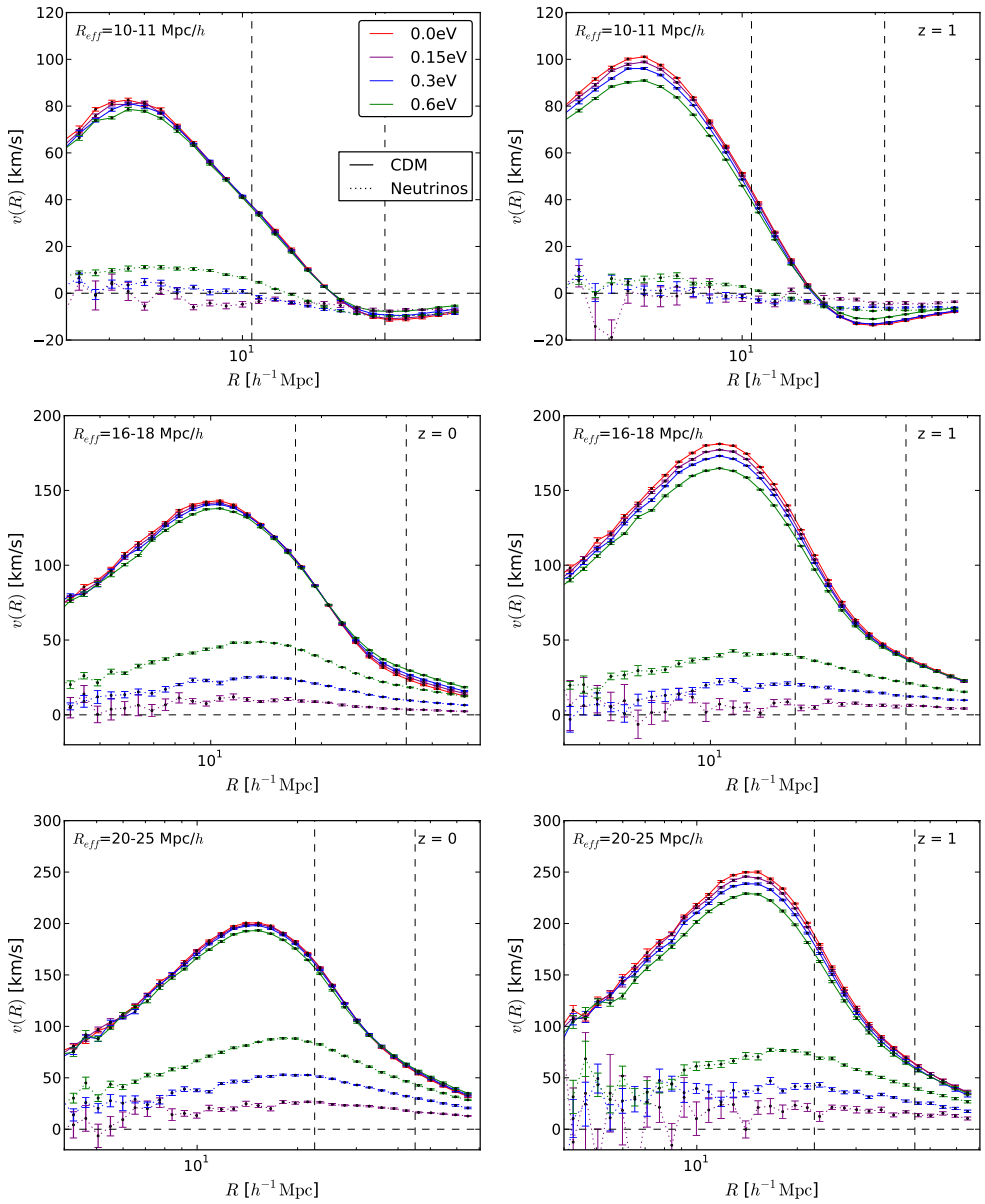

Figure 8.7: Cold dark matter (solid lines) and neutrinos (points) velocity profile measured from simulations around voids with different sizes: $R_{\rm eff}$=10-11 Mpc/h (top), $R_{\rm eff}$=16-18 Mpc/h (center), and $R_{\rm eff}$=20-25 Mpc/h (bottom). Left and right panels are computed at redshift $z = 0$ and $z = 1$, respectively. Red lines indicate the ΛCDM cosmology, and purple, blue and green lines show the 0.15, 0.3 and 0.6 eV cosmologies. The dashed black lines indicate the mean value of the void radii in the selected range and two times the same quantity.

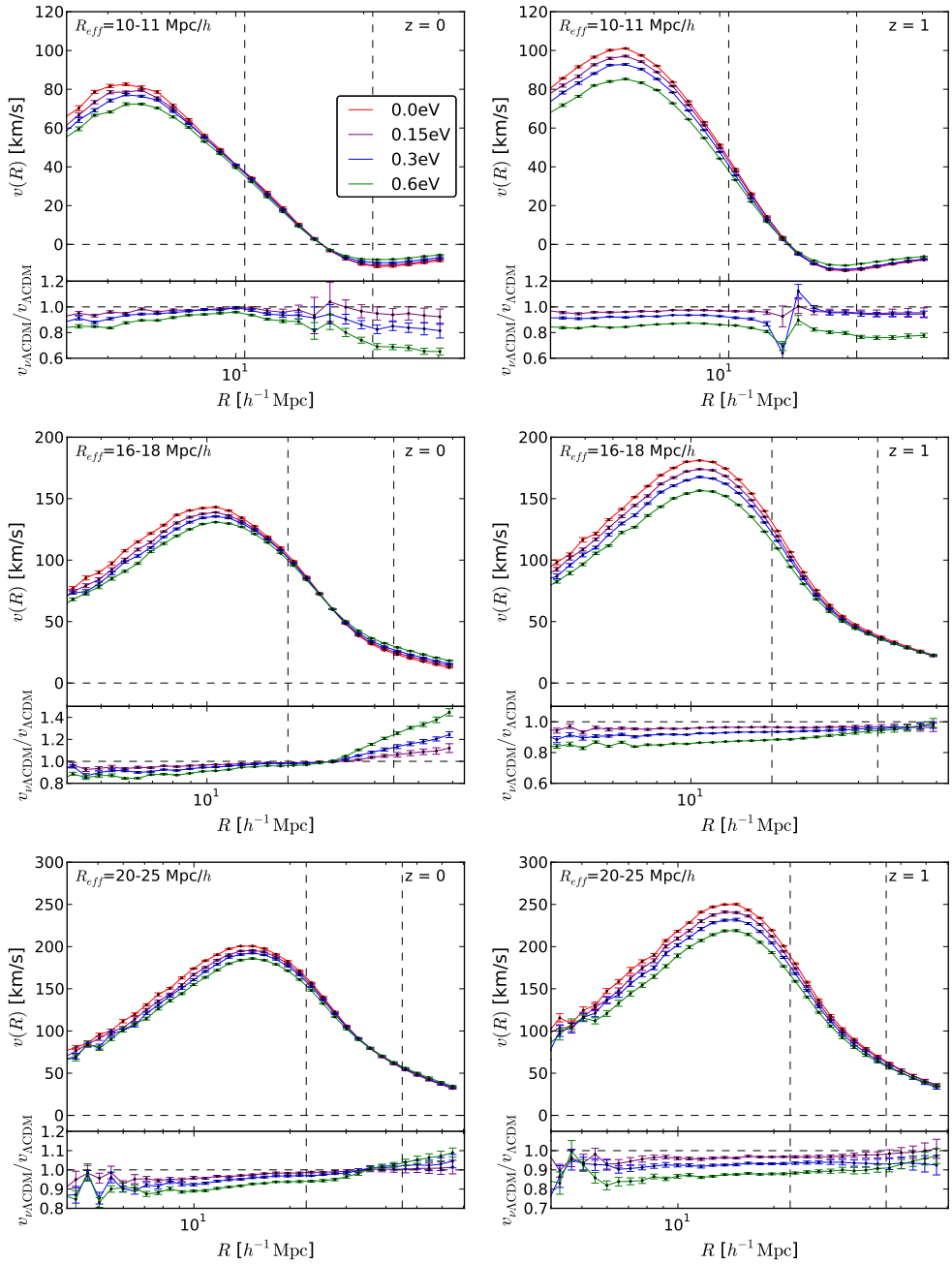

Figure 8.8: Total matter velocity profile measured from simulations around voids with different sizes: $R_{\rm eff}$=10-11 Mpc/h (top), 16-18 Mpc/h (center) and 20-25 Mpc/h (bottom). Left and right panels display results at redshift z=0 and z=1, respectively. Red lines indicate the ΛCDM cosmology, purple, blue and green lines show the 0.15, 0.3 and 0.6 eV cosmologies. At the bottom of each panel there are the residuals between the massive neutrino cosmologies and the ΛCDM one. The dashed black lines indicate the mean value of the void radii in the selected range and two times the same quantity.

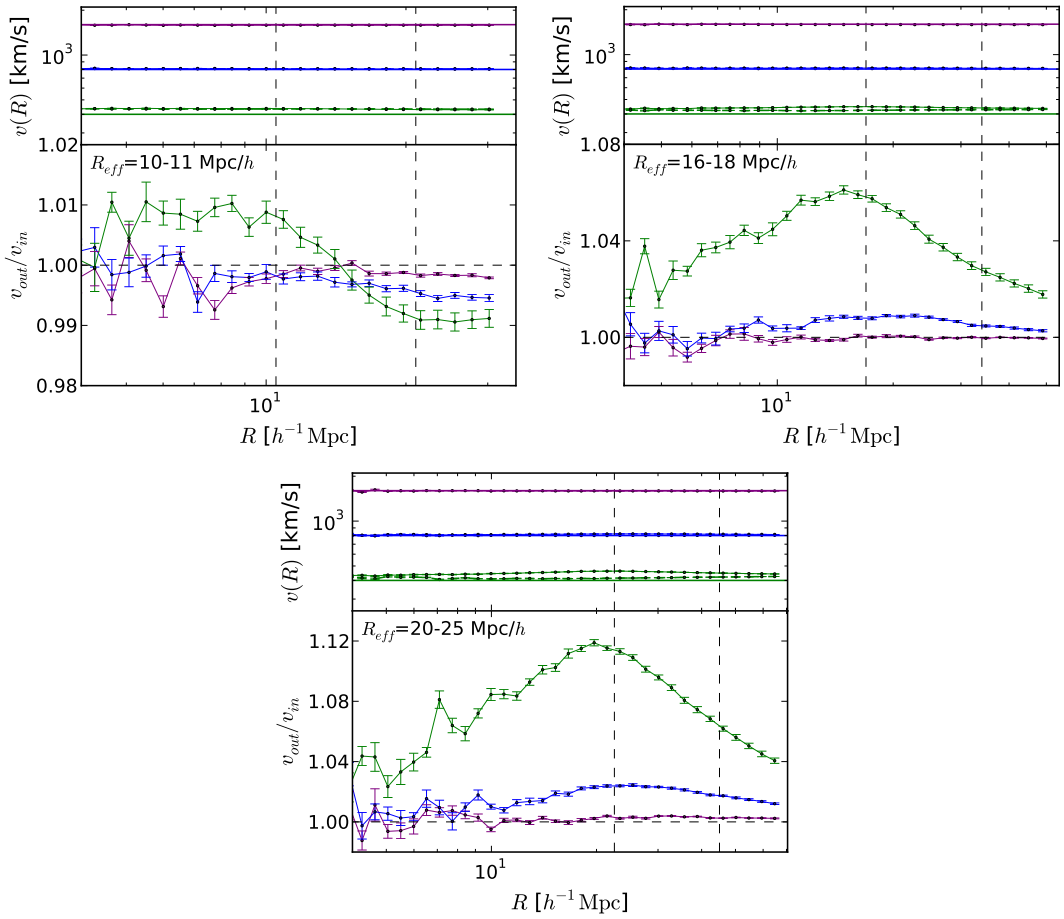

Figure 8.9: Radial velocity profile of outgoing (solid lines) and incoming (dashed lines) neutrinos around voids with different sizes: $R_{\rm eff}$=10-11 Mpc/h (top-left), 16-18 Mpc/h (top-left), and 20-25 Mpc/h (bottom). The solid horizontal lines show the theoretical mean radial velocity; purple, blue and green indicate the 0.15, 0.3 and 0.6 eV cosmologies. At the bottom of each panel there are the ratios between the velocity of outgoing and the incoming neutrino for each cosmology. The dashed black lines indicate the mean value of the void radii in the selected range and two times the same quantity.

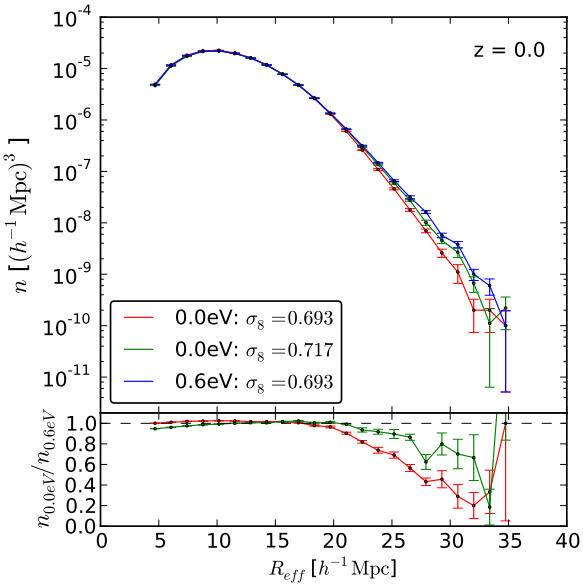

Figure 8.10: Number density of voids as function of their effective radius. The top panel shows the results for different cosmologies: red and green lines are the ΛCDM cosmology with σ_8 equal to the one in the $\sum m_\nu = 0.6$ eV case computed from the total matter and the CDM power spectra, respectively. The blue line correspond to the $\sum m_\nu = 0.6$ eV cosmology. The bottom panels show the ratio between the void number density in massless and massive neutrino cases considered.

more pronounced.

8.6 Ω_ν-σ_8 degeneracy

We also investigate the well known degeneracy between Ω_ν and σ_8 [23, 43, 74]. For instance, the effects of massive neutrinos in many observables such as cluster number counts, can be mimicked by a cosmology with massless neutrinos but with a lower value of σ_8, which is the r.m.s. value of the linear fluctuation in the mass distributions at 8Mpc/h. We want to understand if this is the case for voids too.

We use the simulations in ΛCDM with σ_8 taken from the $\sum m_\nu = 0.6$ eV cosmology (L0s8 and L0s8CDM) to identify voids in the matter density field. If the degeneracy is present also in voids, these simulations should give catalogs very similar to the one of the 0.6 eV case. Moreover, we consider the two different σ_8 values because it has been shown that for halos the degeneracy arises when using the CDM field, since it is the fundamental one in driving the evolution of overdense structures [23]. We must check if this is the case for underdense structures as well.

In order to test all of this, we first compare the number density of voids and we plot the results in figure 8.10. The ΛCDM cosmology with σ_8 computed from the total matter field (red line) matches quite well the predictions from the 0.6 eV case up to void radii equal to ∼17 Mpc/h. Above that, the departure is significant, giving a lack of big voids, and it reaches a disagreement at the level of 70-80% for voids with size ∼30 Mpc/h. Things are different for the ΛCDM cosmology with σ_8 computed from

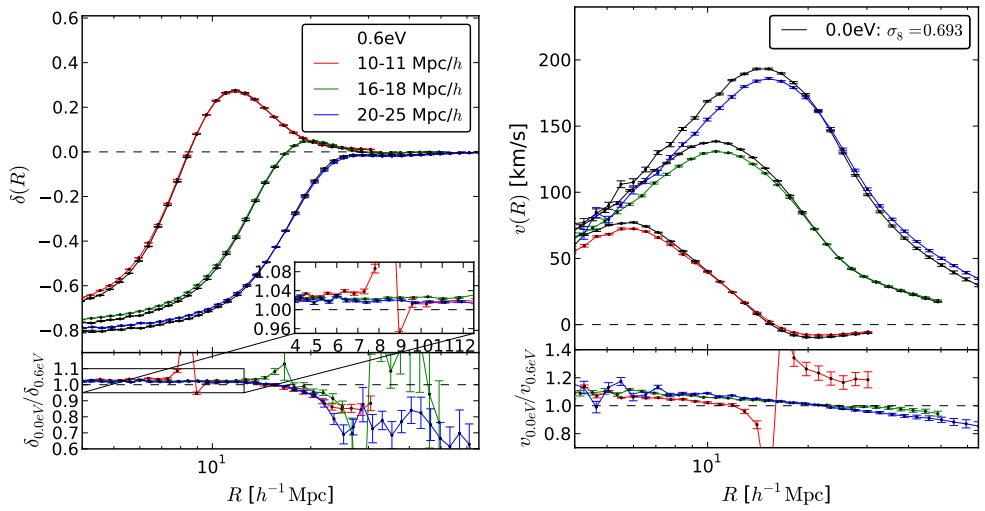

Figure 8.11: Left panel: matter density profile. Right panel: radial velocity profile. In both cases colored lines show the profiles for the $\sum m_\nu = 0.6$ eV cosmology, whereas black lines indicate ΛCDM cosmology with the same σ_8 of the massive neutrino case, when it is computed using the total matter density field. The bottom panels show the ratios between the results from the two cosmologies.

the CDM field (green line). In this case there are fewer small voids and this translates into a worse match with the massive neutrino cosmology, which reach the 5% for very small voids. On the other hand, the number density of big voids increases, mitigating the discrepancies at large $R_{\rm eff}$, which is here at the level of ∼30%.

We also perform the same analysis using the density and velocity profiles, focusing on the comparison between the $\sum m_\nu = 0.6$ eV cosmology and the massless case with same σ_8 computed from the total matter linear power spectrum. Figure 8.11 shows the density and velocity profiles of the matter field around voids selected in ranges of $R_{\rm eff}$. The colored lines show the results for the massive neutrino case and black lines indicate the massless one. The mismatch in the density profile is around 2-4% in the inner part of voids and it increases in the outer part, whereas for the velocity profiles it reaches the 10% in the void core.

For all considered observables, the results in $\sum m_\nu = 0.6$ eV cosmology cannot be reproduced in a ΛCDM cosmology with the same σ_8. This means that the Ω_ν-σ_8 degeneracy is broken. Our understanding is that voids, unlike halos, do not present this degeneracy because they are sensitive to different regions of the linear power spectrum. To be more precise, big voids should be influenced by scales in the $P(k)$ much larger than the ones important for halos. On these large scales, the amplitude in the $\sum m_\nu = 0.6$ eV case is higher than in the two considered massless neutrino cosmologies, and for instance more power corresponds to a higher number density of voids.

The study of statistical properties of voids tells that voids appear to be less evolved in massive neutrino cosmologies, and that this feature cannot be completely explained by the difference in σ_8, thus it is a signal due to the presence of massive neutrinos. This signal could be used to constraints the sum of neutrino masses.

Chapter 9

Voids in the galaxy distribution

It has to be noticed that matter is not (unfortunately) directly observable and usually we rely on large scale structure tracers like galaxies. The distortion in the shape of galaxies caused by the weak gravitational effect can be used to constrain cosmology. The weak lensing signal will depend on the total matter density distribution and it would be interesting to answer the following two questions: 1) what is the matter density profile of the voids identified in the galaxy field? 2) what is the extent to which massive neutrinos impact the reconstructed profile? Recently some work have been done to address the first questions (see for example [26, 61, 76]); here we focus on the second one. Therefore, in this section we present the analysis for voids identified in the galaxy distribution, which is obtained by post-processing N-body simulations. First, we explain how we populate halos with galaxies in order to generate a mock galaxy catalogue. Then we show the main results regarding the study of galaxy voids. Since the volume of our high-resolution simulations is relatively small and the number density of galaxy-voids is low, we cannot perform the analysis as for the voids in the cold dark matter field, studying all the void properties in different cosmologies. Therefore, we present only the number density of galaxy voids and the study of matter inside the identified galaxy voids. In particular, we show the matter density and velocity profiles around these objects.

9.1 Halo Occupation Distribution

In order to construct a mock galaxy catalog, we need to populate with galaxies the dark matter halos in N-body simulations. A commonly used tool is the so-called Halo Occupation Distribution (HOD) model. In this framework, the distribution of galaxies with respect to dark matter halos is described by a few parameters that can be calibrated in order to reproduce some particular features of the observed galaxy population. Here we calibrate the HOD parameters to reproduce the number density and the two-point clustering statistics of galaxies in the main sample of the Sloan Digital Sky Survey (SDSS) II Data Release 7 [129].

The HOD model requires two ingredients: 1) the probability distribution $p(N|M)$ of having N galaxies inside a halo of mass M and 2) the way in which galaxies positions and velocities are related to the underlying matter particles. In our HOD model the first ingredient is described by three parameters: $M_{\rm min}$, α and M_1. We assume that halos

$\sum m_\nu$ (eV)	M_1 $(M_\odot/h)$	α	$M_{\rm min}$ $(M_\odot/h)$
0.0	1.22×10^{14}	1.38	4.92×10^{12}
0.15	1.17×10^{14}	1.38	4.79×10^{12}
0.3	1.18×10^{14}	1.48	4.50×10^{12}
0.6	9.86×10^{13}	1.46	4.16×10^{12}

Table 9.1: Values of the HOD parameters, for four different cosmologies and for galaxies with magnitudes $M_r - 5\log_{10} h = -21.0$.

with masses below $M_{\rm min}$ do not host any galaxies, whereas halos with masses above $M_{\rm min}$ host one central galaxy and a number of satellite galaxies following a Poissonian distribution with a mean equal to $(M/M_1)^\alpha$. We use the following equations:

$$\langle N_c|M\rangle = \begin{cases} 1 & \text{if } M \geq M_{\rm min} \\ 0 & \text{if } M < M_{\rm min} \end{cases} \qquad \langle N_s|M\rangle = \begin{cases} (M/M_1)^\alpha & \text{if } M \geq M_{\rm min} \\ 0 & \text{if } M < M_{\rm min}\,. \end{cases} \tag{9.1}$$

Our second HOD ingredient states that the central galaxy sits in the center of the corresponding halo and that the distribution and velocity of the satellites follow exactly the ones of the underlying cold dark matter particles inside the halo. This means that the galaxy bias and the velocity bias with respect to the cold dark matter field are both equal to 1. The values of the HOD parameters obtained for galaxies with magnitudes $M_r - 5\log_{10} h = -21.0$ in the four different cosmologies are shown in table 9.1.

We focus our study at redshift $z = 0$, where there are good measurements of the clustering of different galaxy populations. Now that we have created a mock galaxy catalog for each cosmology, we can run the void-finder VIDE on top of the galaxy field and identify the galaxy voids.

9.2 Number density

For each cosmology we compute the number of galaxy voids as a function of their size $R_{\rm eff}$ and we show the results in Fig. 9.1. On the upper panel we plot the cumulative number of galaxy voids normalized by the total number and the associated errors, which are computed using error propagation and assuming a Poisson distribution in $R_{\rm eff}$ for the galaxy voids. Different colors indicate different cosmologies. On the bottom panel we display the ratio between the results for the massive neutrino cosmologies and the ones for the ΛCDM model. We can notice some differences among the cosmologies only for voids with $R_{\rm eff} > 30$ Mpc$/h$, where anyway the errors are very large. Moreover, it is interesting to notice that the size of the voids identified in the galaxy field are larger than the ones found in the cold dark matter field. This is just a consequence of the number density of the tracers used to identify voids: a smaller value for the number density of tracers brings to larger voids.

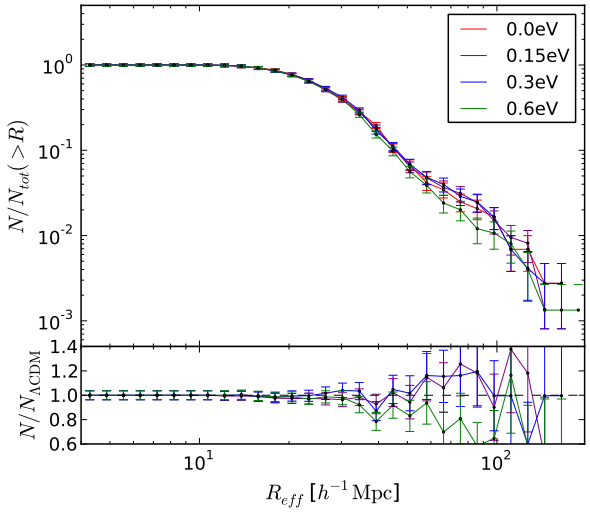

Figure 9.1: Cumulative fraction of galaxy voids at $z = 0$. The top panel shows results from different cosmologies: red line is the ΛCDM cosmology, and purple, blue and green lines correspond to 0.15, 0.3 and 0.6 eV cosmologies. The bottom panel shows the ratio between the same quantity in a massive and a massless neutrino cosmologies.

9.3 Density profile

Here we compute the total (cold dark matter + neutrinos) matter density profile in the identified galaxy voids, once they are divided into four groups, depending on their effective radius: $R_{\rm eff}$=20-25, 25-30, 30-35, 40-45 Mpc/h. Figure 9.2 shows the profiles (top panel of each plot) only for 0.0 eV and 0.6 eV cosmologies, while the residuals between massive and massless cases (bottom panel of each plot) for all the massive neutrino cosmologies are displayed. As in the previous section, the vertical dashed lines indicate the effective radius and two times the same quantity.

We immediately notice that the matter profile here, in galaxy voids, is very different from the one around voids identified in the cold dark matter field (see figure 8.5). First of all, galaxy voids are less empty. Secondly, there is a compensated wall even around very large voids. These differences are due to the fact that galaxy voids incorporate within them many small cold dark matter voids, together with small halos and filaments. Their edge presents an overdensity in the galaxy field, which can sit only in very big overdensities in the cold dark matter field. In other words, this should be due to the galaxy bias b [75]. If we assume that voids are patches where the enclosed number density contrast of the tracers is equal to a certain threshold $\delta_t = -0.8$, and that the tracers are galaxies with a density field $\delta_g = b\,\delta_m$ biased with respect to the matter field, then the corresponding enclosed matter density will be $\delta_m = \delta_t/b$. If the galaxy bias is $b \sim 2$, the enclosed matter density will be 2 times denser then the galaxy one.

Focusing on the comparison among cosmologies, we can notice the same trend as in the cold dark matter voids: the matter profiles of ΛCDM are emptier and they present a higher wall. However, here the small galaxy void statistics makes this trend less clear. Moreover, the differences among ΛCDM and massive neutrinos cosmologies are more noisy, but not less pronounced. In small voids there are smaller differences, whereas in large voids the differences are of the order of 10-20% in the inner part of voids and for

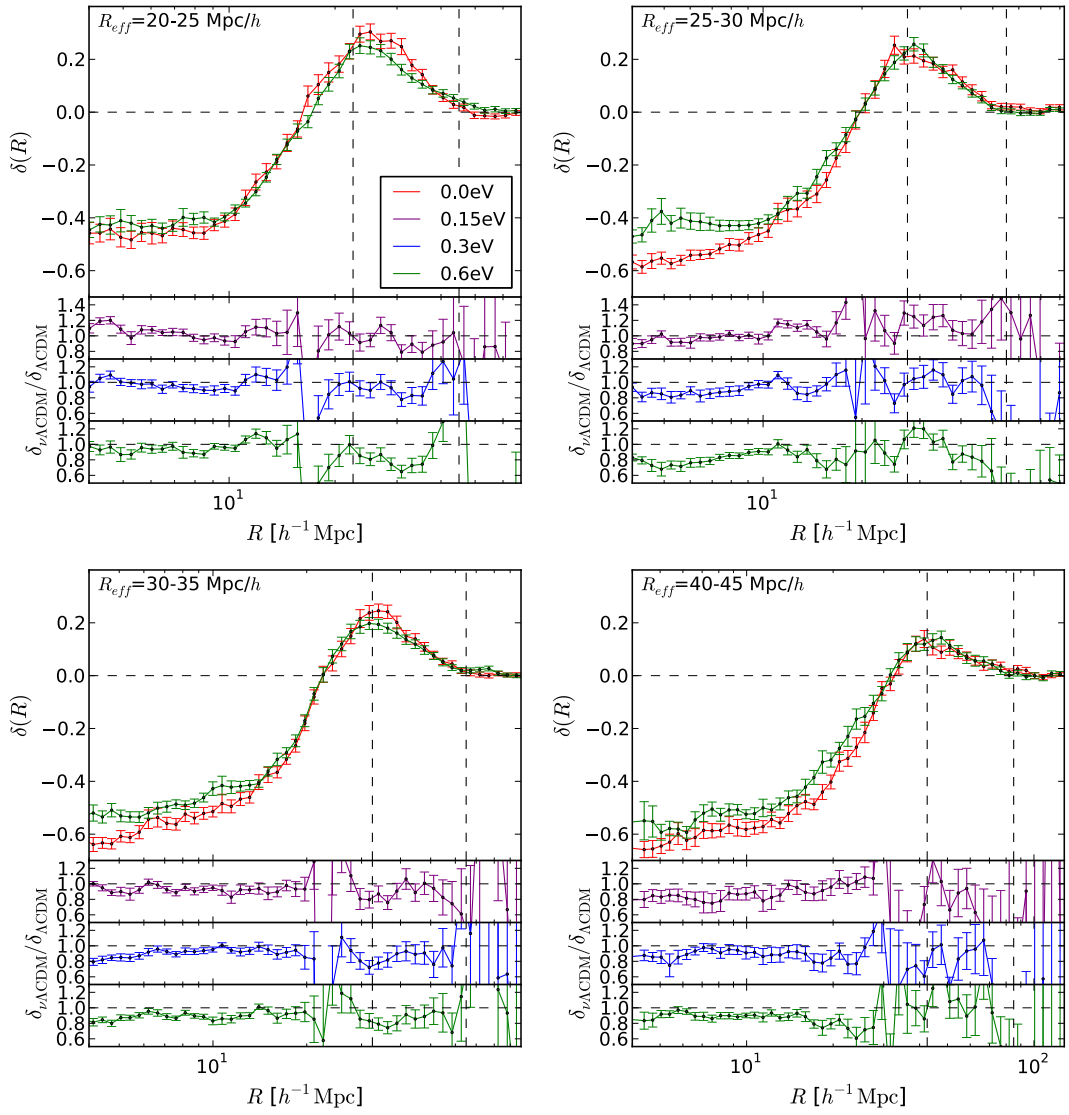

Figure 9.2: Density profile of the total matter field (cdm + neutrinos) around galaxy voids with different sizes: $R_{\rm eff} = 20-25$ Mpc/h (top-left), $R_{\rm eff} = 25-30$ Mpc/h (top-right), $R_{\rm eff} = 30-35$ Mpc/h (bottom-left), and $R_{\rm eff} = 40-45$ Mpc/h (bottom-right). In each plot, the main panel shows the result for the 0.0 eV (red) and the 0.6 eV (green) cosmologies. The bottom panels display the ratios between the results from the massive neutrino cosmologies (0.6 eV but also 0.15 eV in purple and 0.3 eV in blue) to the ΛCDM one. The vertical dashed black lines indicate the mean value of the void radii in the selected range and two times the same quantity.

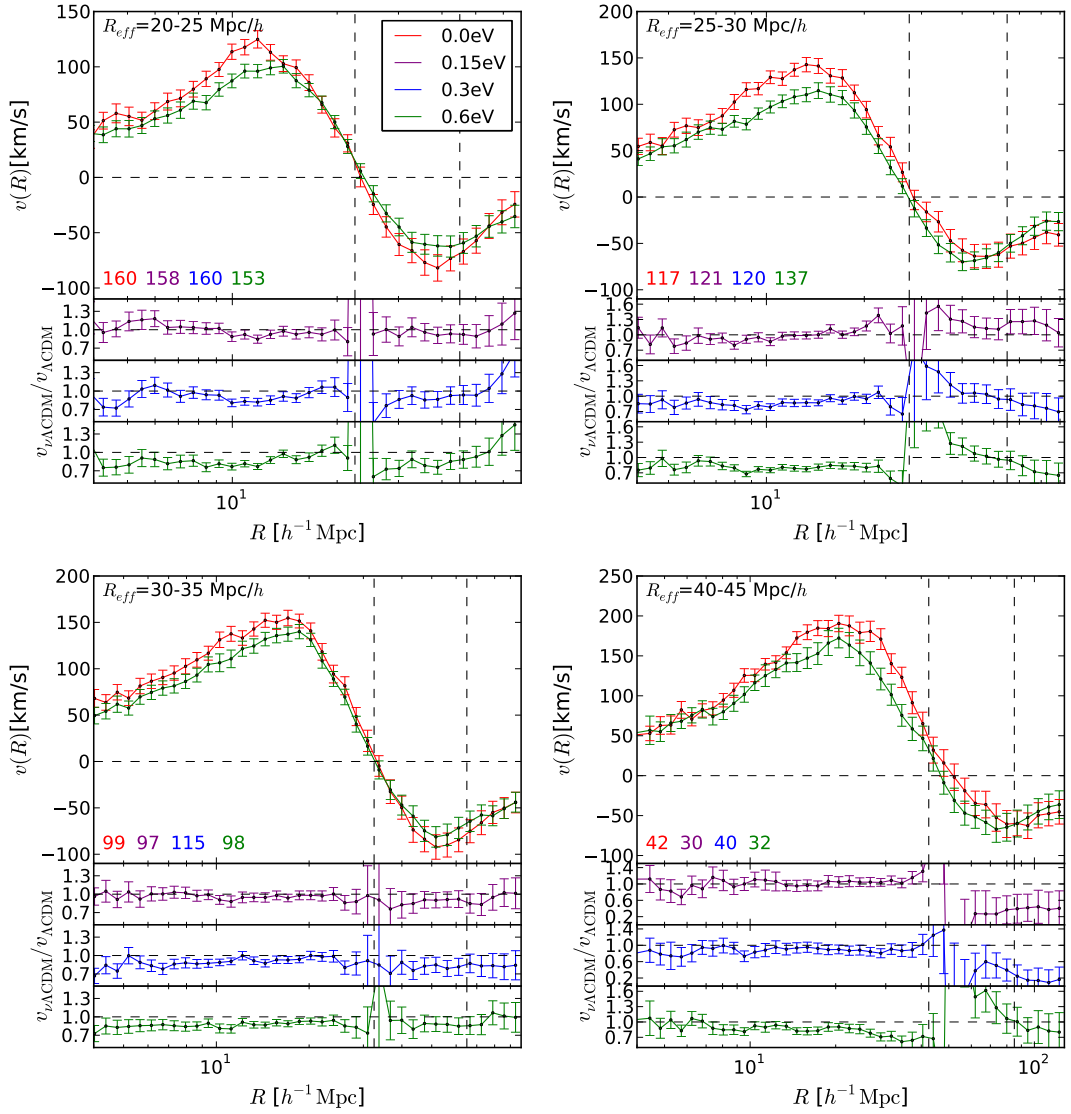

Figure 9.3: Radial velocity profile of the total matter field (cdm + neutrinos) around galaxy voids with different sizes: $R_{\rm eff} = 20 - 25$ Mpc/h (top-left), $R_{\rm eff} = 25 - 30$ Mpc/h (top-right), $R_{\rm eff} = 30 - 35$ Mpc/h (bottom-left), and $R_{\rm eff} = 40 - 45$ Mpc/h (bottom-right). In each plot, the main panel shows the results for the 0.0 eV (red) and the 0.6 eV (green) cosmologies. The bottom panels display the ratios between the results from the massive neutrino cosmologies (0.6 eV but also 0.15 eV in purple and 0.3 eV in blue) to the ΛCDM one. The vertical dashed black lines indicate the mean value of the void radii in the selected range and two times the same quantity, whereas the colored numbers indicate the number of stack voids in each simulation.

all the massive neutrino cosmologies; the discrepancies are less pronounced near the compensated wall.

9.4 Velocity profile

We present here the analysis for the velocity profile of matter around galaxy voids. We select the galaxy voids in the same size ranges as for the density profile. We compute

the radial velocity of matter as a density weighted average between the velocity profiles of cold dark matter and neutrino fields, as shown in Eq.(8.2). The associated errors are computed via error propagation, using the dispersion around the mean values of density and velocity profiles of cold dark matter and neutrinos obtained from the stack of the selected voids in the simulation.

The results are shown in Fig. 9.3. Again we plot the profiles for ΛCDM and 0.6 eV cosmologies only, but we present the residuals with respect to ΛCDM for all the massive neutrino cosmologies considered in this paper. The main feature to notice is the particular shape of the profiles. They are positive in the inner part of the galaxy voids, they reach zero around the effective radius and they are negative outside. Even the profiles around very big voids share the same shape, contrary to what happens in cold dark matter voids (see figure 8.8). It seems that in these regions the cold dark matter is building a wall near the effective radius, with the additional effect of shrinking the underdensity.

If we compare the cosmologies we notice that inside galaxy voids the velocity is higher in ΛCDM, whereas in outer regions the trend is not unique for all the void sizes. However, for most of the cases, the massive neutrino cosmologies have slower motion towards the center of the galaxy voids.

Part IV

Void profiles

Introduction

The abundance and spatial distribution of structures of the cosmic web depend on the nature of the initial conditions, the expansion history of the universe, and the nature of gravity. For what regards halos, predictive models of this dependence have three parts. The first is a description of the gravitational physics of halo formation; the second incorporates this into a statistical treatment aimed at predicting halo abundances; and the third extends this treatment to also describe the spatial distribution of these objects.

The statistical model for the abundances typically identifies those proto-halo patches in the initial conditions which are destined to become halos. The symmetry between over and under-densities of an initially Gaussian random field means that one can use essentially the same procedure to predict the abundance of large voids as is typically used for predicting halo abundances. This procedure also predicts the spatial distribution of the initial patches which are destined to become voids and halos. Proto-halos and proto-voids are predicted to be biased with respect to the full dark matter fluctuation field, and, except for a sign change (proto-halos are more abundant in initially over-dense regions, proto-voids in initially underdense regions), these predictions are qualitatively the same. However, subsequent nonlinear gravitational evolution removes this symmetry.

Since the abundances are predicted from the initial Lagrangian field, whereas the spatial distribution of the fully formed halos and voids is measured in the final evolved Eulerian field, the description of the spatial distribution is done in two steps: the first describes how the spatial distribution of the initial patches is biased with respect to the initial fluctuation field (Lagrangian bias), and the second describes how this bias is modified when the evolved halo distribution is compared to the evolved matter field (Eulerian bias).

The excursion set approach or the peaks theory are usually used to predict the abundance and spatial distribution of nonlinear objects from the initial Lagrangian fluctuation field. In Chapter 10 we show that they also predict the initial density profiles around proto-halo and proto-void patches: indeed, there is a sense in which the halo mass function can be thought of as the generating function of the distribution of profiles at fixed mass. In Chapter 11 we study the evolution of void profiles and linear bias.

Chapter 10

Density profiles in Lagrangian space

This chapter presents the study of density profiles around Lagrangian regions, identified as places where halos or voids will form.

10.1 Over-densities

In literature, the abundance and clustering models have been mainly studied for overdense regions. In this section we consider a sequence of ever more sophisticated models and present how they can be used to compute also density profiles around Lagrangian patches, focusing on overdensities since they are the more familiar case. It will be interesting to notice similarities and differences arising when the same models are applied to underdensities, in Section 10.2. We also discuss the linear halo bias in Lagrangian space, whose form depend on the model for halo formation. The linear bias is usually thought to be the term of proportionality between the halo density field and the matter field and to depend on halo mass only, but in general it is scale dependent. Thus, it is convenient to think at the bias in a different way. We call bias term each scale independent factor of proportionality between the halo density field and the matter density field, eventually multiplied by a scale dependent term. Every constraint used in the definition of a protohalo generates a linear halo bias term.

10.1.1 Overdense patches in the initial conditions

The quantity of interest is the averaged enclosed density profile around proto-halos of size R_p, e.g., in the simplest plausible model for halo formation, around positions which are denser than $\delta_{\rm sc}$ when smoothed on scale R_p (the subscript 'sc' denotes the critical quantity for the 'spherical collapse' to happen, as in Chapter 1). Let δ_j denotes the overdensity when smoothed on scale R_j. This profile is nothing but the cross-correlation between the overdensity δ_q on scale R_q (the proto-halo) and δ_p on the scale $R_p \neq R_q$ (the smoothed matter field), when it is known that $\delta_p \geq \delta_{\rm sc}$, and it is given by

$$\langle \delta_q | \delta_p \geq \delta_{\rm sc} \rangle = \int_{\delta_{\rm sc}}^{\infty} {\rm d}\delta_p \, p(\delta_p) \, \frac{\langle \delta_q | \delta_p \rangle}{p(\delta_p \geq \delta_{\rm sc})} \, . \tag{10.1}$$

Since

$$\langle \delta_q | \delta_p \rangle \equiv \frac{s_0^{pq}}{s_0^{pp}}\, \delta_p\,, \tag{10.2}$$

where $s_j^{RR'}$ is defined in Eq. (1.16), we have that

$$\langle \delta_q | \delta_p \geq \delta_{\rm sc} \rangle = b_{\rm L}(\nu)\, \frac{s_0^{pq}}{s_0^{pp}}, \tag{10.3}$$

with

$$\nu \equiv \delta_{\rm sc}/\sqrt{s_0^{pp}} \tag{10.4}$$

and

$$b_{\rm L}(\nu) \equiv \frac{\nu}{\delta_{\rm sc}}\, \frac{{\rm e}^{-\nu^2/2}/\sqrt{2\pi}}{{\rm erfc}(\nu/\sqrt{2})/2}. \tag{10.5}$$

Evidently, the cross-correlation between the positions identified as being sufficiently overdense on scale R_p and the field smoothed on scale R_q is linearly proportional to the cross-correlation of the field itself when smoothed on the two scales R_p and R_q. Frusciante and Sheth [46] show that this is a generic feature of local Lagrangian bias models such as this one. The constant of proportionality defines the linear bias factor, which is a complicated function of the threshold but is otherwise just a number which is independent of the scale R_q.

The considered model of protohalos of size R_p identifies them with initial patches having $\delta_p \geq \delta_{\rm sc}$. Since $b_{\rm L}$ is always positive for regions above some threshold $\delta_{\rm sc} \geq 0$, tending to $\sqrt{2/\pi}/s_0^{pp}$ as $\nu \to 0$ and to $\nu^2/\delta_{\rm sc}$ as $\nu \to \infty$, the analysis above shows that one then expects there to be a lower limit to $b_{\rm L}$ of protohalo patches. We argue in the next section that although this is too simplistic a model to be realistic, this behaviour – a lower limit to $b_{\rm L}$ – is generic.

There are two ways in which this overdense patch model is particularly simple. First, $b_{\rm L}$ does not change sign. And second, although the bias factor is a complicated function of ν, for a given ν it is just a constant, independent of scale R_q and/or wavevector k. To see this, Fourier transform both sides of Eq. (10.3), and note that the Fourier transform of the left hand side must be proportional to $W(kR_q)$, since it involved smoothing of δ_q on scale R_q. If we write it as $P_{pm}(k)\, W(kR_q)$, where the subscript pm indicates that this is the power spectrum associated with the cross correlation between the subset of positions p that are above threshold on scale R_p and the overdensity which surrounds them on scale R_q, then

$$P_{pm}(k)\, W(kR_q) = b_{\rm L}(\nu)\, P_{\rm L}(k)\, W(kR_p)\, W(kR_q). \tag{10.6}$$

Here, all scale dependence comes from the smoothing filters: the bias factor $b_{\rm L}$ is just a k-independent number.

Finally, note that the expressions above indicate that this profile always has the same sign as s_0^{pq}; if s_0^{pq} crosses zero on some scale R_0, then the average profile does as well.

10.1.2 The excursion set approach: Correlated steps and the upcrossing approximation

The next more realistic model of protohalos – the excursion set approach of [11] (see also Section 1.2.2) – adds the requirement that, in addition to $\delta(R_p) \geq \delta_{\rm sc}$, a

protohalo patch must have $\delta(R_q) \leq \delta_{\rm sc}$ for all $R_q > R_p$. A treatment which accounts more carefully for correlations between scales is tractable (and still rather accurate!) if one modifies the requirements that $\delta(R_q) \leq \delta_{\rm sc}$ for all $R_q > R_p$ to the simpler constraint $\mathcal{C}_p$ that $\delta(R_p + \Delta R) \leq \delta_{\rm sc}$ in addition to $\delta(R_p) \geq \delta_{\rm sc}$, which is the so called upcrossing approximation by [79] (see also Section 1.2.3). In this case, it turns out to be straightforward to generalize the treatment to the case in which the critical $\delta_{\rm sc}$ is not a constant, but depends on scale R_p. Indeed, halo formation is known to be affected by the surrounding shear field [13, 106]. A crude but effective model for this replaces the $\delta \geq \delta_{\rm sc}$ requirement with $\delta \geq \delta_{\rm sc}\,(1 + \sqrt{q^2/q_c^2})$ where q^2 is the traceless shear. Since $\langle q^2 \rangle \propto s_0^{pp}$, the effect of the shear is reasonably well approximated by requiring $\delta \geq \delta_{\rm sc}\,(1 + \sqrt{s_0^{pp}}/q_c)$ [80, 108], with $q_c \approx \sqrt{6}\delta_{\rm sc}$ [37, 104]. If we define $\beta \equiv \delta_{\rm sc}/q_c$ then this means that $\nu_p = \nu\,(1 + \beta/\nu)$, and is the physical motivation for considering models with non-zero β. If this critical density is $\delta_p = \delta_{\rm sc} + \beta\,\sqrt{s_0^{pp}}$, then the predicted cross-correlation between protohalo positions (i.e. those for which $\mathcal{C}_p$ is satisfied) and the density which surrounds them on scale R_q becomes

$$\langle \delta_q | \mathcal{C}_p \rangle = b_{10}(\nu)\, s_0^{pq} + b_{01}(\nu)\, 2 \frac{{\rm d}s_0^{pq}}{{\rm d}\ln s_0^{pp}}, \tag{10.7}$$

where

$$\delta_p\, b_{10}(\nu) + \delta_p\, b_{01}(\nu) = \frac{\delta_p^2}{s_0^{pp}} \equiv \nu_p^2 \tag{10.8}$$

and

$$\delta_{\rm sc} b_{01}(\nu) = \partial \ln G_1 / \partial \ln y|_{y=\gamma\nu} \tag{10.9}$$

with G_1 given by Eq. (1.83) with $F = 1$. (Note that it is δ_p in the first expression, but b_{10} and b_{01} are functions of ν rather than ν_p, so it is $\delta_{\rm sc}$ in the second. When $\beta = 0$ this difference does not matter, of course.) The linear bias term $b_{10}(\nu)$ comes from the constraint to be above the threshold $\delta_{\rm sc}$, while $b_{01}(\nu)$ is associated to the upcrossing requirement. When $\beta = 0$, the bias term $b_{10}(\nu)$ is given by Eq. (1.81), that we rewrite here:

$$\delta_{\rm sc} b_{10} = \nu^2 - 1 + \frac{{\rm e}^{-\Gamma^2\nu^2/2}/\sqrt{2\pi}\Gamma\nu}{{\rm erfc}(-\Gamma\nu/\sqrt{2})/2 + {\rm e}^{-\Gamma^2\nu^2/2}/\sqrt{2\pi}\Gamma\nu}, \tag{10.10}$$

where

$$\Gamma^2 \equiv \frac{\gamma_p^2}{1 - \gamma_p^2}, \quad \gamma_p^2 \equiv \frac{1}{4 s_0^{pp}\,\langle \delta_p' \delta_p' \rangle} \quad \text{and} \quad \delta_p' \equiv \frac{{\rm d}\delta_p}{{\rm d}s_0^{pp}}\,. \tag{10.11}$$

It is useful to rewrite Eq. (10.7) so that b_{01} does not appear explicitly:

$$\langle \delta_q | \mathcal{C}_p \rangle = \delta_p\, 2 \frac{{\rm d}s_0^{pq}}{{\rm d}s_0^{pp}} + b_{10}(\nu)\, s_0^{pq} \left(1 - 2 \frac{{\rm d}\ln s_0^{pq}}{{\rm d}\ln s_0^{pp}}\right). \tag{10.12}$$

We argue shortly that the second term is the usual linear bias term which dominates on large scales, whereas the first should be thought of as a shot-noise like term which is negligible when $R_q \gg R_p$.

In addition, Eq. (10.7) for the cross-correlation, enclosed density profile can be written in a more suggestive form, if we scale its height by its value at R_p. This makes

$$\frac{\langle \delta_q | \mathcal{C}_p \rangle}{\delta_p} = \frac{s_0^{pq}}{s_0^{pp}} \left[1 - \frac{\delta_p\, b_{01}(\nu)}{\nu_p^2} \left(1 - 2 \frac{{\rm d}\ln s_0^{pq}}{{\rm d}\ln s_0^{pp}}\right)\right]. \tag{10.13}$$

The term outside the square brackets on the right hand side has the same shape as the density run around random positions of height δ_p (e.g. compare equation 10.3); the term in square brackets is the correction which comes from the additional excursion set constraint $\mathcal{C}_p$.

In Eq. (10.12) and Eq. (10.13), the quantity $1 - 2\,\mathrm{d}\ln s_0^{pq}/\mathrm{d}\ln s_0^{pp}$ plays a key role. Since it tends to unity when $R_q \gg R_p$, both expressions indicates that $\langle\delta_q|\mathcal{C}_p\rangle \to b_{10}(\nu)\, s_0^{pq}$ in this limit. We can see explicitly this limit considering some specific power spectra and window functions.

For Gaussian filtering of power-law $P(k)$,

$$\frac{s_0^{pq}}{s_0^{pp}} = \left(\frac{2}{R_q^2/R_p^2+1}\right)^{(3+n)/2} \tag{10.14}$$

and

$$1 - 2\,\frac{\mathrm{d}\ln s_0^{pq}}{\mathrm{d}\ln s_0^{pp}} = \frac{(R_q/R_p)^2-1}{(R_q/R_p)^2+1}. \tag{10.15}$$

This means that Eq. (10.12) becomes

$$\frac{\langle\delta_q|\mathcal{C}_p\rangle}{\delta_p} = \left(\frac{2}{R_q^2/R_p^2+1}\right)^{\frac{5+n}{2}} + \frac{b_{10}(\nu)}{\delta_p/s_0^{pq}}\left(\frac{1-(R_p/R_q)^2}{1+(R_p/R_q)^2}\right). \tag{10.16}$$

This shows that when $R_q \gg R_p$ then the '1-halo' term, the first term on the right hand side, falls as $(R_q/R_p)^{-5-n}$; the second term only falls as $(R_q/R_p)^{-3-n}$, so it dominates on large scales.

For a top-hat, these quantities depend on $P(k)$; for $P(k) \propto k^{-2}$,

$$\frac{s_0^{pq}}{s_0^{pp}} = \begin{cases} \frac{5-(R_p/R_q)^2}{4(R_q/R_p)} & \text{if } R_q/R_p \geq 1 \\ \frac{5-(R_q/R_p)^2}{4} & \text{if } R_q/R_p < 1 \end{cases}, \tag{10.17}$$

making

$$1 - 2\frac{\mathrm{d}\ln s_0^{pq}}{\mathrm{d}\ln s_0^{pp}} = \begin{cases} \frac{(R_q/R_p)^2-1}{(R_q/R_p)^2-1/5} & \text{if } R_q/R_p \geq 1 \\ \frac{(R_q/R_p)^2-1}{1-(R_q/R_p)^2/5} & \text{if } R_q/R_p < 1 \end{cases}, \tag{10.18}$$

and so

$$\frac{s_0^{pq}}{s_0^{pp}}\left(1 - 2\frac{\mathrm{d}\ln s_0^{pq}}{\mathrm{d}\ln s_0^{pp}}\right) = \begin{cases} \frac{1-(R_p/R_q)^2}{(4/5)(R_q/R_p)} & \text{if } R_q/R_p \geq 1 \\ \frac{(R_q/R_p)^2-1}{4/5} & \text{if } R_q/R_p < 1 \end{cases}. \tag{10.19}$$

This has some intuitive appeal, since a little algebra shows that

$$\langle\delta_q|\mathcal{C}_p\rangle = \delta_p\left(\frac{R_p}{R_q}\right)^3 + \frac{5}{4}\,s_0^{qq}\,b_{10}\left(1-\frac{R_p^2}{R_q^2}\right) \text{ if } R_q/R_p \geq 1; \tag{10.20}$$

if we think of the left hand side as a cross-correlation function, then the first term on the right hand side is the one-halo term – the contribution from the fact that the enclosed overdensity within R_p is δ_p – so it matters little on large scales where $R_q \gg R_p$. The factor of 5/4 is the $R_q \gg R_p$ limit of s_0^{pq}/s_0^{qq}, so the second term, which represents the two-halo contribution, gives the scale-dependence of the linear bias factor, and goes to zero when $R_q \to R_p$.

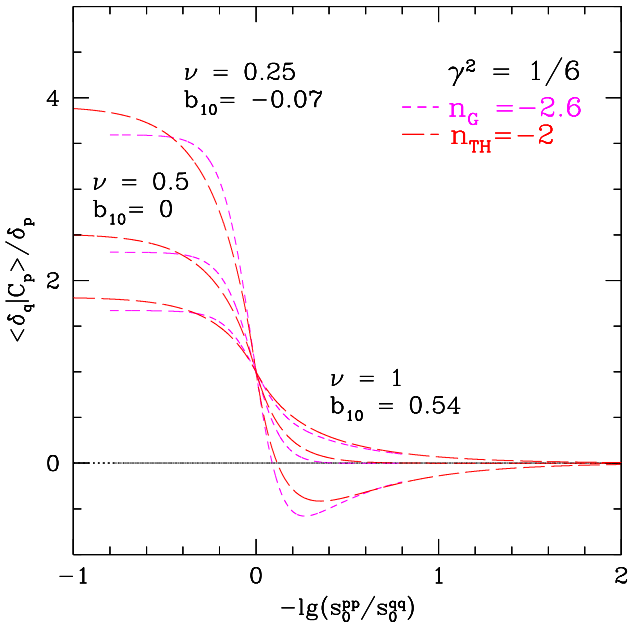

Figure 10.1: Mean enclosed density profiles around protohalos identified by the excursion set approach, shown in scaled units. The predicted profile depends on the scaled overdensity $\nu^2 = \delta_p^2/s_0^{pp}$ of the object, for which we show three values, and the correlation structure of the field, parametrized by Γ, which is determined by the shape of the power spectrum and the form of the smoothing window. We show results for Gaussian and top-hat smoothing of $P(k) \propto k^n$, where n was chosen so that the windows have $\Gamma^2 = 1/5$. Since the large scale bias b_{10} depends on Γ and ν only, it is the same for both filters. However, since n is different for the two filters, the profiles look rather different when shown as a function of R_q/R_p; expressing the scales in terms of s_0^{pp}/s_0^{qq} removes much of this dependence and illustrates that b_{10} is indeed the same for the two filters. It also shows that protohalo patches with smaller ν are predicted to have steeper profiles.

Indeed, the presence of the term proportional to b_{01} indicates that the bias factor becomes k-dependent [79]. E.g., for a Gaussian smoothing filter Eq. (10.7) becomes

$$\langle \delta_q | \mathcal{C}_p \rangle = b_{10}(\nu)\, s_0^{pq} + b_{01}(\nu)\, \frac{s_0^{pp}}{s_1^{pp}}\, s_1^{pq}\,, \tag{10.21}$$

so that the linear bias in Fourier space is

$$b_{\rm L}(\nu) = \frac{P_{pm}(k)}{P_{\rm L}(k) W(kR_p)} = b_{10}(\nu) + b_{01}(\nu)\, \frac{s_0^{pp}}{s_1^{pp}}\, k^2. \tag{10.22}$$

This shows explicitly that $b_{\rm L} \to b_{10}$ as $k \to 0$. For top-hat smoothing, the k-dependence is more complicated, because $\mathrm{d}s_0^{pq}/\mathrm{d}\ln R_p = -3\, j_2(kR_p)$, so the k dependence comes from $-(kR_p) j_2(kR_p)/j_1(kR_p) \approx (kR_p)^2/5 + (kR_p)^4/175$. Therefore it also has $b_{\rm L} \to b_{10}$ as $k \to 0$, with the leading order correction proportional to k^2. In general, the Fourier transform of Eq. (10.7) is

$$\langle \delta_q | \mathcal{C}_p \rangle = \left[b_{10}(\nu)\, W(kR_p) + b_{01}(\nu)\, 2\, \frac{d\, W(kR_p)}{d \ln s_0^{pp}} \right] P_{\rm L}(k) W(kR_q)\,, \tag{10.23}$$

so the linear bias is

$$b_{\rm L}(\nu) = \frac{P_{pm}(k)}{P_{\rm L}(k) W(kR_p)} = b_{10}(\nu) + b_{01}(\nu)\, 2\, \frac{d \ln W(kR_p)}{d \ln s_0^{pp}}\,. \tag{10.24}$$

As a result, the limiting values of b_{10} remain interesting. Since b_{10} is never smaller than about $-1/2\delta_{\rm sc}$, this model also has a lower limit to $b_{\rm L}$. However, it is more interesting than the one in the previous section, both because $b_{\rm L}$ can change sign and because it is k-dependent. Since it too predicts objects with $b_{10} < 0$, their density profiles must pass through zero even if the correlation function of all matter does not. In this case, however, the potential for zero-crossing is more obvious, since $b_{\rm L}$ is k-dependent. Indeed, Figure 4 and related discussion in [79] shows that, because of this k-dependence, one need not be as careful about the probability distribution of δ_q on scales $R_q > R_p$ as when the smoothing filter was sharp in k-space: the naive approach in which it is approximated by a Gaussian is rather accurate.

Figure 10.1 compares the predicted profiles around excursion set patches, defined using Gaussian and top-hat smoothing filters, for a range of choices of ν. Since $\delta_{\rm sc}$ is fixed, different values of ν correspond to different R_p. As a result, when shown as a function of R_q, the dependence on ν appears large. Much of this dependence is removed if we express all scales in units of R_p and all overdensities in units of δ_p, as in Eq. (10.13). As Eq. (10.13) shows, this rescaled profile is primarily a function of one parameter: $\delta_p b_{10}$ although there is a small additional dependence on the shape of $P(k)$ and the smoothing filter. This is why we actually plot $\langle \delta_q | \mathcal{C}_p \rangle / \delta_p$.

To identify generic results which do not depend on the form of the smoothing filter, we show results for Gaussian and top-hat windows applied to $P(k) \propto k^n$, where n was chosen so that the Gaussian and top-hat windows have $\Gamma^2 = 1/5$. Since, for a given ν, the large scale bias b_{10} depends only on Γ, it is the same for both filters. However, since n is different for the two filters ($n = -2.6$ and -2 for the Gaussian and top-hat respectively), the profiles look rather different when shown as a function of R_q/R_p. We have instead expressed the scales in terms of $s_0^{pp}/s_0^{qq} = (R_q/R_p)^{n+3}$ (recall that

because γ is the same for the two filters, n is different); clearly, this removes much of the dependence on the filter. Now it is easy to see that b_{10} is indeed the same for the two filters. When scaled in this way, the Figure also clearly illustrates that protohalo patches with smaller ν are predicted to have steeper profiles. This same trend is true of evolved halos: [82] show that less massive halos, which evolved from protohalo patches having smaller ν, are more concentrated. That this trend is built-in to the initial conditions is a point first made in [103]. We show in the next section that nonlinear evolution does not erase this trend.

Strictly speaking, discussions of evolved halos almost always involve the profile at R_q rather than the profile within R_q, although, as we show below, it is the profile within R_q which determines the evolution. This corresponds to replacing $W(kR_q) \to j_0(kR_q)$ in the integral which defines s_0^{pq}, but does not change the predicted trend with ν. For top-hat smoothing of $P(k) \propto k^{-2}$ the result is analytic, and adds strong support for interpreting the two terms on the right hand side of Eq. (10.12) as the one- and two-halo contributions to the signal. In this case the overdensity in the shell of radius R_q is

$$\frac{\langle \delta_q | \mathcal{C}_p \rangle}{\delta_p} = \frac{5}{2}\left(1 - \frac{R_q^2}{R_p^2}\right) + \frac{\delta_p\, b_{10}}{\nu_p^2}\frac{5}{4}\left(\frac{5R_q^2}{3R_p^2} - 1\right) \tag{10.25}$$

if R_q is smaller than R_p, whereas it is

$$\langle \delta_q | \mathcal{C}_p \rangle = b_{10}\, \xi(R_q) \tag{10.26}$$

when R_q is larger than R_p. Evidently, for this case, there is no scale dependence to bias, except for the sharp cutoff due to exclusion on scales smaller than R_p. I.e., the second term in Eq. (10.20) is the simplest possible two-halo term: it is just $(3/R_q^3)\int_{R_p}^{R_q} \mathrm{d}r\, r^2\, b_{10}\, \xi(r)$, upon noting that $\xi(R_q) = 5s_0^{qq}/6$.

10.1.3 Zero-crossing at small ν

If there is a zero crossing of the enclosed density profile, then it happens on that R_0 where

$$\frac{\nu_p^2}{\delta_p\, b_{01}(\nu)} = 1 - 2\frac{\mathrm{d}\ln s_0^{pq}}{\mathrm{d}\ln s_0^{pp}}. \tag{10.27}$$

For Gaussian smoothing of power-law $P(k)$, the zero-crossing scale R_0 satisfies

$$\frac{\delta_p\, b_{10}(\nu)}{\nu_p^2} = 1 - \frac{\delta_p\, b_{01}(\nu)}{\nu_p^2} = \frac{2}{1 - (R_0/R_p)^2}, \tag{10.28}$$

showing that $R_0 \geq R_p$ requires $b_{10} \leq 0$. Notice that $b_{10} = 0$ has $R_0 \gg R_p$, but that as b_{10} becomes more negative R_0 approaches R_p. Top-hat smoothing is similar. For $P(k) \propto k^{-2}$,

$$\frac{\delta_p\, b_{10}}{\nu_p^2} = 1 - \frac{\delta_p\, b_{01}}{\nu_p^2} = \frac{4/5}{1 - (R_0/R_p)^2}. \tag{10.29}$$

This zero-crossing scale R_0 is potentially interesting, at least in the spherical collapse approximation to the full dynamics where the mapping between Lagrangian and evolved Eulerian space is

$$1 + \delta_{\rm E} = [1 - \delta_{\rm L}/\delta_{\rm sc}]^{-\delta_{\rm sc}} = (R_{\rm L}/R_{\rm E})^3\ . \tag{10.30}$$

This expression indicates that the zero-crossing scale is not changed by nonlinear gravitational evolution (in the spherical approximation). For $\delta_{\rm sc} > 0$, mass that is initially within R_0 flows towards the center, and mass that is beyond R_0 moves even further from it. Hence, halos which formed from protohalo patches having $b_{10} < 0$ may be a crude way to model the statistics of isolated clusters. The analysis above indicates that this corresponds to only counting objects with sufficiently small ν. A more sophisticated model would allow that fraction of larger ν values for which the profile falls sufficiently steeply, but this is beyond the scope of the present study.

10.1.4 Excursion set peaks

The excursion set peaks model is more elaborate still: in addition to $\delta(R_p) \geq \delta_{\rm sc}$ and $\delta(R_p + \Delta R) \leq \delta_{\rm sc}$, $\mathcal{C}_p$ includes the further requirement that $\delta(R_p)$ be a local maximum [13, 79, 90] (see also Section 1.3). In this case the linear bias $b_{\rm L}$ has the same structure as the previous section – meaning that Eq. (10.8) still applies – only the dependence of b_{10} on ν is different. This dependence is still given by Eq. (10.9), but now the peaks constraint means that $F(x)$ in G_n of Eq. (1.83) is given by Eq. (1.84):

$$\delta_c\, b_{10} \equiv -\frac{\partial \ln \nu f_{\rm ESP}(\nu)}{\partial \ln \nu} = \nu^2 + \nu\beta - \Gamma^2\nu^2 \left(\frac{G_2/G_1}{\gamma_p \nu} - 1\right) \tag{10.31}$$

At large $\nu \gg 1$, $G_1 \to \gamma\nu\, G_0$ and $G_2/G_0 - (G_1/G_0)^2$ is what β^{-1} in approximation (6.20) of [6] represents. Their (6.18) shows that their $\beta \to (1-\gamma_p^2)^{-1}$ when $\gamma_p\nu \gg 1$ so that

$$b_{\rm L} \to \frac{\nu^2 + \nu\beta}{\delta_c} \qquad \text{when} \quad \nu \gg 1. \tag{10.32}$$

There is a technical detail associated with the fact that, although for Gaussian filters the quantity γ_p in G_n is the same as that which appears in Eq. (10.11) for the excursion set approach, for top-hat filters the integrals which define γ_p in G_n diverge. We follow [91] in dealing with this by using

$$\gamma_p = s_1^{pp}/\sqrt{s_0^{pp} s_2^{pp}} \tag{10.33}$$

in G_n, but with a top-hat filter for R_p and a Gaussian filter of scale $R_p/\sqrt{5}$ in the integral which defines s_1^{pp}, two top-hats for s_0^{pp} and two Gaussians (each of scale $R_p/\sqrt{5}$) for s_2^{pp}. (This scaling by a factor of $\sqrt{5}$ arises because $\exp(-x^2/2) = 1 - x^2/2 + \ldots$ whereas $(3/x)j_1(x) = 1 - x^2/10 + \ldots$.) This means that, for the enclosed density profiles around peaks in a top-hat smoothed field, the term which multiplies $\delta_p\, b_{01}/\nu^2$ is simply that for a top-hat filter (because we use two top-hats for all s_0 integrals), whereas the value of $b_{01}(\nu)$ depends on the mixture of the two filters through its dependence on γ_p. This simplicity is useful since it is the top-hat smoothed field which may be most closely related to models of the evolution.

In addition, note that our excursion set peaks model for the profile has the same structure as equation (7.10) of [6], but with some important differences. Their expression returns the profile of the overdensity smoothed on scale R_p at a distance R_q from the peak center, rather than the enclosed density within R_q which matters for the dynamics. Therefore, their expression has $W(kR_q) \to W(kR_p)\, j_0(kR_q)$ in the integral

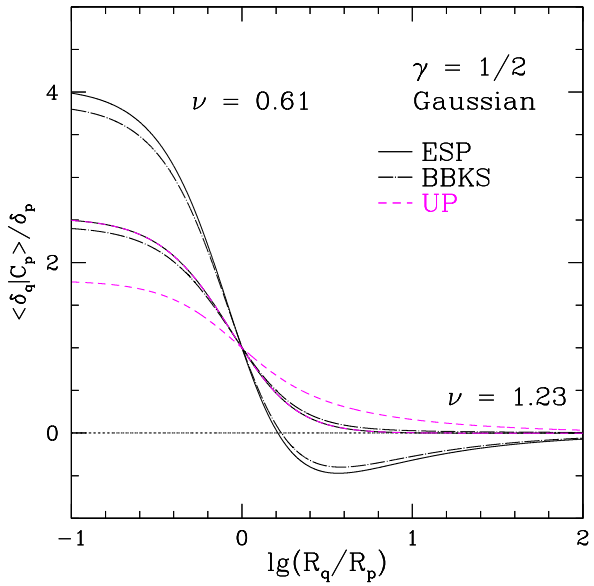

Figure 10.2: Mean enclosed density profiles (solid) around excursion set peaks in a Gaussian smoothed field having $P(k) \propto k^{-7/3}$ for a range of choices of peak height ν. Dot-dashed curves show the peak profile of [6] which ignores the upcrossing constraint, and short dashed curves come from requiring this, but dropping the peaks constraint (i.e. they show profiles for the same model as the previous figure). In all cases, lower peaks have steeper profiles, with the trend being most pronounced for ESP. The values $\nu = 1.23$ and 0.61 have $b_{10} = 0$ for the ESP and no-peak approaches, respectively.

which defines s_0^{pq}. In addition, because their peaks analysis did not include the excursion set constraint, their expression boils down to setting $\delta_{\rm sc} b_{01} = \partial \ln G_0 / \partial \ln y|_{y=\gamma\nu}$; in our expression it is G_1 which appears.

As a result, it is still true that $b_{\rm L} \to b_{10}$ as $k \to 0$ and, for ΛCDM, $\delta_{\rm sc}\, b_{10} > -1$ (see Figure 2 in [90]), meaning that b_{10} cannot be arbitrarily negative. And again, the k-dependence of the bias means that the enclosed density around excursion set peaks with $b_{10} < 0$ must cross zero. Figure 10.2 compares the predicted enclosed overdensity profiles around excursion set patches (short-dashed) and excursion set peaks (solid), defined using Gaussian smoothing filters, for a range of choices of ν. We have chosen $P(k) \propto k^{-7/3}$ since this gives $\gamma_p = 1/2$ for Gaussian smoothing, and this value is close to γ_p for ΛCDM $P(k)$. This value of γ_p is also interesting because mixed top-hat/Gaussian smoothing of $P(k) \propto k^{-2}$ (for which s_0^{pq} is given by Eq. (10.17), and the zero-crossing scale by Eq. (10.29)) has $\gamma_p \approx 0.48$, so $b_{10}(\nu)$ is almost the same as for the pure Gaussian case. Although we do not show it here, we have checked that the excursion set peaks prediction for this case is indeed very similar to that for the pure Gaussian case, when each is plotted as a function of its respective s_0^{pp}/s_0^{qq} (as we did for Figure 10.1). Note that the trend for smaller ν to have steeper profiles is even more pronounced for excursion set peaks.

To illustrate the importance of the excursion set constraint for peaks, the long dashed curves show equation (7.10) of [6], but with our s_0^{pq}/s_0^{pp} in place of their ψ (and the corresponding change for s_1^{pq}), since this includes the effects of the k^2-bias,

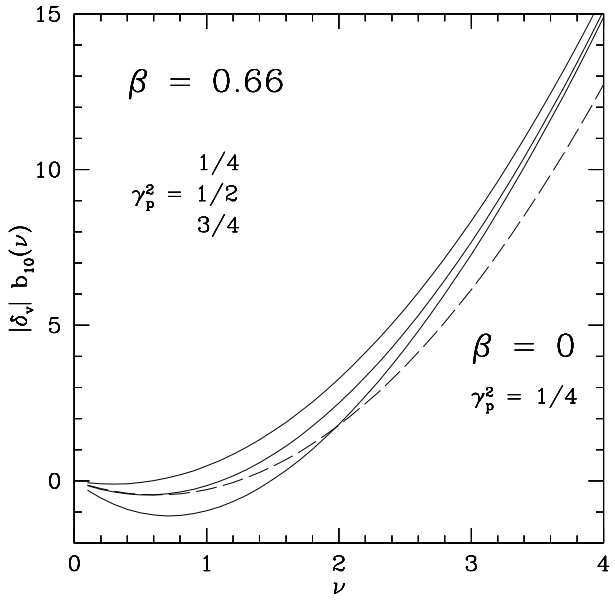

Figure 10.3: Large scale bias with respect to $-\delta_{\rm L}$ for excursion set troughs; the bias with respect to $+\delta_{\rm L}$ has the opposite sign. The bias is shown as a function of depth ν for a range of choices of the correlation parameter γ_p. Solid curves show predictions associated with triaxial troughs; the dashed curve shows the spherical evolution prediction for the value of γ_p which is close to that for ΛCDM.

but ignores the change to the bias factors because of the excursion set constraint. Our excursion set peaks (solid curves) have slightly steeper profiles. As a result, the threshold value of ν below which profiles cross zero is larger for ESP.

10.2 Under-densities

If the initial conditions were Gaussian, then the over/under dense symmetry of the initial fluctuation field means that regions above some threshold $\delta_c \geq 0$ are as abundant as regions below $\delta_v = -\delta_c$. The spatial distribution of these regions is also similar. Therefore, the corresponding threshold, upcrossing excursion set, and excursion set peaks models for protovoids are got by simply replacing $\delta_c \to \delta_v$, and $\delta_{\rm L} \to -\delta_{\rm L}$ in all the previous expressions. E.g., regions below some threshold $\delta_v < 0$ will have Eq. (10.5) for $b_{\rm L}$ but with $\delta_c \to \delta_v$ and $\nu \equiv |\delta_v|/\sqrt{s_0^{pp}}$. In this case, the predicted $b_{\rm L}$ is always negative for regions below some $\delta_v < 0$. I.e., underdense patches are positively biased with respect to $-\delta_{\rm L}$ so they are anti-biased with respect to the overdensity fluctuation field.

As for the protohalo patches which evolve into massive halos, a better estimate of the abundance of the largest voids can be got by taking the excursion set peaks formalism for estimating cluster abundances, and simply replacing δ_c with $|\delta_v|$. This yields equation (13) in [109] (which is our Eq. (1.86) for the excursion set peak mass function). As they discuss, the void-in-cloud problem means this is not the full story for smaller voids, but on the scales relevant to this paper (which we quantify shortly),

this additional complication is irrelevant [87]. Therefore, the excursion set troughs predictions for profiles around protovoids are the same as those for excursion set peaks, provided one sets $\delta_p = \delta_v$. Therefore, the density profiles around protovoids with $|\delta_v|\, b_{10} < 0$ will pass through zero.

We remarked earlier that halo formation is known to be affected by the surrounding shear field. Similarly, for voids, one might reasonably expect the shear to make $\delta \leq \delta_v\,(1 + \sqrt{q^2/q_c^2})$. This would make the critical threshold scale approximately as $\delta_v - (\sigma_0/\sqrt{6})(|\delta_v|/\delta_c)$. Inserting the values of δ_v and δ_c from before yields $-2.7 - 0.7\sigma_0$, which are not far off the measurements of protovoid patches in [3]. Thus, the predicted mass fraction in voids of size $R_{\rm E}$ is given by Eq. (1.86) with $\delta_v = -2.7$ in place of δ_c and $\beta = 0.7$, and the associated large scale linear bias factors are given by Eq. (10.8) and Eq. (10.9) with these same replacements,

$$\delta_v\, b_{10}(\nu) = -\frac{\partial \ln \nu f_{\rm ESV}(\nu)}{\partial \ln \nu} = \nu\,(\nu + \beta) - \delta_v\, b_{01}(\nu)\,, \tag{10.34}$$

$$\delta_v\, b_{01}(\nu) = \frac{\gamma_p^2 \nu^2}{1 - \gamma_p^2}\left(\frac{G_2/G_1}{\gamma_p \nu} - 1\right)\,. \tag{10.35}$$

Figure 10.3 shows how $|\delta_v|\, b_{10}$ depends on ν for a variety of choices of γ_p; mixed-top-hat smoothing for ΛCDM models has $\gamma_p \approx 1/2$. Note that $b_{\rm L}$ never exceeds $+1$ for excursion set troughs for the same reason that it is never less than -1 for excursion set peaks. However, $b_{\rm L} \to \nu^2/\delta_v \ll -1$ for large protovoid patches, because $\delta_v < 0$. I.e., large voids are very anti-biased with respect to the overdensity fluctuation field, $+\delta_{\rm L}$. Finally, it is worth remarking that, although b_{10} can change sign, $|\delta_p|\, b_{01} \geq 0$ for all ν.

Chapter 11

Density profiles in Eulerian space

While the enclose density profile of protohalos and protovoids can be measured in simulations, it is only the halos and voids themselves, rather than the patches in the initial conditions from which they formed, which are observable in the Universe. Therefore, what we really require is a prediction for the density profile of halos and voids in the late time gravitationally evolved space in which they are identified. Being a cross correlation, the density profile is sensitive to the Eulerian bias of the tracer with respect to the evolved density field. In this chapter we will discuss how to evolve the averaged enclosed density profile of biased tracers from the Lagrangian to the Eulerian space and the relation between the corresponding linear biases.

11.1 The spherical model evolution

We describe the prediction of the spherical model in Section 1.1.3 when used to evolve the Lagrangian profiles discussed in Chapter 11. We report here the main formula of the spherical evolution model

$$1+\delta_{\rm E}(z)=\left[1-\frac{(D_z/D_0)\delta_{\rm L}}{\delta_{\rm sc}}\right]^{-\delta_{\rm sc}}=\left(\frac{R_{\rm L}}{R_{\rm E}(z)}\right)^3\,, \tag{11.1}$$

which will be extensively used in this section. From the following analysis, two main differences between halos and voids appear. They are related to the linear bias and the possibility for a profile to experience shell-crossing.

11.1.1 The Eulerian bias

Consider the point process defined by the centers of masses of the protohalo or protovoid patches, and let $\delta_b^{\rm L}$ denote the overdensity fluctuation field when this point process is smoothed on a large scale. Similarly, let $\delta_b^{\rm E}$ denote the (smoothed) overdensity field of the corresponding halos or voids. Then the Lagrangian and Eulerian bias factors are defined by $\delta_b^{\rm L}=b_{\rm L}\,\delta_{\rm L}$ and $\delta_b^{\rm E}=b_{\rm E}\,\delta_{\rm E}$. Suppose that $V_{\rm E}$ and $\delta_{\rm E}$ are the Eulerian volume and density corresponding to the Lagrangian quantities V_0 and δ_0, describing a large scale cell. Then, the number of halos or voids of mass M in an Eulerian region of size $V_{\rm E}$ is

$$\delta_{\rm E}^b=\frac{\mathcal{N}(M|\delta_0,S_0)}{n(M)V_{\rm E}}-1\,, \tag{11.2}$$

where $n(M)$ is the mass function of objects with mass between M and $M + dM$, and $\mathcal{N}(M|\delta_0, S_0)$ is the averaged number of objects in a volume V_0. Using the spherical model prediction and in the limit of small overdensity $\delta_0 \ll 1$, the volumes in the two spaces are related by $V_0/V_{\rm E} = 1 + \delta_{\rm E}$. Now, in the spherical evolution model the halo/void overdensity is

$$1 + \delta_b^{\rm E} = (1 + \delta_{\rm E})\,[1 + b_{\rm L}\,\delta_{\rm L}(\delta_{\rm E})]\,. \tag{11.3}$$

Hence, because $\delta_{\rm L} \approx \delta_{\rm E}$ to leading order [29, 77],

$$b_{\rm E} = 1 + b_{\rm L}\,. \tag{11.4}$$

Although different models may make different predictions for $b_{\rm L}$, Eq. (11.4) which relates the Lagrangian and Eulerian linear bias factors is generic (e.g. [24]). In the next Section we derive the same expression using the Zel'dovich approximation.

Because of the $b_{\rm E} - b_{\rm L}$ relation in Eq. (11.4), there is a substantial difference between halos and voids in the evolved field. Eq. (11.4) indicates that the class of objects which have $b_{\rm L} = -1$ should have $b_{\rm E} = 0$ and should be unclustered on large scales. This is impossible for initially overdense patches, since the discussion in Chapter 10 indicates that $b_{\rm L} > -1$. In addition, we noted that protohalo peak patches and various fitting formulas for the bias of protohalos in simulations all have $b_{\rm L}$ greater than about $-1/2\delta_c$, so none of them can have $b_{\rm E} = 0$ either. However, because the bias of protovoids can be arbitrarily negative, voids for which

$$|\delta_v| = \nu\,\nu_p - \frac{\gamma_p^2\nu^2}{1-\gamma_p^2}\left(\frac{G_2/G_1}{\gamma_p\nu} - 1\right) \tag{11.5}$$

can indeed have $b_{\rm L} \approx -1$ and hence $b_{\rm E} \approx 0$. E.g., for $|\delta_v| = 2.7$ and $\gamma_p = 1/2$ the critical value of ν which satisfies Eq. (11.5) is $\nu_{-1} = (2.25, 1.85)$ for $\beta = (0, 0.66)$. This shows explicitly that nonlinear evolution removes the symmetry between initial over- and under-densities: although a special subset of voids can have $b_{\rm E} = 0$, clusters cannot.

The critical value ν_{-1} singles out protovoids of a particular initial size R_{-1}. Since these had $\delta_v\,(1 + 0.7/\nu_{-1})$ the question arises as to what Eulerian size they should be assigned. One might expect them to be at least

$$R_{\rm E} = R_{-1}\,(1 - \delta_v/\delta_c)^{\delta_c/3} = 1.7R_{-1} \tag{11.6}$$

in size, since using $\delta_v\,(1 + 0.7/\nu_{-1})$ instead would make the predicted $R_{\rm E} \approx 1.9R_{-1}$ (for $\nu_{-1} \approx 2$). The analysis above indicates that these ν_{-1} voids will have $b_{\rm E} = 0$. Mixed-Tophat/Gaussian smoothing of flat ΛCDM with $(\Omega_m, h, \sigma_8) = (0.3, 0.7, 0.9)$ has $\gamma_p \approx 0.5$ on scales of order $R_{\rm L} \approx 4h^{-1}$Mpc. The excursion set troughs model with $\beta = 0.66$ indicates that voids in such a model with $\nu_{-1} = 1.87$ and $R_{\rm E} \approx 1.8 \times 3.8h^{-1} \approx 7h^{-1}$Mpc will be unclustered.

11.1.2 The Eulerian profile

Halos and voids with sufficiently large ν, for which $b_{10}^{\rm L} > 0$ and $b_{10}^{\rm L} < 0$ respectively, present an enclosed density profile that never crosses zero. However, the enclosed overdensity of smaller troughs or peaks can change sign. For such objects there is a zero

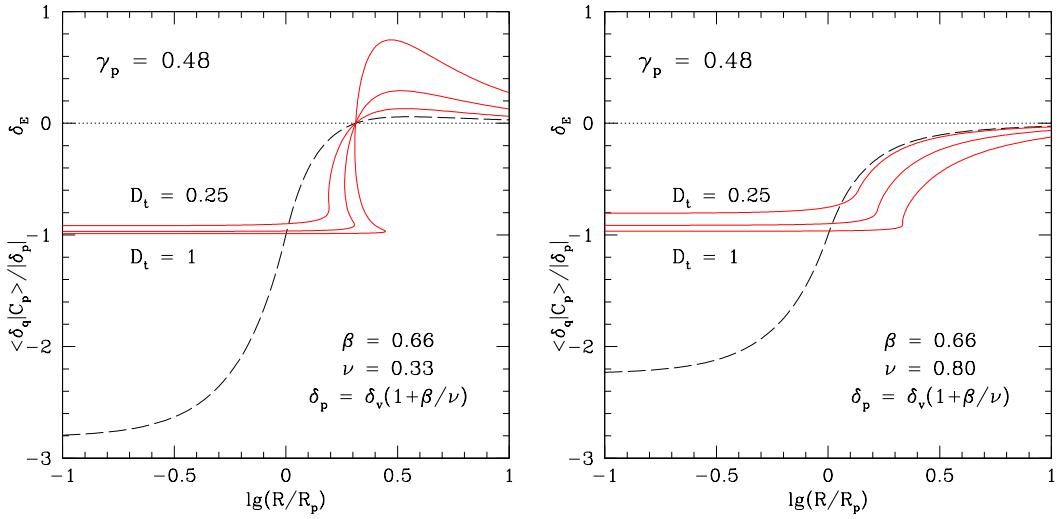

Figure 11.1: Evolution of the density profile around an excursion set trough of height δ_p. The correlation parameter γ_p is that for mixed TopHat/Gaussian smoothing of $P(k) \propto k^{-2}$. Dashed curve shows the Lagrangian profile (i.e. the initial one, evolved using linear theory to the present time); solid curves show the nonlinearly evolved profiles (solid) when the linear theory growth factor is D_t times that of the present time. The two values of $\nu \equiv \delta_v/\sqrt{s_0^{pp}}$ were chosen to illustrate the shell-crossing signature of a wall (top panel) and the smallest ν for which shell crossing does not occur (bottom). The associated values of b_{10} are $-0.08\delta_v$ and $0.24\delta_v$.

crossing scale and a substantial difference in their evolution depending if they are over- or under-dense regions. The spherical model mapping in Eq. (11.1) shows these differences. If the Lagrangian enclose density is positive, $\delta_{\rm L} > 0$, then $(1 - D_z\delta_{\rm L}/\delta_{\rm sc})^{-\delta_{\rm sc}} > 1$ and it grows in time, so also the Eulerian density is positive, $\delta_{\rm E} > 0$, and growing, while the Eulerian size $R_{\rm E}$ shrinks. On the other hand, if $\delta_{\rm L} < 0$ then $\delta_{\rm E} < 0$ and it becomes deeper as time passes, while the Eulerian size increases. Therefore, in a halo the mass within the zero crossing scale moves inwards on average (since the overdensity is positive there), while the mass outside this scale moves outwards (because the density is negative). In a voids, it is exactly the opposite: the mass inside the zero-crossing scale moves outwards, while the mass outside moves inwards on average. So, only in voids the inner and the outer shells near the zero crossing scale cross each other, giving rise to the shell crossing phenomenon. This crushing is manifested as follows. For each $R_{\rm L}/R_p$, inserting the left hand side of Eq. (10.7) into Eq. (11.1) maps the initial density to the evolved one and each $R_{\rm L}/R_p$ to an $R_{\rm E}/R_p$. The net result is a complicated relation between $1 + \delta_{\rm E}$ and $R_{\rm E}/R_p$: this relation is the evolved density profile. If the same $R_{\rm E}$ can have multiple values of $\delta_{\rm E}$, then this signals that initially concentric shells have crossed – so a wall has been formed. This is another way in which the gravitational evolution breaks the symmetry between over-and under-dense regions presents in the initial Lagrangian space.

If in a void the overdensity outside the zero crossing scale is sufficiently dense, then this will cause the entire region to shrink eventually: this is the crushing associated with the void-in-cloud process of [109]. Again the evolution shows a difference between peaks and trough: provoids can disappear because embedded in a larger protohalo,

while protohalos evolve in halos even if they are inside a void.

Figure 11.1 illustrates: the two panels show the evolution of the density profile around excursion set troughs of height $\delta_p = \delta_v(1+0.7/\nu)$ for $\nu \equiv |\delta_v|/\sqrt{s_0^{pp}} = 0.33$ (top) and $\nu = 0.8$ (bottom). The correlation parameter γ_p is that for mixed TopHat/Gaussian smoothing of $P(k) \propto k^{-2}$, for reasons noted previously. The dashed curve shows the initial Lagrangian profile (i.e. evolved using linear theory to the present time); solid curves show the nonlinearly evolved profiles when the linear theory growth factor is $D_t = 1/4, 1/2$ and $1\times$ that of the present time. The two values of ν were chosen to illustrate the shell-crossing signature of a wall (top panel) and the smallest ν for which shell crossing does not occur (bottom). The associated values of b_{10} are $0.08/|\delta_v|$ and $-0.24/|\delta_v|$. While there is no surprise that shell crossing occurs when $b_{10} \geq 0$ (for then the enclosed density profile crosses zero), note that it can occur even when b_{10} is (slightly) negative, as interior shells catch up with the ones which surround them – this is the same effect which leads to shell crossing of an initially tophat, uncompensated profile.

We can use the spherical evolution model to provide a rough estimate of approximately what values of ν shell crossing occurs: since it predicts a wall on the scale $R_{\rm E} = 1.7R_{\rm L}$, it is interesting to find that ν for which $R_0 = 1.7R_p$. Since $1.7^2 \approx 3$, Eq. (10.28) indicates that this happens when $\nu^2 = -2.7b_{10}$. For Gaussian smoothing of $P(k) \propto k^{-7/3}$, for which $\gamma_p = 1/2$, this means $\nu \approx 0.66$, so we might expect the squeezing of voids to matter for smaller values of ν. For mixed TopHat/Gaussian smoothing of $P(k) \propto k^{-2}$, for which $\gamma_p \approx 1/2$, it is voids smaller than $\nu = 0.92$ which are affected. Hence, voids which formed from protovoid patches with $\nu \geq 1$ should be immune to the void-in-cloud squeezing process. In particular, this shows that the voids which are predicted to have $b_{\rm E} = 0$ are also predicted to be immune to the squeezing process. However, these did not have a zero crossing in the first place.

In practice the wall which one's eye notices more readily is the one given by the overdensity at R_q rather than that enclosed within R_q. To appreciate the difference between the two, consider an initial profile which is -2.7 within R_p, and steps sharply up to $2.7/4$ between R_p and $1.7R_p$ before stepping sharply down to zero for all larger scales. The initial enclosed density would be a much smoother function of scale, which would never become positive. The predicted evolved profile would show a thin high wall surrounding a void, whereas the corresponding enclosed density profile would have height $0.2\times$ the background density on scales smaller than $1.7R_p$, and it would step sharply up to the background density on scale $1.7R_p$. For the mixed TopHat/Gaussian excursion set peaks model, the shape of this profile is given by Eq. (10.13), upon simply replacing $W(kR_q) \to j_0(kR_q)$ in the integral which defines s_0^{pq}.

11.1.3 Comparison with N-body simulations

We want to test the spherical model in predicting the evolution of the Lagrangian void profiles from excursion set of peaks, at different redshifts. In principle, given the void mass, the linear bias terms and the Lagrangian profile are fully determined as well as the Eulerian one. However, we do not expect this model to accurately reproduce the measurements of void profiles in simulations, since the void finders cannot identify voids in the same way as they are defined by the theory.

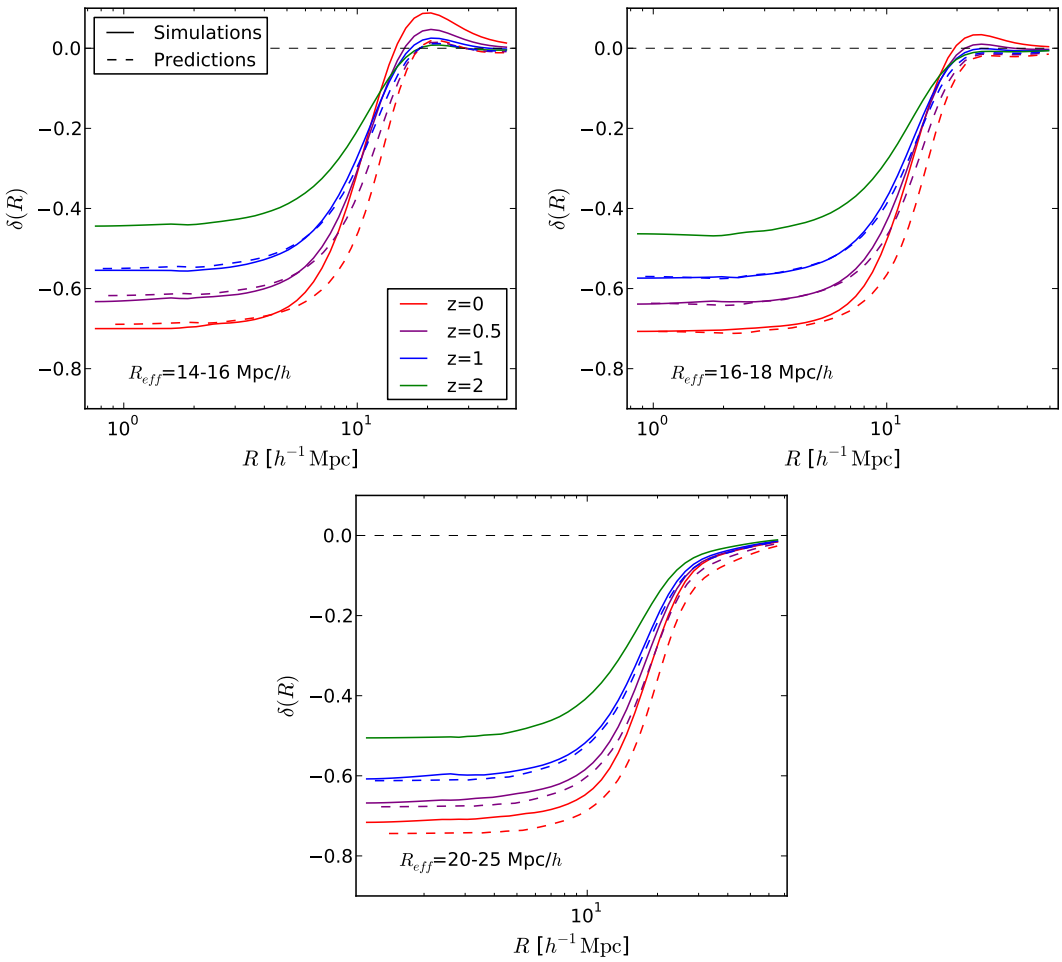

Figure 11.2: Evolution of mean enclosed void density profiles. The solid lines show the average density profiles measured in simulations, while the dashed lines describe the prediction from the spherical model. Different colors indicate different redshifts. The predictions are calculated assuming a Lagrangian profile computed evolving back the measured profile at $z = 2$ via Eq. (11.1).

Another interesting comparison is the one that aims to test the structure of the model, rather than the specific quantitative prediction. In this sense, we want to test the structure of the Lagrangian profile - with a large scale bias factor b_{10} and a bias term b_{01} that multiply a k-dependent term - and the spherical model prediction for the time evolution of the Eulerian profile. Therefore, we measure the Lagrangian profiles at high redshift, $z = 2$, in the simulations and evolve them using Eq. (11.1).

The simulations analyzed are the ones in the bottom part of Table 4.1, run in ΛCDM cosmology. Voids are identified using the void finder VIDE) [116] (see Chapter 4) at redshift zero. In order to have the time evolution of their profile, their particle members are traced back in redshift, where the void centers are identified with the center of mass of the particle members. The profiles are then computed measuring the density around the void centers with the inclusion of the particles that do not belong to the selected voids.

Figure 11.2 shows the comparison between the spherical evolution model and the measurements from simulations. The evolution of the inner part of voids are well reproduced by the model, which seems to be more accurate for smaller voids rather then large ones. However, it fails in describing the edge and the outer part. For this reason in the next section we investigate another approach, the so called Zel'dovich approximation, which is expected to be accurate on large scale.

11.2 Power spectra in Zel'dovich approximation

In this section we present the matter power spectrum computed in the Zel'dovich approximation [131], following the works of Taylor and Hamilton [119] and Bharadwaj [8]. We extend this methodology to compute the tracer-matter cross-power spectrum, which is the Fourier transform of the density profile around biased tracers.

11.2.1 The matter power spectrum

The Lagrangian theory express the density of a fluid in terms of displacement vector filed, in the following way. The mapping between the Eulerian space coordinate $\vec{x}(t)$ of a mass element and its Lagrangian (or initial) coordinate $\vec{q}$ is

$$\vec{x}(t) = \vec{q} + \vec{\xi}(\vec{q}, t)\,, \tag{11.7}$$

where the displacement field $\vec{\xi}(\vec{q}, t)$ is the integral of the velocity field along the particle path. Then the density contrast in Eulerian space is

$$\delta(\vec{x}) = \int d^3q\, \delta_D \left[\vec{x} - \vec{q} - \vec{\xi}(\vec{q})\right] - 1\,, \tag{11.8}$$

where δ_D is the Dirac delta. Following the conventions in Chapter 1, the Fourier transform of the density is

$$\delta(\vec{k}) = \int d^3x\, \delta(\vec{x})\, e^{i\vec{k}\cdot\vec{x}}\,, \tag{11.9}$$

and using Eq. (11.8) it reads

$$\delta(\vec{k}) = \int d^3q\, e^{i\vec{k}\cdot\vec{q}}(e^{i\vec{k}\cdot\vec{\xi}} - 1)\,, \tag{11.10}$$

which relates the Eulerian density field to the Lagrangian displacement vector field.

The power spectrum defined in Eq. (1.5) is easily computed to be

$$P(\vec{k}) = \int d^3q\, e^{i\vec{k}\cdot\vec{q}}(\langle e^{i\vec{k}\cdot\vec{\psi}}\rangle - 1)\,, \tag{11.11}$$

where the angular brackets denotes an ensemble average and the quantity $\vec{\psi}(\vec{q}) = \vec{\xi}(\vec{q}_1) - \vec{\xi}(\vec{q}_2)$ is the differential displacement of points separated by distance $\vec{q} = \vec{q}_1 - \vec{q}_2$. Notice that the power spectrum depends on the difference between displacement fields only, and is not sensitive to the sum of them. This fact is important since it will simplify our calculations.

In order to compute the matter power spectrum we need to specify the expression and evolution of the displacement filed. Here, we assume the Zel'dovich approximation [131], so the displacement field evolves accordingly to linear theory, $\vec{\xi}(\vec{q},t) = (D_t/D_0)\vec{\xi}_{\rm L}(\vec{q})$, where $\vec{\xi}_{\rm L}$ is the linear displacement and D_t/D_0 is the linear growth factor normalized to 1 at present time. Thus, this approach becomes particularly interesting since the coordinate system in Lagrangian space is nonlinear, moving with the particles themselves, but the displacement field in Zel'dovich approximation evolves accordingly to linear theory.

The continuity equation gives the relation between the velocity field and the linear density field

$$\vec{\xi}(\vec{q},t) = i\,\frac{D_t}{D_0}\int \frac{d^3k}{(2\pi)^3}\frac{\vec{k}}{k^2}\,\delta_{\rm L}(\vec{k})\,e^{-i\vec{k}\cdot\vec{q}}\,. \tag{11.12}$$

where $\delta_{\rm L}$ is the initial density field extrapolated to present time using linear theory. If the initial density fluctuations are Gaussian, Eq. (11.12) implies that the linear displacement field is Gaussian, as well as $\vec{\xi}(\vec{q},t)$ at all time t. Thus, the ensemble average in Eq. (11.11) involves a probability distribution function for $\vec{\psi}$ which is Gaussian, yielding

$$\begin{aligned}\langle e^{i\vec{k}\cdot\vec{\psi}}\rangle &= \exp\left(-k_ik_j\langle\psi_i\psi_j\rangle/2\right) \\ &= \exp\left(-k_ik_j\left[\psi_{ij}(\vec{0}) - \psi_{ij}(\vec{q})\right]\right)\,,\end{aligned} \tag{11.13}$$

where $i,j = x,y,z$ indicate the three spacial coordinates and the last equation has been obtained by defining the displacement correlation function $\psi_{ij}(\vec{q}) = \langle\xi_i(\vec{q}_1) - \xi_j(\vec{q}_2)\rangle$ at separation $\vec{q}$ and the same quantity $\psi_{ij}(\vec{0})$ at zero separation, $\vec{q} = 0$. Inserting this result into Eq. (11.11) leads to

$$P(\vec{k}) = \int d^3q\, e^{i\vec{k}\cdot\vec{q}}(e^{-k_ik_j\left[\psi_{ij}(\vec{0})-\psi_{ij}(\vec{q})\right]} - 1)\,, \tag{11.14}$$

where the unit term on the right hand side yields to a delta function at $\vec{k} = 0$. We can ignore it assuming that $\vec{k} \neq 0$.

As a consequence of the Zel'dovich approximation in Eq. (11.12), the nonlinear displacement correlation function evolves in times as the linear one, i.e. $\psi_{ij}(t) = (D_t/D_0)^2\psi_{Lij}$ and, using the definition of the power spectrum in Eq. (1.5), it reads

$$\psi_{ij}(\vec{q}) = \left(\frac{D_t}{D_0}\right)^2\int\frac{d^3k}{(2\pi)^3}\frac{k_ik_j}{k^4}P_{\rm L}(k)\,e^{-i\vec{k}\cdot\vec{q}}\,, \tag{11.15}$$

where $P_{\rm L}$ is the linear power spectrum extrapolated to present time. The displacement correlation at zero separation is simply

$$\psi_{ij}(\vec{0}) = \left(\frac{D_t}{D_0}\right)^2 \frac{\delta_{ij}}{3} \int \frac{d^3k}{(2\pi)^3} k^{-2} P_{\rm L}(k)\,. \tag{11.16}$$

Therefore Eq. (11.14), together with Eqs. (11.15) and (11.16), provide a nonlinear mapping between the initial and the evolved power spectra.

The integral in Eq. (11.15) can be simplified remembering that

$$k_i\, e^{-i\vec{k}\cdot\vec{q}} = i\frac{\partial}{\partial q_i} e^{-i\vec{k}\cdot\vec{q}}\,. \tag{11.17}$$

Then, taking the derivatives outside leads to an integral over the exponential which can be easily computed, leading to

$$\psi_{ij}(\vec{q}) = \left(\frac{D_t}{D_0}\right)^2 \int_0^\infty \frac{dk}{2\pi^2 k^2}\, P_{\rm L}(k)\, \frac{\partial}{\partial q_i}\frac{\partial}{\partial q_j} j_0(kq)\,, \tag{11.18}$$

where j_n is the spherical Bessel function. The first partial derivative $\partial j_0(kq)/\partial q_j = k j_0'(kq)\, q_j/q$, where the prime indicates the derivatives with respect to the argument kq. Then, the second derivatives gives

$$\frac{\partial}{\partial q_i}\frac{\partial}{\partial q_j} j_0(kq) = k^2 \left[\hat{q}_i\hat{q}_j\, j_0''(kq) + (\delta_{ij} - \hat{q}_i\hat{q}_j)\, \frac{j_0'(kq)}{kq}\right]\,. \tag{11.19}$$

Thus, the displacement correlation function $\psi_{ij}(\vec{q})$ can be written in term of components parallel and perpendicular to the separation $\vec{q}$:

$$\psi_{ij}(\vec{q}) = \psi_\parallel(q)\, \hat{q}_i\hat{q}_j + \psi_\perp(q)\, (\delta_{ij} - \hat{q}_i\hat{q}_j)\ , \tag{11.20}$$

with the components being

$$\psi_\parallel(q) = \left(\frac{D_t}{D_0}\right)^2 \int \frac{dk}{2\pi^2} P_{\rm L}(k) \left[j_0(kq) - 2\frac{j_1(kq)}{kq}\right] \tag{11.21}$$

$$\psi_\perp(q) = \left(\frac{D_t}{D_0}\right)^2 \int \frac{dk}{2\pi^2} P_{\rm L}(k) \left[\frac{j_1(kq)}{kq}\right]\,, \tag{11.22}$$

and that are related by the relation $\psi_\parallel(q) = d\,[q\psi_\perp]\,/dq$. It is convenient to rearrange the combination of displacement correlation functions with separations $\vec{q}$ and $\vec{0}$ in Eq. (11.14) as the part proportional to δ_{ij}, and therefore $\sim k^2$, and the part proportional to q_iq_j, which goes like $\sim k^2\mu^2$, with $\mu = \vec{k}\cdot\vec{q}/(kq)$. The former and the latter are

$$\psi_+(q) \equiv \psi_\perp(\vec{0}) - \psi_\perp(q) \tag{11.23}$$

$$\psi_-(q) \equiv \psi_\perp(q) - \psi_\parallel(q) \tag{11.24}$$

respectively. The nonlinear power spectrum in Eq. (11.14) is then isotropic and it reads

$$P(k) = \int d^3q\, e^{ikq\mu - k^2(\psi_+ + \mu^2\psi_-)}\,. \tag{11.25}$$

The same result can be found following the calculation of Bharadwaj [8] for the determination of the nonlinear matter correlation function in Zel'dovich approximation. A system of particles with motion governed by Eq. (11.7) can be described by their distribution function $f(x, \xi, t)$. Because the Liouville's theorem can be applied to the mapping between Eulerian and Lagrangian (initial) coordinates, the distribution satisfies the relation

$$f(\vec{x}, \vec{\xi}(t), t) = f(\vec{x} - \vec{\xi}(t), \vec{\xi}(t_i), t_i)\,, \tag{11.26}$$

where t_i indicates the initial time and $\vec{\xi}(t) = (D_t/D_0)\,\vec{\xi}_{\rm L}$. The two point distribution function is defined to be $\rho(\vec{x}, \vec{\xi}_1, \vec{\xi}_2, t) = \langle f(\vec{x}_1, \vec{\xi}_1, t) f(\vec{x}_2, \vec{\xi}_2, t)\rangle$, where $\vec{x} = \vec{x}_1 - \vec{x}_2$ is the Eulerian separation. The two point correlation function is given by integrating the two point distribution over the displacements:

$$1 + \xi(\vec{x}, t) = \int d^3\xi_1 d^3\xi_2\, \rho(\vec{x}, \vec{\xi}_1, \vec{\xi}_2, t)\,, \tag{11.27}$$

which is the quantity we aim to compute. Using Eq. (11.26), the two point distribution becomes

$$\rho(\vec{x}, \vec{\xi}_1, \vec{\xi}_2, t) = \rho\left[\vec{x} - [\vec{\xi}_1(t) - \vec{\xi}_2(t)], \vec{\xi}_1(t_i), \vec{\xi}_2(t_i), t_i\right]\,, \tag{11.28}$$

and it can be written in terms of an integral over a Dirac delta,

$$\rho(\vec{x}, \vec{\xi}_1, \vec{\xi}_2, t) = \int d^3q\, \delta_D\left\{\vec{q} - \left[\vec{x} - (\vec{\xi}_1(t) - \vec{\xi}_2(t))\right]\right\} \rho\left[\vec{q}, \vec{\xi}_1(t_i), \vec{\xi}_2(t_i), t_i\right]\,. \tag{11.29}$$

Using the integral representation for the Dirac delta $\delta_D(\vec{x}) = \int \exp(-i\vec{k}\cdot\vec{x}) d^3k/(2\pi)^3$, and its symmetric property $\delta_D(\vec{x}) = \delta_D(-\vec{x})$, the two point correlation function reads

$$1 + \xi(x, t) = \int \frac{d^3k}{(2\pi)^3}\, e^{-i\vec{k}\cdot\vec{x}} \int d^3q\, e^{i\vec{k}\cdot\vec{q}} \int d^3\xi_1 d^3\xi_2\, e^{i\vec{k}\cdot(\vec{\xi}_1 - \vec{\xi}_2) D_t/D_i} \rho\left[\vec{q}, \vec{\xi}_1, \vec{\xi}_2, t_i\right]\,, \tag{11.30}$$

where we wrote $\vec{\xi}(t_i)$ as $\vec{\xi}$, for simplicity. The two point distribution is Gaussian in the displacements. Transforming them to differential and center of mass coordinates

$$(\vec{\xi}_1, \vec{\xi}_2) \to (\vec{\psi} \equiv \vec{\xi}_1 - \vec{\xi}_2, \vec{\chi} \equiv \vec{\xi}_1 + \vec{\xi}_2) \tag{11.31}$$

the integral over the center of mass displacement gives 1, while the integral over the differential coordinates yields $\exp\left[-k_i k_j \langle \psi_i(t)\psi_j(t)\rangle/2\right]$. Thus the resulting correlation function is

$$1 + \xi(x, t) = \int \frac{d^3k}{(2\pi)^3}\, e^{-i\vec{k}\cdot\vec{x}} \int d^3q\, e^{i\vec{k}\cdot\vec{q}} e^{-k_i k_j \left[\psi_{ij}(\vec{0}) - \psi_{ij}(\vec{q})\right]}\,, \tag{11.32}$$

where we used the definition of the displacement correlation function ψ_{ij} introduced above. We can notice that $d^3k/(2\pi)^3\, e^{-i\vec{k}\cdot\vec{x}}$ is acting as a Fourier transform of the expression on its the right, which is the power spectrum already found in Eq. (11.14) following the calculation of Taylor and Hamilton [119]. This second approach by Bharadwaj [8] will be very useful to compute the cross-power spectrum of biased tracers and matter.

Initial power-law spectrum

The power spectrum in Zel'dovich approximation can be computed analytically for an initial power-law spectrum, $P_{\rm L} \propto k^n$, with index $n = -2$. In this case, $\psi_+ = \psi_- = (D_t/D_0)^2 Aq$, once the initial power spectrum has been conveniently normalized by the constant A. Thus, the power spectrum in Eq. (11.25) becomes

$$P(k) = \frac{32\pi A(D_t/D_0)^2}{k^2\left[1+4A^2(D_t/D_0)^4k^2\right]^2}\left[1+\frac{3\pi A(D_t/D_0)^2 k}{4\left[1+4A^2(D_t/D_0)^4k^2\right]^2}\right]. \tag{11.33}$$

In the linear regime, i.e. expanding the power spectrum for $k \to 0$, it is

$$P(k) \simeq \left(\frac{D_t}{D_0}\right)^2 \frac{32\pi A}{k^2} \tag{11.34}$$

while in the fully nonlinear regime $P(k) \propto (D_t/D_0)^{-6}/k^6$.

11.2.2 Tracer-matter cross-power spectrum

We described the profile around voids or peaks as the cross-correlation between these objects and the surrounding matter field. Thus, the Fourier transform of the profile is the cross-power spectrum of biased tracers and matter, which is the quantity we aim to compute in this section, in the particular case of the Zel'dovich approximation.

Here we use the Lognormal model, which provide a good insight on the Eulerian evolution of the cross-power spectrum. Let assume $1+\delta_{\rm b} = \exp(b\,\delta_{\rm L})$, where the subscript 'b' denotes the biased tracers and 'L' the Lagrangian space. The bias factor b is a free parameter that enhances large values of $\delta_{\rm L}$. We ask for the mean value of $1+\delta_{\rm b}$ to be normalized to 1. Then, assuming the linear density $\delta_{\rm L}$ to be Gaussian, the actual Lognormal transformation is

$$1+\delta_{\rm b} = e^{\,b\delta_{\rm L} - b^2\langle\delta_{\rm L}^2\rangle/2}\,, \tag{11.35}$$

where $\langle\delta_{\rm L}^2\rangle$ is the variance of the Lagrangian density field. From here on we drop the subscript 'L' since the density field written will always be Lagrangian, unless specified.

We compute the tracer-matter cross-power spectrum as it has been done for the matter-matter case, with the only difference that now one of the two positions is not a random point of the density field, but it is a special position corresponding to a biased tracer described using the Lognormal model. Therefore, the two point distribution in Eq. (11.30) must be substitute with the probability distribution function of two displacements where one is on a biased tracer:

$$p\left(\vec{\xi}_1,\vec{\xi}_2;\vec{q},t_i\right) \to \int \delta_1\, p\left(\delta_1,\vec{\xi}_1,\vec{\xi}_2;\vec{q},t_i\right) e^{\,b\delta_1 - b^2\langle\delta_1^2\rangle/2}\,, \tag{11.36}$$

where the displacements, the density field and the bias factor are at initial time, t_i. Therefore, the tracer-matter cross-power spectrum is

$$P_{\rm bm}(k,t) = \int d^3q\, e^{i\vec{k}\cdot\vec{q}} \int d^3\xi_1 d^3\xi_2\, e^{i\vec{k}\cdot(\vec{\xi}_1-\vec{\xi}_2)D_t/D_i} \int d\delta_1 p\left(\delta_1,\vec{\xi}_1,\vec{\xi}_2;\vec{q},t_i\right) e^{\,b\delta_1 - b^2\langle\delta_1^2\rangle/2} \tag{11.37}$$

We adopt the change of variables in (11.31) and write the probability distribution as $p\left(\delta_1,\vec{\psi},\vec{\chi}\right)=p\left(\vec{\psi},\vec{\chi}\right)p\left(\delta_1|\vec{\psi},\vec{\chi}\right)$, so the cross-power spectrum reads

$$P_{\rm bm}(k,t)=\int d^3q\,e^{i\vec{k}\cdot\vec{q}}\int d^3\psi d^3\chi\,e^{i\vec{k}\cdot\vec{\psi}D_t/D_i}p\left(\vec{\psi},\vec{\chi}\right)\int d\delta_1 p\left(\delta_1|\vec{\psi},\vec{\chi}\right)e^{\,b\delta_1-b^2\langle\delta_1^2\rangle/2} \tag{11.38}$$

The differential and center of mass displacements can be decomposed into the components parallel and perpendicular to the Lagrangian separation $\vec{q}$. This decomposition is particularly useful since the matter field correlates with parallel displacements only. Thus, the conditional distribution is a Gaussian with non-zero mean, that depend only on the two parallel components $\chi_\parallel$ and $\psi_\parallel$. The integral over the density field yields

$$\int d\delta_1 p\left(\delta_1|\vec{\psi},\vec{\chi}\right)e^{\,b\delta_1-b^2\langle\delta_1^2\rangle/2}=\exp\left[b\left(\psi_\parallel\frac{\langle\psi_\parallel\delta_1\rangle}{\langle\psi_\parallel^2\rangle}+\chi_\parallel\frac{\langle\chi_\parallel\delta_1\rangle}{\langle\chi_\parallel^2\rangle}\right)-\frac{b^2}{2}\left(\frac{\langle\psi_\parallel\delta_1\rangle^2}{\langle\psi_\parallel^2\rangle}+\frac{\langle\chi_\parallel\delta_1\rangle^2}{\langle\chi_\parallel^2\rangle}\right)\right]. \tag{11.39}$$

The probability distribution function of the displacements is Gaussian and depends in principle on two parallel and four perpendicular quantities. However, the result in Eq. (11.39) depends on parallel components only and thus the product of this results and $p\left(\vec{\psi},\vec{\chi}\right)$ is a function of the two perpendicular components, $\chi_\perp=\sqrt{\chi_{\perp x}^2+\chi_{\perp y}^2}$ and $\psi_\perp=\sqrt{\psi_{\perp x}^2+\psi_{\perp y}^2}$, and two parallel components, $\chi_\parallel$ and $\psi_\parallel$. It is a Gaussian with zero mean in the perpendicular components and with mean shifted by a term of the type $b\langle\psi_\parallel\delta_1\rangle$ in the parallel ones. The only other quantity in Eq. (11.38) depending on displacements is the exponential $e^{i\vec{k}\cdot\vec{\psi}D_t/D_i}$. Therefore the integrals in the center of mass coordinates give 1 and the integral in the differential coordinates yields

$$P_{\rm bm}(k,t)=\int d^3q\,e^{i\vec{k}\cdot\vec{q}}\exp\left\{-\frac{1}{2}\frac{D_t^2}{D_i^2}\left[k_\parallel^2\langle\psi_\parallel^2\rangle+k_\perp^2\langle\psi_\perp^2\rangle+2i\,b\frac{D_i}{D_t}\,k_\parallel\langle\psi_\parallel\delta_1\rangle\right]\right\}. \tag{11.40}$$

The two point correlation function of the initial parallel and perpendicular components are

$$\langle\psi_\parallel^2\rangle = \left(\frac{D_i}{D_0}\right)^2\int\frac{dk}{2\pi^2}P_{\rm L}(k)\frac{2}{3}\left[1-3j_0(kq)+6\frac{j_1(kq)}{kq}\right] \tag{11.41}$$

$$\langle\psi_\perp^2\rangle = \left(\frac{D_i}{D_0}\right)^2\int\frac{dk}{2\pi^2}P_{\rm L}(k)\frac{2}{3}\left[1-3\frac{j_1(kq)}{kq}\right], \tag{11.42}$$

and the displacement-density cross correlation is

$$\langle\psi_\parallel\delta_1\rangle = \left(\frac{D_i}{D_0}\right)^2\int\frac{dk}{2\pi^2}P_{\rm L}(k)k\,j_1(kq), \tag{11.43}$$

where the linear power spectrum is extrapolated to present time. Then, given the relations $k_\parallel=k\mu$ and $k_\perp=k\sqrt{1-\mu^2}$, with $\mu=\hat{k}\cdot\hat{q}$, the cross power spectrum becomes

$$P_{\rm bm}(k,t)=\int d^3q\exp\left[ik\mu\left(q-\frac{D_0}{D_t}b_{\rm L}\,\langle\psi_\parallel\delta_1\rangle\right)-k^2\left(\psi_+ +\mu^2\psi_-\right)\right], \tag{11.44}$$

where we have used the definitions in Eq. (11.24) and the relation between the initial bias at generic time t_i and the Lagrangian bias at present time $b_{\rm L}=b(t_i)D_i/D_0$. Thus,

the tracer-matter cross-power spectrum in Zel'dovich approximation is described by a similar integral to the one for the matter-matter power spectrum in Eq. (11.25), with an additional term containing the bias of the tracers with respect to the matter field and the correlation between the differential displacement along the separation $\vec{q}$ and the linear density field.

Initial power-law spectrum

We consider again the special case of initial power-law spectrum with index $n = -2$. In this case Eq. (11.44) becomes

$$P_{\rm bm}(k,t) = \int d^3q \, \exp\left[ikq(1+\mu^2)A\left(\frac{D_t}{D_0}\right)^2 - 4ik\mu A\left(\frac{D_t}{D_0}\right)^2 \frac{D_0}{D_t} b_{\rm L} \langle \psi_\parallel \delta_1 \rangle\right] . \tag{11.45}$$

If the power spectrum is evaluated at some early time t such that $D_t << D_0$, the exponential can be expanded and truncated at the first order in D_t/D_0 and the integral yields

$$P_{\rm bm}(k,t) \simeq \left(\frac{D_t}{D_0}\right)^2 \left(\frac{b_{\rm L} + D_t/D_0}{D_t/D_0}\right) \frac{32\pi A}{k^2} \tag{11.46}$$

which differs from the linear matter power spectrum in Eq. (11.34) for the presence of the bias factor. From this specific case we can argue that the linear Eulerian bias of a tracer $b_E(t)$ - defined with respect to the matter power spectrum at time t - is related to the Lagrangian bias via

$$b_{\rm E}(t) = \frac{b_{\rm L} + D_t/D_0}{D_t/D_0} \, . \tag{11.47}$$

This relation reduces to $b_{\rm E} = 1 + b_{\rm L}$ when evaluated at present time, and thus is the generalization to arbitrary time t of Eq. (11.4). We will use and test this import result below.

However, the Lagrangian excursion set model for peaks and troughs presents a more complicated structure for the linear bias. In this context, the discussion above reproduce the case $b^{\rm L}_{01} = 0$. Since we have already argued that $b_{\rm L} \to b^{\rm L}_{10}$ on large scales, then Eq. (11.4), when combined with Eq. (10.8), implies that

$$b^{\rm E}_{10} = b^{\rm L}_{10} + 1 \qquad \text{and} \qquad b^{\rm E}_{01} = b^{\rm L}_{01} - 1 \, . \tag{11.48}$$

At generic time t, Eq. (11.47) suggests that the relations between the bias factors are

$$b^{\rm E}_{10} = \frac{b^{\rm L}_{10} + D_t/D_0}{D_t/D_0} \qquad \text{and} \qquad b^{\rm E}_{01} = \frac{b^{\rm L}_{01} - D_t/D_0}{D_t/D_0} \tag{11.49}$$

on large scales, in agreement with [36] (see their equations 66 and 71). In what follows, we use this general expression (i.e., not just its large scale limit) to estimate the shape of the evolved profile.

11.2.3 Cross-power spectrum at different times

The formalism used above can be apply to compute the cross-power spectrum of a biased tracer at time t_1 and the matter field at time t_2, with $t_1 \neq t_2$. In this case, the

correlations in Eqs. (11.41), (11.42) and (11.43) become

$$\langle\psi_\parallel^2\rangle = \int \frac{dk}{2\pi^2} P_{\rm L}(k) \frac{2}{3} \left[\frac{D_1^2+D_2^2}{D_0^2} \frac{1}{2} + \frac{D_1 D_2}{D_0^2} \left(-3 j_0(kq) + 6 \frac{j_1(kq)}{kq} \right) \right] \quad (11.50)$$

$$\langle\psi_\perp^2\rangle = \int \frac{dk}{2\pi^2} P_{\rm L}(k) \frac{2}{3} \left[\frac{D_1^2+D_2^2}{D_0^2} \frac{1}{2} - \frac{D_1 D_2}{D_0^2} 3 \frac{j_1(kq)}{kq} \right] \quad (11.51)$$

$$\langle\psi_\parallel \delta_1\rangle = \frac{D_1 D_2}{D_0^2} \int \frac{dk}{2\pi^2} P_{\rm L}(k) k\, j_1(kq)\,. \quad (11.52)$$

In analogy with Eq. (11.40), the cross-power spectrum is given by

$$\langle\delta_1^{\rm b}\delta_2\rangle = \int d^3q\, e^{i\vec{k}\cdot\vec{q}} \exp\left\{ -\frac{1}{2} \left[k^2\mu^2\langle\psi_\parallel^2\rangle + k^2(1-\mu^2)\langle\psi_\perp^2\rangle + 2i\, b\, k\mu\langle\psi_\parallel\delta_1\rangle \right] \right\}, \quad (11.53)$$

where b here indicates the bias at time t_1. Grouping together the terms according to their dependence on μ, this equation becomes

$$\langle\delta_1^{\rm b}\delta_2\rangle = \exp\left[-\frac{(D_1-D_2)^2}{D_0^2} \frac{k^2}{6} \sigma_{-1}^2 \right] \int d^3q\, e^{i\vec{k}\cdot\vec{q}} \quad (11.54)$$
$$\times \exp\left[-\frac{D_1 D_2}{D_0^2} k^2(\psi_+ + \mu^2\psi_-) - ik\mu \frac{D_2}{D_0} b_{\rm L} \langle\psi_\parallel\delta_1\rangle \right],$$

where in this case ψ_+ and ψ_- are defined as in Eq. (11.24), but are evaluated at present time to highlight the combination of the growth factors. The exponential outside the integral has the form of a propagator, depends on the linear matter displacement dispersion $\sigma_{-1}^2 = \int dk/(2\pi^2) P(k)$ and is equal to 1 when $t_1 = t_2$.

Initial power-law spectrum

Unfortunately, it is not possible to compute the Zel'dovich cross-power spectrum at different times for a initial power-law spectrum with index $n = -2$, since in that case the linear matter displacement dispersion is divergent.

11.2.4 Comparison with N-body simulations

The Zel'dovich approximation predicts the relation in Eq. (11.49) between the Lagrangian and Eulerian bias terms of peaks and troughs. We test these relations in N-body simulations, measuring the ratio

$$\frac{D_z}{D_0} \frac{\langle\delta_{\rm v}(z)\delta_{\rm m}(z)\rangle}{\langle[\delta_{\rm m}^{\rm L}(z)]^2\rangle} \quad (11.55)$$

between the void-matter cross-power spectrum at redshift z and the linear matter power spectrum evolved to the same time. For a Gaussian smoothing window, Eqs. (10.22) and (11.49) lead to a prediction for the ratio,

$$\frac{D_z}{D_0} \frac{\langle\delta_{\rm v}(z)\delta_{\rm m}(z)\rangle}{\langle[\delta_{\rm m}^{\rm L}(z)]^2\rangle} = \left(b_{10}^{\rm L} + \frac{D_z}{D_0} \right) W(kR_p) + \left(b_{01}^{\rm L} - \frac{D_z}{D_0} \right) \frac{s_0^{pp}}{s_1^{pp}} k^2 W(kR_p)\,, \quad (11.56)$$

where $W(kR_p) \to 1 - k^2R_p^2/2$ as $k \to 0$. The top panels in figure 11.3 show the measurements at different redshifts and for two void sizes. The growth factor in the

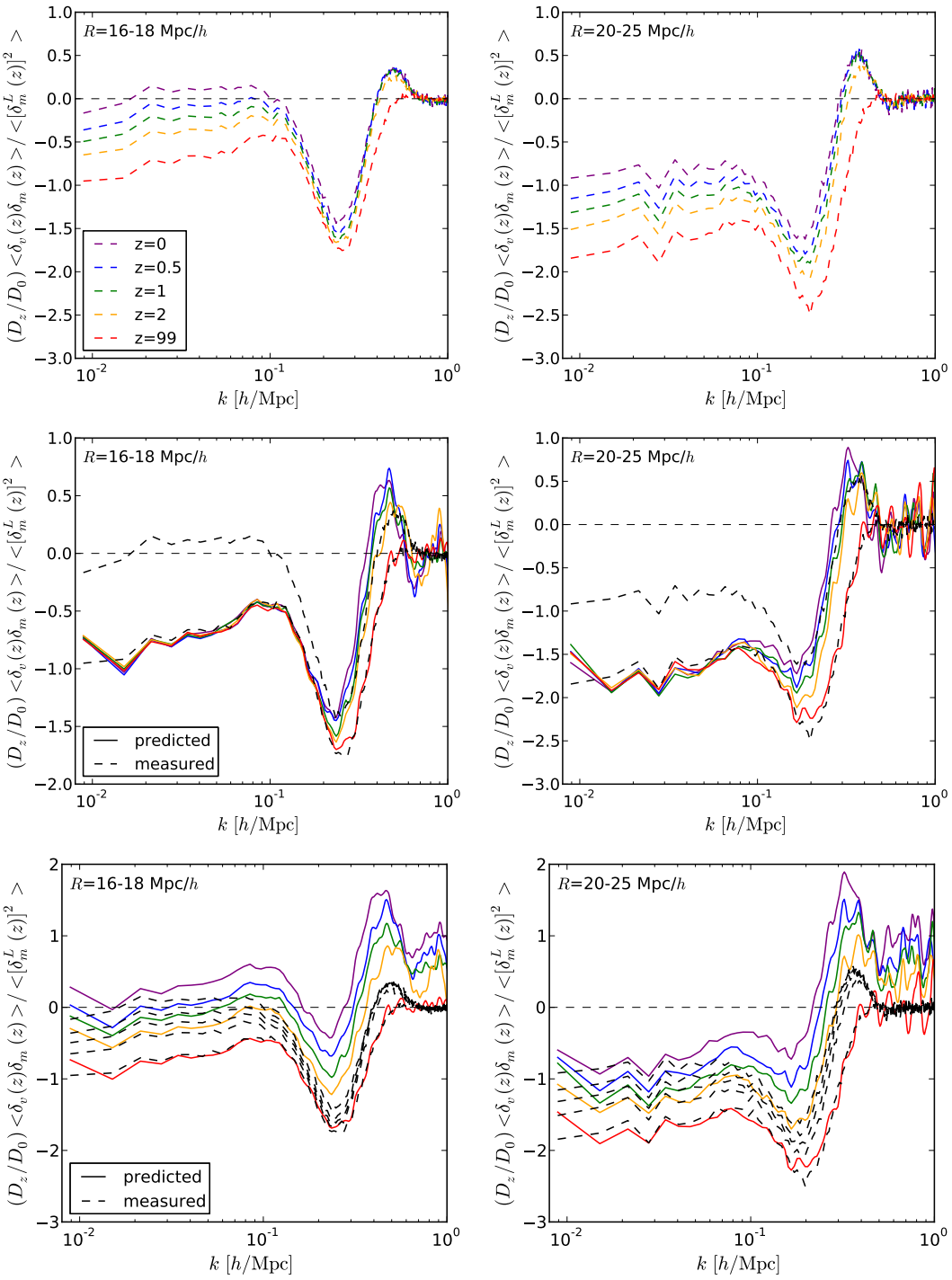

Figure 11.3: Ratio between the void-matter cross-power spectrum and the linear matter power spectrum. The voids considered have size in the ranges: 14-16 Mpc/h, 16-18 Mpc/h and 20-25 Mpc/h. Different colors indicate different redshifts, while solid and dashed lines stay for quantity predicted and measured, respectively. Top panel: measurements from simulations. Central panel: predictions using the spherical model and measurements at $z = 99$ and $z = 0$. Bottom panel: prediction using an additional term equal to the linear matter power spectrum.

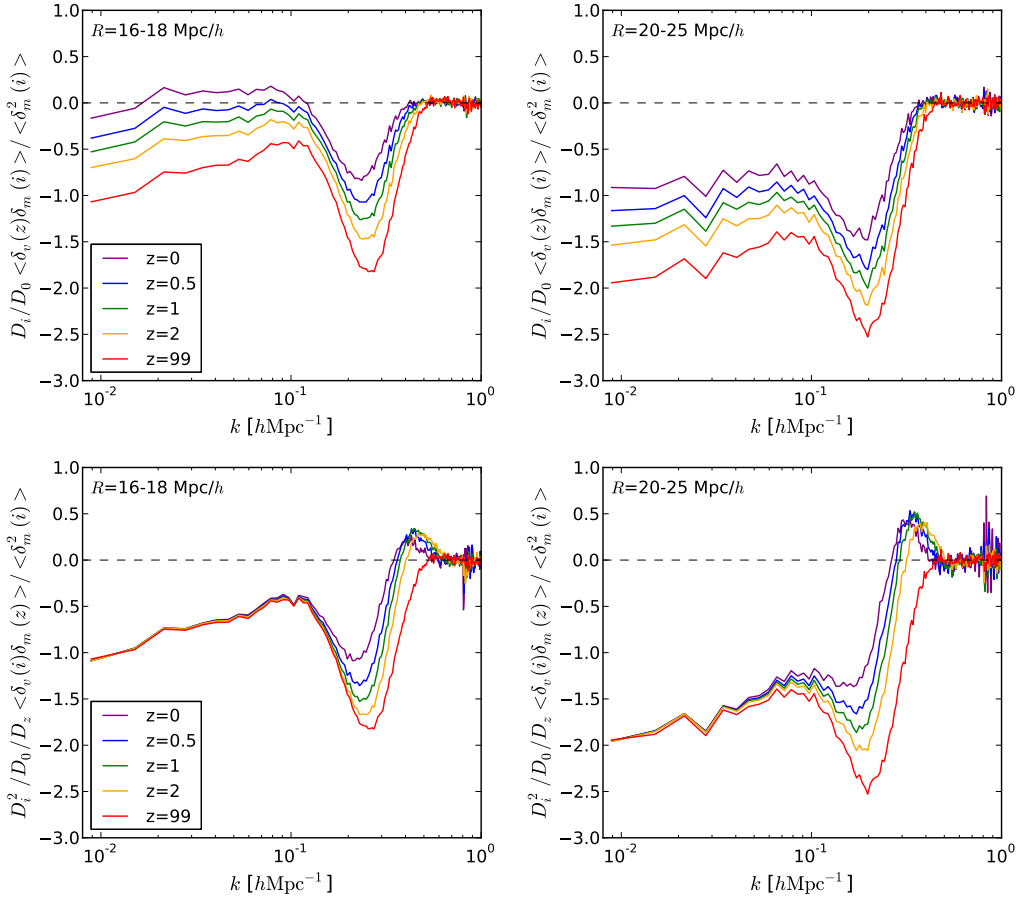

Figure 11.4: Ratio between the void-matter cross-power spectrum - at different times - and the linear matter power spectrum, as measured in simulations.

initial conditions - at redshift $z = 99$ - is very small and thus the ratio is expected to be $b_{10}^{\rm L}$ on large scales. On the other hand, at $z = 0$ the growth factor is equal to 1 and the ratio becomes $b_{10}^{\rm L} + 1$. The measurements show that the difference between the ratio at ICs and at present time is $\simeq 1$, as expected.

As done above in real space, we want to predict the measured profile in Fourier space - described by the ratio in Eq. (11.55) - at late time redshifts, assuming as Lagrangian profile the one measured in the ICs, at $z = 99$. First, we assume the spherical model in Eq. (11.1) to understand how well it works in Fourier space, where the large scale can be better understood. The results are displayed in the central panels of Figure 11.3, where the solid colored lines are the predictions, while the dashed black lines are the measurements in the ICs and at $z = 0$. Clearly the spherical model cannot reproduce the large scale limit and account for the linear bias evolution. However, it well reproduce the ratio at small scales where it raises before reaching zero.

The Lagrangian profile is expected to be of the form $[b_{10}^{\rm L}+b_{01}^{\rm L}s_0^{pp}/s_1^{pp}\,k^2]W(kR_p)P_{\rm L}(k)$ and the spherical model predict its evolution to be given by the growth factor on large scales. In order to have the right evolution on these scales, we do the following assumption: the real evolution is given by adding the linear matter power spectrum, which evolves with the second power of the growth factor. In this way we recover the right

evolution for the Eulerian bias $b_{10}^{\rm E}$. The results are plotted in the bottom panel of Figure 11.3, which show that the ansatz can capture the large scale behavior, but makes completely wrong predictions on small scales. We will discuss some more sophisticated model in the following Section.

The cross-power spectrum at different times seems to be a good way to test the structure of the void profiles. The ratio in Eq. (11.55) is constant on large scales, and the first corrections appearing on smaller scale are all of the order k^2. These corrections come from the Lagrangian bias term proportional to $b_{01}^{\rm L}$, its evolution (given by the velocity bias), and the window function. Measurements involving different times seem promising since they could in principle disentangle the k^2-contribution of different terms, and giving insights on the evolution. Figure 11.4 shows: on top the ratio

$$\frac{D_i}{D_0}\frac{\langle\delta_{\rm v}(z)\delta_{\rm m}(i)\rangle}{\langle[\delta_{\rm m}(i)]^2\rangle}\,, \tag{11.57}$$

which gives the correlation between the evolved void and the initial matter field, and on bottom the ratio

$$\frac{D_i^2}{D_0 D_z}\frac{\langle\delta_{\rm v}(i)\delta_{\rm m}(z)\rangle}{\langle[\delta_{\rm m}(i)]^2\rangle}\,, \tag{11.58}$$

which correlates the protovoids in the ICs and the evolved matter field.

From the Zel'dovich approximation, the first ratio is expected to be

$$\frac{D_i}{D_0}\frac{\langle\delta_{\rm v}(z)\delta_{\rm m}(i)\rangle}{\langle[\delta_{\rm m}(i)]^2\rangle} = \left[\left(b_{10}^{\rm L}+\frac{D_z}{D_0}\right)+\left(b_{01}^{\rm L}-\frac{D_z}{D_0}\right)\frac{s_0^{pp}}{s_1^{pp}}\,k^2\right]W(kR_p)G(k) \tag{11.59}$$

where $G(k)$ is the peak/trough propagator arising when correlating fields at different redshifts, as resulting in Eq. (11.54). Since we are considering troughs - the same would hold for peaks - and not just some generic biased tracers as we assumed in the Lognormal model, the peak/trough propagator between $z=i$ and z is

$$G(k) = \exp\left[-\frac{(D_z-D_i)^2}{D_0^2}\frac{k^2}{6}\left(s_{-1}^{pp}-\frac{(s_0^{pp})^2}{s_1^{pp}}\right)\right]\,, \tag{11.60}$$

which gives as well a k^2-contribution. The top panel of Figure 11.4 shows that the void profile evolution is the expected one on large scales. The evolution on intermediate/small scales is different compared to the top panel of Figure 11.3.

The Zel'dovich prediction for the second ratio is

$$\frac{D_i^2}{D_0 D_z}\frac{\langle\delta_{\rm v}(i)\delta_{\rm m}(z)\rangle}{\langle[\delta_{\rm m}(i)]^2\rangle} = \left[b_{10}^{\rm L}+b_{01}^{\rm L}\frac{s_0^{pp}}{s_1^{pp}}\,k^2\right]W(kR_p)G_m(k)\,, \tag{11.61}$$

where the matter propagator is by definition

$$\frac{\langle\delta_{\rm m}(z)\delta_{\rm m}(i)\rangle}{\langle[\delta_{\rm m}(i)]^2\rangle}\frac{D_i}{D_z} \equiv G_m(k) \tag{11.62}$$

and thus $G_m(k) = \exp[-(D_z^2-D_i^2)/D_0^2\,k^2\sigma_{-1}^2/6]$ and $\sigma_{-1}^2 = \int dk\,P(k)/(2\pi^2)$. As predicted, the bottom panel of Figure 11.4 shows no evolution on large scales, meaning that the evolution seen in the previous plots is really due to the linear Eulerian void bias.

11.3 Models for the void profile

Inspired by the measurements in N-body simulations and the rough predictions done in the previous Section, we present here three different models to describe the mean void profiles. Our approach is similar to the one used to compute the halo-matter cross-correlation, where the small scale behavior can be described by the NFW [83] profile and the large scale one can be modeled with the linear matter correlation function multiplied by the linear bias. Here, we describe the small scale profile using the spherical evolution, that seems to work well in predicting the evolution of the inner part of void profiles (see Figure 11.2), and a linear theory prediction to model the large scale behavior, having in mind the predictions of the Zel'dovich approximations. Indeed, we want the model to behave as in Eq. (11.56) on large scales.

The three models in Fourier space are

$$a) \quad \langle \delta_{\rm v}(z)\delta_{\rm m}(z)\rangle = {\rm FT[s.c.]} + \left(\frac{D_z}{D_0}\right)^2 b_v(k) W(kR_p) P_{\rm L}(k) e^{-k^2(R_p/7)^2} \tag{11.63}$$

$$b) \quad \langle \delta_{\rm v}(z)\delta_{\rm m}(z)\rangle = {\rm FT[s.c.]} + \left(\frac{D_z}{D_0}\right)^2 b_v(k) W(kR_p) P_{\rm L}(k) G(k) \tag{11.64}$$

$$c) \quad \langle \delta_{\rm v}(z)\delta_{\rm m}(z)\rangle = {\rm FT[s.c.]}\,\{1 - G(k)\} + \tag{11.65}$$
$$+ \left(\frac{D_z}{D_0}\right)\left[b_L(k) + \frac{D_z}{D_0} b_v(k)\right] W(kR_p) P_{\rm L}(k) G(k)\,,$$

where FT[s.c.] is the Fourier transform of the Eulerian density $\delta_{\rm E}$ at $R_{\rm E}$ predicted by the spherical evolution model in Eq. (11.1). In that equation the density is computed within a shell of radius $R_{\rm E}$, $\delta_{\rm E}(< R_{\rm E})$, rather then at $R_{\rm E}$. The two quantities are related by

$$\delta_{\rm E}(R_{\rm E}) = \frac{R_{\rm E}}{3}\frac{d}{dR_{\rm E}}\delta_{\rm E}(< R_{\rm E}) + \delta_{\rm E}(< R_{\rm E})\,. \tag{11.66}$$

The peak/trough propagator $G(k)$ is given by Eq. (11.60), $b_v(k)$ is the velocity bias

$$b_v(k) = 1 - \frac{s_0^{pp}}{s_1^{pp}}\,k^2\,, \tag{11.67}$$

and b_L is the Lagrangian bias in Eq. (10.24), that reduces to Eq. (10.22) for a Gaussian smoothing window.

In models a) and b) the large scale Lagrangian bias is given by the spherical collapse term, while its evolution to the Eulerian space is described by the velocity bias. In model c) the spherical collapse model describes only the small scale profile, since $G(k) \to 1$ as $k \to 0$. The large scale behavior is completely given by the linear term. Figure 11.5 shows the comparison between the predictions from the three models - once the Lagrangian profile has been assumed to be the one measured in the ICs - and the measurements from N-body simulations, at different redshifts. All the models can reproduce the large scale behavior, while the small scales are better described by model a). However, further analysis needs to be done in order to understand how to model the transition between the spherical model term and the linear one.

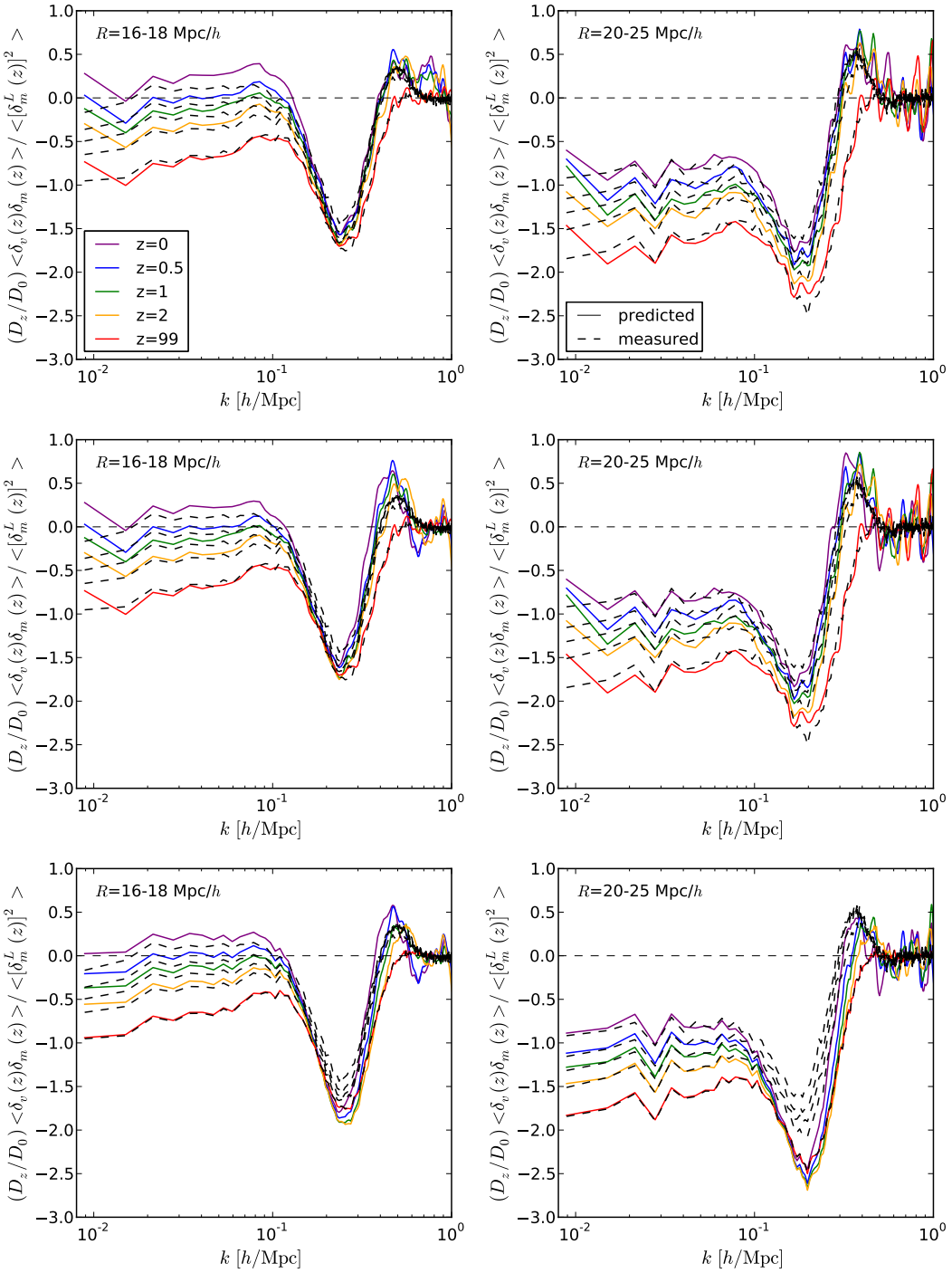

Figure 11.5: Ratio between the void-matter cross-power spectrum and the linear matter power spectrum, as measured in simulations. The void considered have size in the ranges: 14-16 Mpc/h, 16-18 Mpc/h and 20-25 Mpc/h. Different colors indicate different redshifts, while solid and dashed lines show quantity predicted and measured, respectively.

Part V

Conclusions

Chapter 12

Conclusions

In this thesis we studied the impact of massive neutrinos on the large scale structure. In particular, we developed a model to compute the nonlinear matter power spectrum in massive neutrinos cosmologies and we performed a comprehensive study of statistical void properties in order to understand how the presence of massive neutrinos changes them. In principle, voids are good environments where to study neutrinos and these understandings are the first step to use observables related to voids to constrain the neutrino masses. The other main topic of this thesis are voids. A part from studying their statistical properties in massive neutrino cosmologies, we presented a framework to model the void density profile starting from theoretical assumptions on void formation. In particular we considered different Lagrangian models for describing the void/halo abundance and spatial distribution, such as the excursion set peak, the upcrossing model, the peak model and the excursion set of peaks. All these models can be used to predict the Lagrangian density profiles around peaks or troughs. Then, we study the evolution of these profiles to the Eulerian space. This work was motivated by recent measurements on void density profiles in survey and N-body simulations. Moreover, since void are underdense regions where screening mechanisms are expected not to work, void profiles are in principle very interesting observables for the study of modified theories of gravity. We recap here the main results of the different parts of the thesis.

The fist part was devoted to introducing all the concepts and results available in the literature useful to understand the following parts where the original work have been presented.

The purpose of Part II has been to extend the halo model to account for the effects of massive neutrinos. We have run a set of 8 large box-size N-body simulations containing massive neutrinos as additional particles. Our simulation suite comprises four different cosmological models with different neutrino masses: $\sum m_\nu = 0.0$, 0.15, 0.30 and 0.60 eV. For each model we have run two different simulations with two different box-sizes, in order to extract the power spectra over a wide range of wave numbers.

We have reviewed the standard framework of the halo model and used it to compute the fully nonlinear matter power spectrum for the considered massless ΛCDM cosmology. The comparison with the matter power spectrum from the N-body simulations showed

a very good agreement on large and small scales, whereas a disagreement at the 20% (at $z = 0$) and 30% (at $z = 1$) level is present on intermediate scales, $k \sim 0.2 - 2\,h$/Mpc. These scales represent the transition between the 1-halo and 2-halo terms, where the halo model is not very accurate.

We then focused on cosmologies with massive neutrinos, where the total matter power spectrum can be expressed as the mass-weighted sum of three different power spectra: CDM auto-power spectrum, neutrinos auto-power spectrum and CDM-neutrinos cross-power spectrum. Thus, in our extension of the halo model we need to model separately the density field of both CDM and massive neutrinos.

The CDM density field is modeled in the same spirit the halo model describes the distribution of matter in a massless neutrino cosmology: all CDM is bound within c-halos (CDM halos). A key ingredient is to account for the fact that the clustering properties of the c-halos depend only on the CDM field [23, 55] (this is called the cold dark matter prescription), thus, both the mass function and the halo bias are computed using the linear CDM power spectrum.

The neutrino density field can not be modeled as the CDM field, i.e. assuming that all particles are within halos, since the neutrinos large thermal velocities prevent their clustering within c-halos. Thus, we have modeled the neutrino density field as the sum of a linear and a clustered component, differently from what present in literature (see [1]). We emphasize that in order to have a good description of both the cross and the neutrinos auto-power spectrum we need to account for the tiny, fully nonlinear, clustering of neutrinos within c-halos.

While the clustered neutrino component is important to determine the cross and the neutrino power spectra at small scales, it is negligible in the computation of the total matter power spectrum. Therefore, in order to compute the total matter power spectrum in massive neutrino cosmologies an excellent assumption is that neutrinos follow linear theory and that the cross power spectrum is the linear one. We find that our model is capable of reproducing the total matter power spectrum from simulations on large and small scales within a 10%, whereas at intermediate scales, the most challenging for the halo model, it can reproduce the results of the N-body simulations within a $\sim 20 - 30\%$.

We have computed the ratio between the matter power spectrum of a massive and massless neutrinos cosmology, $\Delta^2_\nu(k)/\Delta^2_{\Lambda\rm CDM}(k)$. Linear theory fails to explain the spoon-shape trend present in that ratio around $k \sim 1$ h/Mpc, whereas our model succeeds in doing it. In fact, the disagreement between our predictions for the ratio $\Delta^2_\nu(k)/\Delta^2_{\Lambda\rm CDM}(k)$ and simulations is below 2%, 5%, 10% for $\sum m_\nu = 0.15$, 0.3, 0.6 eV cosmologies, at both $z = 0$ and $z = 1$ and over the whole range of scales investigated.

Finally, we have investigated the clustering of galaxies, in massless and massive neutrinos cosmologies, using a simple HOD model and our halo model extension. We computed the projected correlation function of galaxies with magnitudes $M_r - 5\log_{10} h = -21.0$ taking the HOD parameters calibrated by Villaescusa-Navarro et al. [124]. We find an excellent agreement between the galaxy clustering predicted by our model and the SDSS observations against with the values of the HOD parameters were calibrated. This result points out that our extension of the halo model can be used to calibrate the HOD parameters in cosmologies with massive neutrinos. Whereas the calibration of the HOD parameters directly from N-body simulations is computationally very

demanding and is subjected to problems like resolution and cosmic variance, the halo model provides a fast, and very accurate framework to carry out this task.

Overall, the neutrino halo model presented here is a simple tool to quantitatively address nonlinearities induced by neutrinos, which has also the big advantage of offering physical insights on the relative interplay between neutrino and cold dark matter around virialized structures.

In Part III we analyzed the relative differences in the void properties due to the presence of massive neutrinos. We have run two sets of N-body simulations, one with low resolution and another with higher resolution. Each set of simulations have been computed in four different cosmologies, i.e. with neutrino masses equal to 0.0 eV, 0.15 eV, 0.3 eV and 0.6 eV. We have used the low resolution simulations to identify voids in the CDM particle distribution and the high resolution ones for studying voids in the galaxy field.

In Chapter 8 we have considered voids in the CDM field. We have studied the number density of voids at redshift $z = 0$ and $z = 1$. In both cases, the number density of small voids is higher in massive neutrino cosmologies, whereas the number density of big voids is lower. The difference between ΛCDM and cosmologies with massive neutrinos increases with the neutrino mass, but it decreases with the redshift. This can be understood in terms of the total mass contained in the void. Indeed, neutrinos have high thermal velocity which prevents them to feel the void dynamics and to create a deep underdensity around the void center. This translates into an extra mass within the void that will evolve slowly. Therefore voids in the massive neutrino universe are smaller. However, the additional mass has a smaller effect at high redshift, where voids are denser, thus resulting in smaller differences at $z = 1$.

Secondly we studied the distribution of void ellipticities and computed the correlation function of voids having radius within specific ranges. Both observables indicates that voids in massive neutrinos universes are younger than in their massless neutrino cosmology corresponding model.

Another interesting property of voids is their density profile. We computed the CDM, the neutrino, and the total matter density profiles for different void sizes and in the four different cosmologies. We found that small voids present a compensated wall at the edge, whereas large voids have a non-positive profile. Again, we can understand the differences between massive and massless cosmologies once we consider that voids are effectively less evolved in the presence of massive neutrinos. Indeed, voids evolve by evacuating particles, becoming progressively emptier and building the wall. For each void size in both CDM and matter density field, ΛCDM cosmology presents higher walls and emptier cores, in agreement with this explanation. Instead, the neutrino profile is flatter, given the neutrinos' high thermal velocities. They also tend to follow the CDM one: around small voids there is a positive overdensity of neutrinos in correspondence with the wall, whereas the neutrino profile presents usually an underdensity in the core of big voids. All departures from the mean background get more pronounced as the neutrino mass increases. Focusing on the total matter profile, which is the most important one since most of the observables depend on the total matter distribution, we obtained the following results. In the void core, the differences between ΛCDM and the 0.15 eV cosmology are at the level of 1-3%, depending on the void radius, and they

reach the 10% for the 0.6 eV case. Near the wall and for the very small voids, the difference is at the 5% level for 0.15 eV and at the 20% level for 0.6 eV cosmologies. The differences increase at redshift $z = 1$.

The last investigated property of voids identified in the CDM field is the radial velocity profile of CDM, neutrino, and total matter around voids. The CDM and total matter profiles have the following behavior: the radial velocity is positive inside the void radius around which it reaches the maximum, then it decreases and it becomes negative for very small voids. It remains positive, but at a small value, for large ones. This means that particles inside voids move towards the edge, evacuating and expanding the voids, whereas the outer particles have different behaviors depending on the void size. In small voids they move towards the center participating in the building up of the wall and eventually making the void collapse (the void-in-cloud effect). Instead, in big voids they go far away, but at somewhat smaller velocity than the ones in the inner parts, giving rise to a concentration of mass around the edge of the void. The neutrino radial velocity follows the same behavior, but it has a smaller magnitude, and this is due only to a cancellation effect. Indeed, neutrinos have high thermal velocities that make them free-stream in every direction and the average velocity is close to zero.

In Chapter 9 we have analyzed the high resolution N-body simulations. We have populated these simulations with galaxies, following the HOD prescriptions, and we have identified voids in the galaxy distribution. We have shown the cumulative fraction of voids at redshfit $z = 0$. There are some differences among the cosmologies only for voids with $R_{\rm eff} > 30$ Mpc$/h$, where the errors are very large due to the small volume probed by our high resolution simulations. Moreover, the voids are bigger than the ones selected in the CDM field, since the number of tracers here is low given the small box-size. Current surveys can span a larger volume: for example the Sloan Digital Sky Survey[1] III (SDSS-III) with the Data Release 9 (DR9) CMASS sample can cover an effective volume of nearly 1.5 (Gpc$/h)^3$, which is about 20 times bigger than our box-size.

Finally we studied the total matter density and velocity profiles around the galaxy voids, since future surveys like Euclid[2] and DESI[3] are expected to significantly increase the number of observed galaxies. Furthermore, the weak lensing signal will allow to measure the total matter density field. The matter density profiles present some differences with respect to the ones in the CDM voids: they are less underdense and they present the wall even around very big voids. We argued that this is probably due to the galaxy bias with respect to the matter density field. Instead, for what regards comparison among cosmologies, we found the same behavior as in the CDM voids. The velocity profiles show a peculiar shape shared by all the void sizes analyzed, despite of what happens for the CDM voids. The profiles are positive in the inner part of the galaxy voids, they reach zero around the effective radius and they are negative outside. In the inner regions the velocity is higher in ΛCDM, whereas in the outer part of the voids the trend is not unique.

Part IV has been devoted to the study of halo and void profiles. These objects are

[1] http://www.sdss.org
[2] www.euclid-ec.org
[3] desi.lbl.gov

thought to form in special positions of the initial density field, whose characteristics depend on the halo/void formation model considered. However, all models predict the abundance and spacial distribution of halos and voids in the Lagrangian space. We have shown that they also describe the enclosed density profile around biased tracers. Since we can only measure quantity in the evolved Eulerian field, there is the need to evolve the proto-void and proto-halo profiles.

In Chapter 10 we have worked in the Lagrangian space. We have presented different halo/void formation models, such as excursion set, upcrossing model, and excursion set of peaks. We have shown how they can be used to describe the density profile of proto-halos and proto-voids in the Lagrangian field. Indeed, the enclosed density profile around biased tracers is the cross-correlation between the center of tracers and the matter field. Being a cross-correlation, it depends on the bias of the tracers with respect to the underlying density field. Then, we have discussed the shape of profiles and the one of the linear bias. Small voids, as small halos, present a profile that changes sign, while big objects do not. The associated large scale bias presents a lower bound for the halos, $b_{\rm L} > -1$, while it can be arbitrary negative for voids.

In Chapter 11 we have studied the evolution of void Lagrangian profiles. First, we have applied the spherical evolution model and studied the predictions for the Eulerian profiles and linear bias. Two main differences arise between halos and voids. The first is related to the linear bias. Voids can have arbitrary negative bias and therefore, there exists a class of voids with $b_{\rm L} = -1$ for which we have ab Eulerian bias $b_{\rm E} = 0$. These voids should be unclustered on large scales. The same cannot happen for halos, since their Lagrangian bias is $b_{\rm L} > -1$ and thus $b_{\rm E} > 0$. The second difference is related to the density profile. The motion of shell around voids and halos is such that only in voids the gravitational evolution leads to shell-crossing. Finally, we have compared the spherical model predictions with void density profile measurements in N-body simulations. The evolution predicted by the model is in good agreement with measurements of the inner part of voids, but it fails in reproducing the outer part.

We have also studied a second model for the evolution, the so called Zel'dovich approximation. This model gives a good prediction for the evolution on large scales and allows to clearly model the linear bias evolution. Measurements of the void-matter cross-power spectrum have confirmed the predictions on large scales. In this setting, we have also computed and measured the void-matter cross-power spectrum when the voids and the matter field are evaluated at two different times. This analysis can give further insight on the structure and evolution of the void profile and bias.

Finally, we have proposed three similar models for the void density profiles in the evolved field, which are based on the spherical evolution model and the predictions of the Zel'dovich approximation. Further studies are needed to understand which of these models better reproduce the whole void profile, both on large and small scales.

Bibliography

[1] K. Abazajian, E. R. Switzer, S. Dodelson, K. Heitmann, and S. Habib. Nonlinear cosmological matter power spectrum with massive neutrinos: The halo model. *Phys. Rev. D*, 71(4):043507, February 2005.

[2] K. N. Abazajian, J. K. Adelman-McCarthy, M. A. Agüeros, S. S. Allam, C. Allende Prieto, D. An, K. S. J. Anderson, S. F. Anderson, J. Annis, N. A. Bahcall, and et al. The Seventh Data Release of the Sloan Digital Sky Survey. *Astrophys. J. Suppl.*, 182:543–558, June 2009.

[3] I. Achitouv, M. Neyrinck, and A. Paranjape. Testing spherical evolution for modelling void abundances. *Mon.Not.Roy.Astron.Soc.*, 451:3964–3974, August 2015.

[4] S. Agarwal and H. A. Feldman. The effect of massive neutrinos on the matter power spectrum. *Mon. Not. Roy. Astron. Soc.*, 410:1647–1654, January 2011.

[5] Y. Ali-Haïmoud and S. Bird. An efficient implementation of massive neutrinos in non-linear structure formation simulations. *Mon. Not. Roy. Astron. Soc.*, 428:3375–3389, February 2013.

[6] J. M. Bardeen, J. R. Bond, N. Kaiser, and A. S. Szalay. The statistics of peaks of Gaussian random fields. *Astrophys. J.*, 304:15–61, May 1986.

[7] F. Bernardeau. The effects of smoothing on the statistical properties of large-scale cosmic fields. *Astron. Astrophys.*, 291:697–712, November 1994.

[8] S. Bharadwaj. The evolution of correlation functions in the zeldovich approximation and its implications for the validity of perturbation theory. *Astrophys. J.*, 472(1):1, 1996.

[9] M. Biagetti, V. Desjacques, A. Kehagias, and A. Riotto. Nonlocal halo bias with and without massive neutrinos. *Phys. Rev. D*, 90(4):045022, August 2014.

[10] S. Bird, M. Viel, and M. G. Haehnelt. Massive neutrinos and the non-linear matter power spectrum. *Mon. Not. Roy. Astron. Soc.*, 420:2551–2561, March 2012.

[11] J. R. Bond, S. Cole, G. Efstathiou, and N. Kaiser. Excursion set mass functions for hierarchical Gaussian fluctuations. *Astrophys. J.*, 379:440–460, October 1991.

[12] J. R. Bond, G. Efstathiou, and J. Silk. Massive Neutrinos and the Large Scale Structure of the Universe. *Phys. Rev. Lett.*, 45:1980–1984, 1980.

[13] J. R. Bond and S. T. Myers. The Peak-Patch Picture of Cosmic Catalogs. I. Algorithms. *Astrophys. J. Suppl.*, 103:1, March 1996.

[14] Stefano Borgani and Luigi Guzzo. X-ray clusters of galaxies as tracers of structure in the universe. *Nature*, 409:39, 2001.

[15] J. Brandbyge and S. Hannestad. Grid based linear neutrino perturbations in

cosmological N-body simulations. *JCAP*, 5:002, May 2009.

[16] J. Brandbyge, S. Hannestad, T. Haugbølle, and B. Thomsen. The effect of thermal neutrino motion on the non-linear cosmological matter power spectrum. *JCAP*, 8:20, August 2008.

[17] J. Brandbyge, S. Hannestad, T. Haugbølle, and Y. Y. Y. Wong. Neutrinos in non-linear structure formation - the effect on halo properties. *JCAP*, 9:14, September 2010.

[18] R. Brunino, I. Trujillo, F. R. Pearce, and P. A. Thomas. The orientation of galaxy dark matter haloes around cosmic voids. *Mon. Not. Roy. Astron. Soc.*, 375:184–190, February 2007.

[19] G. L. Bryan and M. L. Norman. Statistical Properties of X-Ray Clusters: Analytic and Numerical Comparisons. *Astrophys. J.*, 495:80–99, March 1998.

[20] J. S. Bullock, T. S. Kolatt, Y. Sigad, R. S. Somerville, A. V. Kravtsov, A. A. Klypin, J. R. Primack, and A. Dekel. Profiles of dark haloes: evolution, scatter and environment. *Mon. Not. Roy. Astron. Soc.*, 321:559–575, March 2001.

[21] Yan-Chuan Cai, Mark C. Neyrinck, Istvan Szapudi, Shaun Cole, and Carlos S. Frenk. A Possible Cold Imprint of Voids on the Microwave Background Radiation. *Astrophys.J.*, 786:110, 2014.

[22] Yan-Chuan Cai, Nelson Padilla, and Baojiu Li. Testing Gravity using Void Profiles. 2014.

[23] E. Castorina, E. Sefusatti, R. K. Sheth, F. Villaescusa-Navarro, and M. Viel. Cosmology with massive neutrinos II: on the universality of the halo mass function and bias. *JCAP*, 2:49, February 2014.

[24] K. C. Chan, R. Scoccimarro, and R. K. Sheth. Gravity and large-scale nonlocal bias. *Phys. Rev. D*, 85(8):083509, April 2012.

[25] K. C. Chan, R. K. Sheth, and R. Scoccimarro. Effective Window Function for Lagrangian Halos. *ArXiv e-prints*, November 2015.

[26] Joseph Clampitt and Bhuvnesh Jain. Lensing Measurements of the Mass Distribution in SDSS Voids. 2014.

[27] J. M. Colberg, F. Pearce, C. Foster, E. Platen, R. Brunino, M. Neyrinck, S. Basilakos, A. Fairall, H. Feldman, S. Gottlöber, O. Hahn, F. Hoyle, V. Müller, L. Nelson, M. Plionis, C. Porciani, S. Shandarin, M. S. Vogeley, and R. van de Weygaert. The Aspen-Amsterdam void finder comparison project. *Mon. Not. Roy. Astron. Soc.*, 387:933–944, June 2008.

[28] J. M. Colberg, R. K. Sheth, A. Diaferio, L. Gao, and N. Yoshida. Voids in a ΛCDM universe. *Mon. Not. Roy. Astron. Soc.*, 360:216–226, June 2005.

[29] S. Cole and N. Kaiser. Biased clustering in the cold dark matter cosmogony. *Mon.Not.Roy.Astron.Soc.*, 237:1127–1146, April 1989.

[30] M. Colless, G. Dalton, S. Maddox, W. Sutherland, P. Norberg, S. Cole, J. Bland-Hawthorn, T. Bridges, R. Cannon, C. Collins, W. Couch, N. Cross, K. Deeley, R. De Propris, S. P. Driver, G. Efstathiou, R. S. Ellis, C. S. Frenk, K. Glazebrook, C. Jackson, O. Lahav, I. Lewis, S. Lumsden, D. Madgwick, J. A. Peacock, B. A. Peterson, I. Price, M. Seaborne, and K. Taylor. The 2dF Galaxy Redshift Survey: spectra and redshifts. *Mon. Not. Roy. Astron. Soc.*, 328:1039–1063, December 2001.

[31] A. Cooray and R. Sheth. Halo models of large scale structure. *Phys.Rept.*,

372:1–129, December 2002.

[32] M. Costanzi, F. Villaescusa-Navarro, M. Viel, J.-Q. Xia, S. Borgani, E. Castorina, and E. Sefusatti. Cosmology with massive neutrinos III: the halo mass function and an application to galaxy clusters. *JCAP*, 12:12, December 2013.

[33] C. L. Cowan, Jr., F. Reines, F. B. Harrison, H. W. Kruse, and A. D. McGuire. Detection of the Free Neutrino: A Confirmation. *Science*, 124:103–104, July 1956.

[34] D. J. Croton, V. Springel, S. D. M. White, G. De Lucia, C. S. Frenk, L. Gao, A. Jenkins, G. Kauffmann, J. F. Navarro, and N. Yoshida. The many lives of active galactic nuclei: cooling flows, black holes and the luminosities and colours of galaxies. *Mon. Not. Roy. Astron. Soc.*, 365:11–28, January 2006.

[35] Marc Davis and P.J.E. Peebles. A Survey of galaxy redshifts. 5. The Two point position and velocity correlations. *Astrophys.J.*, 267:465–482, 1982.

[36] V. Desjacques, M. Crocce, R. Scoccimarro, and R. K. Sheth. Modeling scale-dependent bias on the baryonic acoustic scale with the statistics of peaks of Gaussian random fields. *Phys. Rev. D*, 82(10):103529, November 2010.

[37] G. Despali, G. Tormen, and R. K. Sheth. Ellipsoidal halo finders and implications for models of triaxial halo formation. *Mon.Not.Roy.Astron.Soc.*, 431:1143–1159, May 2013.

[38] Scott Dodelson. *Modern Cosmology*. Academic Press, Amsterdam, 2003.

[39] H. El-Ad, T. Piran, and L. N. Dacosta. A catalogue of the voids in the IRAS 1.2-Jy survey. *Mon. Not. Roy. Astron. Soc.*, 287:790–798, June 1997.

[40] C. Fedeli. The clustering of baryonic matter. I: a halo-model approach. *JCAP*, 4:28, April 2014.

[41] C. Fedeli, E. Semboloni, M. Velliscig, M. Van Daalen, J. Schaye, and H. Hoekstra. The clustering of baryonic matter. II: halo model and hydrodynamic simulations. *JCAP*, 8:28, August 2014.

[42] G. L. Fogli, E. Lisi, A. Marrone, and A. Palazzo. Global analysis of three-flavor neutrino masses and mixings. *Progress in Particle and Nuclear Physics*, 57:742–795, October 2006.

[43] F. Fontanot, F. Villaescusa-Navarro, D. Bianchi, and M. Viel. Semi-Analytic Galaxy Formation in Massive Neutrinos Cosmologies. *ArXiv e-prints*, September 2014.

[44] J. E. Forero-Romero, Y. Hoffman, S. Gottlöber, A. Klypin, and G. Yepes. A dynamical classification of the cosmic web. *Mon. Not. Roy. Astron. Soc.*, 396:1815–1824, July 2009.

[45] C. Foster and L. A. Nelson. The Size, Shape, and Orientation of Cosmological Voids in the Sloan Digital Sky Survey. *Astrophys. J.*, 699:1252–1260, July 2009.

[46] N. Frusciante and R. K. Sheth. Lagrangian bias in the local bias model. *JCAP*, 11:016, November 2012.

[47] S. Gottlöber, E. L. Łokas, A. Klypin, and Y. Hoffman. The structure of voids. *Mon. Not. Roy. Astron. Soc.*, 344:715–724, September 2003.

[48] S. A. Gregory and L. A. Thompson. The Coma/A1367 supercluster and its environs. *Astrophys. J.*, 222:784–799, June 1978.

[49] O. Hahn, C. Porciani, C. M. Carollo, and A. Dekel. Properties of dark matter haloes in clusters, filaments, sheets and voids. *Mon. Not. Roy. Astron. Soc.*, 375:489–499, February 2007.

[50] Nico Hamaus, P.M. Sutter, and Benjamin D. Wandelt. Universal Density Profile for Cosmic Voids. *Phys.Rev.Lett.*, 112:251302, 2014.

[51] Nico Hamaus, Benjamin D. Wandelt, P.M. Sutter, Guilhem Lavaux, and Michael S. Warren. Cosmology with Void-Galaxy Correlations. *Phys.Rev.Lett.*, 112(4):041304, 2014.

[52] A. J. S. Hamilton, Alex Matthews, P. Kumar, and Edward Lu. Reconstructing the primordial spectrum of fluctuations of the universe from the observed nonlinear clustering of galaxies. *Astrophys. J.*, 374:L1, 1991.

[53] F. Hoyle and M. S. Vogeley. Voids in the Point Source Catalogue Survey and the Updated Zwicky Catalog. *Astrophys. J.*, 566:641–651, February 2002.

[54] W. Hu, D. J. Eisenstein, and M. Tegmark. Weighing Neutrinos with Galaxy Surveys. *Physical Review Letters*, 80:5255–5258, June 1998.

[55] K. Ichiki and M. Takada. Impact of massive neutrinos on the abundance of massive clusters. *Phys. Rev. D*, 85(6):063521, March 2012.

[56] V. Icke. Voids and filaments. *Mon. Not. Roy. Astron. Soc.*, 206:1P–3P, January 1984.

[57] S. Ilić, M. Langer, and M. Douspis. Detecting the integrated Sachs-Wolfe effect with stacked voids. *Astron. Astrophys.*, 556:A51, August 2013.

[58] M. Jõeveer, J. Einasto, and E. Tago. Spatial distribution of galaxies and of clusters of galaxies in the southern galactic hemisphere. *Mon. Not. Roy. Astron. Soc.*, 185:357–370, November 1978.

[59] Y. P. Jing. The Density Profile of Equilibrium and Nonequilibrium Dark Matter Halos. *Astrophys. J.*, 535:30–36, May 2000.

[60] Nick Kaiser and Gordon Squires. Mapping the dark matter with weak gravitational lensing. *Astrophys. J.*, 404:441–450, 1993.

[61] Elisabeth Krause, Tzu-Ching Chang, Olivier Dore, and Keiichi Umetsu. The Weight of Emptiness: The Gravitational Lensing Signal of Stacked Voids. *Astrophys.J.*, 762:L20, 2013.

[62] C. Lacey and S. Cole. Merger rates in hierarchical models of galaxy formation. *Mon. Not. Roy. Astron. Soc.*, 262:627–649, June 1993.

[63] S. D. Landy and A. S. Szalay. Bias and variance of angular correlation functions. *Astrophys. J.*, 412:64–71, July 1993.

[64] G. Lavaux and B. D. Wandelt. Precision cosmology with voids: definition, methods, dynamics. *Mon. Not. Roy. Astron. Soc.*, 403:1392–1408, April 2010.

[65] G. Lavaux and B. D. Wandelt. Precision Cosmography with Stacked Voids. *Astrophys. J.*, 754:109, August 2012.

[66] J. Lee and D. Park. Constraining the Dark Energy Equation of State with Cosmic Voids. *Astrophys. J.*, 696:L10–L12, May 2009.

[67] J. Lesgourgues and S. Pastor. Massive neutrinos and cosmology. *Phys. Rept.*, 429:307–379, 2006.

[68] A. Lewis, A. Challinor, and A. Lasenby. Efficient Computation of Cosmic Microwave Background Anisotropies in Closed Friedmann-Robertson-Walker Models. *Astrophys. J.*, 538:473–476, August 2000.

[69] M. LoVerde. Halo bias in mixed dark matter cosmologies. *ArXiv e-prints*, May 2014.

[70] M. LoVerde. Spherical collapse in $\nu \Lambda CDM$. *ArXiv e-prints*, May

2014.

[71] M. LoVerde and M. Zaldarriaga. Neutrino clustering around spherical dark matter halos. *Phys. Rev. D*, 89(6):063502, March 2014.

[72] M. Maltoni, T. Schwetz, M. A. Tortola, and J. W. F. Valle. Status of global fits to neutrino oscillations. *New J. Phys.*, 6:122, 2004.

[73] G. Mangano, G. Miele, S. Pastor, T. Pinto, O. Pisanti, and P. D. Serpico. Relic neutrino decoupling including flavour oscillations. *Nuclear Physics B*, 729:221–234, November 2005.

[74] F. Marulli, C. Carbone, M. Viel, L. Moscardini, and A. Cimatti. Effects of massive neutrinos on the large-scale structure of the Universe. *Mon. Not. Roy. Astron. Soc.*, 418:346–356, November 2011.

[75] E. Massara et al. (in prep.). 2016.

[76] Peter Melchior, P.M. Sutter, Erin S. Sheldon, Elisabeth Krause, and Benjamin D. Wandelt. First measurement of gravitational lensing by cosmic voids in SDSS. *Mon.Not.Roy.Astron.Soc.*, 440(4):2922–2927, 2014.

[77] H. J. Mo and S. D. M. White. An analytic model for the spatial clustering of dark matter haloes. *Mon. Not. Roy. Astron. Soc.*, 282:347–361, September 1996.

[78] V. Müller, S. Arbabi-Bidgoli, J. Einasto, and D. Tucker. Voids in the Las Campanas Redshift Survey versus cold dark matter models. *Mon. Not. Roy. Astron. Soc.*, 318:280–288, October 2000.

[79] M. Musso and R. K. Sheth. One step beyond: the excursion set approach with correlated steps. *Mon. Not. Roy. Astron. Soc.*, 423:L102–L106, June 2012.

[80] M. Musso and R. K. Sheth. Stochasticity in halo formation and the excursion set approach. *Mon.Not.Roy.Astron.Soc.*, 442:401–405, July 2014.

[81] A. Natarajan, A. R. Zentner, N. Battaglia, and H. Trac. Systematic errors in the measurement of neutrino masses due to baryonic feedback processes: Prospects for stage IV lensing surveys. *Phys. Rev. D*, 90(6):063516, September 2014.

[82] J. F. Navarro, C. S. Frenk, and S. D. M. White. The Structure of Cold Dark Matter Halos. *Astrophys. J.*, 462:563, May 1996.

[83] J. F. Navarro, C. S. Frenk, and S. D. M. White. A Universal Density Profile from Hierarchical Clustering. *Astrophys. J.*, 490:493–508, December 1997.

[84] M. C. Neyrinck. ZOBOV: a parameter-free void-finding algorithm. *Mon. Not. Roy. Astron. Soc.*, 386:2101–2109, June 2008.

[85] K.A. Olive and Particle Data Group. Review of particle physics. *Chinese Physics C*, 38(9):090001, 2014.

[86] N. Palanque-Delabrouille, C. Yèche, J. Baur, C. Magneville, G. Rossi, J. Lesgourgues, A. Borde, E. Burtin, J.-M. LeGoff, J. Rich, M. Viel, and D. Weinberg. Neutrino masses and cosmology with Lyman-alpha forest power spectrum. *JCAP*, 11:011, November 2015.

[87] A. Paranjape, T. Y. Lam, and R. K. Sheth. A hierarchy of voids: more ado about nothing. *Mon.Not.Roy.Astron.Soc.*, 420:1648–1655, February 2012.

[88] A. Paranjape, E. Sefusatti, K. C. Chan, V. Desjacques, P. Monaco, and R. K. Sheth. Bias deconstructed: unravelling the scale dependence of halo bias using real-space measurements. *Mon.Not.Roy.Astron.Soc.*, 436:449–459, November 2013.

[89] A. Paranjape and R. K. Sheth. Halo bias in the excursion set approach with

correlated steps. *Mon. Not. Roy. Astron. Soc.*, 419:132–137, January 2012.

[90] A. Paranjape and R. K. Sheth. Peaks theory and the excursion set approach. *Mon. Not. Roy. Astron. Soc.*, 426:2789–2796, November 2012.

[91] A. Paranjape, R. K. Sheth, and V. Desjacques. Excursion set peaks: a self-consistent model of dark halo abundances and clustering. *Mon.Not.Roy.Astron.Soc.*, 431:1503–1512, May 2013.

[92] S. G. Patiri, J. E. Betancort-Rijo, F. Prada, A. Klypin, and S. Gottlöber. Statistics of voids in the two-degree Field Galaxy Redshift Survey. *Mon. Not. Roy. Astron. Soc.*, 369:335–348, June 2006.

[93] D. Paz, M. Lares, L. Ceccarelli, N. Padilla, and D. G. Lambas. Clues on void evolution-II. Measuring density and velocity profiles on SDSS galaxy redshift space distortions. *Mon. Not. Roy. Astron. Soc.*, 436:3480–3491, December 2013.

[94] J. A. Peacock and S. J. Dodds. Reconstructing the Linear Power Spectrum of Cosmological Mass Fluctuations. *Mon. Not. Roy. Astron. Soc.*, 267:1020, April 1994.

[95] Alice Pisani, P.M. Sutter, Nico Hamaus, Esfandiar Alizadeh, Rahul Biswas, et al. Counting voids to probe dark energy. 2015.

[96] Planck Collaboration, P. A. R. Ade, N. Aghanim, M. Arnaud, M. Ashdown, J. Aumont, C. Baccigalupi, A. J. Banday, R. B. Barreiro, J. G. Bartlett, and et al. Planck 2015 results. XIII. Cosmological parameters. *ArXiv e-prints*, February 2015.

[97] Erwin Platen, Rien van de Weygaert, and Bernard J.T. Jones. A Cosmic Watershed: The WVF Void Detection Technique. *Mon.Not.Roy.Astron.Soc.*, 380:551–570, 2007.

[98] M. Plionis and S. Basilakos. The size and shape of local voids. *Mon. Not. Roy. Astron. Soc.*, 330:399–404, February 2002.

[99] W. H. Press and P. Schechter. Formation of Galaxies and Clusters of Galaxies by Self-Similar Gravitational Condensation. *Astrophys. J.*, 187:425–438, February 1974.

[100] A. Ringwald and Y. Y. Y. Wong. Gravitational clustering of relic neutrinos and implications for their detection. *JCAP*, 12:5, December 2004.

[101] S. Shandarin, H. A. Feldman, K. Heitmann, and S. Habib. Shapes and sizes of voids in the Lambda cold dark matter universe: excursion set approach. *Mon. Not. Roy. Astron. Soc.*, 367:1629–1640, April 2006.

[102] R. K. Sheth. An excursion set model for the distribution of dark matter and dark matter haloes. *Mon. Not. Roy. Astron. Soc.*, 300:1057–1070, November 1998.

[103] R. K. Sheth. Dark Matters. In G. Borner and H. Mo, editors, *From Stars to Galaxies to the Universe*, page 31, 1999.

[104] R. K. Sheth, K. C. Chan, and R. Scoccimarro. Nonlocal Lagrangian bias. *Phys. Rev. D*, 87(8):083002, April 2013.

[105] R. K. Sheth and G. Lemson. Biasing and the distribution of dark matter haloes. *Mon.Not.Roy.Astron.Soc.*, 304:767–792, April 1999.

[106] R. K. Sheth, H. J. Mo, and G. Tormen. Ellipsoidal collapse and an improved model for the number and spatial distribution of dark matter haloes. *Mon.Not.Roy.Astron.Soc.*, 323:1–12, May 2001.

[107] R. K. Sheth and G. Tormen. Large-scale bias and the peak background split.

Mon. Not. Roy. Astron. Soc., 308:119–126, September 1999.

[108] R. K. Sheth and G. Tormen. An excursion set model of hierarchical clustering: ellipsoidal collapse and the moving barrier. *Mon.Not.Roy.Astron.Soc.*, 329:61–75, January 2002.

[109] R. K. Sheth and R. van de Weygaert. A hierarchy of voids: much ado about nothing. *Mon. Not. Roy. Astron. Soc.*, 350:517–538, May 2004.

[110] M. Shoji and E. Komatsu. Erratum: Massive neutrinos in cosmology: Analytic solutions and fluid approximation [Phys. Rev. D 81, 123516 (2010)]. *Phys. Rev. D*, 82(8):089901, October 2010.

[111] S. Singh and C.-P. Ma. Neutrino clustering in cold dark matter halos: Implications for ultrahigh energy cosmic rays. *Phys. Rev. D*, 67(2):023506, January 2003.

[112] R. E. Smith, J. A. Peacock, A. Jenkins, S. D. M. White, C. S. Frenk, F. R. Pearce, P. A. Thomas, G. Efstathiou, and H. M. P. Couchmann. Stable clustering, the halo model and nonlinear cosmological power spectra. *Mon. Not. Roy. Astron. Soc.*, 341:1311, 2003.

[113] V. Springel. The cosmological simulation code GADGET-2. *Mon. Not. Roy. Astron. Soc.*, 364:1105–1134, December 2005.

[114] Casey W. Stark, Andreu Font-Ribera, Martin White, and Khee-Gan Lee. Voids in Lyα Forest Tomographic Maps. 2015.

[115] G. Steigman, D. N. Schramm, and J. E. Gunn. Cosmological limits to the number of massive leptons. *Physics Letters B*, 66:202–204, January 1977.

[116] P. M. Sutter, G. Lavaux, N. Hamaus, A. Pisani, B. D. Wandelt, M. Warren, F. Villaescusa-Navarro, P. Zivick, Q. Mao, and B. B. Thompson. VIDE: The Void IDentification and Examination toolkit. *Astronomy and Computing*, 9:1–9, March 2015.

[117] István Szapudi, András Kovács, Benjamin R. Granett, Zsolt Frei, Joseph Silk, et al. Detection of a Supervoid Aligned with the Cold Spot of the Cosmic Microwave Background. *Mon.Not.Roy.Astron.Soc.*, 450:288–294, 2015.

[118] R. Takahashi, M. Sato, T. Nishimichi, A. Taruya, and M. Oguri. Revising the Halofit Model for the Nonlinear Matter Power Spectrum. *Astrophys. J.*, 761:152, December 2012.

[119] A. N. Taylor and A. J. S. Hamilton. Non-linear cosmological power spectra in real and redshift space. *Mon.Not.Roy.Astron.Soc.*, 282:767–778, October 1996.

[120] M. P. van Daalen, J. Schaye, C. M. Booth, and C. Dalla Vecchia. The effects of galaxy formation on the matter power spectrum: a challenge for precision cosmology. *Mon. Not. Roy. Astron. Soc.*, 415:3649–3665, August 2011.

[121] M. Viel, M. G. Haehnelt, and V. Springel. The effect of neutrinos on the matter distribution as probed by the intergalactic medium. *JCAP*, 6:015, June 2010.

[122] Matteo Viel, Joerg M. Colberg, and Tae-Sun Kim. On the importance of high redshift intergalactic voids. *Mon.Not.Roy.Astron.Soc.*, 386:1285, 2008.

[123] F. Villaescusa-Navarro, S. Bird, C. Peña-Garay, and M. Viel. Non-linear evolution of the cosmic neutrino background. *JCAP*, 3:019, March 2013.

[124] F. Villaescusa-Navarro, F. Marulli, M. Viel, E. Branchini, E. Castorina, E. Sefusatti, and S. Saito. Cosmology with massive neutrinos I: towards a realistic modeling of the relation between matter, haloes and galaxies. *JCAP*, 3:11, March 2014.

[125] F. Villaescusa-Navarro, J. Miralda-Escudé, C. Peña-Garay, and V. Quilis. Neutrino halos in clusters of galaxies and their weak lensing signature. *JCAP*, 6:27, June 2011.

[126] F. Villaescusa-Navarro, M. Vogelsberger, M. Viel, and A. Loeb. Neutrino Signatures on the High Transmission Regions of the Lyman-alpha Forest. *ArXiv e-prints*, June 2011.

[127] C. Wagner, L. Verde, and R. Jimenez. Effects of the Neutrino Mass Splitting on the Nonlinear Matter Power Spectrum. *Astrophys. J.*, 752:L31, June 2012.

[128] D. G. York and SDSS Collaboration. The Sloan Digital Sky Survey: Technical Summary. *Astron. J.*, 120:1579–1587, September 2000.

[129] I. Zehavi, Z. Zheng, D. H. Weinberg, M. R. Blanton, N. A. Bahcall, A. A. Berlind, J. Brinkmann, J. A. Frieman, J. E. Gunn, R. H. Lupton, R. C. Nichol, W. J. Percival, D. P. Schneider, R. A. Skibba, M. A. Strauss, M. Tegmark, and D. G. York. Galaxy Clustering in the Completed SDSS Redshift Survey: The Dependence on Color and Luminosity. *Astrophys. J.*, 736:59, July 2011.

[130] Idit Zehavi et al. The Luminosity and color dependence of the galaxy correlation function. *Astrophys.J.*, 630:1–27, 2005.

[131] Y. B. Zel'dovich. Gravitational instability: An approximate theory for large density perturbations. *Astron.Astrophys*, 5:84–89, March 1970.

[132] Paul Zivick and P.M. Sutter. Distinguishing f(R) gravity with cosmic voids. 2014.